

# Measurement of the spin structure function $g_1^D$ of the deuteron and its moments at low $Q^2$

Krishna P. Adhikari, Sebastian E. Kuhn,  
Alexander Deur, Lamiaa El Fassi, Hyekoo Kang, Sarah K. Phillips,  
Marco Ripani, Karl Slifer, Raffaella De Vita, Gail E. Dodge,  
Xiaochao Zheng

March 6, 2017

# Contents

<b>1</b>	<b>Introduction</b>	<b>4</b>
1.1	Inclusive Electron Scattering . . . . .	7
1.1.1	Kinematic Variables . . . . .	7
1.1.2	Differential Cross Section and Structure Functions . . .	9
1.2	Moments of $g_1$ and Sum Rules . . . . .	10
1.2.1	First moment $\Gamma_1$ of $g_1$ . . . . .	11
1.2.2	Generalized GDH Integral . . . . .	13
1.2.3	Generalized Forward Spin Polarizability $\gamma_0$ . . . . .	15
<b>2</b>	<b>EG4 run</b>	<b>17</b>
2.1	New CC in the 6 <sup>th</sup> Sector . . . . .	18
<b>3</b>	<b>Data Analysis Procedure</b>	<b>21</b>
3.1	Raw Data Processing - Calibration and Reconstruction . . . . .	22
3.2	Helicity States . . . . .	24
3.3	Electron Identification . . . . .	24
3.3.1	Electromagnetic Calorimeter Cuts . . . . .	26
3.3.2	Cerenkov Counter Cuts . . . . .	35
3.3.3	Minimum/Maximum Momentum cuts . . . . .	41
3.3.4	Vertex-Z cuts . . . . .	42
3.3.5	Fiducial Cuts . . . . .	44
3.4	Data Quality and Stability Checks . . . . .	51
3.5	Kinematic Corrections . . . . .	54
3.5.1	Incoming Energy Loss Correction . . . . .	54
3.5.2	Tracking Corrections . . . . .	55
3.5.3	Momentum Correction . . . . .	62
3.5.4	Outgoing Ionization Loss Correction . . . . .	66
3.6	Cerenkov Counter (CC) Efficiency . . . . .	67

3.6.1	Procedure . . . . .	69
3.7	Pion Contamination Corrections . . . . .	74
3.7.1	Method . . . . .	74
3.8	$e^+e^-$ -Pair Symmetric Contamination Corrections . . . . .	76
3.9	Study of NH <sub>3</sub> Contamination of EG4 ND <sub>3</sub> Target . . . . .	78
3.9.1	Procedure . . . . .	78
3.9.2	Event Selection . . . . .	79
3.9.3	Extracting the Contamination . . . . .	81
3.9.4	Results and Conclusion . . . . .	82
<b>4</b>	<b>Monte Carlo Simulations and Extraction of <math>g_1</math> and <math>A_1 F_1</math></b>	<b>84</b>
4.1	Simulation and Approach to Analysis . . . . .	84
4.1.1	Outline of the method . . . . .	87
4.2	Radiative Corrections . . . . .	89
4.3	“Standard” simulation . . . . .	89
4.3.1	RCSLACPOL . . . . .	90
4.3.2	Event Generator . . . . .	90
4.3.3	GSIM - CLAS Detector Simulation . . . . .	93
4.3.4	GSIM POST PROCESSOR (GPP) . . . . .	93
4.3.5	Finding the width of the real CLAS data elastic peak. .	96
4.4	Comparison of Data and Simulation . . . . .	100
4.5	Method to Extract $g_1$ and $A_1 F_1$ . . . . .	109
4.5.1	‘Variation’ of the standard simulation . . . . .	109
<b>5</b>	<b>Systematic Uncertainties</b>	<b>114</b>
5.1	Model uncertainties . . . . .	117
5.2	Combining uncertainties . . . . .	119
5.2.1	Combining uncertainties from the two beam energies .	119
5.2.2	Combining uncertainties from the ten sources . . . .	120
5.2.3	Combining data from the two beam energies . . . . .	120
<b>6</b>	<b>Results</b>	<b>132</b>
6.1	Extracted $g_1$ and $A_1 F_1$ . . . . .	132
6.2	Moments of Deuteron Spin Structure functions . . . . .	141
6.2.1	First moment of $g_1$ ( $\Gamma_1$ ) . . . . .	143
6.2.2	The extended GDH integral $\bar{I}_{TT}$ . . . . .	145
6.2.3	The Generalized Forward Spin Polarizability $\gamma_0$ . . . .	147

<b>7 Conclusions</b>	<b>150</b>
<b>A FFREAD cards used by GSIM</b>	<b>158</b>

# <sup>1</sup> Chapter 1

## <sup>2</sup> Introduction

<sup>3</sup>

<sup>4</sup> A truly vast amount of data on the inelastic structure of the nucleon has  
<sup>5</sup> been accumulated since the late 1960s from both fixed target and colliding  
<sup>6</sup> beam experiments with polarized as well as un-polarized incident photons,  
<sup>7</sup> (anti)electrons, muons and (anti)neutrinos as well as (anti)protons on a vari-  
<sup>8</sup> ety of targets (both polarized and unpolarized) from hydrogen through iron  
<sup>9</sup> [1]. The initial measurements at SLAC confirmed the picture of the nucleon  
<sup>10</sup> as made up of partons (now identified with quarks and gluons). Since then  
<sup>11</sup> more precise measurements have been conducted at several accelerators, im-  
<sup>12</sup> proving our knowledge and understanding about the nucleon structure (both  
<sup>13</sup> spin-dependent and spin-averaged), and, at the same time, continuing to give  
<sup>14</sup> us new and sometimes very surprising results such as the original “European  
<sup>15</sup> Muon Collaboration (EMC)-Effect” [2], the violation of the Gottfried sum  
<sup>16</sup> rule [3, 4], and the so-called ”Spin-Crisis” [5, 6] (see below). **Will soon work**  
<sup>17</sup> **on the order of references/citations.**

<sup>18</sup> With such a vast amount of experimental data available, a lot is now  
<sup>19</sup> known about the spin-averaged quark structure of the nucleon, but a lot less  
<sup>20</sup> is known about the spin-structure of the nucleon in terms of its constituents  
<sup>21</sup> quarks and gluons [1]. In a simple non-relativistic model one would expect  
<sup>22</sup> the quarks to carry the entire spin of the nucleon, but one of the early more  
<sup>23</sup> realistic theories that explained the partonic substructure of the nucleon,  
<sup>24</sup> the Naive Parton Model (NPM), predicted that 60% of the nucleon spin is  
<sup>25</sup> carried by the quarks [7].

<sup>26</sup> The polarized beam and target technologies have greatly advanced dur-  
<sup>27</sup> ing the last three decades, and many subsequent experiments on nucleons

and some nuclei have contributed to the extraction of their spin structure functions  $g_1$  and  $g_2$ , which carry information on how the spin is distributed inside the target. One of the first experiments carried out at SLAC, in a limited kinematic region, seemed to confirm the predictions of the NPM. However, a subsequent, more precise measurement over a larger kinematic region performed by the EMC experiment at CERN reported that, contrary to the NPM predictions, only  $12 \pm 17\%$  of the spin is carried by the quarks [5, 6]. This discovery of the so-called “spin crisis” sparked a large interest in measuring the spin content of the nucleon, giving birth to several experiments (completed, underway and proposed) around the globe. The theoretical developments of Quantum Chromodynamics (QCD) - the quantum field theory that describes the nuclear interaction between the quarks and gluons - have clarified our picture of the nucleon spin structure in great details. With the discovery of a unique QCD property known as “asymptotic freedom”, quarks are known to be essentially free at high energies (typically several GeV) allowing perturbative QCD (PQCD) calculations of testable predictions for processes involving high energy or high momentum transfers [8]. Verifying Bjorken sum rule, Reference to be added soon which relates results from inclusive, polarized deep inelastic scattering (DIS) to the axial coupling constant  $g_A$  of neutron beta decay, is a precise test of QCD in its spin sector. The DIS results have verified the Bjorken sum rule at the level of 10% accuracy and has shown that only about  $30 \pm 10\%$  of the nucleon spin is carried by the quarks; the rest of the spin must reside either in gluons or orbital angular momentum of its constituents. Experiments to measure the gluon contribution are underway at Brookhaven National Laboratory (BNL) and CERN.

Probing nucleon structure on the other end of the energy scale (i.e. probing with low momentum transfers) provides information about long distance structure, which is also associated with static properties of the nucleon. In this low energy regime, however, QCD calculations with the established perturbative methods become difficult or even impossible because the strong coupling ( $\alpha_s$ ) becomes large. Thus perturbative expansions do not converge. In this energy regime, the partons become very strongly coupled to the point of being confined into hadrons which now emerge as the effective degrees of freedom for the interaction. Therefore, other methods must be relied on to make predictions in these non-perturbative energy scales. For example, effective theories such as chiral perturbation theory ( $\chi$ PT) are used. There is also an intermediate region where neither of these approaches (PQCD or  $\chi$ PT)

is expected to work. In this region, it is expected that lattice QCD methods will provide testable predictions in the near future. There are also some phenomenological models aimed at describing the entire kinematic range. The description of the low energy regime in terms of these theories and models is challenging and theories used here still face difficulties (see below). There are several predictions (for both nucleons as well as some light nuclei such as the deuteron and Helium-3) from these low energy theories and models on various observables which can be tested experimentally. Therefore, having high precision data at the lowest possible momentum transfer is necessary to test these predictions. In addition, new results will also help constrain future calculations and provide input for detailed corrections to higher energy data.

With that perspective and motivation, the “EG4” experiment (E06-017) for a precision double polarization measurement at low momentum transfer using both proton and deuteron targets and the Hall B CLAS detector was performed at Jefferson Lab. In addition to the usefulness of the measured deuteron data for testing theoretical predictions calculated for the deuteron itself, the data are also necessary for extracting neutron data in combination with similar data from the proton target. An experiment with the similar goal of probing the neutron at low momentum transfers but using  $^3\text{He}$  was performed in Hall A [9]. However, to be able to control nuclear medium effects, neutron information must be extracted from both  $^3\text{He}$  and  $^2\text{D}$ . The data on the deuteron (and eventually on the neutron) will not only be useful to test the theoretical predictions at low but non-zero momentum transfers but they can also be extrapolated to the real photon limit, thus testing some long standing predictions such as the Gerasimov-Drell-Hearn (GDH) sum rule Reference to be added soon derived from general principles. The analysis of the deuteron data is the subject of this note.

In the future, we will extract information from the deuteron and proton data from the EG4 experiment to provide a self-consistent determination of the Bjorken sum, helping us to understand the transition from the partonic to hadronic descriptions of the strong interaction. The data will also be useful in studying the validity of quark-hadron duality in the spin sector, thus helping further to understand the transition from the partonic to hadronic pictures.

<sub>99</sub> **1.1 Inclusive Electron Scattering**

<sub>100</sub> High energy particle scattering processes provide very powerful microscopes  
<sub>101</sub> to examine objects such as nuclei and nucleons. Scattering of leptons (most  
<sub>102</sub> commonly electrons) is one of the most extensively used processes. For ex-  
<sub>103</sub> ample, the scattering of high energy leptons off nucleons has played a key role  
<sub>104</sub> in determining the partonic structure of the nucleons. Following are some of  
<sub>105</sub> the advantages of lepton (and in particular electron) scattering:

- <sub>106</sub> • Leptons interact through the electroweak interaction which is very well  
<sub>107</sub> understood.
- <sub>108</sub> • The interaction is relatively weak, thus allowing the use of perturbative  
<sub>109</sub> QED.
- <sub>110</sub> • In electron scattering, one can, moreover, control and vary the po-  
<sub>111</sub> larization of the virtual photon (exchanged during the interaction) by  
<sub>112</sub> changing the electron kinematics. This allows the separation of the  
<sub>113</sub> charge and current interaction. Data from the scattering of polarized  
<sub>114</sub> electrons by polarized targets allows one to examine the target's strong-  
<sub>115</sub> interaction spin structure.
- <sub>116</sub> • A great advantage of electrons is that they can be copiously produced  
<sub>117</sub> in the laboratory relatively easily and at low costs, and since they are  
<sub>118</sub> charged, they can readily be accelerated and detected. (It is not as  
<sub>119</sub> easy and cheap to produce and handle the other lepton types.

<sub>120</sub> In this section, we discuss the process of inclusive electron scattering (in  
<sub>121</sub> which only the scattered electron is detected ignoring the rest of the com-  
<sub>122</sub> ponents of the final state after the interaction). In doing so, the relevant  
<sub>123</sub> kinematic variables and related physical quantities to be measured or calcu-  
<sub>124</sub> lated from the process will be introduced and some of their relations with  
<sub>125</sub> one another will be deduced and discussed.

<sub>126</sub> **1.1.1 Kinematic Variables**

<sub>127</sub> A lepton scattering process, in which an incoming lepton represented by  $l(p)$   
<sub>128</sub> of four momentum  $p = p^\mu = (E, \vec{k})$  scatters off a target  $N(P)$  which is usually

<sup>129</sup> a nucleon or a nucleus at rest and with four momentum  $P = P^\mu = (M, \vec{0})$ ,  
<sup>130</sup> can simply be represented by

$$l(p) + N(P) \rightarrow l(p') + X(P') \quad (1.1)$$

<sup>131</sup> where  $l(p')$  and  $X(P')$  represent the scattered lepton and the rest of the  
<sup>132</sup> final state (which can have any number of particles) with four momenta  
<sup>133</sup>  $p'^\mu = (E', \vec{k}')$  and  $P'^\mu = (E_X, \vec{k}_X)$  respectively. The scattering angle which is  
<sup>134</sup> the angle between the incident and outgoing path/direction of the electron  
<sup>135</sup> is denoted by  $\theta$ . The final (hadronic) state denoted by  $x$  is not measured,  
<sup>136</sup> with only the scattered electron detected and measured by the detector(s).  
<sup>137</sup> In the first order (Born) approximation of the process, a virtual photon is  
<sup>138</sup> exchanged (as depicted in Fig (1.1)) whose four momentum is equal to the  
<sup>139</sup> difference between that of the incident and the scattered electron and is given  
<sup>140</sup> by  $(p - p')^\mu = (\nu, \vec{q})$ , where  $\nu = (P \cdot q)/M$  and  $\vec{q}$  represent the energy and  
<sup>141</sup> 3-momentum transferred by the incident electron to the target  $N(P)$ .

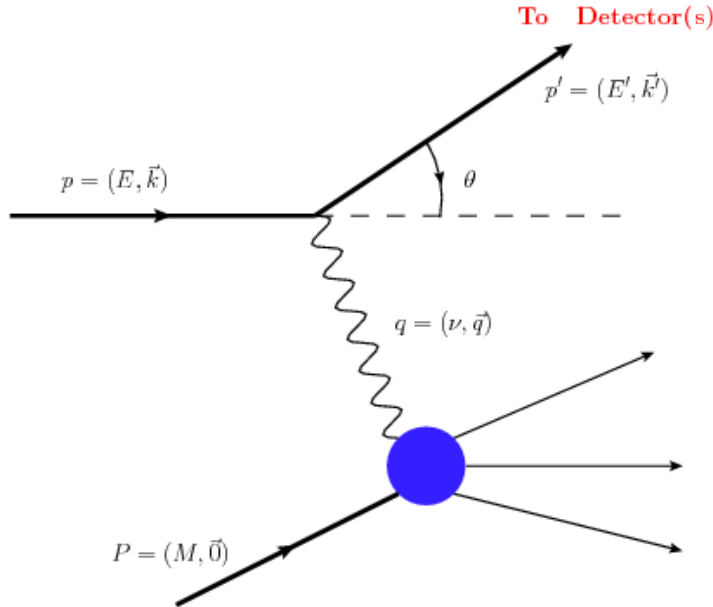


**Figure 1.1:** Lowest order (Born approximation) Feynmann diagram representing the process of inclusive lepton scattering

<sup>142</sup> The kinematics of the scattering process, for a given beam energy  $E$ , can  
<sup>143</sup> be completely described in terms of two of the following Lorentz invariant

144 variables.

$$\nu = E - E' \quad (1.2)$$

$$Q^2 = -q^2 \simeq 4EE' \sin^2 \frac{\theta}{2} \quad (1.3)$$

$$W = \sqrt{(P+q)^2} = \sqrt{M^2 + 2M\nu - Q^2} \quad (1.4)$$

$$x = \frac{Q^2}{2P \cdot q} = \frac{Q^2}{2M\nu} \quad (1.5)$$

$$y = \frac{q \cdot P}{p \cdot P} = \frac{\nu}{E} \quad (1.6)$$

145 where  $Q^2 = -q^2$  is the negative of the squared four-momentum transferred  
146 (with electron mass neglected in the expression for  $Q^2$ ), which defines the  
147 resolution of the electron probe;  $W$  is the invariant mass of the unmeasured  
148 final state ( $x$ );  $x$  is known as the Bjorken scaling variable, which is also  
149 interpreted as the momentum fraction carried by the struck quark (parton)  
150 in the infinite momentum frame;  $M$  is the nucleon mass  $\approx 0.939$  GeV, and  
151 lastly,  $y$  is the fraction of the energy that is lost by the lepton during the  
152 process.

### 153 1.1.2 Differential Cross Section and Structure Functions

154

155 The differential cross section for the process of inclusive (polarized) elec-  
156 tron scattering on (polarized) targets can be expressed, in the Born ap-  
157 proximation, in terms of four dimensionless structure functions  $F_1(x, Q^2)$ ,  
158  $F_2(x, Q^2)$ ,  $g_1(x, Q^2)$ , and  $g_2(x, Q^2)$ , effectively parameterizing the internal  
159 hadronic structure information into four response functions. For example,  
160 in the case of the anti-parallel or parallel beam and target polarizations,  
161 the spin-dependent (polarized) inclusive cross sections can be expressed as  
162 follows:

$$\frac{d^2\sigma}{d\Omega dE'} = \left( \frac{d\sigma}{d\Omega} \right)_{Point} \left[ \frac{2}{M} F_1(x, Q^2) \tan^2 \frac{\theta}{2} + \frac{1}{\nu} F_2(x, Q^2) \right. \\ \left. \pm 2 \tan^2 \frac{\theta}{2} \left[ (E + E' \cos \theta) \frac{M^2}{\nu} g_1(Q^2, \nu) - \gamma^2 M^2 g_2(Q^2, \nu) \right] \right]^{(1.7)}$$

163 where “+” refers to anti-parallel beam helicity and target polarization,  
 164 while “-” refers to the parallel case. And the Point cross section (for the  
 165 lepton scattering from a Dirac particle - a spin-1/2 point particle of charge  
 166 +e) given by

$$\left( \frac{d\sigma}{d\Omega} \right)_{Point} = \frac{\alpha^2 \cos^2 \frac{\theta}{2}}{4E^2 \sin^4 \frac{\theta}{2}} \frac{E'}{E} \quad (1.8)$$

167 with  $\frac{E'}{E}$  being the recoil factor.

168 These kind of relationships allow the measurement of structure functions  
 169 by measuring cross-sections corresponding to different combinations of beam  
 170 and target polarizations. For example, one can extract the first two structure  
 171 functions  $F_1$  and  $F_2$  from the unpolarized scattering experiments, whereas,  
 172 the spin structure functions  $g_1$  and  $g_2$  can be measured in experiments with  
 173 polarized electron beam and polarized targets and by measuring the cross  
 174 section difference between the anti-parallel and parallel beam-target polar-  
 175 izations.

## 176 1.2 Moments of $g_1$ and Sum Rules

177 Moments of structure functions are their integrals (over the complete x range)  
 178 weighted by various powers of the variable x. The  $n^{th}$  moment of  $g_1$  , for  
 179 example, is given by

$$\Gamma_n(Q^2) = \int_0^1 g_1(x, Q^2) x^{(n-1)} dx \quad (1.9)$$

180 The moments allow the studies of the ( $Q^2$  dependence of) fundamental  
 181 properties of nucleon structure. For example, the first moment of  $xF_1$  of a  
 182 nucleon gives the total momentum or mass fraction carried by quarks and  
 183 the first moment of  $g_1$  gives the fraction of the nucleon spin contributed by  
 184 the quark helicities. These integrals get their particular significance from  
 185 the fact that they can be predicted from rigorous theoretical methods, such  
 186 as in the sum rules derived from general assumptions or from the method of  
 187 Operator Product Expansion, lattice QCD calculations and  $\chi$ PT calculations

<sup>188</sup> <sup>1</sup> (see Sec. ??). Their importance can be highlighted from the fact that it  
<sup>189</sup> was the experimental tests of the sum rules involving the first moments of  
<sup>190</sup> nucleon that led to the discovery of the original “spin crisis” and provided a  
<sup>191</sup> significant test of QCD in the spin sector [10].

<sup>192</sup> In this section, three integrals are considered which have been calculated  
<sup>193</sup> from the EG4 data on the deuteron - the first moment of  $g_1$  ( $\Gamma_1$ ), the gen-  
<sup>194</sup> eralized GDH integral ( $\bar{I}_{TT}$ ), and the generalized forward spin polarizability  
<sup>195</sup> ( $\gamma_0$ ).

### <sup>196</sup> 1.2.1 First moment $\Gamma_1$ of $g_1$

<sup>197</sup> The first moment of  $g_1$  is the integral of  $g_1$  over the complete range of the  
<sup>198</sup> Bjorken scaling variable  $x$ .

$$\Gamma_1(Q^2) = \int_0^1 g_1(x, Q^2) dx \quad (1.10)$$

<sup>199</sup> This moment gives, in the quark-parton model, the fraction of the nu-  
<sup>200</sup> cleon spin contributed by the quark helicities and enters directly into two  
<sup>201</sup> historically important sum rules - Ellis-Jaffe sum rule and Bjorken sum rule.  
<sup>202</sup> Measurements of the moment on the proton by the European Muon Collabo-  
<sup>203</sup> ration (EMC) in 1988 showed that the Ellis-Jaffe sum rule is violated, which  
<sup>204</sup> meant that the long held belief that all the proton spin is carried by quarks  
<sup>205</sup> is not true, thus, sparking the well known “spin crisis”. On the other hand,  
<sup>206</sup> measurements from SLAC, CERN, Fermilab, DESY, and more recently, from  
<sup>207</sup> JLab, have confirmed the Bjorken sum rule (which relates the difference of  
<sup>208</sup> the first moments of the proton and the neutron to the fundamental axial  
<sup>209</sup> coupling constant ( $g_A$ ) of neutron beta decay) at the level of 10% accuracy,  
<sup>210</sup> thus helping establish the QCD as the correct theory of the strong interac-  
<sup>211</sup> tions. The moment also enters into the virtual photon extension of another  
<sup>212</sup> famous sum rule - the GDH sum rule (see below).

<sup>213</sup> In addition, the moment is studied on its own right because it provides  
<sup>214</sup> a powerful tool to test the validity of various theories and models in which  
<sup>215</sup> it is calculable. In the past, it has been measured on proton, deuteron and

---

<sup>1</sup>In contrast, the same is not true about the structure functions because presently their complete description based on QCD first principles has not been possible yet (especially in the low to intermediate momentum transfer regions due to the strong coupling property of QCD).

216 neutron ( ${}^3\text{He}$ ) at SLAC, CERN and DESY in the DIS region in order to  
217 understand the quark spin contribution as well as to test the validity of the  
218 Bjorken sum rule and hence QCD as a result [10]. Recently, it has also  
219 been measured at JLab from DIS down to a fairly low  $Q^2$  region. In the  
220 intermediate and low momentum transfers, some phenomenological model  
221 predictions are available, whereas in the very low  $Q^2$  region, several chiral  
222 perturbation theory ( $\chi\text{PT}$ ) calculations are available.

223 **1.2.2 Generalized GDH Integral**

224 **GDH Sum Rule**

225 The Gerasimov-Drell-Hearn (GDH) sum rule [11, 12] relates the energy weighted  
226 sum of a particle's photo-absorption cross sections to its anomalous magnetic  
227 moment  $\kappa$ . For a target of arbitrary spin  $S$ , the sum rule is:

$$\int_{\nu_{th}}^{\infty} \frac{\sigma_P(\nu) - \sigma_A(\nu)}{\nu} = -4\pi^2 \alpha S \left(\frac{\kappa}{M}\right)^2 \quad (1.11)$$

228 where  $\sigma_P$  and  $\sigma_A$  are the photoabsorption cross sections with photon helicity  
229 parallel and anti-parallel to the target spin respectively.  $M$  and  $\kappa$  represent  
230 the target mass and anomalous magnetic moment respectively and  $S$  rep-  
231 resents the target spin. The integration extends from the onset  $\nu_{th}$  of the  
232 inelastic region <sup>2</sup> through the entire kinematic range and is weighted by the  
233 inverse of the photon energy  $\nu$ .

234 The sum rule for the proton has been measured (at various places such  
235 as Mainz, Bonn, BNL and others) and verified to within 10% [13–16] and  
236 some deuteron results exist from Mainz and Bonn, but there is very little or  
237 no data available on neutron and other targets;

238 **Implications of the sum rule** The sum rule relates the static property  
239  $\kappa$  of a particle's ground state with the sum of the dynamic properties of  
240 all the excited states. One deeper significance of this sum rule is that if a  
241 particle has a non-zero anomalous magnetic moment, then it must have some  
242 internal structure, and, therefore, a finite size, in order to have the excited  
243 states (a point-like particle cannot have excited states). Because of the same  
244 reason, the discovery of nucleon anomalous magnetic moments provided one  
245 of the first strong indications that the nucleons had some intrinsic internal  
246 structure.

247 In addition to the benefit of that implication, the sum rule and its exten-  
248 sion to  $Q^2 > 0$  provides an important testing ground for various theoretical  
249 predictions based on QCD and its effective theories/models.

---

247<sup>2</sup>The pion photo-production threshold given by  $\nu_{th} = m_\pi(1 + m_\pi/2M) \approx 150\text{MeV}$  marks the onset of the inelastic region for the nucleons, but for nuclei, the summation starts from the first nuclear excitation level

250 **Generalization of the GDH Sum (Rule)**

251 In order to investigate the “spin crisis” of the 1980’s, Anselmino *et al.* [17]  
 252 proposed that the real photon ( $Q^2=0$ ) GDH integral could be extended to  
 253 electroproduction cross sections (finite  $Q^2$ ) and that the experimental deter-  
 254 mination of the extended integral would shed light on the transition from  
 255 the perturbative to non-perturbative QCD. The idea was to use the virtual  
 256 photoabsorption cross sections in place of the real photoabsorption cross sec-  
 257 tions and proceed in exactly the same way as when deriving the real photon  
 258 GDH sum rule. This extension depends somewhat on the choice of the vir-  
 259 tual photon flux and on how the spin structure function  $g_2$  is considered [18].  
 260 In one extension the virtual photon flux given by  $K = \nu$  is chosen and the  
 261 real photoabsorption cross section difference in Eq. 1.11 are replaced by  
 262 the corresponding virtual photoabsorption cross section difference  $2\sigma_{TT}$ . As  
 263 a result, we get the following extended GDH integral (considering only the  
 264 inelastic contribution starting from the pion production threshold) [10]

$$\bar{I}_{TT} = \frac{2M^2}{Q^2} \int_0^{x_0(Q^2)} dx [g_1(x, Q^2) - \frac{4M^2 x^2}{Q^2} g_2(x, Q^2)] \quad (1.12)$$

265 where  $x_0(Q^2) = Q^2/(Q^2 + m_\pi(2M + m_\pi))$  is the pion production threshold  
 266 that defines the onset of the inelastic region.

267 The integral can also be expressed in terms of the first moment of the  
 268 product  $A_1 F_1$  as follows:

$$\bar{I}_{TT} = \frac{2M^2}{Q^2} \int_0^{x_0(Q^2)} dx A_1(x, Q^2) F_1(x, Q^2) \quad (1.13)$$

269 where  $A_1$  is the virtual photon asymmetry as given by:

$$A_1(x, Q^2) = \frac{\sigma_{\frac{1}{2}}^T - \sigma_{\frac{3}{2}}^T}{\sigma_{\frac{1}{2}}^T + \sigma_{\frac{3}{2}}^T} = \frac{g_1(x, Q^2) - \gamma^2 g_2(x, Q^2)}{F_1(x, Q^2)} \quad (1.14)$$

$$(1.15)$$

270    **1.2.3 Generalized Forward Spin Polarizability  $\gamma_0$**

271    Polarizabilities are fundamental observables (quantities) that characterize the  
 272    structure of composite objects such as nucleons or deuteron. They reflect the  
 273    response to external perturbations such as external electromagnetic fields.  
 274    Like the GDH sum, they are also integrals over the excitation spectrum of  
 275    the target and their derivations rely on the same basic assumptions. At  
 276    the real photon point, for example, the electric and magnetic polarizabilities  
 277     $\alpha$  and  $\beta$  represent the target's response to external electric and magnetic  
 278    fields respectively. The generalized polarizabilities represent the extensions  
 279    of these quantities to the case of virtual photon Compton scattering. Because  
 280    the integrals defining the polarizabilities involve weighting by some powers  
 281    of  $1/\nu$  or  $x$ , they converge faster than the first moments and thus are more  
 282    easily determined from low energy measurements. In other words, they have  
 283    reduced dependence on the extrapolations to the unmeasured regions at large  
 284     $\nu$ , and higher sensitivity to the low energy behavior of the cross sections  
 285    (particularly the threshold behavior), thus providing better testing grounds  
 286    for theoretical predictions such as from  $\chi$ PT and phenomenological models  
 287    [18].

288    The GDH sum rule comes from the first term of the low energy expansion  
 289    of the forward Compton amplitude [19]. Likewise, we get another sum rule  
 290    from the second, i.e., the next-to-leading term (which is in the third power  
 291    of  $\nu$ ). The second coefficient of the expansion is known as the forward spin  
 292    polarizability  $\gamma_0$  and by comparing the coefficients of the  $\nu^2$  terms on both  
 293    sides (coming from the dispersion relations on the left side and from the low  
 294    energy expansion on the right side) gives us the following expression for the  
 295    polarizability [20]:

$$\gamma_0 = -\frac{1}{4\pi^2} \int_{thr}^{\infty} \frac{\sigma_{\frac{1}{2}} - \sigma_{\frac{3}{2}}}{\nu^3} d\nu \quad (1.16)$$

296    Now, by considering the case of forward scattering of a virtual photon and  
 297    using the same general approach as for getting the generalized GDH sum rule,  
 298    the  $\mathcal{O}(\nu^3)$  (NLO) term in the low energy expansion of VVCS (doubly virtual  
 299    Compton scattering) amplitude  $g_{TT}(x, Q^2)$  gives the following generalization  
 300    of the forward spin polarizability [21] [10]:

$$\begin{aligned}\gamma_0(Q^2) \equiv \gamma_{TT}(Q^2) &= \frac{16\alpha M^2}{Q^6} \int_0^{x_0} \left[ g_1(x, Q^2) - \frac{4M^2 x^2}{Q^2} g_2(x, Q^2) \right] x^2 dx \\ &= \frac{16\alpha M^2}{Q^6} \int_0^{x_0} A_1(x, Q^2) F_1(x, Q^2) x^2 dx\end{aligned}\quad (1.18)$$

301 where  $\alpha = \frac{e^2}{4\pi}$  is the fine structure constant. At large  $Q^2$ , the  $g_2$  dependent  
 302 term in the integrand becomes negligible and  $\gamma_0$  reduces to the third moment  
 303 of  $g_1$ [21].

304 In exactly the same manner, from the  $\mathcal{O}(\nu^2)$  term of the low energy  
 305 expansion of the VVCS amplitude  $g_{LT}(x, Q^2)$  one gets another polarizability  
 306 - the generalized longitudinal-transverse polarizability as follows:

$$\delta_0(Q^2) \equiv \delta_{LT}(Q^2) = \frac{16\alpha M^2}{Q^6} \int_0^{x_0} [g_1(x, Q^2) + g_2(x, Q^2)] x^2 dx \quad (1.19)$$

307 This latter polarizability is not considered here because we did not measure  
 308 the transverse target configuration.

309 Because the generalized polarizabilities can be expressed with the mo-  
 310 ments of the structure functions, it is possible to measure them using mea-  
 311 surements of the structure functions. As stated earlier, because of the weight-  
 312 ing by some powers of  $\nu$  or  $x$ , these integrals converges more rapidly in energy  
 313 than the GDH integral and therefore can more easily be determined by low  
 314 beam energy measurements. These integrals are valuable because they shed  
 315 light on the long distance (soft), non-perturbative aspects of the target struc-  
 316 ture. The integrals are possible to be calculated using effective or approxi-  
 317 mate theories such as  $\chi$ PT and lattice methods. Thus the measurements of  
 318 these quantities provide benchmark tests of such theories.

319 The first measurement of  $\gamma_0$  for a proton target at the real photon point  
 320 was done by the GDH experiment at Mainz [20]. Recently the JLab EG1b  
 321 experiment has provided some finite  $Q^2$  results for both deuteron (see Fig.  
 322 ??) as well as nucleon targets [22].

<sup>323</sup> **Chapter 2**

<sup>324</sup> **EG4 run**

<sup>325</sup> The deuteron target part of the EG4 experiment ran for about a month  
<sup>326</sup> in 2006, mostly with longitudinally polarized frozen  $^{15}\text{ND}_3$  as the target. In  
<sup>327</sup> between these deuteron runs, some small amount of data was also collected on  
<sup>328</sup> carbon-12 and empty cell targets, which are important in various auxiliary  
<sup>329</sup> studies during the data analysis (such as their use in estimating nuclear  
<sup>330</sup> background while developing momentum corrections, estimating the length  
<sup>331</sup> of the target material or estimating unpolarized background). A total of 113  
<sup>332</sup> data runs (from run ID 51896 to 52040) were collected for the lower beam  
<sup>333</sup> energy (1.3 GeV) and 221 runs (from 51593 to 51867) for the 2.0 GeV case  
<sup>334</sup> (with each run consisting of about  $3.0 \times 10^7$  event triggers) [23]. Each run  
<sup>335</sup> took about 2 hours and collected about 2 GB of data in raw format and  
<sup>336</sup> saved as about 20-30 BOS files (see next section). With the combination of  
<sup>337</sup> low beam energies and low scattering angles, low momentum transfers can  
<sup>338</sup> be measured down to about 0.02 GeV<sup>2</sup> within the kinematic coverage of the  
<sup>339</sup> resonance region ( $1.08 < W < 2.0$  GeV.)

<sup>340</sup> In addition to the use of low beam energies and low  $\theta$  measurements, in  
<sup>341</sup> order to maximize the statistics in the low momentum transfers, following  
<sup>342</sup> measures were taken that were unique to the experiment:

- <sup>343</sup> • Used electron outbending torus field configuration to enhance the low  
<sup>344</sup> angle acceptance (so that more of very forward going electrons would  
<sup>345</sup> be bent towards and detected by the CLAS detector).
- <sup>346</sup> • Used (in the 6<sup>th</sup> sector<sup>1</sup>) a newly built Cerenkov Counter (CC) (see  
<sup>347</sup> Figs. 2.1 and 2.2) that was designed to optimize electron detection in

---

<sup>1</sup>For reasons of limited resources, only one new CC was built and the 6<sup>th</sup> sector alone

348 the outbending torus configuration such that the detection efficiency  
349 would be better and more uniform than with the existing counters<sup>2</sup>  
350 which were optimized for electron inbending configuration.

- 351 • To further enhance the low angle coverage, the polarized target was  
352 placed in a more retracted position along the beam line i.e. at about  
353 -101.0 cm upstream of the CLAS center.

354 Other than that the CLAS detector was used in the standard configura-  
355 tion like in any other polarized target experiments using CLAS.

## 356 2.1 New CC in the 6<sup>th</sup> Sector

357 The Cherenkov Counters (CC) serve the dual function of triggering on elec-  
358 trons and separating electrons from pions (or identifying charged particles).  
359 These detectors use the light emitted by Cherenkov radiation (emission of  
360 light when the charged particle travels faster than light in that medium)  
361 to measure the particle velocity (and, therefore,  $\beta = v/c$ ). The knowledge  
362 of  $\beta$  combined with the particle momentum (from the tracking detectors)  
363 determines the particle's mass, thus giving us information on the particle  
364 identification. The index of refraction ( $n$ ) is carefully optimized for the par-  
365 ticle masses and momentum range of the experiments in question. Thresh-  
366 old counters record all light produced, thus providing a signal whenever  $\beta$  is  
367 above the threshold  $\beta_t = 1/n$ . In the standard configuration, CLAS uses one  
368 Cherenkov threshold detector in each of the six sectors in the forward region  
369 from 8° to 45°.

370 The standard CLAS Cherenkov detectors (as shown by Figs. ?? and ??)  
371 were designed such that their optics, geometry, module position and mir-  
372 ror orientation were optimized for low rate high  $Q^2$  experiments that mostly  
373 use(d) electron in-bending torus fields. The design was a compromise between  
374 the desired kinematic coverage and the complexities of the CLAS detector

---

was used to detect the scattered electrons

<sup>2</sup>The standard CLAS Cherenkov detectors were designed such that their optics, geometry, module position and mirror orientation were optimized for low rate high  $Q^2$  experiments that mostly use(d) electron in-bending torus fields. The design was a compromise between the desired kinematic coverage and the complexities of the CLAS detector system including the effect of the torus field.

375 system including the effect of the torus field. As a consequence, light col-  
376 lection is constrained causing the number of photoelectrons to be strongly  
377 dependent on scattering angles, and making the detection efficiency non-  
378 uniform, and strongly reduced in some regions (for example, up to 30% drop  
379 in the middle of the sector and at forward angles) [20]. While it would still be  
380 possible to detect electrons, the use of the existing CC would mean that the  
381 absolute cross-section measurement would require large and complex correc-  
382 tions which are difficult to evaluate. That would significantly contribute to  
383 the systematic uncertainties, thus not meeting the proposed high accuracy  
384 requirement of the measurements.

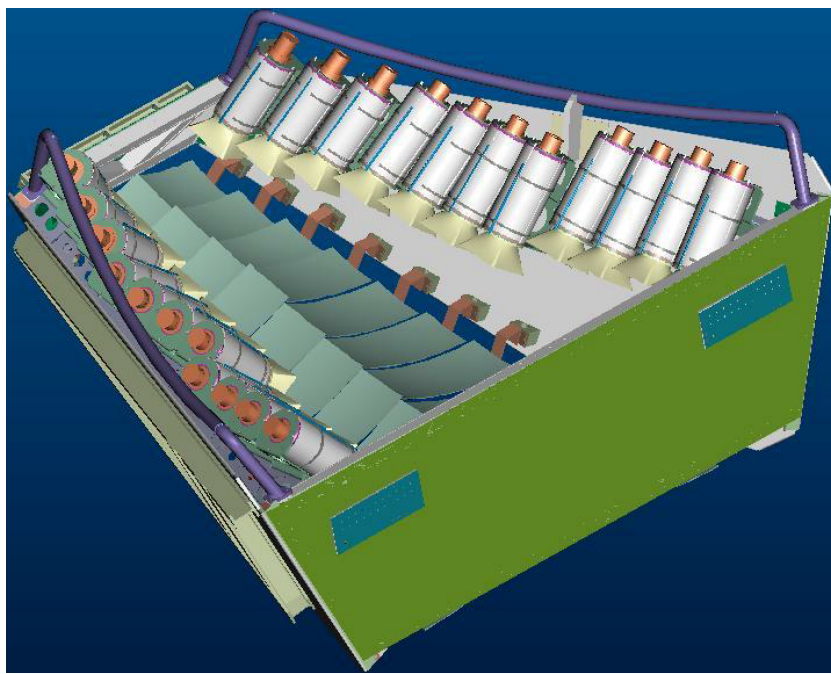


**Figure 2.1:** The new Cherenkov counter (courtesy of INFN, Genova)

385 In order to avoid having all those CC-related issues in the new measure-  
386 ments, a new gas threshold cherenkov counter (designed and built by INFN  
387 - Genova, Italy) was installed in the sixth sector. This new CC detector (see  
388 Fig. 2.1 for its CAD rendition) is specifically optimized for the out-bending  
389 field configuration, which is necessary to reach the desired low momentum  
390 transfer (measurements down to 6 degrees). The detector uses the same ra-  
391 diator gas ( $C_4F_{10}$  - perfluorobutane) and the same gas flow control system

392 as the old one, but it uses a different design. In the new CC, the number  
 393 of CC-modules is now 11 instead of the 18 in the standard ones. In order  
 394 to maximize the light collection, a single reflection design (see Fig. 2.2(b))  
 395 using spherical mirrors is used (the standard CC used double relections from  
 396 elliptical and hyperbolic mirrors). The geometry, the size, the mirror size,  
 397 position, and orientation, the dimensions as well as the assembly of the mod-  
 398 ules were optimized for the experiment and the performance study was done  
 399 using a complete GEANT simulation [20].

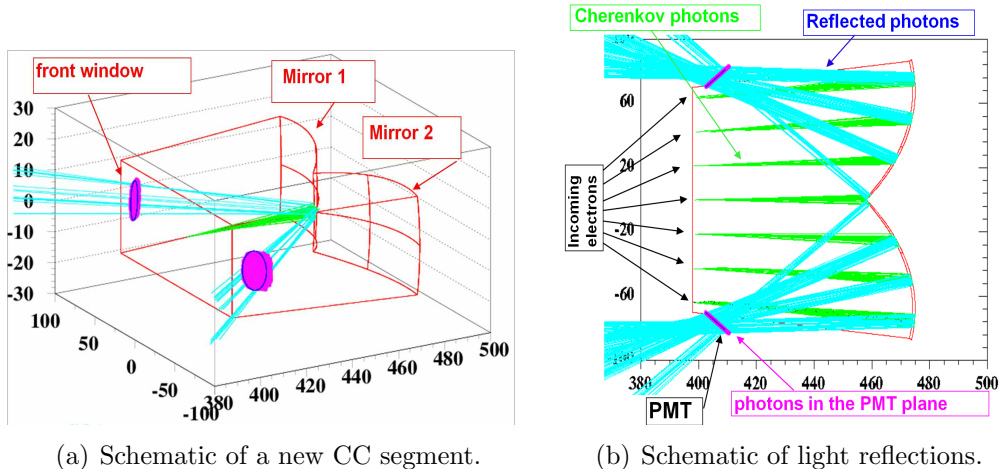


**Figure 2.2:** Schematic of a new CC segment showing the arrangements of the mirrors, PMTs and the light reflections (courtesy of INFN, Genova).

400 **Chapter 3**

401 **Data Analysis Procedure**

402 The goal of this data analysis is to extract the spin structure function  $g_1$  for  
403 the deuteron and evaluate its moments. Since the product  $A_1 F_1$ , which is  
404 proportional to  $\sigma_{TT}$ , directly enters sum rules for the real photon point, which  
405 leads to the generalized GDH integral ( $\bar{I}_{TT}$ ) and the generalized forward spin  
406 polarizability ( $\gamma_0$ ) being expressed in terms of the first and third moments of  
407 the product  $A_1 F_1$ , we decided also to extract the product  $A_1 F_1$  using exactly  
408 the same procedure as for  $g_1$ .

409 The extraction of both  $g_1$  and  $A_1 F_1$  depend directly on the measurement  
410 of the following polarized cross-section difference:

$$\Delta\sigma_{\parallel} = \frac{d^2\sigma^{\downarrow\uparrow}}{d\Omega dE'} - \frac{d^2\sigma^{\uparrow\uparrow}}{d\Omega dE'} = \frac{1}{N_t} \cdot \left[ \frac{N^+}{N_{e^-}^+} - \frac{N^-}{N_{e^-}^-} \right] \cdot \frac{1}{P_b P_t} \cdot \frac{1}{\Delta\Omega} \cdot \frac{1}{\eta_{detector}} \quad (3.1)$$

411 where,

- 412 •  $N_t$  = Number of deuteron nuclei in the target
- 413 •  $N^{+/-}$ : Number of scattered electrons (off deuteron only) for each helicity state (+/-).
- 414 •  $N_{e^-}^{+/-}$ : Number of incident electrons for +/- helicity states
- 415 •  $P_b P_t$  = Product of the beam and target polarizations
- 416 •  $\Delta\Omega = \sin\theta \cdot \Delta\theta \cdot \Delta\phi$ : The solid angle for the given kinematic bin. This term includes the “detector acceptance”.

419     •  $\eta_{detector}$  accounts for the detector efficiencies  
420     The data analysis to extract the physics quantities involves accurately  
421     measuring each of these quantities, either separately or in some combined  
422     form. To do so, the data must be properly reconstructed, calibrated and  
423     corrected to build all the scattering events during the experiment. Since  
424     the reconstructed events include a wide range of physical processes in ad-  
425     dition to the electron-deuteron scattering process that we are interested in,  
426     proper event selection cuts must be applied. In this chapter, all these steps  
427     from the data reconstruction and calibration through the extraction of  $g_1$  are  
428     described.

429

### 430     **3.1 Raw Data Processing - Calibration and** 431     **Reconstruction**

432     The raw data recorded by the CLAS DAQ system, which consists of ADC  
433     and TDC values registered by various detector components as well as the  
434     beam related information such as beam helicity and Faraday Cup readings,  
435     are organized into banks (with each bank carrying data belonging to a par-  
436     ticular detector component or some part of it) and saved in special format  
437     (BOS) files. These raw data are next processed with a standard CLAS soft-  
438     ware package called RECSIS, which analyzes and combines the matching bits  
439     and pieces of the raw information to reconstruct particles and events that  
440     produced them. Such reconstruction produces output data that consist of  
441     event and particle IDs, particle positions and energies and momenta (in the  
442     lab frame CLAS coordinate system), and also some static particle properties  
443     such as charge and mass. The reconstruction program uses geometric pa-  
444     rameters and calibration constants (from the CLAS Calibration Database)  
445     for the detector in order to properly process and transform the raw data into  
446     the reconstructed tracks.

447     The first part of the data processing is the detector calibration. In this  
448     phase, a small sample (about 10%) of raw data (uniformly selected over the  
449     entire run period to ensure time stability verification) is chosen and the en-  
450     ergy and time calibration constants are adjusted to give the correct behavior  
451     while constantly monitoring related variables. This is done separately for  
452     each run period to consider the different running conditions, the possibility

453 of unwanted changes in hardware that may have occurred, as well as drift  
454 of detector response over time. This process of adjusting the calibration  
455 constants and reconstructing the data is repeated until a desired level of ac-  
456 curacy is reached. Once that level is reached, the calibration constants are  
457 “frozen” and the final reconstruction is done. The resulting output is saved  
458 in especial formats<sup>1</sup>.

459 These saved data provided the starting point for our higher level data  
460 analysis as described in this dissertation. The details of the calibration and  
461 reconstruction process can be found in [24].

462 The iterative work of data reconstruction and detector calibration, which  
463 was a very computing intensive and time consuming, was done by R. De  
464 Vita - one of the EG4 collaborators from INFN, Genova, with good expertise  
465 on CLAS data reconstruction - soon after the data collection was completed  
466 (from 2006-2007). The data from this “Pass1” reconstruction was first an-  
467 alyzed as part of the Ph. D. dissertations by three graduate students, but  
468 during these analyses, a few anomalies<sup>2</sup> in reconstruction were observed which  
469 were later tracked down to a mixing up of codes from two EG4 sub-packages  
470 for the reconstruction software. After the mix-up was sorted out, a new pass  
471 (Pass2) of reconstruction was performed by L. El Fassi (still using the same  
472 calibration constants as used by the Pass1 reconstruction). The data from  
473 this latest pass of reconstruction was used for the analysis reported in this  
474 note

---

<sup>1</sup>Two especial data formats - BOS and ntuple (h10) - were used

<sup>2</sup>The anomalies observed in the pass1 analysis were the discretized reconstruction of vertex and wrong reconstruction of track positions in DC1.

475 **3.2 Helicity States**

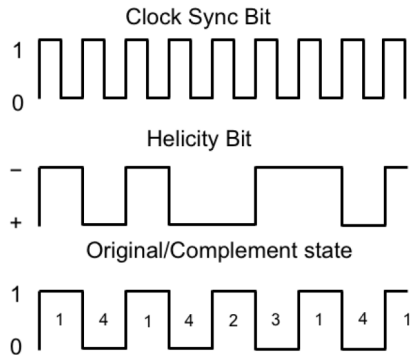


**Figure 3.1:** Different data signals sent from the injector that monitor the helicity states of beam electrons. (Fig. courtesy of N. Guler [22] ).

476 As we saw from Eq. 3.1, the physics extraction depends on measurements of  
477 the number of events in the two (+/-) electron helicity states. The CEBAF  
478 accelerator provides the polarized electrons in closely and equally spaced  
479 bunches. These bunches are further grouped into “buckets” according to  
480 their helicity states, which are alternated pseudo-randomly at the injector  
481 with a frequency of 30 Hz. The information on the helicity state of each of  
482 the buckets and the total integrated charge contained in it is injected into the  
483 DAQ data stream immediately after the helicity flip. Using a combination of  
484 different types of sequence control signals sent from the injector (see Fig. 3.1),  
485 it is possible to determine which helicity state a particular event belonged  
486 to, which then can be used to label the helicity state of the event in the data  
487 stream, together with the total beam charge of the state.

488 **3.3 Electron Identification**

489 In CLAS electron-scattering experiments, the scattered electron defines the  
490 timing of each event. In addition, in inclusive measurements, the scattered

491 electron is the only particle to be detected and measured. So, it is particu-  
492 larly important to make sure that electrons are well measured and properly  
493 identified and are not contaminated with misidentified particles such as neg-  
494 ative pions ( $\pi^-$ ) or lost by being misidentified.

495 The process of identifying the primary scattered electrons starts by first  
496 rejecting all those particle candidates which are not the first entries (i.e., the  
497 trigger particles) in the event bank. The remaining sample of the candidates  
498 is refined further by rejecting those with positive charges. Then, the sample  
499 is further refined by applying a set of cuts that are listed and described below.  
500 An electron candidate is considered good if it passes all of these cuts.

## 501 1. Good Electron Cuts

- 502 (a) **Cut on particle charge:**  $q=-1$
- 503 (b) **Detector status cuts:**
  - 504 i. **DC status:**  $dc>0; dc\_part>0$
  - 505 ii. **SC status:**  $sc>0; sc\_part>0$
  - 506 iii. **EC status:**  $ec>0; ec\_part>0$
  - 507 iv. **CC status:**  $cc>0; cc\_part>0$   
(For simulated data, all of the above except those on CC  
508 variables are used.)
- 510 (c) **Electromagnetic Calorimeter Cuts** (see Sec. 3.3.1)
- 511 (d) **Osipenko cuts** Cuts on CC angle  $\theta$ ,  $\phi$  and time matching be-  
512 tween CC and other detectors. (see Sec. 3.3.2)
- 513 (e) **Cut on minimum number of photoelectrons** (see Sec. 3.3.2)

## 514 2. Good Event Cuts

- 515 (a) **Cut on minimum number of particles detected and recon-  
516 structed in the event:**  $gpart>0$
- 517 (b) **Minimum/maximum momentum cuts** (see Sec. 3.3.3)
- 518 (c) **Sector cut**  $dc\_sect = 6; cc\_sect = 6$  (to select electrons from the  
519 sector where the low momentum Cherenkov detector was installed)
- 520 (d) **Scattering vertex-z cuts** (see Sec. 3.3.4)
- 521 (e) **Fiducial cuts** (see Sec. 3.3.5)

522 This data analysis relied on comparing the experimental data with a  
523 Monte-Carlo simulated data set that was as realistic as practically possible.  
524 Thus, we also have to analyze the simulated data in the same way as the  
525 experimental data. In the ideal situation, all cuts would be the same for  
526 both experimental and simulated data. However, we could not make our  
527 simulation match perfectly with our experimental data. Therefore, some of  
528 the data selection cuts are defined separately for the two cases and sometimes  
529 separately even for different  $Q^2$  bins (to make sure we have the same fractions  
530 of events in corresponding kinematic bins for both type of data).

### 531 **3.3.1 Electromagnetic Calorimeter Cuts**

532 The EC cuts consist of two different cuts applied together. One of these  
533 is on the sampling fraction i.e. the fraction of the energy deposited in the  
534 calorimeter, and the other is on the energy fraction deposited in the inner  
535 part of the calorimeter.

#### 536 **Cuts on EC sampling fraction**

537 While moving through the EC, charged pions are minimum ionizing particles  
538 in the momentum range detectable by CLAS. On the other hand, each elec-  
539 tron deposits its total energy  $E_{tot}$  in the EC<sup>3</sup> by producing electromagnetic  
540 showers. Therefore, the sampling fraction  $E_{tot}/p$  should be independent of  
541 the momentum for electrons (in reality there is a slight dependence).

---

<sup>3</sup>Because some of the deposited energy is in the lead part of the EC rather than the scintillator, only a fraction of the electron energy is detected in the EC.

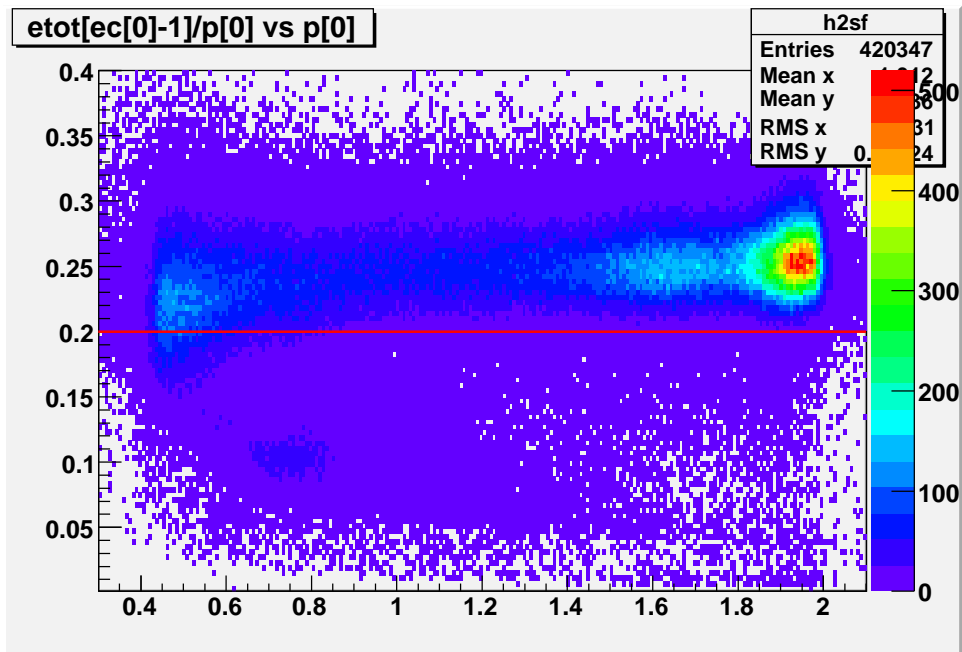


**Figure 3.2:** An example of the cut on the EC sampling fraction (2.0 GeV data). The plots shows the distribution of the sampling fraction (in Y-axis) plotted against the particle momentum (in X-axis). The brighter stripe above about 0.2 in the energy fraction are due to the electrons whereas those below are the pions.

542 For the EC in CLAS, the electron sampling fraction ( $etot/p$ ) is about 0.25  
543 and pions give signals that are mostly below 0.2 (see Fig. 3.2 or others that  
544 follow). Therefore, a lower cut of  $etot/p > 0.2$  is usually chosen to reject  
545 most of the pions without significantly losing good electrons. However, in  
546 our low beam energy experiment, few pions are produced and the electron  
547 peaks are cleaner in lower kinematic bins as can be seen in the low  $Q^2$  bins  
548 of Fig. 3.3. Therefore, a  $Q^2$  bin dependent cut of  $etot/p > (\mu - 3\sigma)$  was  
549 chosen, where  $\mu$  and  $\sigma$  are the Gaussian fit parameters representing the mean  
550 and standard deviation of the distribution in the corresponding  $Q^2$  bin. The  
551 choice of  $3\sigma$  was decided by looking at the sampling fraction distributions in  
552 each of the  $Q^2$  bins and making sure that no pion signal was observed in any  
553 of the bins.

554 On simulated data also, a corresponding  $3\sigma$  cut was applied by first re-  
555 peating the exact same procedure to get the corresponding values of  $\mu$  and  
556  $\sigma$  from the simulated data. Using same- $\sigma$  cuts in corresponding  $Q^2$  bins of  
557 both experimental and simulated data ensures that we had the same fraction  
558 of data in corresponding bins from both experimental and simulated sides.

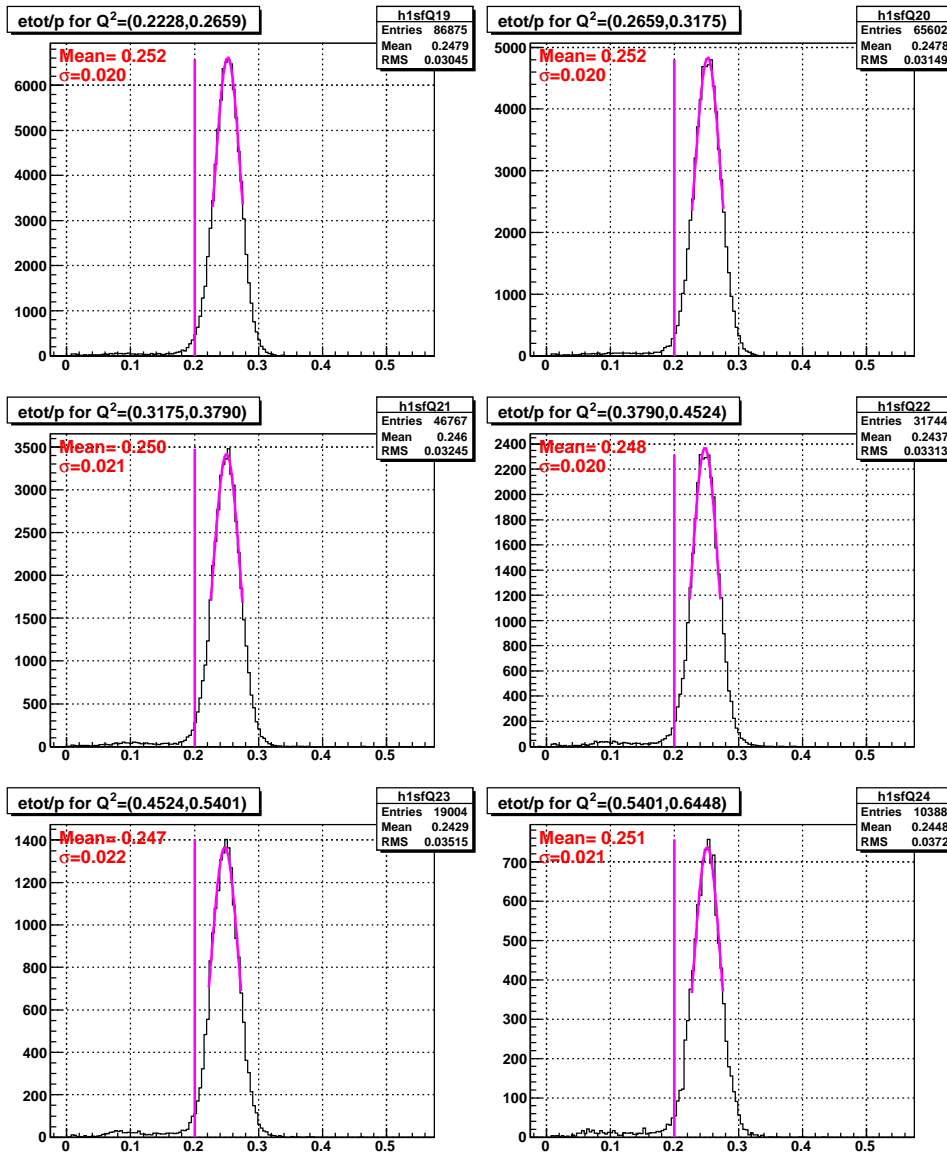


**Figure 3.3:** The  $Q^2$  dependent cuts on the EC sampling fraction for 2.0 GeV experimental data. Events below the red lines are rejected.

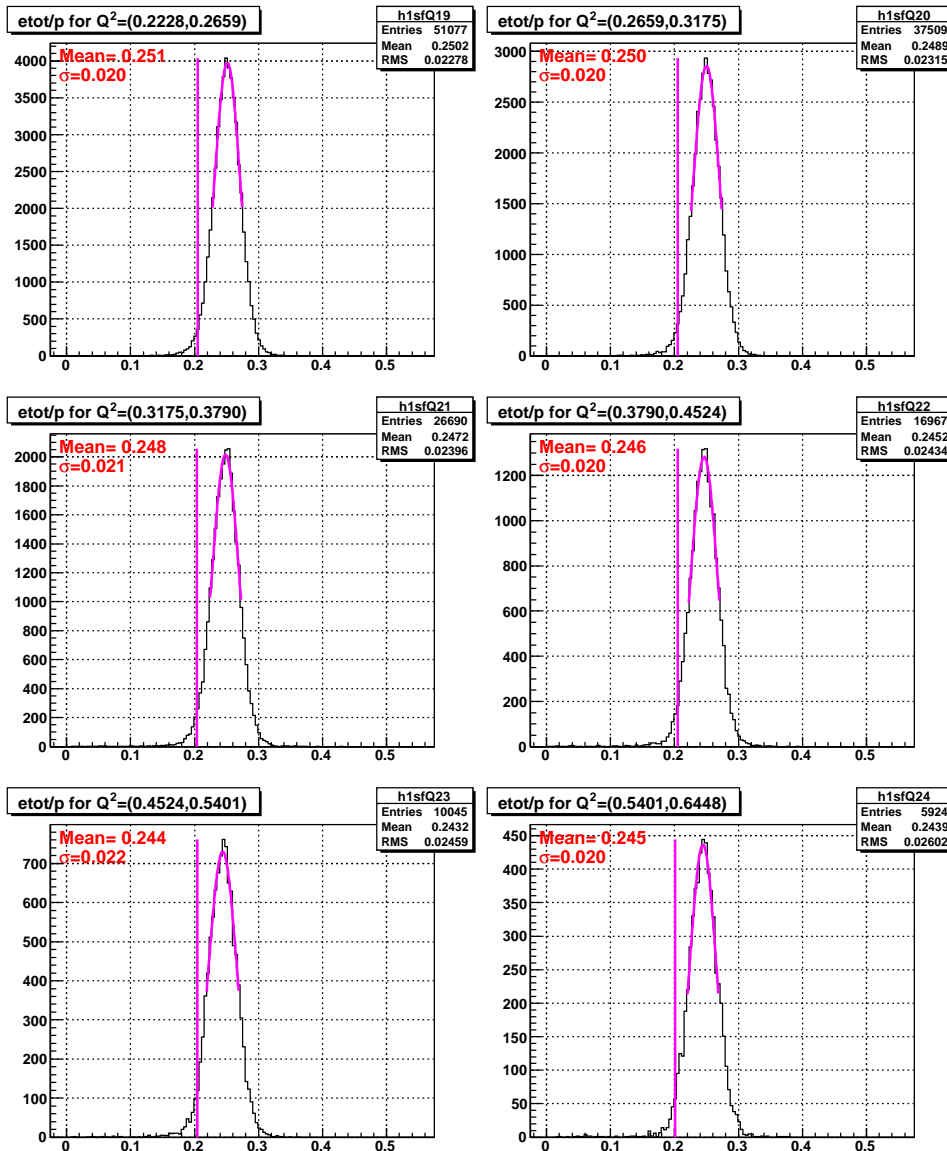


**Figure 3.4:** The  $Q^2$  dependent cuts on the EC sampling fraction for 2.0 GeV simulation data. Events below the red lines are rejected.

559    Cuts on  $E_{in}$

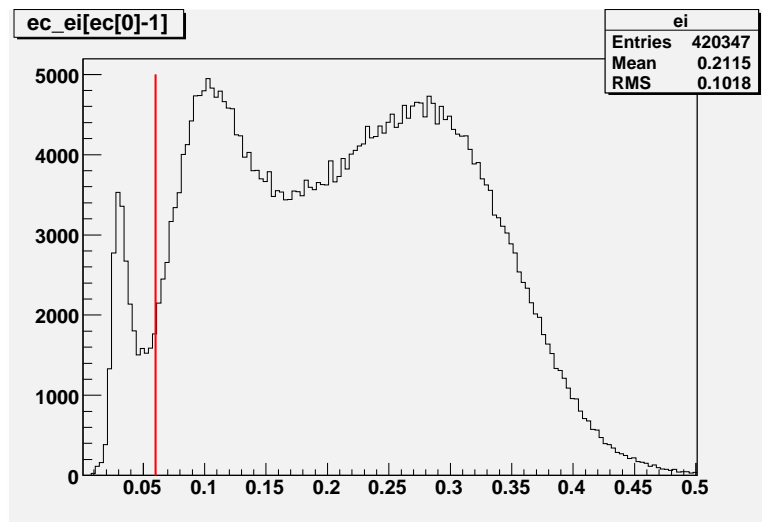


**Figure 3.5:** Energy deposited (GeV) in the inner EC and the cut (red line) used to reject pions (seen as a peak at about 0.03 GeV) from a sample of electron candidates of 2.0 GeV data.

560    Pions, which do not shower and are minimum ionizing particles in the  
561    momentum range detected in CLAS, deposit only a small amount of energy  
562    in the inner part of the EC, independent of their momentum. When  $E_{in}$  is

563 histogrammed, the small pion signal peak at about 0.03 clearly stands out  
564 from the large electron sample, with little overlap in between. So, a universal  
565 cut of  $E_{in}=0.05$  on both data and simulation (as shown by figures 3.5, 3.6  
566 and 3.7) safely rejects most of the pions from the electron candidate sample.

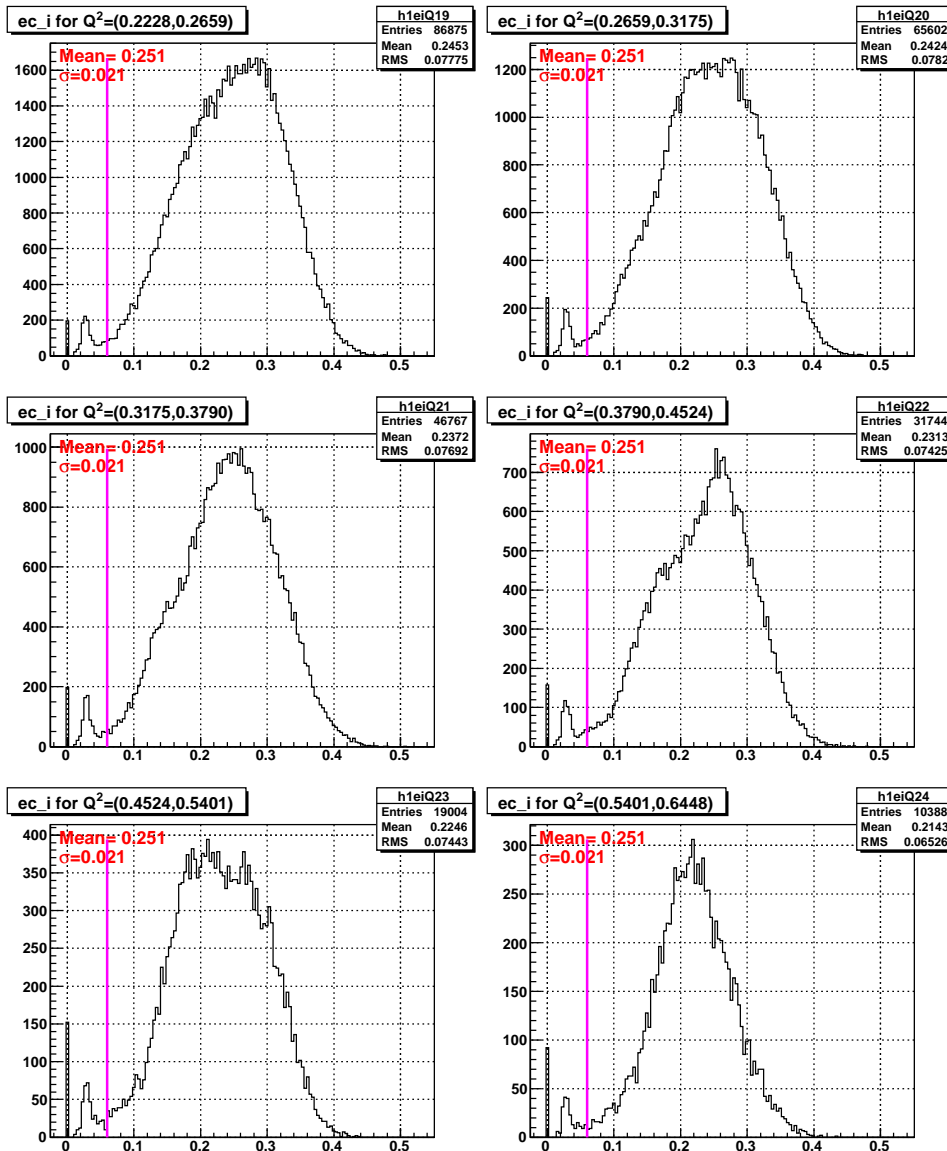


**Figure 3.6:** The EC-inner cut on a sample of 2.0 GeV experimental data in various  $Q^2$  bins.

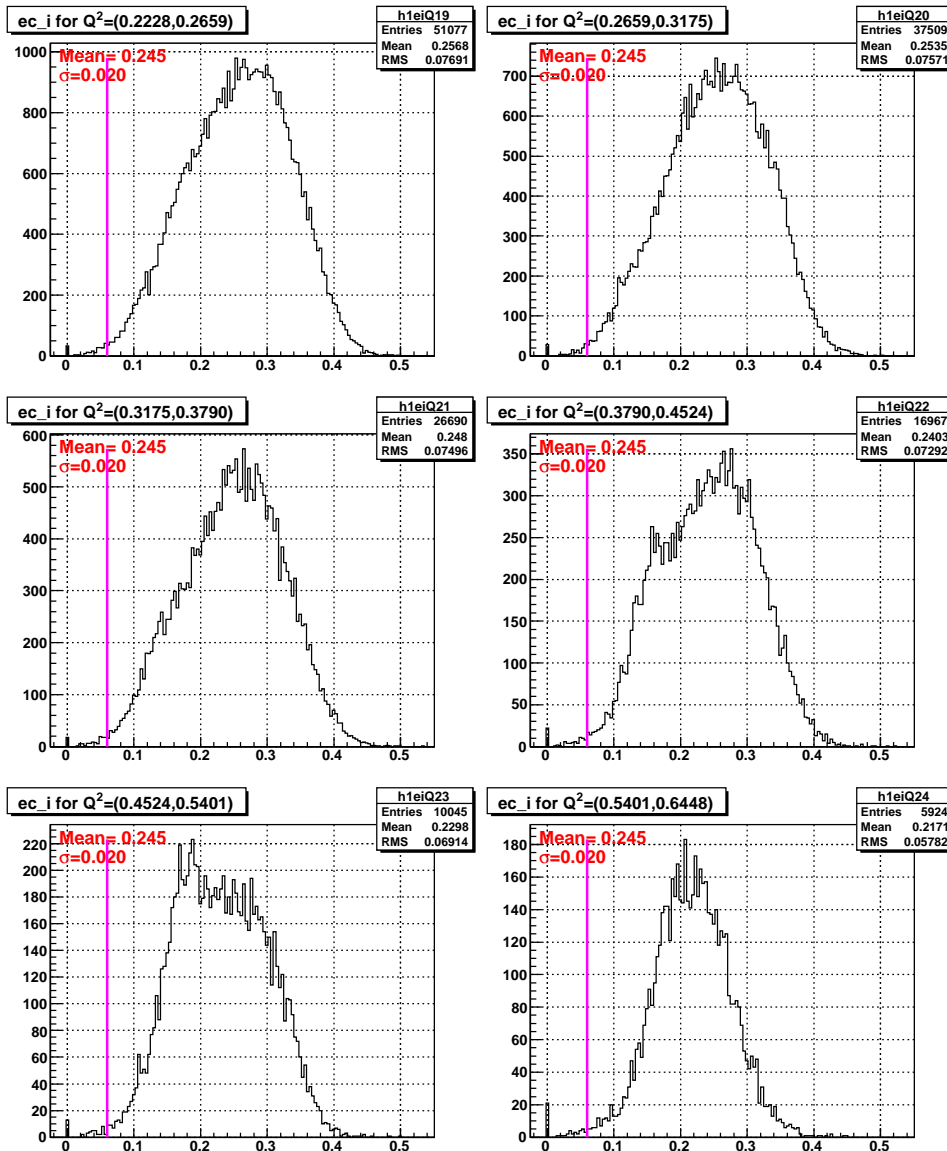


**Figure 3.7:** The EC-inner cut on a sample of 2.0 GeV simulation data in various  $Q^2$  bins.

567    **3.3.2 Cerenkov Counter Cuts**

568    **Osipenko (CC Geometry and Time Matching) Cuts**

569    As discussed in section 2the new EG4-dedicated CC consists of 11 modules  
570    each consisting of a pair of mirrors and PMTs. The segments are placed  
571    along the CLAS polar angle covering 15 to 45 degrees, i.e., the segments are  
572    at different polar angular positions. During normal operation, the PMTs of  
573    these segments may produce thermal noise that is equivalent to that produced  
574    by one photo-electron passing through it. As a result, when a noise pulse in  
575    the CC and a pion track measured by DC coincides within the trigger window  
576    of the CLAS detector, the track gets registered as an electron candidate by  
577    the event reconstruction program, thus contributing to the contamination of  
578    electron candidates with the misidentified pion tracks. In fact, this turns out  
579    to be the biggest source of pion contamination. In order to minimize such  
580    contamination and help better identify electrons from pions, CC geometric  
581    and time-matching cuts are applied.

582    This category of cuts for this experiment is mostly based on a similar  
583    analysis done for another CLAS experiment by M. Osipenko [25].

584    The first requirement in the CC-matching is for the electron candidate  
585    track (as reconstructed by DC) to have a corresponding signal in CC. In ad-  
586    dition, the track needs to meet several matching conditions to be acceptable  
587    as described in the next sections.

588    **CC  $\theta$  Matching** As said above, the CC segments are at different average  
589    polar angle positions (between 15 and 45 degrees), so in principle, one can  
590    expect a one-to-one correspondence between the polar angle of the track (as  
591    measured at the vertex) and the CC-segment. However, the torus magnetic  
592    field bends the particles towards or away from the beamline, so it's more  
593    convenient to use the CC projected polar angle  $\theta_{proj}$  rather than the vertex  
594    angle  $\theta$ , where  $\theta_{proj}$  is defined as the polar angle of the position vector defined  
595    by the point of intersection of the track with the plane at which the CC  
596    PMTs reside as reflected by the CC mirrors (another projected angle  $\phi_{proj}$   
597    is the azimuthal angle of the same vector). These projected angles can be  
598    uniquely calculated for each track based on the DC signals of the track as  
599    well as the CC geometry information. To simplify the later analysis process,  
600    these projected angles for each track were calcuated during the final data  
601    reconstruction process and then saved in the output files just like all the other

602 information for the events and particles. Finally, for the actual electrons  
 603 a one-to-one correspondence between  $\theta_{proj}$  and the segment number can be  
 604 established, which discriminates against background noise and the accidental  
 605 pions (or any other negative charge candidates). For each segment, the  $\theta_{proj}$   
 606 distribution (see Fig. 3.8) is fitted with a gaussian to determine its mean ( $\mu$ )  
 607 and width ( $\sigma$ ) and then saved for future use in cuts. These fit parameters  
 608 are then used during the data analysis to define these CC- $\theta$ -matching cuts.  
 609 The events that have  $\mu - 3\sigma < \theta_{proj} < \mu + 3\sigma$  pass this cut, and the others  
 610 are rejected as not genuinely being electrons.

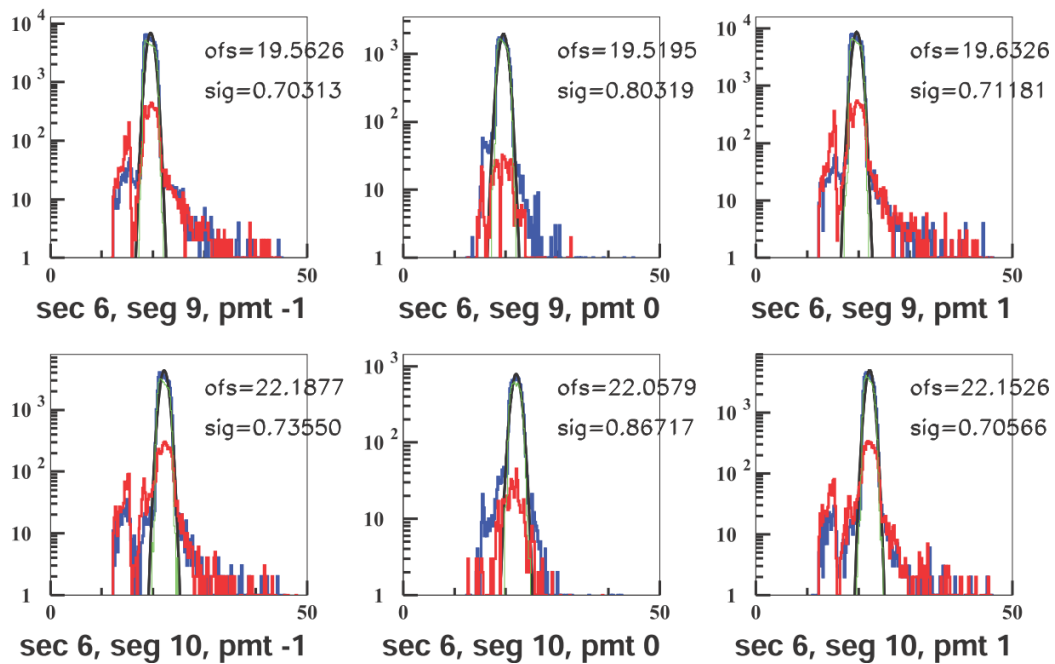


**Figure 3.8:** The  $\theta_{proj}$  distributions in two (9<sup>th</sup> and 10<sup>th</sup>) of the CC-segments (figures used from [26]). Here, the first, second and third columns correspond to events that fired the left, both and the right PMTs respectively. The blue lines are for good electron candidates that pass the EC cuts as well as  $Nphe > 2.5$ . The red ones are for those that pass the EC cuts but with  $Nphe < 2.5$  (thus likely pions), and the green are for those which pass both EC cuts and all Osipenko cuts. The Gaussian fits which are used to define the  $\theta$  matching cuts are shown in black ("ofs" and "sig" in the panel refer to  $\mu$  and  $\sigma$ , respectively). If the candidate falls outside  $\pm 3\sigma$  limits given by the fit,  $\theta_{proj}$  is taken as not matching with the corresponding segment and, therefore, the event is rejected.

611 **CC  $\phi$  Matching** One can also have a one to one correspondence between  
612 the other CC-projected angle  $\phi_{proj}$  and the left or right PMT in the corre-  
613 sponding CC-segment, because when the track is on the right side of the CC,  
614 the right PMT should fire and vice versa. However, there are some excep-  
615 tional cases of events which fire both PMTs. That happens when  $\phi_{proj}$  of the  
616 track is less than 4 degrees (when measured relative to the sector mid-plane),  
617 in which case the Cerenkov light hits both PMTs but with less efficiency (be-  
618 cause the Cherenkov photons are shared between the two). Fig. 3.9 shows  
619 for two of the segments the  $\phi_{proj}$  distributions and the Gaussian fits that are  
620 used to define these cuts.

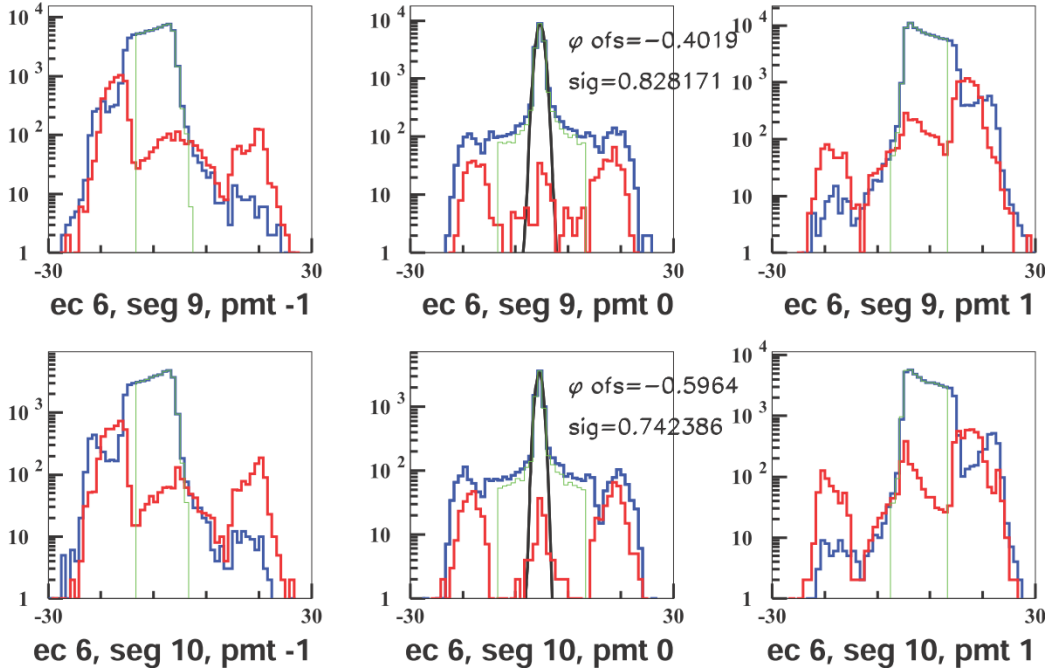


**Figure 3.9:** The  $\phi_{proj}$  distributions in two ( $9^{th}$  and  $10^{th}$ ) of the CC-segments (figure used from [26]). Here, the first, second and third columns correspond to events that fired the left, both and the right PMTs respectively. The blue lines are for good electron candidates that pass the EC cuts as well as  $Nphe > 2.5$ . The red ones are for those that pass the EC cuts but with  $Nphe < 2.5$  (thus likely pions), and the green are for those which pass both EC cuts and all Osipenko cuts. The Gaussian fits to the distributions that fired both left and right PMTs are shown in black ("ofs" and "sig" in the panel refer to  $\mu$  and  $\sigma$ , respectively). If the candidate falls outside  $3\sigma$  on the positive (negative) side but the left (right) PMT is fired, we take it as having left-right inconsistency and, therefore, the event is rejected. In other words, if  $\theta < \mu - 3\sigma$  but  $PMT = 1$ , or if  $\theta > \mu + 3\sigma$  but  $PMT = -1$ , the event is rejected.

621    **CC Time Matching** The difference  $\Delta T$  between the track time recorded  
 622    on a CC segment and the corresponding time recorded on the TOF (or SC),  
 623    corrected for the path length from the CC to the TOF, is used to define one of  
 624    the time-matching cuts  $\Delta t_{SC-CC} > -6.0\text{ns}$  which was chosen to reduce pion  
 625    contamination without losing too many electron candidates (see Fig 3.10).  
 626    Likewise, the time between CC and EC is also used to define another cut  
 627     $\Delta t_{EC-CC} > -6.0\text{ns}$  (see Fig 3.11) to further reduce the pion contamination.

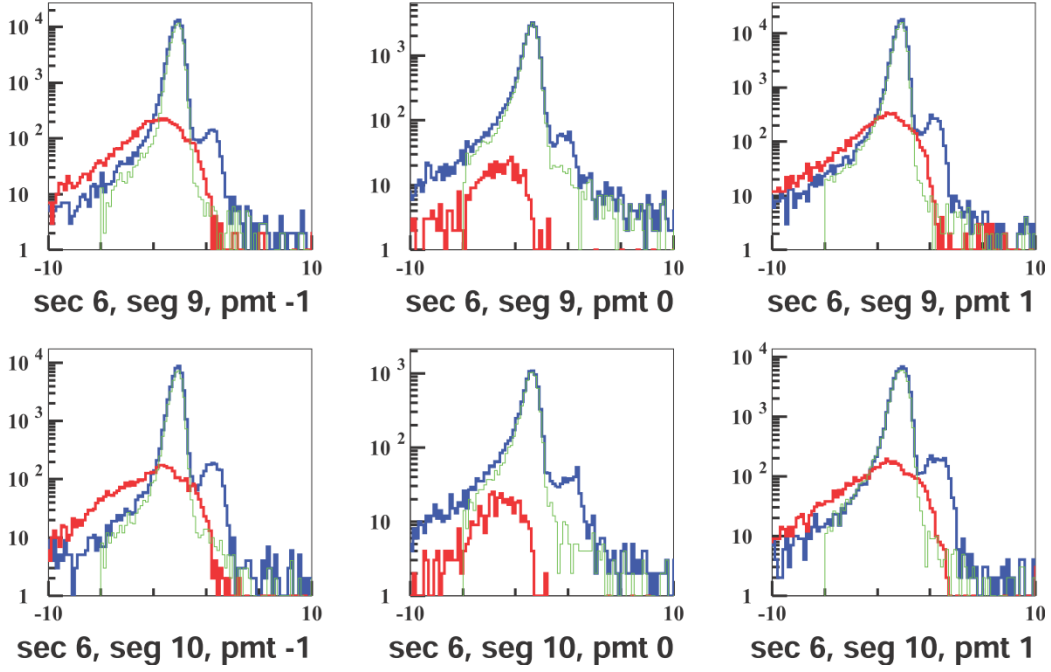


**Figure 3.10:** The  $\Delta t_{SC-CC}$  distributions for two of the CC-segments (figure used from [26]). Here, the first, second and third columns correspond to events that fired the left, both and the right PMTs respectively. The blue lines are for good electron candidates that pass the EC cuts as well as  $Nphe > 2.5$ . The red ones are for those that pass the EC cuts but with  $Nphe < 2.5$  (thus likely pions), and the green are for those which pass both EC cuts and all Osipenko cuts. The  $\Delta t_{SC-CC} > -6.0\text{ns}$  cut was chosen to reduce pion contamination without losing too many electron candidates. (The small peaks at about +3 ns are due to particles hitting PMTs directly.)

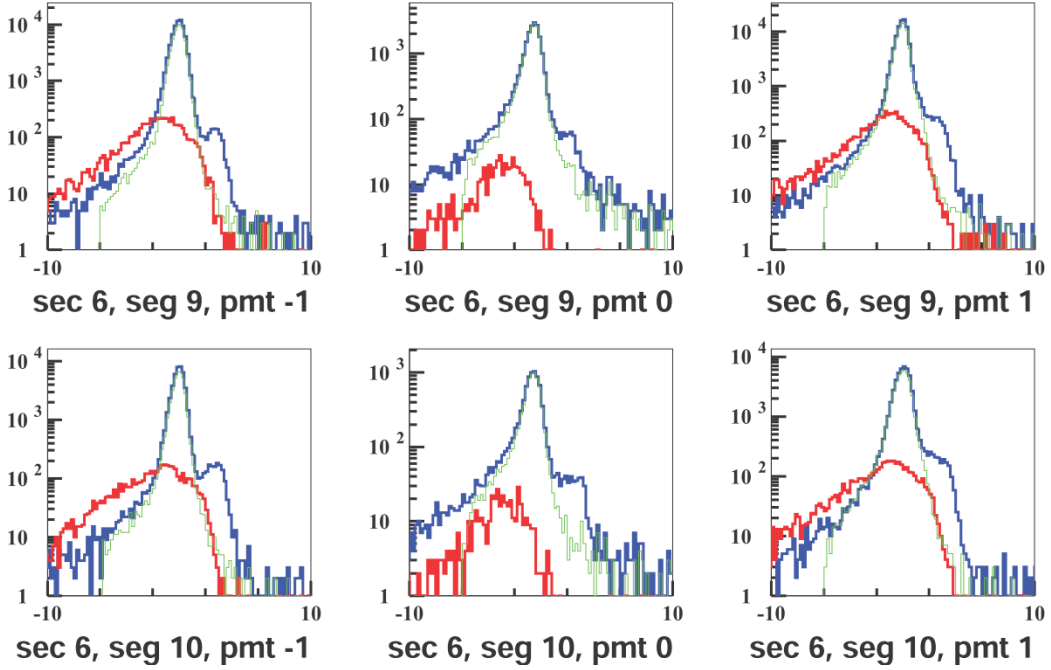


**Figure 3.11:** The  $\Delta t_{EC-CC}$  distributions for two of the CC-segments (figure used from [26]). Here, the first, second and third columns correspond to events that fired the left, both and the right PMTs respectively. The blue lines are for good electron candidates that pass the EC cuts as well as  $Nphe > 2.5$ . The red ones are for those that pass the EC cuts but with  $Nphe < 2.5$  (thus likely pions), and the green are for those which pass both EC cuts and all Osipenko cuts. The  $\Delta t_{EC-CC} > -6.0\text{ns}$  cut was chosen to reduce pion contamination without losing too many electron candidates. (The small peaks at about +3 ns are due to particles hitting PMTs directly.)

## 628 Cut on Minimum Number of Photoelectrons

629 The “nphe” variable in the data ntuple which represents the ADC signal from  
 630 the CC converted to “number of photoelectrons” and multiplied by 10 is also  
 631 used to discriminate electrons from pions and the background. The number  
 632 of photoelectrons produced in CC by an electron is typically between 5 and 25  
 633 or between 50 and 250 in the units of nphe, where the electronic background  
 634 and negative pions produce signals equivalent to one photo-electron (or 10 in  
 635 nphe units) and so a cut is determined somewhere between these two regions  
 636 based on the shapes and sizes of the electron and pion peaks. In our case,

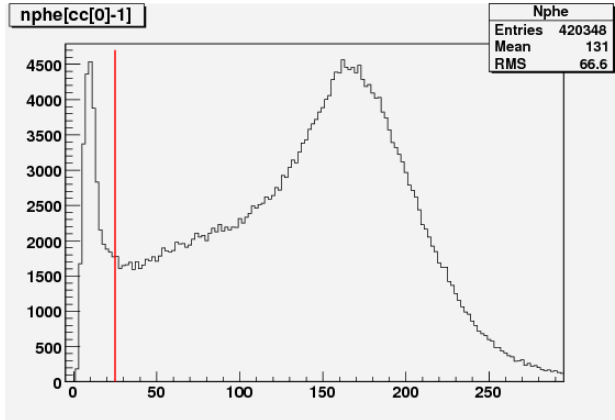


**Figure 3.12:** The cut (the red straight line at 25) on the number of photo-electrons produced in CC times 10 (from 2.0 GeV data). The signals below the red line are mostly pions and noise and above the line are mostly electrons.

637 we chose to have the cut  $Nphe > 25$  as depicted by the straight line in Fig.  
 638 3.12.

### 639 3.3.3 Minimum/Maximum Momentum cuts

640 A study [27] of the inclusive cross section at various beam energies in CLAS  
 641 developed a parametrization of the low momentum cut  $p_{min}$  as a function of  
 642 the calorimeter low trigger threshold (in milli-Volts)

$$p_{min} \text{ (MeV)} = 214 + 2.47 \times EC_{threshold} \text{ (mV)} \quad (3.2)$$

643 The low threshold for EC-total energy for EG4 was 65 mV [28], so, the  
 644 minimum momentum cut was determined to be at:  $p_{min} = 0.37 \approx 0.4 \text{ GeV}$ .  
 645 In addition, another minimum cut of  $p_{min} = 0.2 * E_{beam}$  was added, so the  
 646 actual minimum cut amounted to the larger of those two. Likewise, the  
 647 momentum cannot be more than that of the beam energy (in natural units),  
 648 therefore, the upper cut on the momentum is:  $p_{max} = E_{beam}$ .

649 Fig. 3.13 shows the momentum distribution of the electron candidates  
 650 for the 2 GeV data and the minimum and maximum cuts.

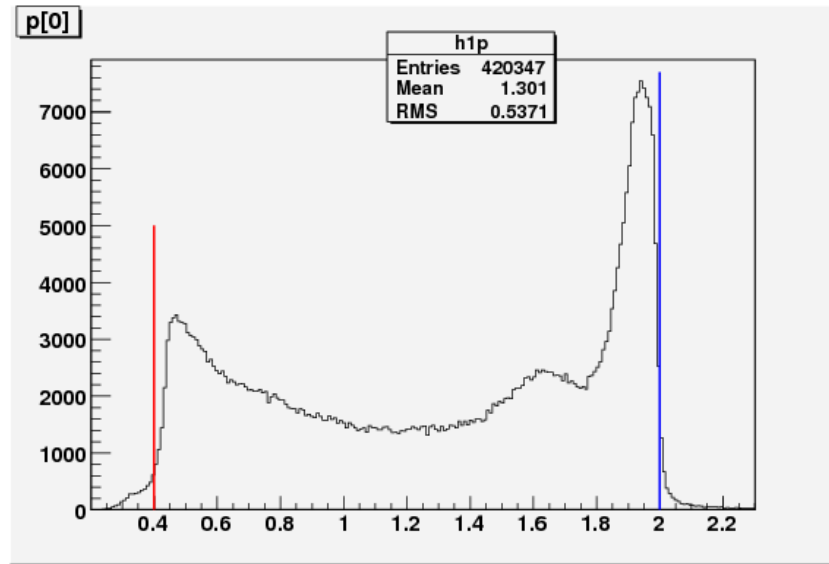


**Figure 3.13:** The maximum and minimum momentum cuts (on 2.0 GeV ND<sub>3</sub> data).

### 651    3.3.4    Vertex-Z cuts

652    In the EG4 experiment, the ND<sub>3</sub> polarized target was of 1 cm long and was  
 653    placed at ( $x = 0$ ,  $y = 0$ ,  $z = -100.93$  cm) in the CLAS coordinate system.  
 654    Since the beam electrons have to go through a few foils before reaching the  
 655    target as well as the detector, we want to reject electron tracks with vertices  
 656    outside the target volume. For this purpose, use a cut on the reconstructed  
 657    vertex co-ordinate " $v_z$ ". However the vertex resolution demands reasonably  
 658    wide " $v_z$ " cuts so as not to lose too many good events. That is why the  
 659    distribution of " $v_z$ " was studied and based on the position and width of  
 660    the distribution as well as our knowledge of the location of various foils and  
 661    target materials, the cuts on " $v_z$ " were decided. It was seen (see Figs. 3.14  
 662    and 3.15) that the resolutions get worse and the distributions get wider as  
 663    we go to lower  $Q^2$  values, so again  $Q^2$  dependent cuts were chosen for both  
 664    data and simulation with the cuts tightening as  $Q^2$  increases.

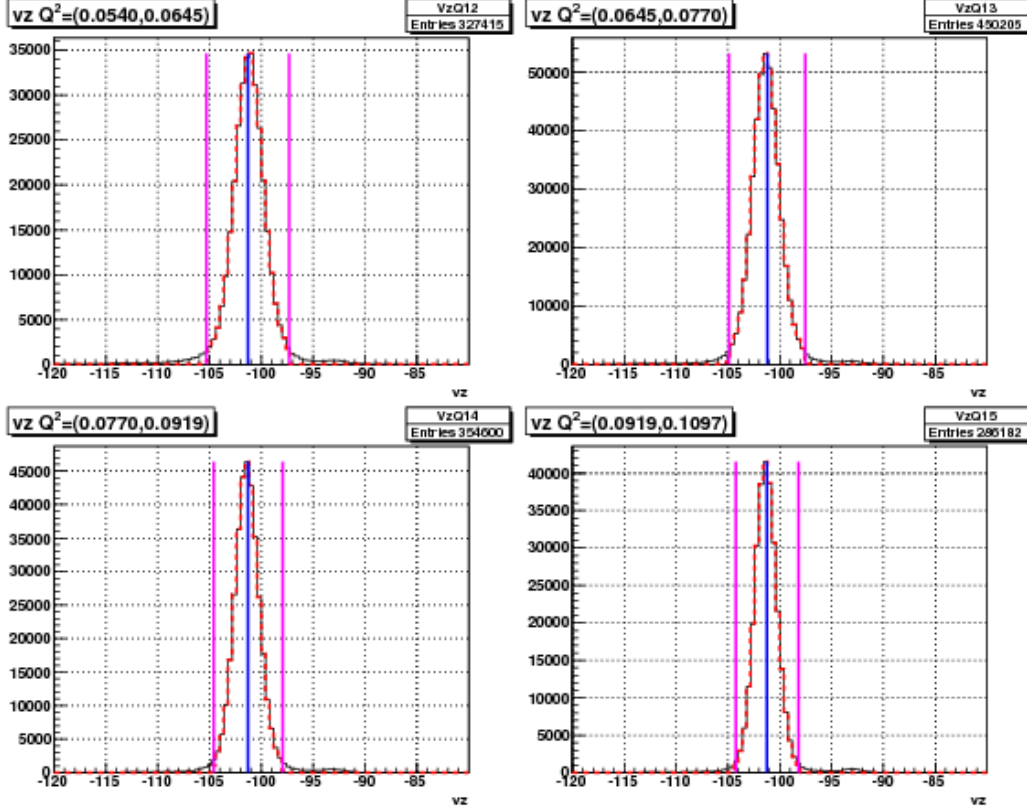


**Figure 3.14:** 2.0 GeV data showing the  $Q^2$  dependent  $v_z$ -cuts (the magenta lines on the left and right of the peaks) in some of the  $Q^2$  bins. The continuous black line represents events before applying all the other event selection cuts (except on  $v_z$ ) and the thicker dotted red line are the events after the cuts. The blue lines are the centers of the distributions, from which the cuts are 3 times  $\sigma$  away on each side, where  $\sigma$  is the standard deviation for the distribution in the given  $Q^2$  bin (both the central value and the  $\sigma$  are determined during the cut development studies).

665 As in the case of EC variables, the reconstructed “ $v_z$ ” distribution in  
 666 the simulation does not come out quite the same as in the experimental  
 667 data . To have the same fraction of events in the corresponding  $Q^2$  bins as  
 668 in the experimental data, a separate set of cuts (determined based on the  
 669 distributions of both types of data) had to be used for simulation. For this  
 670 purpose, the Gaussian fit parameters  $\mu$  and  $\sigma$  (representing the mean and  
 671 standard deviation) for all the  $Q^2$  bins were tabulated separately for both

672 data and simulation and separate sets of  $\pm 3\sigma$  cuts were determined for all  
 673 bins. For example, if  $\mu_q$  and  $\sigma_q$  were the two Gaussian fit parameters for the  
 674  $q^{th}$   $Q^2$  bin of either data or simulation, then the lower and upper cuts for  
 675 “ $v_z$ ” for that data set in the given  $Q^2$  bin would be  $\mu_q - 3\sigma_q$  and  $\mu_q + 3\sigma_q$   
 676 respectively (as shown by the magenta vertical lines in Figs. 3.14 and 3.15).

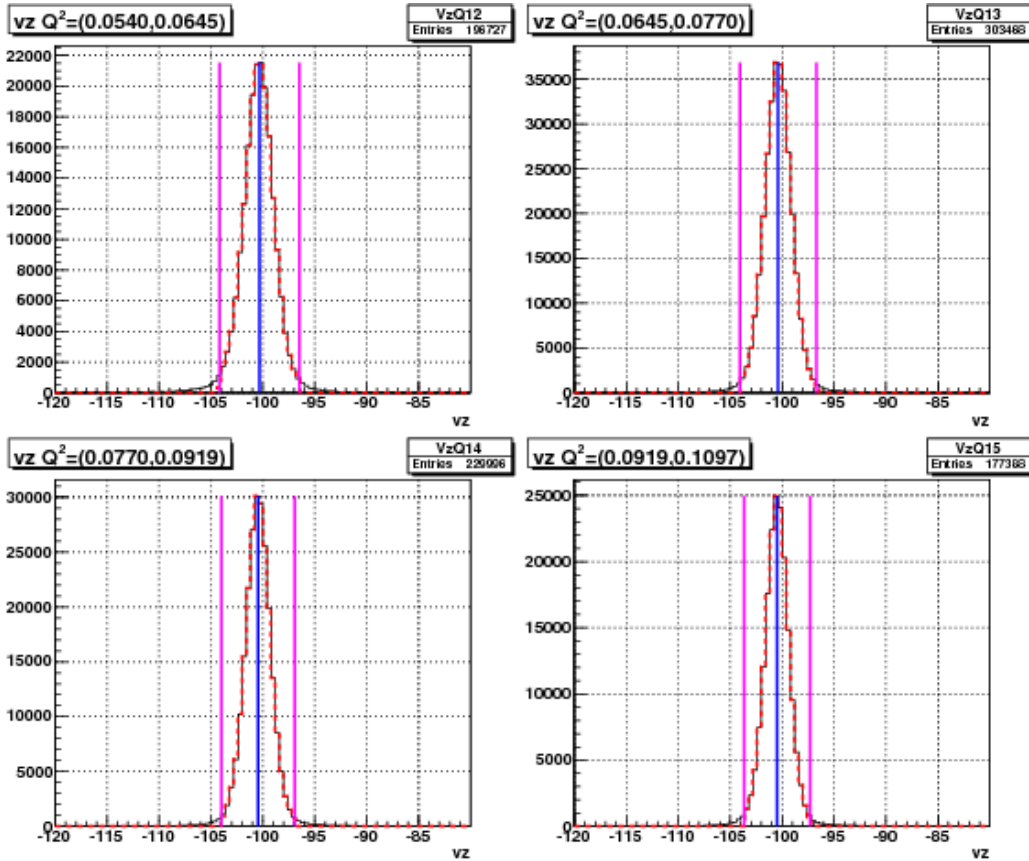


**Figure 3.15:**  $Q^2$  dependent  $v_z$ -cuts on simulation data (similar to Fig. 3.14).

### 677 3.3.5 Fiducial Cuts

678 Similar to the cuts discussed so far, we also had to match the region of good  
 679 efficiency of the physical detector with the corresponding region from the  
 680 simulation. For the experimental and simulation data to be comparable,  
 681 they must have the same detector acceptance. Two event variables polar

682 angle ( $\theta_{vtx}$ ) measured at the vertex and the azimuthal angle  $\phi_{DC1}$  measured  
 683 at the drift chamber layer 1 are chosen to define the good efficiency regions of  
 684 the detector. The reason for the choice of the variable  $\theta_{vtx}$  should be obvious  
 685 because it is directly related with the kinematic variables  $Q^2$  and  $W$  used in  
 686 the analysis. However, due to the momentum dependent rotational effect of  
 687 the magnetic field on the reconstructed azimuthal angle ( $\phi_{vtx}$ ) at the vertex,  
 688 the angle  $\phi_{DC1}$  is preferred over  $\phi_{vtx}$  to define the fiducial region because  
 689 that allows the easy selection (rejection) of the events which passed through  
 690 and got detected by the more (less) reliable central (marginal) regions of  
 691 the Cerenkov Counters. After a careful and extensive study of the event  
 692 distributions on both data and simulation, we arrived at four sets of fiducial  
 693 cuts in terms of the variables  $\theta_{vtx}$ ,  $\phi_{DC1}$  and the torus current normalized  
 694 inverse momentum i.e.,  $I_{torus}/(2250p)$ .

695 The first set of fiducial cuts (see Fig. 3.16) were determined by comparing  
 696 regular and EC-only data (which were taken using triggers that didn't  
 697 involve CC) and selecting cuts such that regions with relatively darker spots  
 698 (reflecting very low CC-efficiency) were rejected.

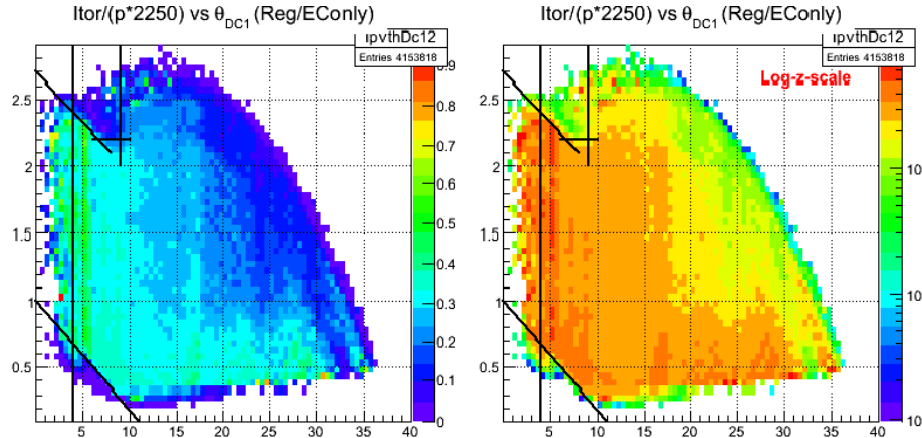


**Figure 3.16:** Fiducial cuts determined by comparing the distributions of regular and EC-only **experimental data** as a function of  $I_{torus}/(2250p)$  and  $\theta_{DC1}$ . Here in the top panels, we see distributions of ratios of the regular and EC-only data respectively in linear and log scales in the color axis respectively. Inefficient regions of the CC are excluded using the indicated cuts.

699 The second set of cuts came from a similar comparison between the regu-  
 700 lar and EC-only data in the  $I_{torus}/(2250p)$  vs  $\theta_{vtx}$  (instead of  $\theta_{DC1}$ ) space (see

701 Fig. 3.17) .

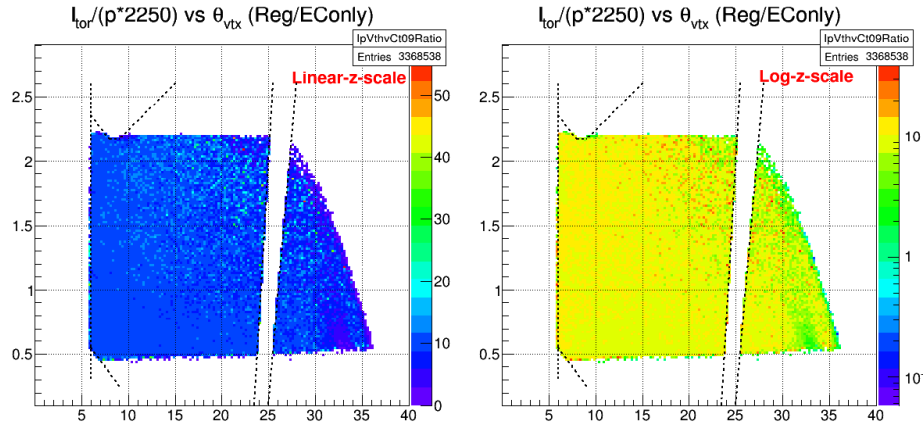


**Figure 3.17:** Fiducial cuts determined by comparing the distributions of regular and EC-only **experimental data** as a function of  $I_{torus}/(2250p)$  and vertex angle  $\theta_{vtx}$ . Here, the vertical cut near  $\theta_{vtx}=25$  degrees is to avoid the region of low efficiency possibly due to dead wires in DC.

702 The third set of cuts came from a comparison between the experimental  
703 and the corresponding simulated data as shown in the Fig. 3.18. as indicated  
704 by various straight lines in the two plots.

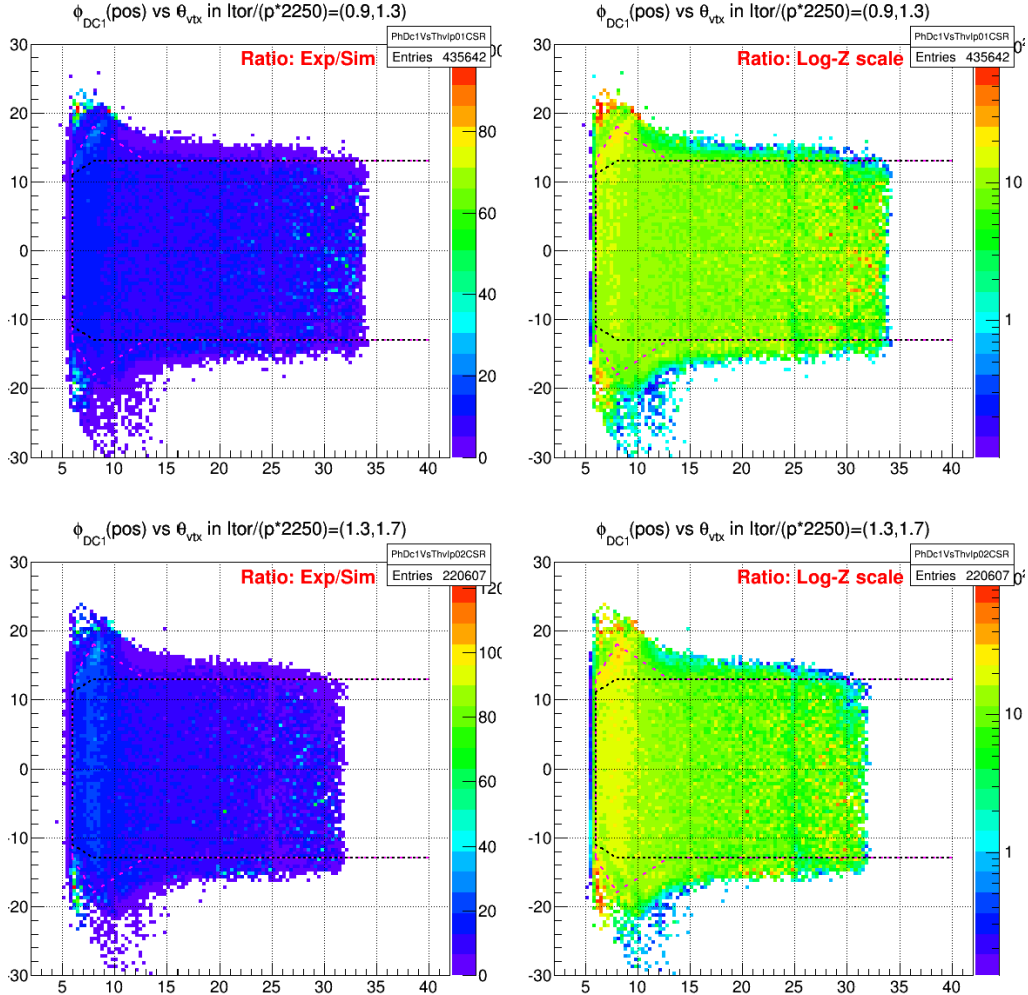


**Figure 3.18:** Distribution (in two of six bins of  $I_{torus}/(2250p)$ ) of ratios of **experimental** and **simulated** data (for 2.0 GeV) (both in linear and log-z scales) as a function of vertex angle  $\theta$  and azimuthal angle  $\phi_{DC1}$  as measured by the track position at the first drift chamber layer (angles in degrees). The dotted lines indicate the fiducial cuts for accepting good electrons.

705     Lastly, further sets of cuts were developed based on the distribution of average  
 706     number of photo electrons (nphe) as recorded by the Cerenkov Counter  
 707     (CC) (see Fig. ??).

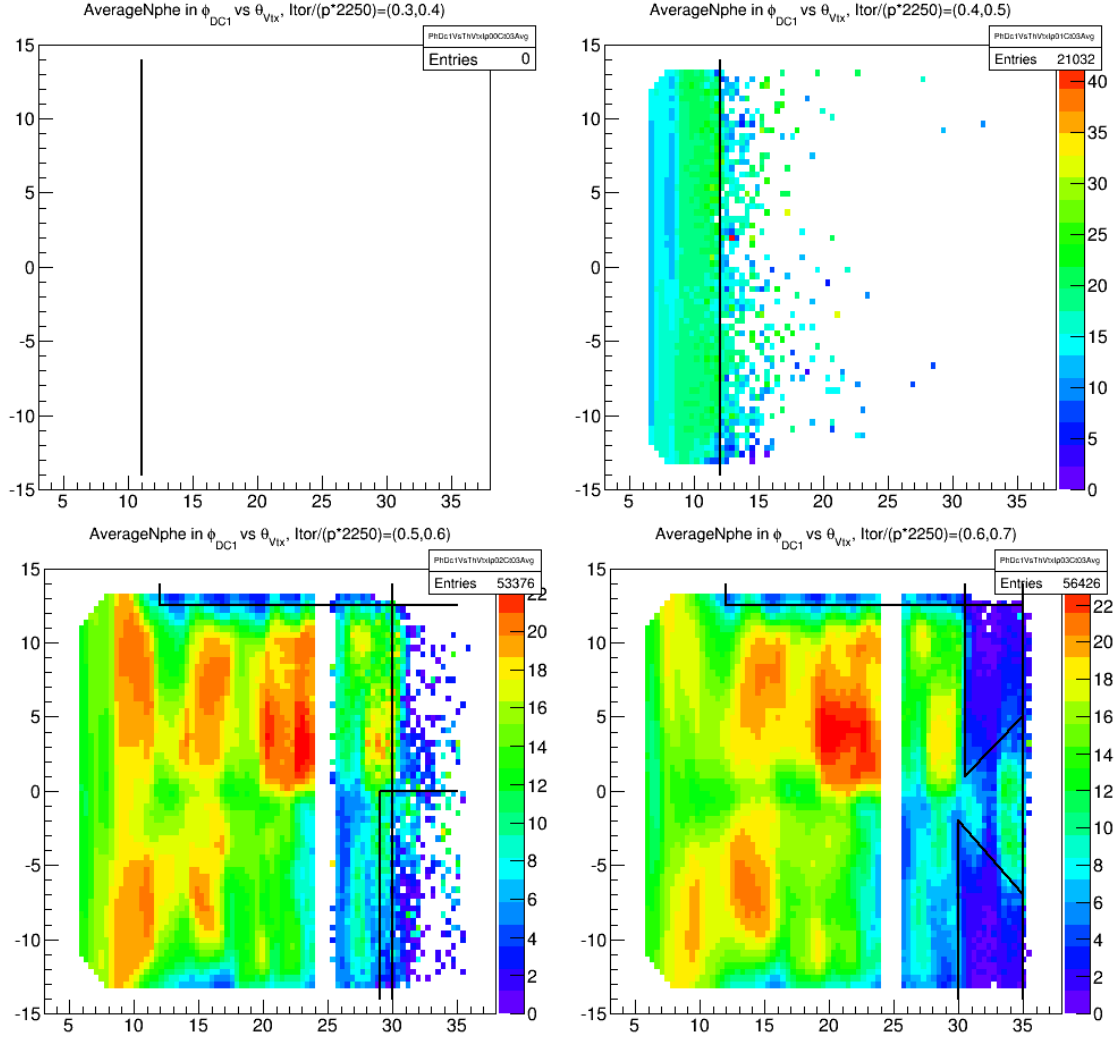


**Figure 3.19:** Average Nphe distributions as a function of  $\phi_{DC1}$  (along Y-axis) and  $\theta_{vtx}$  (along X-axis) in first four bins of  $\frac{I_{tor}}{p \cdot 2250}$ . The black lines show the cuts that reject the very low CC-inefficiency regions.

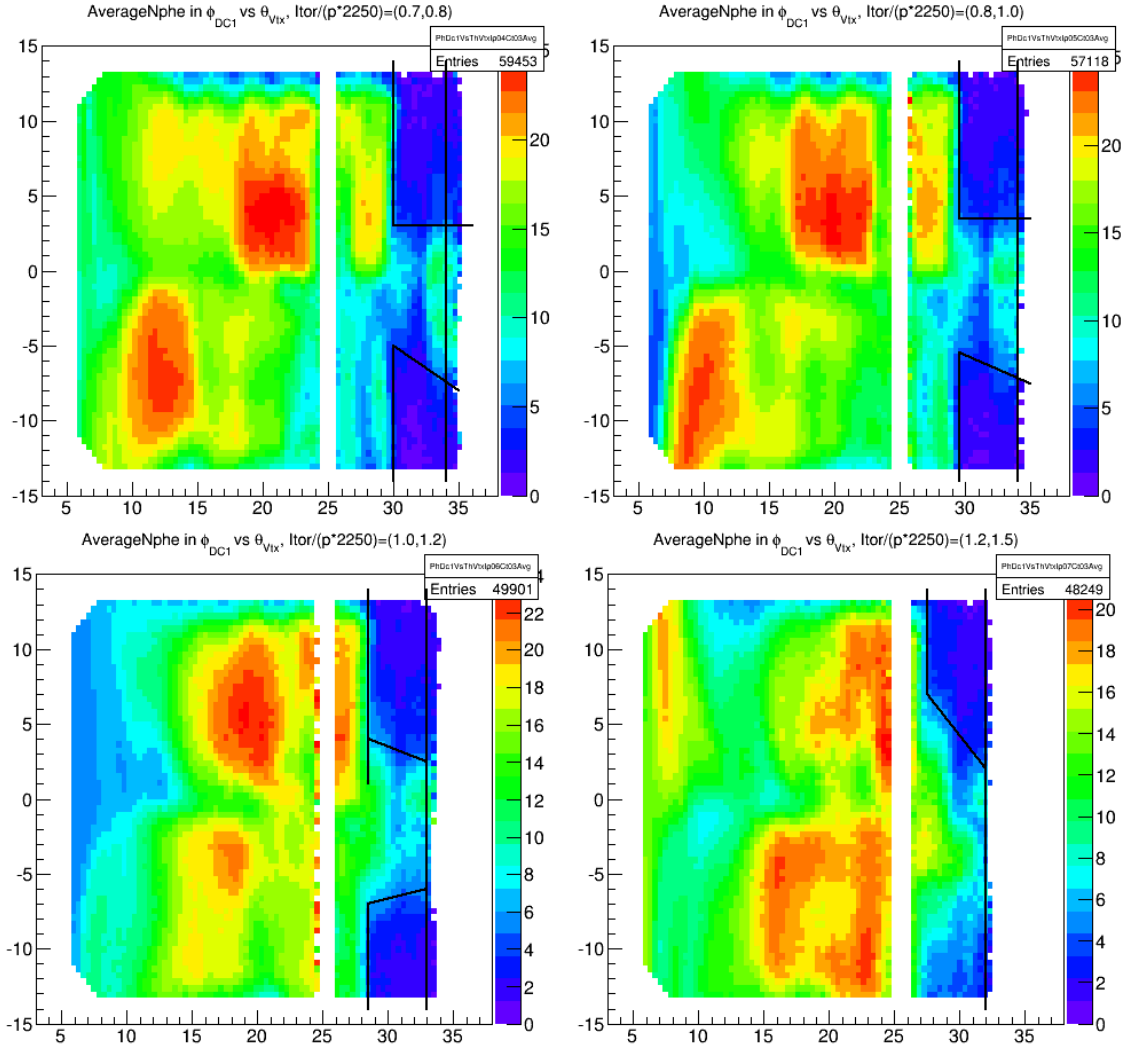


**Figure 3.20:** Average Nphe distributions as a function of  $\phi_{DC1}$  (along Y-axis) and  $\theta_{vtx}$  (along X-axis) in next four bins of  $\frac{I_{tor}}{p \cdot 2250}$ . The black lines show the cuts that reject the very low CC-inefficiency regions.

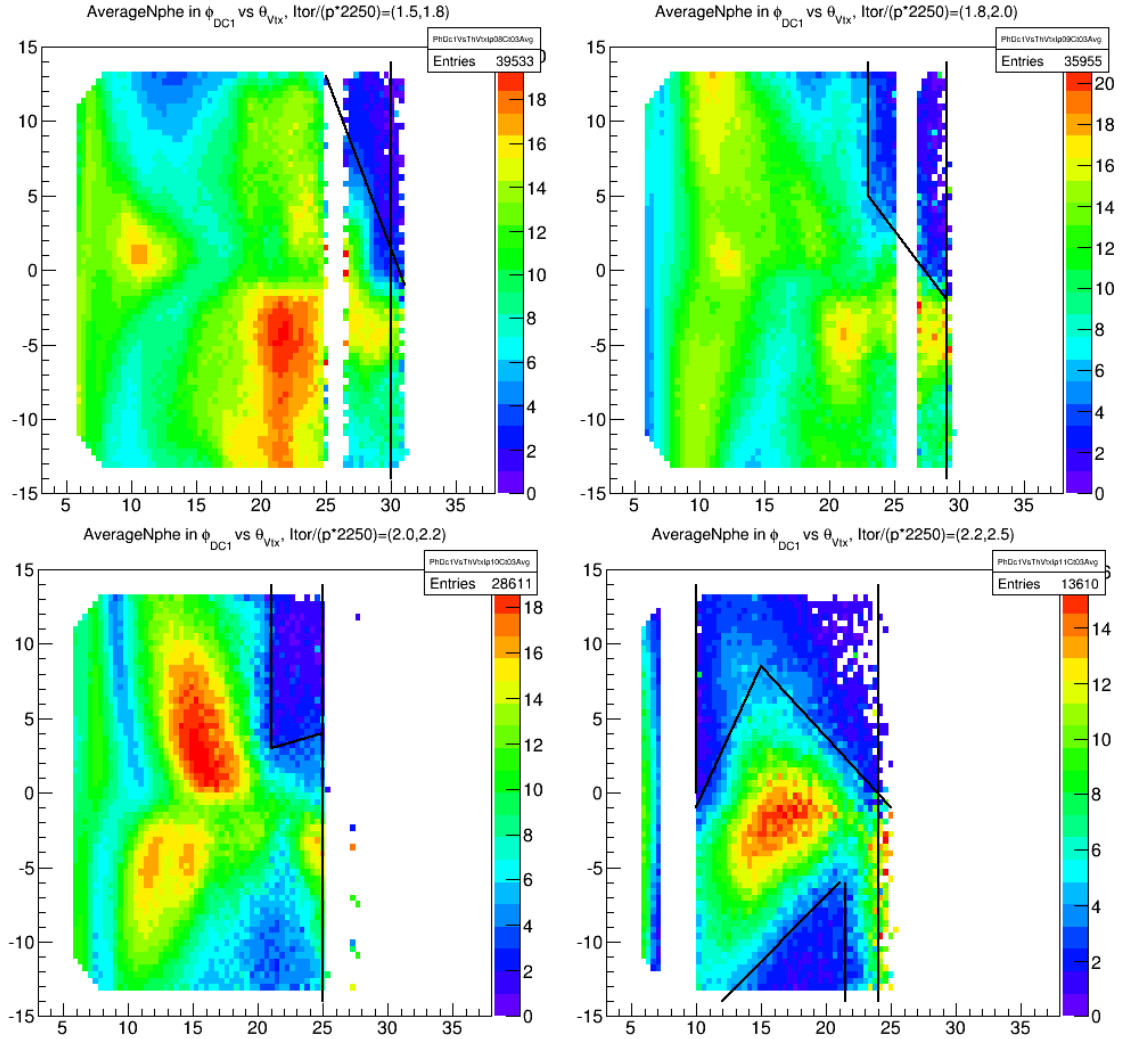


**Figure 3.21:** Average Nphe distributions as a function of  $\phi_{DC1}$  (along Y-axis) and  $\theta_{vtx}$  (along X-axis) in last four bins of  $\frac{I_{tor}}{p \cdot 2250}$ . The black lines show the cuts that reject the very low CC-inefficiency regions.

## 708 3.4 Data Quality and Stability Checks

709 With an available set of good event/electron selection cuts, beam charge  
710 (measured by Faraday cup) normalized total event counts (sometimes also  
711 known as event “yield”), as well as polarization dependent differences, were  
712 calculated for each of the data files for all the runs and then plotted against  
713 the run number to study the data quality and stability as shown by Figs.  
714 3.22, 3.23 and 3.24.

715 If nothing unusual happened or if the experimental conditions are not  
716 changed, then it is expected that the event yield as well as the count differ-  
717 ences remain constant over time. Therefore, the graphs of these event counts  
718 plotted versus time or run number (which also roughly reflect the flow of  
719 time) should indicate the stability and quality of the data collected. For  
720 example, Fig. 3.22 shows such a total yield plot for all the data files from  
721 the 2.0 GeV beam energy data set on deuteron target. We can see that these  
722 data runs display some features of instability over the full period of time, but  
723 stability over short time periods. For example, all the data with run numbers  
724 below about 51610 show significantly higher event yield than the runs after  
725 that run (possibly due to beam-target misalignment as indicated by raster  
726 magnet ADC values in Fig 3.24).

727 Likewise, the stability of the polarized count differences in the elastic  
728 region ( $0.9 \text{ GeV} < W < 1.0 \text{ GeV}$ ) as well as separately in the delta ( $\Delta$ )  
729 resonance region were studied by plotting them versus the same run numbers  
730 (here the elastic and  $\Delta$ -resonance regions are considered separately, because  
731 the spin asymmetries in these two regions have opposite signs, which would  
732 have decreased the observed difference if combined. To further enhance the  
733 sensitivity of the observation, the difference of the count differences measured  
734 in the elastic and  $\Delta$ -resonance regions as given by

$$\Delta N_{elastic} - \Delta N_{\Delta-res} = \frac{1}{P_b P_t} \left[ \left( \frac{N^+}{FC^+} - \frac{N^-}{FC^-} \right)_{elastic} - \left( \frac{N^+}{FC^+} - \frac{N^-}{FC^-} \right)_{\Delta} \right] \quad (3.3)$$

735 were plotted (see Fig. 3.23). It was observed that this elastic normalized  
736 count difference (which is what really matters to our analysis, in the end)  
737 was much more stable than the total yield.

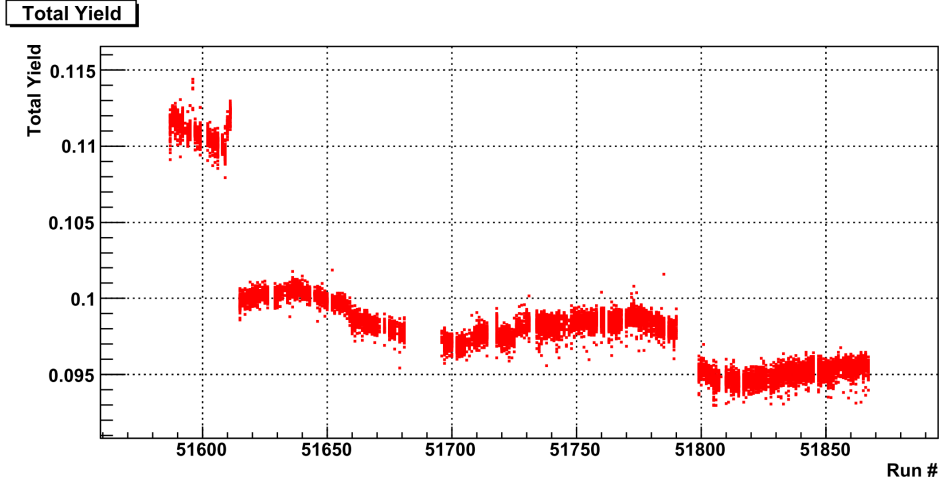


**Figure 3.22:** Total normalized yield ( $= \frac{N^+ + N^-}{FC^+ + FC^-}$ ) for 2.0 GeV ND<sub>3</sub> runs.

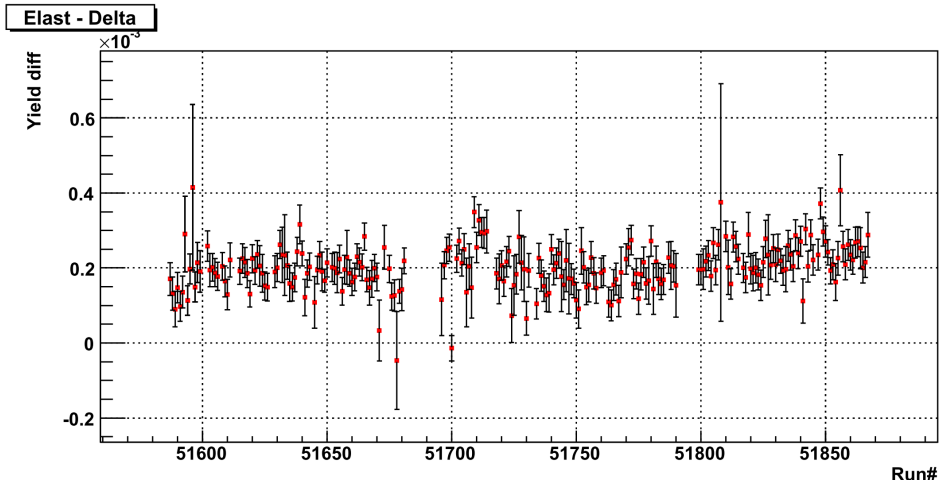


**Figure 3.23:** Polarized yield differences (Eq. 3.3) normalized with  $P_b P_t$  and BPM/F-cup for elastic peak minus that for the  $\Delta$  peak for the 2.0 GeV ND<sub>3</sub> runs.

738      The same was also repeated for the other variables such as the root-  
 739      mean-square of the ADC values (see Fig. 3.24) which carry information on  
 740      the X and Y coordinates of the beam at the interaction vertex, thus their  
 741      plots giving us somewhat more direct information on whether there was any  
 742      misalignment between the beam and the target.

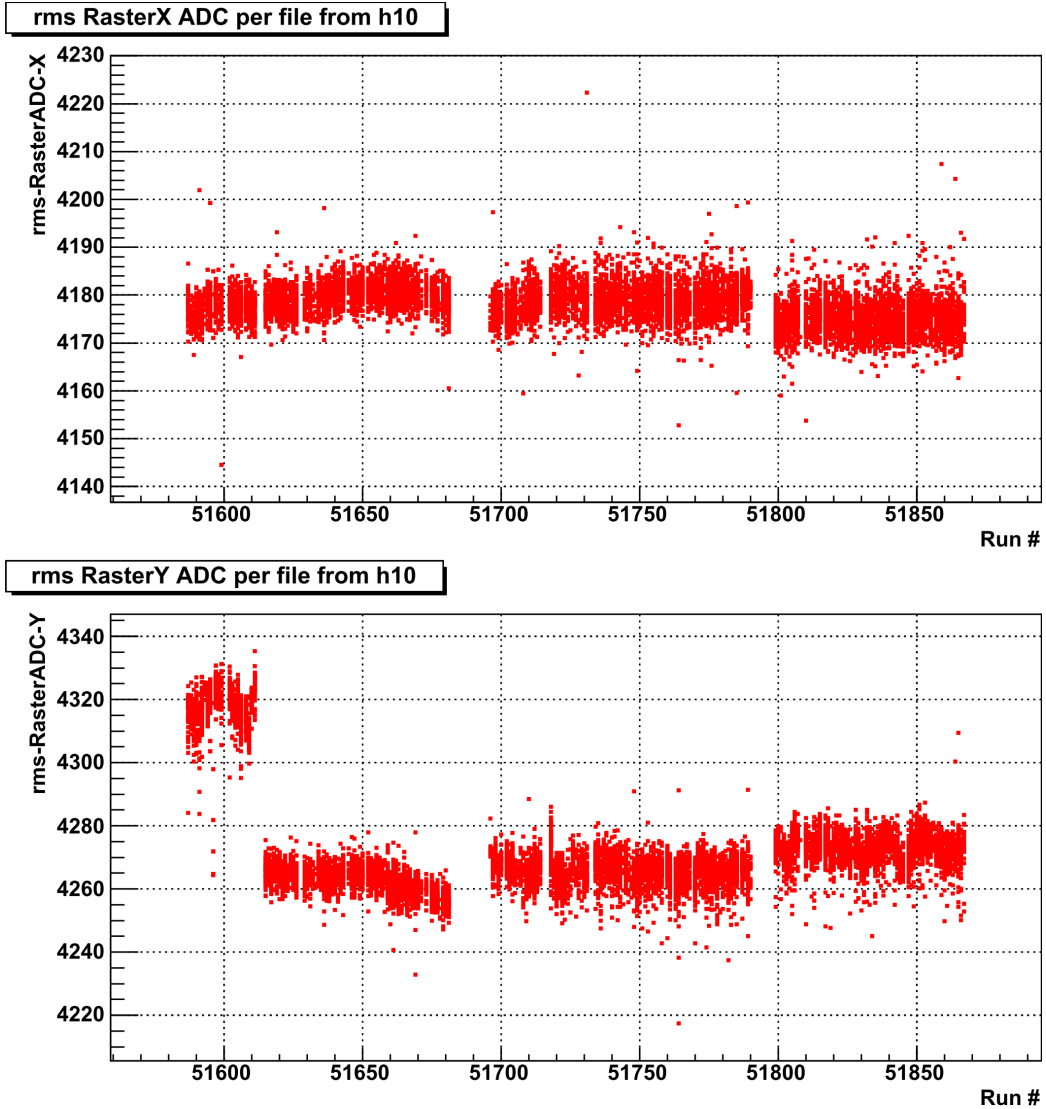


**Figure 3.24:** Root-mean-square of the ADC values for the raster magnet currents in the directions X and Y. The distributions show a larger raster size in the y-direction for the first group of runs, indicating that the beam may have been hitting the edges and the walls of the target or other more dense structure support materials, thus explaining the higher total yield for the corresponding runs as shown by the Fig. 3.22. This does not affect our final analysis because these off-target materials are not polarized and, hence, do not contribute to the polarization dependent count difference ( $\Delta N$ ) used in the final analysis.

743 Based on the studies of these quality and stability plots, the data runs  
744 were divided into subgroups with each beam energy data set. In each sub-  
745 group, the data showed more stability than over the whole run period for  
746 the given beam energy. For example, in case of the 2.0 GeV deuteron data,  
747 the runs were divided into four distinct sub groups corresponding to the four  
748 separate bands as seen in the Fig. 3.22. These subgroups were later treated  
749 and analyzed separately to get the corresponding normalized polarized count  
750 differences (with all data runs from each subgroup combined together). After  
751 the initial combination within the subgroups, they were again combined into  
752 the grand total by properly considering the half-wave-plate status, and the  
753 target polarization directions.

### 754 **3.5 Kinematic Corrections**

755 The reconstructed event vertices and associated particle 4-momenta are slightly  
756 off from their true values for several reasons. First, RECSIS does not take  
757 into account the fact that the beam is rastered in polarized target experi-  
758 ments. Next, any imperfections and mis-alignments of detectors and other  
759 components of the experimental set-up are not accounted for. Furthermore,  
760 the torus field map is not known precisely. In addition, the effects of multiple-  
761 scattering and particle energy losses are not considered in RECSIS. There-  
762 fore, to get more accurate results from the data analysis, the data quality  
763 must be improved by applying various kinematic corrections. Following is  
764 the list of the corrections that were applied for the analysis:

- 765 1. Incoming (beam) energy loss correction (due to ionization)
- 766 2. Tracking corrections
- 767 3. Drift chamber dependent momentum correction
- 768 4. Outgoing energy loss correction (due to ionization after scattering)

#### 769 **3.5.1 Incoming Energy Loss Correction**

770 The first correction listed above considers the loss of beam energy due to  
771 atomic collisions before the actual nuclear scattering takes place. A good  
772 estimate for this loss is 2 MeV on average [29, 30], which is subtracted from

773 the nominal beam energy. This correction is applied during the analysis  
774 whenever the beam energy is involved<sup>4</sup>, and therefore it is not included in  
775 the correction package described below.

### 776 3.5.2 Tracking Corrections

777 This work is mostly based on the work documented in the EG1-DVCS-TN-  
778 004[32] , in which a routine or method is developed to swim the particles  
779 through the field map of the target magnet to the drift chambers in order  
780 to determine the particle angles and position at the target, provided the di-  
781 rection cosines of the tracks at DC and the beam position from the raster  
782 magnets are known. It is expected that the method improves both the angu-  
783 lar resolution and the reconstructed longitudinal vertex position. The slightly  
784 modified version of the corresponding C/C++ routine is used with some of  
785 the constants in the routine replaced by new parameters to be determined  
786 by the method of  **$\chi^2$ -square minimization** using ep-elastic events. (Since  
787 this data set didn't have enough  $e^+e^-$  pairs, we didn't use them in the min-  
788 imization like in the EG1DVCS.)

### 789 Method

790 First of all, in order to convert raster magnet ADCs into corresponding  
791 beam positions  $x_0$  and  $y_0$ , we need conversion parameters. These param-  
792 eters are determined by using a method outlined in EG1-DVCS-TN-002[33].  
793 The method determines the values of the slopes and offsets that convert the  
794 X- and Y-raster ADC readings to corresponding beam positions  $x_0$  and  $y_0$   
795 in cm by minimizing the sensitivity of target vertex position ( $v_z$ ) for charged  
796 tracks to beam motion.

797 Next, ep-elastic events are skimmed (from all of the  $NH_3$  target data-  
798 set) using electron ID cuts for the electrons (see section 3.3) in the sixth  
799 sector and proton ID consisting mainly of the time-of-flight cuts are used to  
800 select protons in the third sector (opposite to the sixth one). Then missing  
801 momentum cuts (less than 0.1 GeV for each of the four components  $P_x$ ,  
802  $P_y$ ,  $P_z$  and  $E$ ) based on 4-momentum conservation requirements (within  
803 measurement uncertainties) are used to help further clean up the accidental

---

799  
800  
801  
802  
803  
804  
805  
806  
807  
808  
809  
810  
811  
812  
813  
814  
815  
816  
817  
818  
819  
820  
821  
822  
823  
824  
825  
826  
827  
828  
829  
830  
831  
832  
833  
834  
835  
836  
837  
838  
839  
840  
841  
842  
843  
844  
845  
846  
847  
848  
849  
850  
851  
852  
853  
854  
855  
856  
857  
858  
859  
860  
861  
862  
863  
864  
865  
866  
867  
868  
869  
870  
871  
872  
873  
874  
875  
876  
877  
878  
879  
880  
881  
882  
883  
884  
885  
886  
887  
888  
889  
890  
891  
892  
893  
894  
895  
896  
897  
898  
899  
900  
901  
902  
903  
904  
905  
906  
907  
908  
909  
910  
911  
912  
913  
914  
915  
916  
917  
918  
919  
920  
921  
922  
923  
924  
925  
926  
927  
928  
929  
930  
931  
932  
933  
934  
935  
936  
937  
938  
939  
940  
941  
942  
943  
944  
945  
946  
947  
948  
949  
950  
951  
952  
953  
954  
955  
956  
957  
958  
959  
960  
961  
962  
963  
964  
965  
966  
967  
968  
969  
970  
971  
972  
973  
974  
975  
976  
977  
978  
979  
980  
981  
982  
983  
984  
985  
986  
987  
988  
989  
990  
991  
992  
993  
994  
995  
996  
997  
998  
999  
1000  
1001  
1002  
1003  
1004  
1005  
1006  
1007  
1008  
1009  
10010  
10011  
10012  
10013  
10014  
10015  
10016  
10017  
10018  
10019  
10020  
10021  
10022  
10023  
10024  
10025  
10026  
10027  
10028  
10029  
10030  
10031  
10032  
10033  
10034  
10035  
10036  
10037  
10038  
10039  
10040  
10041  
10042  
10043  
10044  
10045  
10046  
10047  
10048  
10049  
10050  
10051  
10052  
10053  
10054  
10055  
10056  
10057  
10058  
10059  
10060  
10061  
10062  
10063  
10064  
10065  
10066  
10067  
10068  
10069  
10070  
10071  
10072  
10073  
10074  
10075  
10076  
10077  
10078  
10079  
10080  
10081  
10082  
10083  
10084  
10085  
10086  
10087  
10088  
10089  
10090  
10091  
10092  
10093  
10094  
10095  
10096  
10097  
10098  
10099  
100100  
100101  
100102  
100103  
100104  
100105  
100106  
100107  
100108  
100109  
100110  
100111  
100112  
100113  
100114  
100115  
100116  
100117  
100118  
100119  
100120  
100121  
100122  
100123  
100124  
100125  
100126  
100127  
100128  
100129  
100130  
100131  
100132  
100133  
100134  
100135  
100136  
100137  
100138  
100139  
100140  
100141  
100142  
100143  
100144  
100145  
100146  
100147  
100148  
100149  
100150  
100151  
100152  
100153  
100154  
100155  
100156  
100157  
100158  
100159  
100160  
100161  
100162  
100163  
100164  
100165  
100166  
100167  
100168  
100169  
100170  
100171  
100172  
100173  
100174  
100175  
100176  
100177  
100178  
100179  
100180  
100181  
100182  
100183  
100184  
100185  
100186  
100187  
100188  
100189  
100190  
100191  
100192  
100193  
100194  
100195  
100196  
100197  
100198  
100199  
100200  
100201  
100202  
100203  
100204  
100205  
100206  
100207  
100208  
100209  
100210  
100211  
100212  
100213  
100214  
100215  
100216  
100217  
100218  
100219  
100220  
100221  
100222  
100223  
100224  
100225  
100226  
100227  
100228  
100229  
100230  
100231  
100232  
100233  
100234  
100235  
100236  
100237  
100238  
100239  
100240  
100241  
100242  
100243  
100244  
100245  
100246  
100247  
100248  
100249  
100250  
100251  
100252  
100253  
100254  
100255  
100256  
100257  
100258  
100259  
100260  
100261  
100262  
100263  
100264  
100265  
100266  
100267  
100268  
100269  
100270  
100271  
100272  
100273  
100274  
100275  
100276  
100277  
100278  
100279  
100280  
100281  
100282  
100283  
100284  
100285  
100286  
100287  
100288  
100289  
100290  
100291  
100292  
100293  
100294  
100295  
100296  
100297  
100298  
100299  
100300  
100301  
100302  
100303  
100304  
100305  
100306  
100307  
100308  
100309  
100310  
100311  
100312  
100313  
100314  
100315  
100316  
100317  
100318  
100319  
100320  
100321  
100322  
100323  
100324  
100325  
100326  
100327  
100328  
100329  
100330  
100331  
100332  
100333  
100334  
100335  
100336  
100337  
100338  
100339  
100340  
100341  
100342  
100343  
100344  
100345  
100346  
100347  
100348  
100349  
100350  
100351  
100352  
100353  
100354  
100355  
100356  
100357  
100358  
100359  
100360  
100361  
100362  
100363  
100364  
100365  
100366  
100367  
100368  
100369  
100370  
100371  
100372  
100373  
100374  
100375  
100376  
100377  
100378  
100379  
100380  
100381  
100382  
100383  
100384  
100385  
100386  
100387  
100388  
100389  
100390  
100391  
100392  
100393  
100394  
100395  
100396  
100397  
100398  
100399  
100400  
100401  
100402  
100403  
100404  
100405  
100406  
100407  
100408  
100409  
100410  
100411  
100412  
100413  
100414  
100415  
100416  
100417  
100418  
100419  
100420  
100421  
100422  
100423  
100424  
100425  
100426  
100427  
100428  
100429  
100430  
100431  
100432  
100433  
100434  
100435  
100436  
100437  
100438  
100439  
100440  
100441  
100442  
100443  
100444  
100445  
100446  
100447  
100448  
100449  
100450  
100451  
100452  
100453  
100454  
100455  
100456  
100457  
100458  
100459  
100460  
100461  
100462  
100463  
100464  
100465  
100466  
100467  
100468  
100469  
100470  
100471  
100472  
100473  
100474  
100475  
100476  
100477  
100478  
100479  
100480  
100481  
100482  
100483  
100484  
100485  
100486  
100487  
100488  
100489  
100490  
100491  
100492  
100493  
100494  
100495  
100496  
100497  
100498  
100499  
100500  
100501  
100502  
100503  
100504  
100505  
100506  
100507  
100508  
100509  
100510  
100511  
100512  
100513  
100514  
100515  
100516  
100517  
100518  
100519  
100520  
100521  
100522  
100523  
100524  
100525  
100526  
100527  
100528  
100529  
100530  
100531  
100532  
100533  
100534  
100535  
100536  
100537  
100538  
100539  
100540  
100541  
100542  
100543  
100544  
100545  
100546  
100547  
100548  
100549  
100550  
100551  
100552  
100553  
100554  
100555  
100556  
100557  
100558  
100559  
100560  
100561  
100562  
100563  
100564  
100565  
100566  
100567  
100568  
100569  
100570  
100571  
100572  
100573  
100574  
100575  
100576  
100577  
100578  
100579  
100580  
100581  
100582  
100583  
100584  
100585  
100586  
100587  
100588  
100589  
100590  
100591  
100592  
100593  
100594  
100595  
100596  
100597  
100598  
100599  
100600  
100601  
100602  
100603  
100604  
100605  
100606  
100607  
100608  
100609  
100610  
100611  
100612  
100613  
100614  
100615  
100616  
100617  
100618  
100619  
100620  
100621  
100622  
100623  
100624  
100625  
100626  
100627  
100628  
100629  
100630  
100631  
100632  
100633  
100634  
100635  
100636  
100637  
100638  
100639  
100640  
100641  
100642  
100643  
100644  
100645  
100646  
100647  
100648  
100649  
100650  
100651  
100652  
100653  
100654  
100655  
100656  
100657  
100658  
100659  
100660  
100661  
100662  
100663  
100664  
100665  
100666  
100667  
100668  
100669  
100670  
100671  
100672  
100673  
100674  
100675  
100676  
100677  
100678  
100679  
100680  
100681  
100682  
100683  
100684  
100685  
100686  
100687  
100688  
100689  
100690  
100691  
100692  
100693  
100694  
100695  
100696  
100697  
100698  
100699  
100700  
100701  
100702  
100703  
100704  
100705  
100706  
100707  
100708  
100709  
100710  
100711  
100712  
100713  
100714  
100715  
100716  
100717  
100718  
100719  
100720  
100721  
100722  
100723  
100724  
100725  
100726  
100727  
100728  
100729  
100730  
100731  
100732  
100733  
100734  
100735  
100736  
100737  
100738  
100739  
100740  
100741  
100742  
100743  
100744  
100745  
100746  
100747  
100748  
100749  
100750  
100751  
100752  
100753  
100754  
100755  
100756  
100757  
100758  
100759  
100760  
100761  
100762  
100763  
100764  
100765  
100766  
100767  
100768  
100769  
100770  
100771  
100772  
100773  
100774  
100775  
100776  
100777  
100778  
100779  
100780  
100781  
100782  
100783  
100784  
100785  
100786  
100787  
100788  
100789  
100790  
100791  
100792  
100793  
100794  
100795  
100796  
100797  
100798  
100799  
100800  
100801  
100802  
100803  
100804  
100805  
100806  
100807  
100808  
100809  
100810  
100811  
100812  
100813  
100814  
100815  
100816  
100817  
100818  
100819  
100820  
100821  
100822  
100823  
100824  
100825  
100826  
100827  
100828  
100829  
100830  
100831  
100832  
100833  
100834  
100835  
100836  
100837  
100838  
100839  
100840  
100841  
100842  
100843  
100844  
100845  
100846  
100847  
100848  
100849  
100850  
100851  
100852  
100853  
100854  
100855  
100856  
100857  
100858  
100859  
100860  
100861  
100862  
100863  
100864  
100865  
100866  
100867  
100868  
100869  
100870  
100871  
100872  
100873  
100874  
100875  
100876  
100877  
100878  
100879  
100880  
100881  
100882  
100883  
100884  
100885  
100886  
100887  
100888  
100889  
100890  
100891  
100892  
100893  
100894  
100895  
100896  
100897  
100898  
100899  
100900  
100901  
100902  
100903  
100904  
100905  
100906  
100907  
100908  
100909  
100910  
100911  
100912  
100913  
100914  
100915  
100916  
100917  
100918  
100919  
100920  
100921  
100922  
100923  
100924  
100925  
100926  
100927  
100928  
100929  
100930  
100931  
100932  
100933  
100934  
100935  
100936  
100937  
100938  
100939  
100940  
100941  
100942  
100943  
100944  
100945  
100946  
100947  
100948  
100949  
100950  
100951  
100952  
100953  
100954  
100955  
100956  
100957  
100958  
100959  
100960  
100961  
100962  
100963  
100964  
100965  
100966  
100967  
100968  
100969  
100970  
100971  
100972  
100973  
100974  
100975  
100976  
100977  
100978  
100979  
100980  
100981  
100982  
100983  
100984  
100985  
100986  
100987  
100988  
100989  
100990  
100991  
100992  
100993  
100994  
100995  
100996  
100997  
100998  
100999  
1001000  
1001001  
1001002  
1001003  
1001004  
1001005  
1001006  
1001007  
1001008  
1001009  
1001010  
1001011  
1001012  
1001013  
1001014  
1001015  
1001016  
1001017  
1001018  
1001019  
1001020  
1001021  
1001022  
1001023  
1001024  
1001025  
1001026  
1001027  
1001028  
1001029  
1001030  
1001031  
1001032  
1001033  
1001034  
1001035  
1001036  
1001037  
1001038  
1001039  
1001040  
1001041  
1001042  
1001043  
1001044  
1001045  
1001046  
1001047  
1001048  
1001049  
1001050  
1001051  
1001052  
1001053  
1001054  
1001055  
1001056  
1001057  
1001058  
1001059  
1001060  
1001061  
1001062  
1001063  
1001064  
1001065  
1001066  
1001067  
1001068  
1001069  
1001070  
1001071  
1001072  
1001073  
1001074  
1001075  
1001076  
1001077  
1001078  
1001079  
1001080  
1001081  
1001082  
1001083  
1001084  
1001085  
1001086  
1001087  
1001088  
1001089  
1001090  
1001091  
1001092  
1001093  
1001094  
1001095  
1001096  
1001097  
1001098  
1001099  
1001100  
1001101  
1001102  
1001103  
1001104  
1001105  
1001106  
1001107  
1001108  
1001109  
1001110  
1001111  
1001112  
1001113  
1001114  
1001115  
1001116  
1001117  
1001118  
1001119  
1001120  
1001121  
1001122  
1001123  
1001124  
1001125  
1001126  
1001127  
1001128  
1001129  
1001130  
1001131  
1001132  
1001133  
1001134  
1001135  
1001136  
1001137  
1001138  
1001139  
1001140  
1001141  
1001142  
1001143  
1001144  
1001145  
1001146  
1001147  
1001148  
1001149  
1001150  
1001151  
1001152  
1001153  
1001154  
1001155  
1001156  
1001157  
1001158  
1001159  
1001160  
1001161  
1001162  
1001163  
1001164  
1001165  
1001166  
1001167  
1001168  
1001169  
1001170  
1001171  
1001172  
1001173  
1001174  
1001175

804 coincidences. These skimmed events are saved in root files and later reused  
805 for the minimization process described here.

806 The cuts used in the initial data skimming required that each of the four  
807 missing components  $(Px, Py, Pz, E)_{miss}$  be less than 0.1 GeV.

808 After that a correction routine involving a set of correction equations  
809 with several unknown parameters are established. Then with the help of  
810 TMinuit (ROOT version of Minuit), several sets of trial values are given to  
811 these unknown parameters and the corresponding correction is applied to  
812 the particles in the skimmed events. For each set of these trial values, a  
813 specifically defined  $\chi^2$  (see below) is evaluated looping over all the skimmed  
814 events and the Minuit tries to find the optimum set of these parameter values  
815 for which the  $\chi^2$  is minimum. Such an optimal set of values are chosen as  
816 the correct values of these parameters and is used in the eventual correction  
817 routine.

818 **The correction routine**

819 The routine uses 17 constants (free parameters determined by the above  
820 mentioned process of  $\chi^2$ -minimization) and the following input and output  
821 variables:

- 822 • **Input variables:**  $x_r, y_r, \text{cxd}, \text{cyd}, \text{xdc}, \text{ydc}, \text{zdc}, p, q$ .

823 –  $x_r, y_r$  are x & y beam positions as returned by the raster correction  
824 routine (see appendix)  
825 – **cxd, cyd** are direction cosines of the track as measured at DC1  
826 – **xdc, ydc, zdc** are the coordinates of the track measured at DC1  
827 – p, q are the momentum and charge of the track

- 828 • **Output variables:** cxc, cyc, czc, vzc (all three corrected direction  
829 cosines and the corrected Z-coordinate at the vertex) .

830 The sequence of calculation steps taken (inside the routine) to arrive at the  
831 output results are as follows (where, I am also using the notations of P.  
832 Bosted i.e., subscripts '0' used to indicate variables at vertex, subscript 'f'  
833 for those at the drift chambers (these are the tl1\_ variables in the ntuples),  
834 and the values of (x, y, z) are in cm):

- 835 • First of all, get ready the following constants and variables:

- $f_c = \frac{B}{50} = 0.995$  is the overall field correction
    - \* (i.e., the  $B.dl$  correction factor. Our  $B = 4.97T$ , with B in kG  $f_c$  is 0.995)
  - $targsign = 1$
  - $\theta_f = \arccos(cz_{dc})$
  - $\phi_f = \text{atan2}(cy_{dc}, cx_{dc})$
- Then,  $\theta_f$  is corrected (for the misalignment of the DC) as follows:
  - If it's the electron in the event,
    - \*  $\theta_f = \theta_f + (\text{par}[0] + \text{par}[1] \times \phi_f) \frac{\cos\theta_f}{\cos\phi_f} + (\text{par}[2] + \text{par}[3] \times \phi_f) \sin\theta_f$
  - else if its the proton,
    - \*  $\theta_f = \theta_f + (\text{par}[4] + \text{par}[5] \times \phi_f)$
- Next, get  $\phi_0$  without raster corrections yet
  - $\phi_0 = \phi_f + targsign \times f_c (0.186 + \text{par}[10] + (0.045 + \text{par}[11]) \theta^2 + (0.008 + \text{par}[12]) \theta_f^3 + (0.0032 + \text{par}[13]) \theta_f^3/p^2) \frac{q}{p}$
- Correction to polar angle from focusing effect. First, get focusing term for beam (x,y)=0.
  - $\delta\theta = f_c (0.90 \theta_f + 1.2 \theta_f^3)/(100 p^2)$
- Displacement of beam along trajectory ( $x_p$ ) and perpendicular to it ( $y_p$ )
  - $x_p = x_r \cos\phi_0 + y_r \sin\phi_0$
  - $y_p = -(x_r + \text{par}[6]) \sin\phi_0 + (y_r + \text{par}[7]) \cos\phi_0$
- Correction to  $\delta\theta$  from radial target field, which only depends on raster x and y but not vertex z. Also, no effect on peak at zero!
  - $\delta\theta = \delta\theta (1. + targsign q p (0.5/\theta_f) (y_p/0.75))$

862     • Now can get cz

863        –  $\theta_0 = \theta_f + \delta\theta$

864        –  $cz_c = \cos\theta_0$

865     • Now  $\phi_0$  again, this time including raster correction

866        –  $\phi_0 = \phi_f + \text{targsign } f_c (0.186 + \text{par}[10] + (0.045 + \text{par}[11]) \theta^2 +$   
867                     $(0.008 + \text{par}[12]) \theta_f^3 + (0.0032 + \text{par}[13]) \theta_f^3/p^2) \frac{q}{p} (1 - (0.09 +$   
868                     $\text{par}[14]) \frac{0.35 - \text{par}[15]}{\theta_f} x_p)$

869     • Get cx and cy using this cz

870        –  $cx_c = \sin\theta_0 \cos\phi_0$

871        –  $cy_c = \sin\theta_0 \sin\phi_0$

872     • Renormalize czc

873        –  $cz_c = \sqrt{1.0 - cx_c^2 - cy_c^2}$

874     • Apply target field rotation correction

875        –  $cx_c = cx_c - \text{targsign } q \text{par}[8] cz_c/p$

876        –  $cy_c = cy_c + \text{targsign } q \text{par}[9] cz_c/p$

877     • Renormalize again:

878        –  $czc = \sqrt{1.0 - cx_c^2 - cy_c^2}$

879        –  $\theta_0 = \arccos(cz_c)$

880     • Get vertex z in cm

881        –  $r_{dc} = \sqrt{(x_{dc} - x_r)^2 + (y_{dc} - y_r)^2}$

882        –  $Z_c = Z_{dc} - \frac{r_{dc} - (22 + \text{par}[16]) \cos\theta_0 (\tan\theta_0 - \tan\theta_f)}{\tan\theta_f}$

883     • Finally, the routine outputs (returns) the four corrected quantities

884        –  $cx_c, cy_c, cz_c, Z_c$ .

885    **Calculation of  $\chi^2$  (to be minimized)**

886    The chi-square has different components as follows:

$$887 \quad \chi^2 = \chi_{\text{Zvar}}^2(\mathbf{e}) + \chi_{\text{Zvar}}^2(\mathbf{p}) + \chi_{\text{Evar}}^2 + \chi_{\text{miss}}^2 + \chi_{\text{Ppen}}^2 + \chi_{\text{Epen}}^2 + \chi_{\text{Zpen}}^2 + \chi_{\Delta E}^2$$

888    where,

- 889    •  $\chi_{\text{Zvar}}^2(\mathbf{e})$  and  $\chi_{\text{Zvar}}^2(\mathbf{p})$  are Z-variance contributions from electron and  
890    proton candidates in the ep-elastic events and are calculated as  $\chi_{\text{Zvar}}^2 =$   
891     $\frac{1}{N_{ep}-1} \left( \sum Z_c^2 - \frac{(\sum Z_c)^2}{N_{ep}} \right) / (0.05)^2$  separately for the electrons and protons.  
892    (Here,  $Z_c$  is the corrected  $Z$  of vertex and  $N_{ep}$  is the number ep-elastic  
893    events used in the minimization)
- 894    •  $\chi_{\text{Evar}}^2 = \frac{1}{N_{ep}-1} \left( \sum E_b^2 - \frac{(\sum E_b)^2}{N_{ep}} \right) / (0.005)^2$  is  $E_b$ -variance contribution.  
895    (Here,  $E_b = M_p \left( \frac{1}{\tan(\theta_p)\tan(\theta_e/2)} - 1 \right)$  is the beam energy calculated after  
896    the angles are corrected by the correction routine.)
- 897    •  $\chi_{\text{miss}}^2 = 100 \times \left( \frac{\sum p_x^2(\text{miss}) + \sum p_y^2(\text{miss})}{0.02^2} + \frac{\sum p_z^2(\text{miss}) + \sum E^2(\text{miss})}{0.05^2} \right)$  is missing  
898    four-momentum contribution. (Here, 100 is an arbitrary number to  
899    make the weight of this contribution comparable to others.)
- 900    •  $\chi_{\text{Ppen}}^2 = \sum_{i=0}^{16} \frac{(par[i] - iPar[i])^2}{0.01^2}$  is the contribution due to runaway penalty  
901    on free parameters of the minimization. (Here, par[i] & iPar[i] are the  
902    current and initial values of the 'i'th parameter. In the first iteration,  
903    initial values were set to either zeros or the corresponding values as  
904    determined for EG1-DVCS by P. Bosted. In later iterations, they were  
905    set to the values determined from the previous iteration of the mini-  
906    mization.)
- 907    •  $\chi_{\text{Zpen}}^2 = \sum_{e,p} \left( \sum_{N_{ep}} \frac{(Z_c - (-100.93))^2}{0.05^2} \right)$  is a penalty term when  $Z_c$  runs away  
908    from the known/nominal target center (-100.93 cm)
- 909    •  $\chi_{\text{Epen}}^2 = \sum_{i=2}^4 \left( \frac{\sum_{N_{ep}} E_b}{N_{ep}} - E_0 \right)^2 / (0.005)^2$  is a penalty term to constrain  $E_b$   
910    running away from the nominal values  $E_0$  of beam energy.

- 911        •  $\chi^2_{\Delta E} = \left( \sum_{i=2}^4 \frac{\sum N_{ep}}{N_{ep}} (E_b - E_0)^2 \right) / (0.005)^2$  is another penalty term to constrain  
 912               $E_b$  running away from the nominal values  $E_0$  of beam energy.

913        **Minimization**

914        TMinuit is used to minimize the value of  $\chi^2$  as calculated above and, thereby,  
 915              determine the values of the free parameters used in the correction routine.  
 916        The minimization was done in such a way that the parameters were deter-  
 917              mined step by step - first deciding the first six parameters (keeping others  
 918              fixed to initial values), then next two, then next two, then next four, then  
 919              next 2 and finally the last one respectively.

920        **Tracking Correction Results**

921        With the method of  $\chi^2$ -minimization described above, the following set of  
 922              values were determined for the 17 parameters from par[0] through par[16]  
 923              respectively:  
 924              -0.00165789, -0.00131314, -0.00643021, -0.00721441, -0.00775272, 0.00483673,  
 925              0.063387, -0.0615822, 0.00133127, 0.000839944, 0.0210091, -0.0363265, 0.00335536,  
 926              0.00104193, 2.51519, -0.0313527, -1.29325

927        As a result of the corrections with these newly determined parameter  
 928              values, various quantities before and after the corrections looked as shown in  
 929              the following figure:

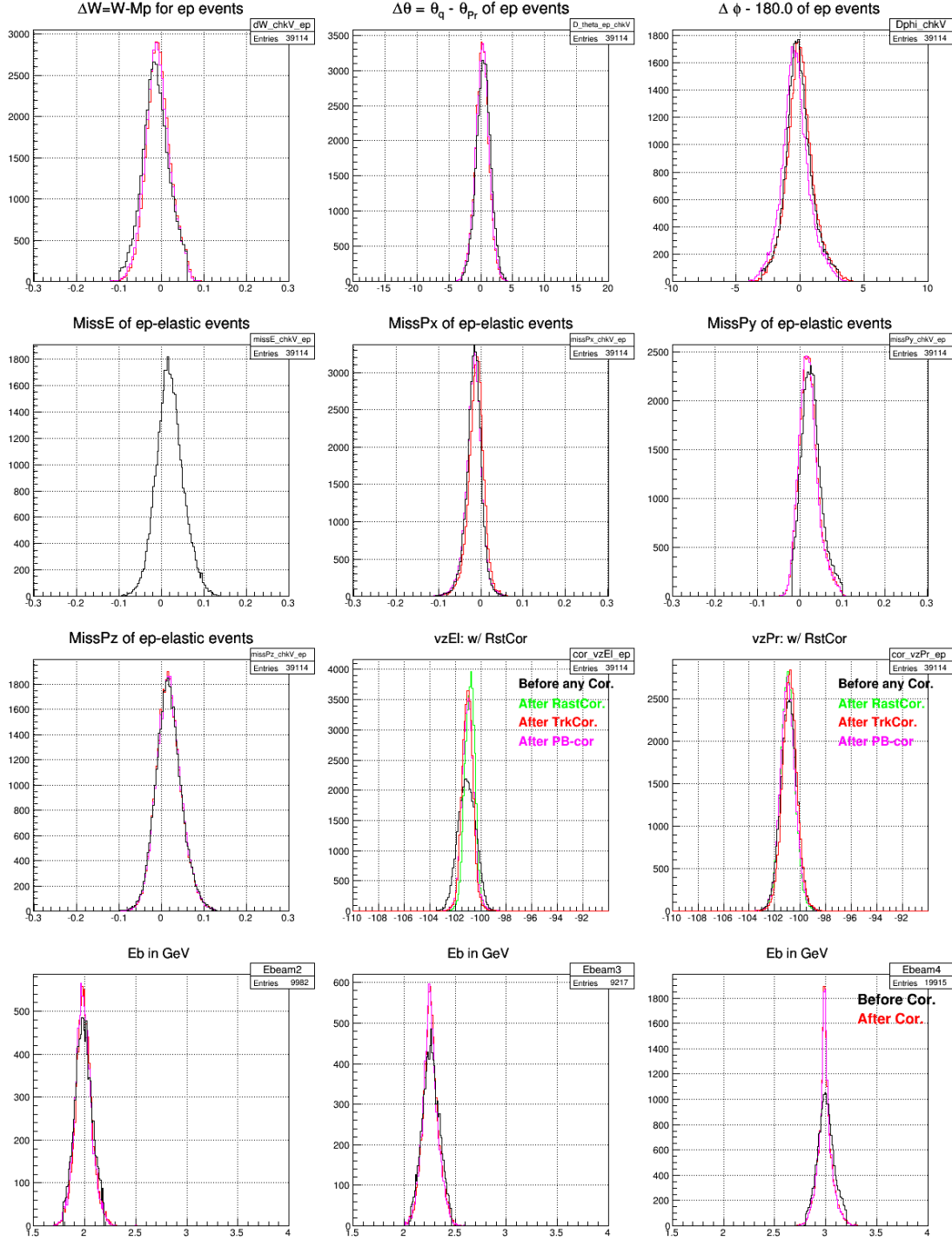


**Figure 3.25:** Comparing various quantities before and after the tracking corrections which affects only the angles (and ~~not~~ the magnitude 'p') of the momentum.

930 **3.5.3 Momentum Correction**

931 Different DC related factors contribute to the biggest part of the system-  
 932 atic deviations of particle momenta as reconstructed by RECSIS. The drift  
 933 chambers could be misaligned relative to their nominal positions or the sur-  
 934vey results that is used by RECSIS could be inaccurate or out-of-date. The  
 935 effects of physical deformations (due to thermal and stress distortions) of  
 936 the chamber including wire-sag, incorrect wire positions may not have been  
 937 incorporated properly. The torus field map used by the reconstruction soft-  
 938 ware may not have been accurate and complete enough [34]. Effects on angles  
 939  $\theta$  and  $\phi$  due to these contributions are already factored in the tracking cor-  
 940 rection described earlier. However, a separate method is developed to correct  
 941 for the effect on the magnitude  $p$  of the momentum. This  $p$ -correction meth-  
 942 ods picks up and builds on some of the ideas outlined in the CLAS-NOTE  
 943 2003-005 [34].

944 **Procedure to determine the first 11 parameters**

945 The procedure involved dividing the covered kinematic space into a number  
 946 of bins, finding in them the magnitude of shifts of the inclusive elastic peaks  
 947 w.r.t. the expected position and use that to fit to a function to get an  
 948 analytical expression for the correction. The following angular bins were  
 949 used:

- 950     • Six  $\theta_{dc1}$  bins: (0,8),(8,10),(10,12),(12,15),(15,20),(20,30) degrees
- 951     • Five  $\phi_{dc1}$  bins: (-10,-6),(-6,-2), (-2,2), (2,6), (6,10) degrees

952 where the angles used are the ones measured at the first drift chamber and  
 953  $\phi_{dc1}$  is measured w.r.t the sector mid-plane (thus the maximum range allowed  
 954 is (-30.0,30.0)).

$$E'_{elastic} = \frac{E_{beam}}{1 + \frac{2E_{beam}}{M_p} \sin^2(\theta_e/2)} \quad (3.4)$$

955 In each of these kinematic bins, the quantity  $\Delta E = E'_{elastic} - p$  (see Eq.  
 956 3.4) is histogrammed for both NH<sub>3</sub> and <sup>12</sup>C data separately. Next, the carbon  
 957 histogram is cross-normalized with the ammonia histogram (by comparing  
 958 the two in the region left to the quasi-elastic peak) and subtracted from the

959 latter one to remove the nuclear background. The difference gives histograms  
 960 for the elastic events (as shown by the dashed green histogram in Fig. 3.26).  
 961 A Gaussian fit to the extracted elastic histogram gives the position and width  
 962 of the distribution. The offset or shift of average position of the peak with  
 963 respect to the expected  $\Delta E = 0$  gives us the needed correction on energy  
 964  $E \approx p$  for the electron. This process is repeated for all of the bins listed  
 965 above and the corresponding  $\Delta E$  offsets or the corrections are determined  
 966 for each of them. Additionally,  $\Delta E$  distributions using  $^{15}N$  nuclear mass  
 967 in calculating  $E'_{elastic}$  are also made and off-sets in the corresponding elastic  
 968 peaks are also recorded whenever possible (particularly from the lower  $\theta$  bins  
 969 from low beam energy data where the nuclear-elastic and quasi-elastic peaks  
 970 are well separated). Finally, these values of corrections for different average  
 971 values of  $\theta_{dc1}$  and  $\phi_{dc1}$  are fit to Eq. 3.5 (which is based on similar work done  
 972 for EG1b analysis[22]) and using the method of  $\chi^2$ -minimization in order to  
 973 determine the values of the 11 fit parameters.

$$\frac{\Delta p}{p} = Pcorr1 + Pcorr2 + PatchCorr \quad (3.5)$$

974 where,  $\frac{\Delta p}{p}$  is the ratio of the correction ( $\Delta p$ ) to the magnitude ( $p$ ) of the  
 975 momentum and

$$Pcorr1 = \left( (E + F\phi) \frac{\cos\theta}{\sin\phi} + (G + H\phi) \sin\theta \right) \frac{p}{qB_{torus}} \quad (3.6)$$

$$Pcorr2 = (J\cos\theta + K\sin\theta) + (M\cos\theta + N\sin\theta)\phi \quad (3.7)$$

$$PatchCorr = 0.02 \left( P + (Q + R \frac{\phi_{deg}}{30^\circ}) (\frac{10^\circ}{\theta_{deg}})^3 \right) \quad (3.8)$$

976 The quantity  $B_{tor}$  stands for  $\int B_\perp dl$  along the track length multiplied by  
 977 the speed of light in the units of m/ns ( $c = 0.29979$  m/ns) and is given by

$$B_{tor} = 0.76 \frac{I_{tor} \sin^2(4\theta)}{3375\theta/rad} \quad \text{for } \theta < \frac{\pi}{8} \quad (3.9)$$

$$B_{tor} = 0.76 \frac{I_{tor}}{3375\theta/rad} \quad \text{for } \theta > \frac{\pi}{8} \quad (3.10)$$

978 In all these equations, sector number,  $\theta$ ,  $\phi$ ,  $\theta_{deg}$ , and  $\phi_{deg}$  come from the  
 979 angle information measured at DC1. The direction cosine variables tl1\_cx,  
 980 tl1\_cy, tl1\_cz (from pass1 ntuple) are used to derive these quantities. C++  
 981 standard functions `acos()` and `atan2()` are used to evaluate  $\theta$ ,  $\phi$  (w.r.t the  
 982 sector mid plane).

983 These total of eleven unknown parameters were determined by fitting  
 984 above mentioned momentum offsets (in combination with ionization energy  
 985 loss correction for electrons (see Sec.3.5.4 below)) to the correction function  
 986 given by the Eq. 3.5.

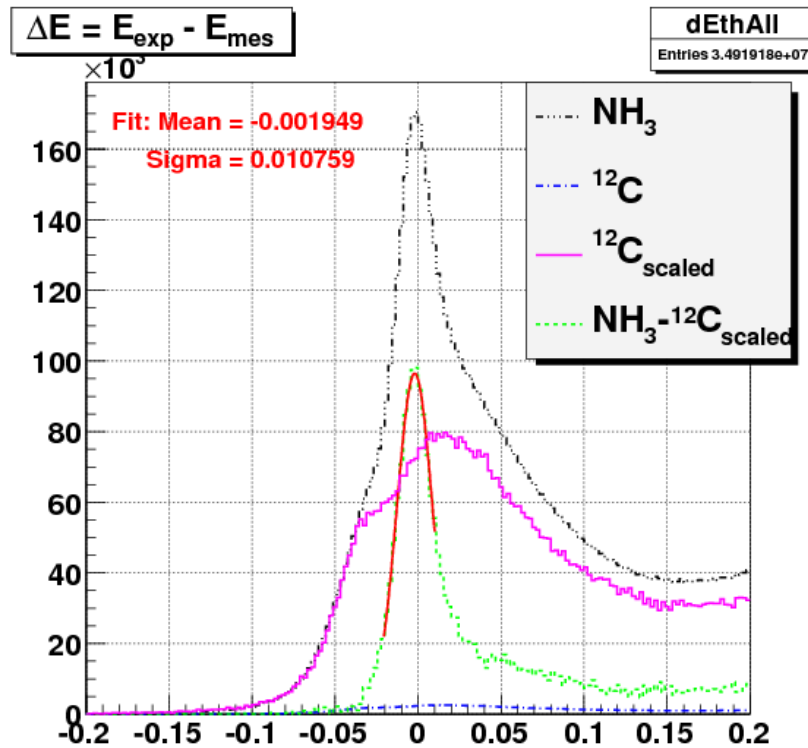


**Figure 3.26:** Plots showing background removal from the  $\Delta E$  counts from  $\text{NH}_3$  (shown by “ $\text{NH}_3$ ” line) data (by subtracting cross-normalized counts from  $^{12}\text{C}$  data (shown by “ $^{12}\text{C}_{\text{scaled}}$ ” line)) to separate the elastic peak (shown by “ $\text{NH}_3 - ^{12}\text{C}_{\text{scaled}}$ ” line) in one of the kinematic bins, thereby getting the momentum offset for that bin. The  $^{12}\text{C}$  data is used to account for the nuclear elastic background from  $^{15}\text{N}$  nucleii in the ammonia target. It would have been best to have data from  $^{15}\text{N}$  target itself but due to technical difficulties that was not possible and, therefore,  $^{12}\text{C}$  target was chosen as the closest possible approximation of  $^{15}\text{N}$  target.

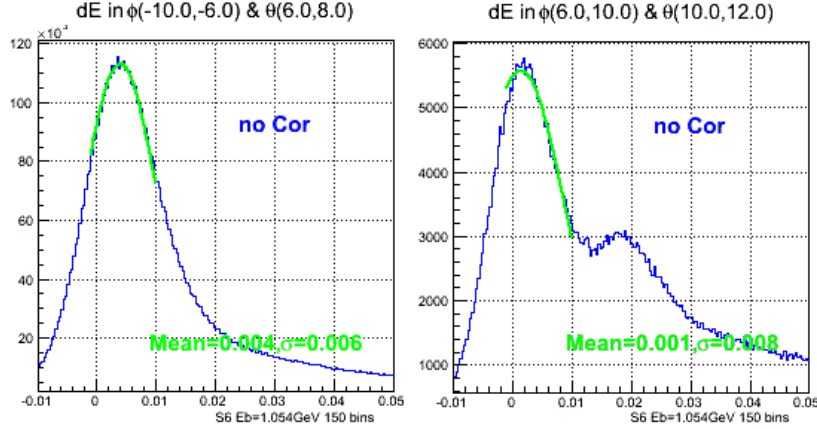


**Figure 3.27:** Nuclear elastic peaks from  $^{15}\text{N}$  target and the Gaussian fits in two of many kinematic bins as seen in  $\Delta E = E'_{\text{elastic}} - p$  distributions from NH<sub>3</sub> data before the momentum corrections. In this case  $E'_{\text{elastic}}$  is evaluated using known mass of  $^{15}\text{N}$  in Eq. 3.4. In the second plot, the proton elastic peak is also visible. Ideally, after all the corrections, the nuclear elastic peak is expected to be centered at zero. But, as is obvious from these figures, these peaks show offsets. These offsets (given by the mean values of the Gaussian fits) are collected from those bins in which the nuclear elastic peaks are very well separated (particularly the first few angular bins) and used in the  $\chi^2$ -minimization along with all the offsets of elastic peaks (see Fig. 3.26)

### 3.5.4 Outgoing Ionization Loss Correction

In addition to the corrections described above, the energy (E) of each of the particles is corrected for the outgoing ionization loss by adding an estimation of ionization loss as follows:  $E_{\text{cor}} = E + \Delta E$  with  $\Delta E = \frac{dE}{dX}\tau$  where the factor  $\tau$  is the total effective mass thickness traversed by the particle and

$$\frac{dE}{dX} \approx 2.8 \text{ MeV}/(\text{g cm}^{-2}) \quad \text{for electrons} \quad (3.11a)$$

and, for hadrons [35]

$$\frac{dE}{dX} \approx 0.307 \times \frac{0.5}{\beta^2} \left( \ln \left( 2.0 \times 511.0 \frac{\beta^2 \gamma^2}{0.090} \right) - \beta^2 \right) \text{ MeV} \quad (3.11b)$$

which is an approximation of the Bethe-Block formula [35]:

$$-\frac{1}{\rho} \frac{dE}{dx} = 4\pi N_a r_e^2 m_e c^2 \frac{Z}{A} \frac{1}{\beta^2} \left( \ln \left( \frac{2m_e c^2 \gamma^2 \beta^2}{I} \right) - \beta^2 \right) \quad (3.12)$$

994 The total effective mass thickness  $\tau$  (in cm) is calculated as follows:

995     •  $\tau = \tau_{||}/\cos\theta$     if  $\theta \leq \pi/4$

996     •  $\tau = \tau_{||}/\cos(\pi/4)$     if  $\theta > \pi/4$

997 where  $\tau_{||}$  is calculated as:

998     •  $\tau_{||} = \Delta z \times 0.6 + 0.4$     if  $\Delta z > 0.0$  and  $\Delta z < 1.0$

999     •  $\tau_{||} = 0.6 + 0.4$     if  $\Delta z \geq 1.0$

1000     •  $\tau_{||} = 0.4$     if  $\Delta z \leq 0.0$

1001 with  $\Delta z = z_{target\_center} - z_{ave} + L_{target}/2 = (-101.0 \text{ cm} - z_{ave} + 0.5) \text{ cm}$  being  
1002 the physical distance (along the target length) traveled by the particle  
1003 through the polarized target material (e.g. the EG4 ND<sub>3</sub> target has length  
1004 1.0 cm and is positioned at  $z = -101.0 \text{ cm}$ ). The factor 0.6 is the effective  
1005 mass thickness of ND<sub>3</sub> (density of ND<sub>3</sub> ( $\sim 1 \text{ g/cm}^3$ ) multiplied by the pack-  
1006 ing fraction which is roughly 0.6 [36], whereas 0.4 is the sum of the mass  
1007 thicknesses of He ( $\sim 0.3$ ) and that of window foils ( $\sim 0.1$ ) [22].

1008 Using the ionization loss corrected energy and the rest mass of the parti-  
1009 cle, momentum is recalculated as  $p_{cor} = \sqrt{E_{cor}^2 - m^2}$  (where  $m$  is the mass  
1010 of the particle). Finally, this new  $p$  is used along with the previously cor-  
1011 rected angles to evaluate the three cartesian components  $p_x$ ,  $p_y$  and  $p_z$  of the  
1012 momentum as follows:

$$\begin{aligned} p_x &= p \sin \theta \cos \phi \\ p_y &= p \sin \theta \sin \phi \\ p_z &= p \cos \theta \end{aligned} \tag{3.13}$$

1013

## 1014 3.6 Cerenkov Counter (CC) Efficiency

1015 In the EG4 experiment, the Cherenkov Counter (CC) signal plays a major  
1016 part in forming the event trigger for the data-acquisition system (DAQ). As  
1017 stated earlier (see 2.1), for the purpose of achieving low  $Q^2$  measurements  
1018 with high detector efficiency<sup>5</sup>, a new dedicated CC was designed and placed

---

<sup>5</sup>High detection efficiency is crucial for achieving smaller systematic uncertainties in the extracted physics quantities.

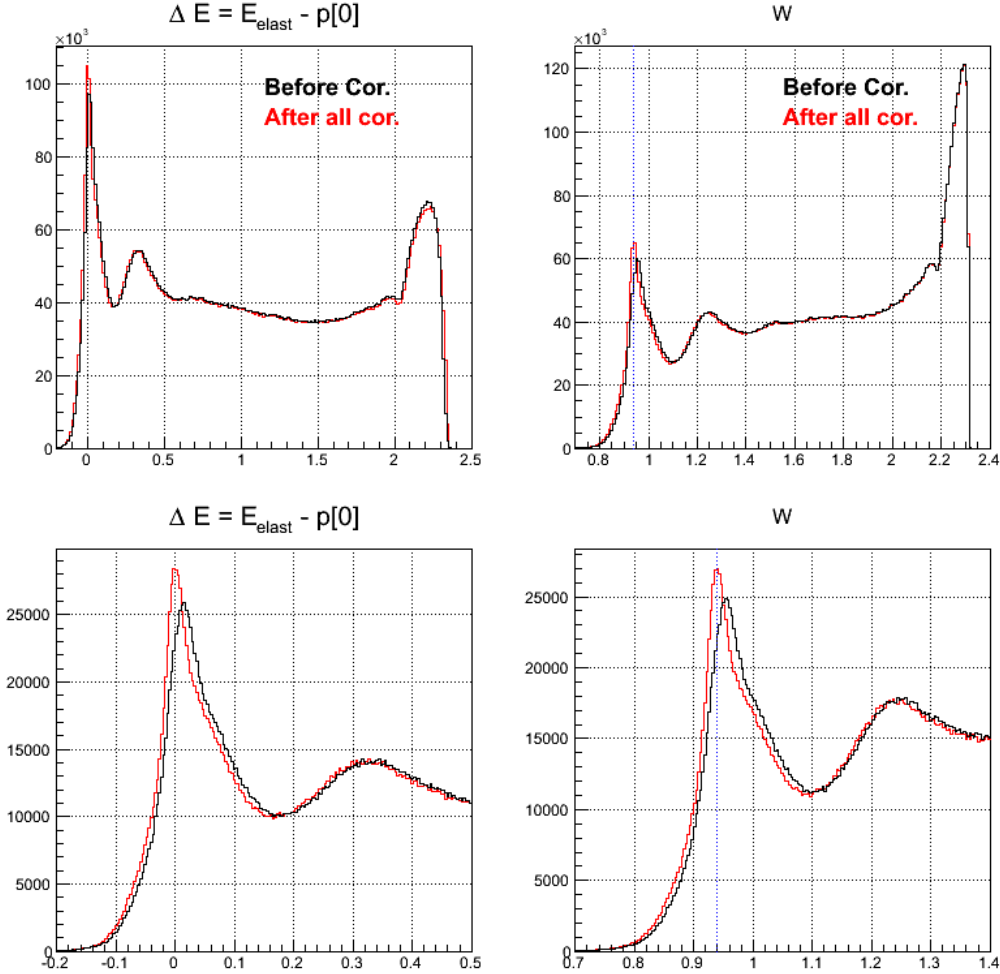


**Figure 3.28:** Effects of kinematic corrections on inclusive events from 3 GeV NH<sub>3</sub> data. Here, distributions of  $\Delta E$  and  $W$  are shown in two different ranges. The upper ones show the full range distributions, whereas the lower two show the distributions near the quasi-elastic peak. The distributions before the corrections are shown by **black continuous** lines and the ones after the corrections are shown by the **red** lines. Here,  $E_{\text{elast}}$  is the calculated or expected energy of the scattered electron assuming it was scattered off elastically, whereas,  $p[0]$  is the momentum as measured by CLAS. From these plots it is evident that the momentum correction works as expected because the peak of  $\Delta E$  is narrower and better centered at zero after the correction.

1019 in the sixth sector. Even though the new CC was designed to have a very  
1020 high and uniform detection efficiency, some variation occurs over the covered  
1021 kinematic range and therefore the knowledge of the detector efficiency as a  
1022 function of the kinematics is required by our method of absolute cross-section  
1023 difference. Therefore, a study was done to determine the CC efficiency as  
1024 follows.

1025 **3.6.1 Procedure**

1026 The efficiency for some specific kinematic bin depends on the average num-  
1027 ber of photoelectrons produced by electrons in that bin which, in turn, is  
1028 determined by the hit location on the Cerenkov PMT-projected plane as  
1029 well as the angle with which the electron hits (or intersects) the plane. In  
1030 the following, we describe how we determined the efficiency as a function of  
1031 kinematic variables.

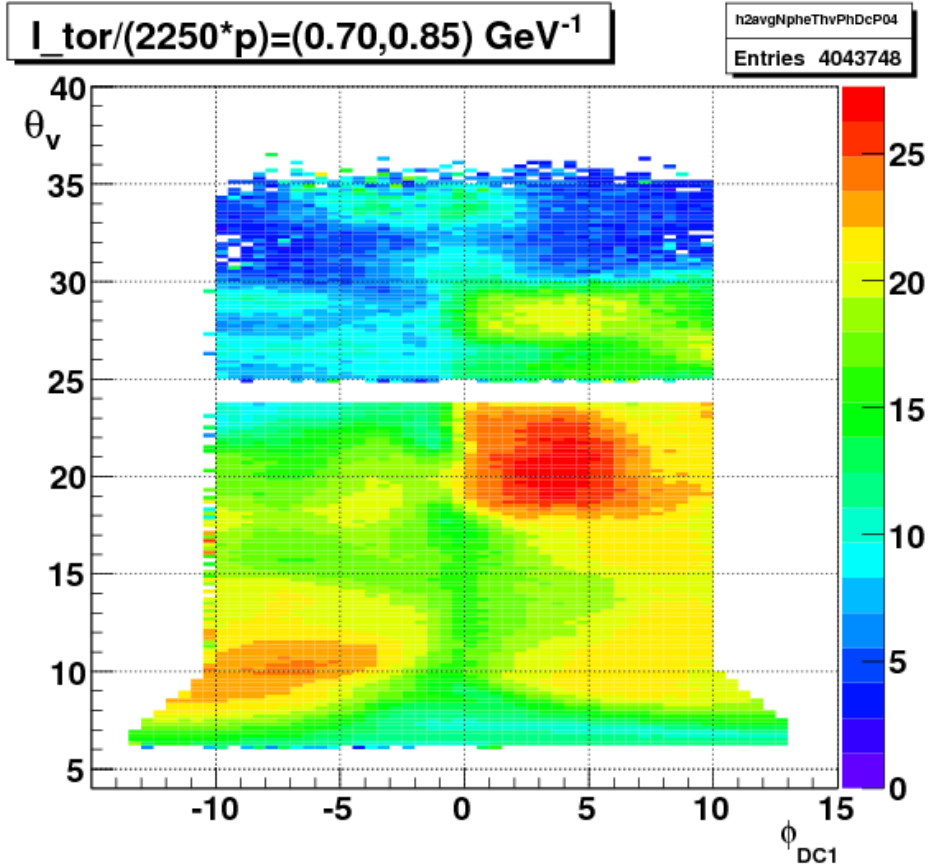


**Figure 3.29:** Average photoelectron number (color-coded) produced in the 6th sector CC as a function of  $\theta_{vtx}$  and  $\phi_{DC1}$  in the second bin of the variable  $ip = (I_{tor}/2250)/p$  (from the 2.3 GeV NH<sub>3</sub> data).

- 1032 1. First, we define a torus-current normalized inverse-momentum variable
- 1033  $ip = (I_{tor}/2250)/p$  (see above), and divide the whole kinematic space
- 1034 into 12 bins in “ip” as follows: (0.3, 0.4, 0.5, 0.6, 0.7, 0.85, 1.0, 1.25,
- 1035 1.5, 1.75, 2.0, 2.25, 2.53). (For example, a 0.5 GeV electron during a
- 1036 2 GeV run, which used 2250 A for torus current, would have  $ip = 2.0$
- 1037  $\text{GeV}^{-1}$ )
- 1038 2. Next, for each bin in “ip”, a 2D map of the average number of photoelec-
- 1039 trons is produced in a kinematic space defined by  $\theta_{vtx}$  (scattering angle
- 1040 measured at the event vertex) and  $\phi_{DC1}$  (azimuthal angle as measured

1041 at DC1). For this step, some data from NH<sub>3</sub> production runs<sup>6</sup> are used  
1042 with the standard electron selection cuts. One of these average-nphe  
1043 maps is shown in the Fig. 3.29.

- 1044 3. Next, using the “EC-only-trigger” data runs, good electron candidates  
1045 are selected using the same cuts as before but without any CC-related  
1046 cuts. For each of the selected electrons, the expected number of photo-  
1047 electrons in the CC is determined in a look-up from the above average  
1048 N<sub>ph</sub>-maps based on its momentum and angles. This expected N<sub>ph</sub> is  
1049 then histogrammed in two ways - one histogram for those electrons  
1050 which either didn’t trigger CC or didn’t pass all of the CC related  
1051 cuts and another histogram for all electrons. The ratio of these two  
1052 histograms (shown in the top-right and top-left panels of Fig. 3.30 re-  
1053 spectively) gives us the inefficiency of the CC-detector as a function of  
1054 N<sub>ph</sub> (as shown by the bottom two panels of the same figure). (Errors  
1055 in the inefficiencies have not been drawn (for the purpose of cleaning)  
1056 in the figures but they were calculated using the fact that the error in  
1057 a ratio N2/N1 is  $\sqrt{N2(1 - N2/N1)/N1}$ ).  
1058
- 1059 4. The ideally expected CC intrinsic inefficiency is given by the Poisson  
1060 distribution, since we require more than 2 photoelectrons, the theoreti-  
1061 cal prediction for the inefficiency is actually  $(1 + N_{ph} + 1/2 N_{ph}^2) * \exp(-N_{ph})$ . However, we found empirically that if we calculate N<sub>ph</sub> only with  
1062 electrons that exceed the threshold of 2.5, then we find that the func-  
1063 tional form is pretty close to the form  $y = p_0 + p_1 \cdot \exp(-p_2 x)$ , where  
1064 x represents  $\langle N_{ph} \rangle$ , and y represents the inefficiency. This form was  
1065 used to fit with the above measured inefficiency and the result of the  
1066 fit is shown in Fig. 3.30. We find that the inefficiency agrees very well  
1067 with the expectation at low nphe, but remains at a very small constant  
1068 value of around 0.01 (we call it the “constant background”) at higher  
1069 nphe.

---

<sup>6</sup>This method relies on the use of two different sets of data. One is the regular NH<sub>3</sub> target data and another is the “EC-only” data runs which were collected without using CC in the trigger. Since the latter type of data were collected with NH<sub>3</sub> as target, to be consistent, NH<sub>3</sub> production data was chosen rather than the ND<sub>3</sub> ones to make the N<sub>ph</sub>-maps.

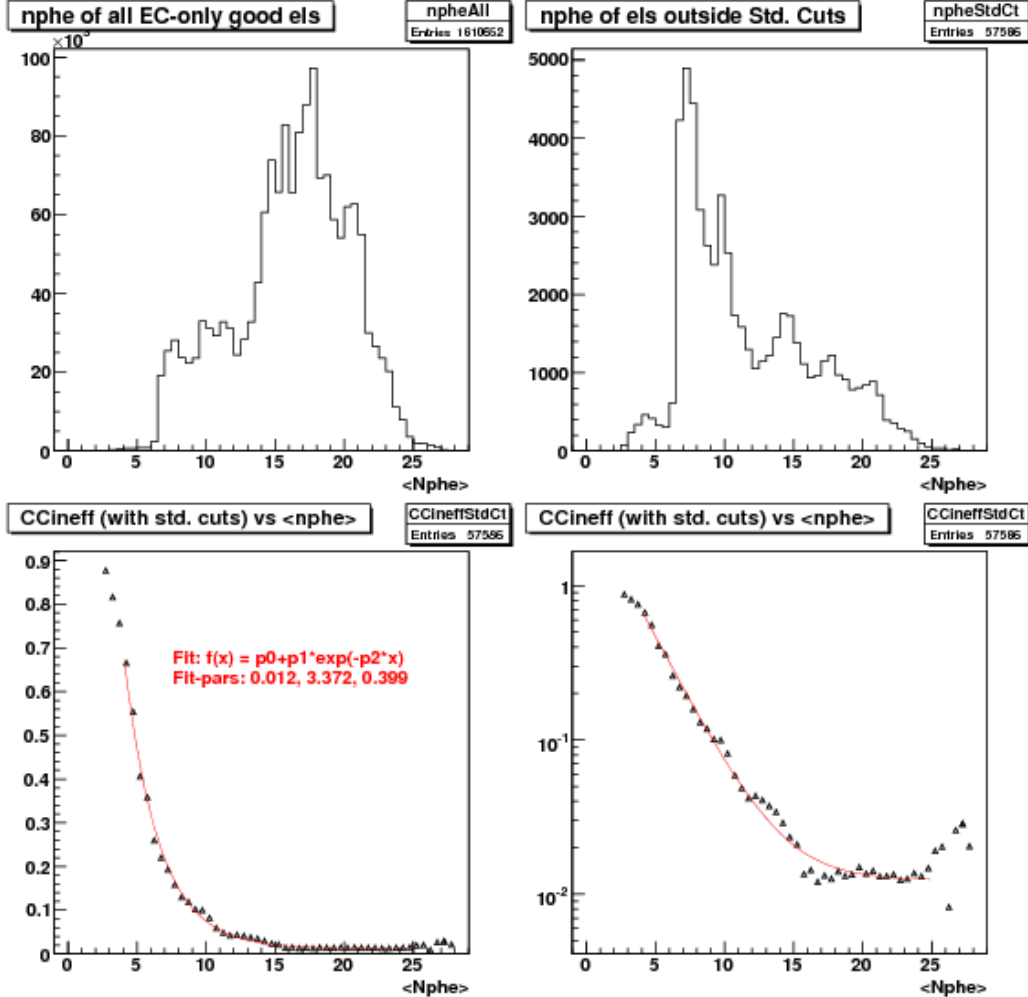


**Figure 3.30:** EC detected good electrons (for all momenta) as a function of  $<N_{ph}>$  (top left). Similar distribution (top right) for those good electrons that were detected by the EC but were rejected by the standard set of event selection cuts which includes CC-dependent cuts. By dividing the latter with the former, one gets the calculated CC inefficiency. The bottom two plots show the inefficiency distribution and a fit (red continuous line) in both linear (in third panel) and logarithmic (fourth panel) scales. Looking at the first plot, it can be seen that most electrons are above  $N_{ph} = 15$  where the inefficiency is at most 1-2 %.

- 1070        5. Finally we use the inefficiency fit just developed to evaluate the corre-  
 1071        sponding efficiencies and transform the 2D map of  $N_{ph}$  into the corre-

1072 sponding efficiency maps (see Fig. 3.31 for such a map in one momen-  
 1073 tum bin.). These maps are later used to apply the efficiency correction  
 1074 on an event by event basis in the simulation.

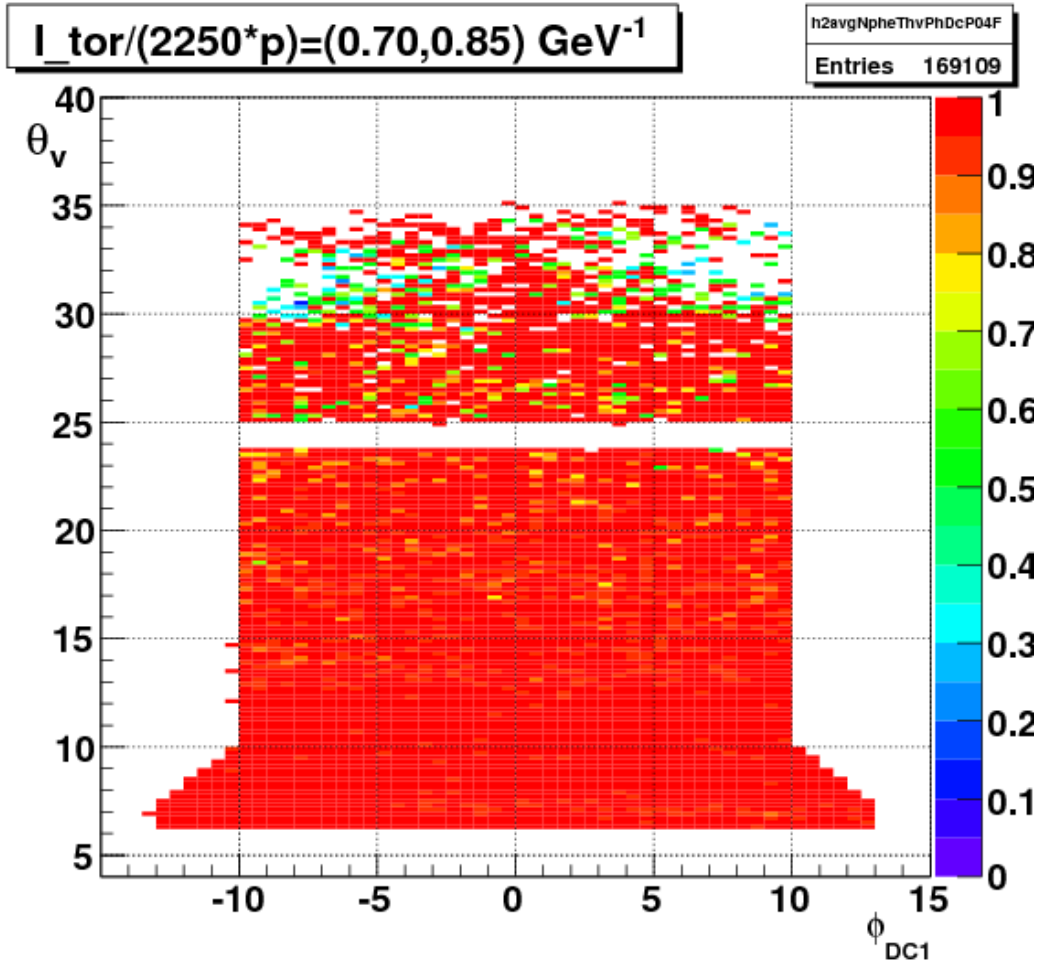


**Figure 3.31:** CC-efficiency in a momentum bin .

1075 From this study, we see that the CC is very efficient in most of the  
 1076 kinematic region (see Fig. 3.31). Once, the CC-(in)efficiency was estimated,  
 1077 we use the calculated CC efficiency to multiply our simulation (i.e., for each  
 1078 simulated event, we look up the CC efficiency and weigh the event with it).

## **3.7 Pion Contamination Corrections**

One of the two major sources of backgrounds in the measured EG4 electron rates comes from misidentified negatively charged pions ( $\pi^-$ ) that produce similar set of signals as electrons in various detector components and thus pass the electron ID cuts. In the EG4 experiment, signals from the electromagnetic calorimeter (EC) and Cherenkov counter (CC) are used to identify electrons from pions, but even with stringent conditions on these signals, some of the pions get misidentified as electrons. To avoid limiting statistics too much in order to minimize the final statistical error in a given kinematic bin, a trade-off in purity versus efficiency (statistics) is made by quantifying the amount of this kind of contamination.

### **3.7.1 Method**

First, the whole kinematic space covered by EG4 is divided into 90 two-dimensional bins - 9 in  $p$  and 10 in  $\theta$ <sup>7</sup>.

For each kinematic bin, a histogram of the number of photo-electrons (variable ' $N_{phe}$ ' in the data ntuple) produced by the electron candidates (selected using the standard particle selection conditions (cuts) except that no cut on ' $N_{phe}$ ' is included is made (see Fig. ??). Likewise, using a very stringent set of cuts, a similar histogram is made for the cleanest possible sample of pion candidates in the same kinematic bin.

- **Estimating the contamination in each bin:** A 7th order polynomial is fit to the  $N_{phe}$  histogram for electrons in the  $N_{phe}$  range extending from  $N_{phe} = 1.8$  to  $N_{phe}=10$ . The fit is then extrapolated down to  $N_{phe} = 0$  (see Fig. ??). Subtracting the extrapolated fit from the impure electron distribution results in the extraction of the contaminating pion peak<sup>8</sup>. Rescaling the pure pion sample to the extracted

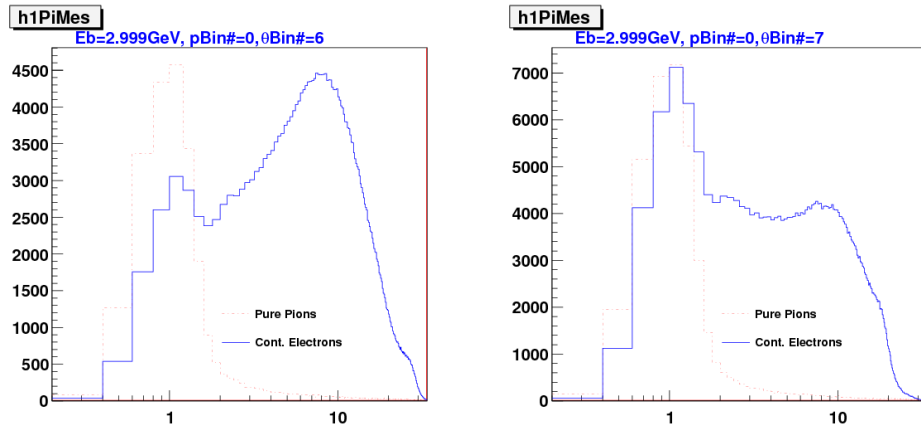
---

<sup>7</sup>For 2 GeV or higher beam energy data sets, the  $p$ -bin boundaries are chosen as (0.30, 0.60, 0.90, 1.20, 1.50, 1.80, 2.20, 2.60, 3.00) and (0.30, 0.45, 0.60, 0.75, 0.9, 1.1, 1.4) for others. And, for  $\theta$ , the boundaries are (5.0, 6.0, 7.0, 8.0, 9.0, 10.0, 12.0, 15.0, 19.0, 25, 49). The choice of the binning was rather arbitrary. Nevertheless higher statistics region was divided into relatively finer bins (event population peaks around  $\theta= 10$  degrees).

<sup>8</sup>Beyond  $N_{phe} = 1.8$ , the electron sample is nearly pure except for a tiny fraction due to the pion tail, so any function that fits that section of the  $N_{phe}$ -distribution is supposed to represent the pure electron distribution. In order to simplify the situation, we chose to fit only from 1.8 to 7.0 rather than covering the full range beyond 7.0.

peak gives us the distribution of the actual pion contamination over the complete range of  $N_{phe}$ . Finally, the counts corresponding to this rescaled pure sample in the region above the standard cut  $N_{phe} > 2.5$  is calculated. Then the ratio of this count to the impure electron count in the same standard  $N_{phe}$  range gives the measured contamination for the bin.

- The contaminations thus evaluated for different momentum bins belonging to a particular  $\theta$ -bin are then plotted against the corresponding momenta. Then, this is fit to an exponential function.
- The parameters par1 and par2 of the exponential fit performed in different theta bins are next graphed together to see the presumed linear dependence.
- Finally, a global fit is performed on all the contaminations in different  $\theta$ - and p- bins (not on the fit parameters). The fit parameters from the earlier two fits only give us a hint to the type of the dependence, thus allowing us decide the form of the fit function.



(a) For the first in momentum and seventh in  $\theta$  bin. (b) For the first in momentum and eighth in  $\theta$  bin.

**Figure 3.32:** Number of photo-electrons produced in CC by clean pion and contaminated electron samples (3.0 GeV data)

1121 From the study, it is found that the typically pion contamination is less  
1122 than 1 %.

### 1123 **3.8 $e^+e^-$ -Pair Symmetric Contamination Cor-** 1124 **rections**

1125 The next major source of background is the secondary electrons from various  
1126  $e^+e^-$  pair production processes. When an electron originating from such a  
1127 pair passes through the detector, the detector has no way to distinguish it  
1128 from the electrons that actually scattered off the target. Therefore, the detec-  
1129 tor simply accepts it as a true scattered electron candidate, thus producing  
1130 a contamination that has to be estimated and corrected for. The first such  
1131 source is the wide-angle  $e^+e^-$  pair production from bremsstrahlung photons  
1132 generated in the target. The other major source is hadron decay such as  
1133 the Dalitz decay ( $\pi^0 \rightarrow e^+e^-\gamma$ ),  $\pi^0 \rightarrow \gamma\gamma$  and then conversion of these photons  
1134 into  $e^+e^-$  pairs. Likewise, the pseudoscalar particle  $\eta$ , and the vector mesons  
1135  $\rho$ ,  $\omega$ ,  $\phi$  also decay to  $e^+e^-$ , but they are not major contributors because of  
1136 their very small decay probabilities as well as the small population compared  
1137 to the  $\pi^0$  and photons. Of all these sources, the biggest contributor to the  
1138 secondary electrons is the  $\pi^0 \rightarrow \gamma\gamma$  with  $\gamma$  conversion to  $e^+e^-$  [37].

1139 The amount of contamination from this type of process can be estimated  
1140 by monitoring the amount of positrons that were recorded under the same  
1141 experimental and kinematic conditions. Because of the symmetry in the  
1142 amount of electrons and positrons produced from these sources, the positron  
1143 to electron ratio gives us the amount of the pair-symmetric contamination.  
1144 However, due to the presence of the strong magnetic field inside the detector  
1145 and the fact that the positrons have opposite charges, their detector accep-  
1146 tance would be different in a given setting. By reversing the magnetic field  
1147 while keeping everything else the same, it is possible to estimate the con-  
1148 tamination. For some of the beam energies used for the NH<sub>3</sub> data of the  
1149 EG4 experiment, some data were collected with identical experimental set-  
1150 ting but with the torus field reversed. The data from those runs were used  
1151 to estimate the amount of positrons in somewhat the same fashion as pion  
1152 contamination. For example, Fig. 3.34 shows one estimate (both data points  
1153 and the fit) of the contamination in EG4 compared with those determined  
1154 for the EG1b experiment [22].

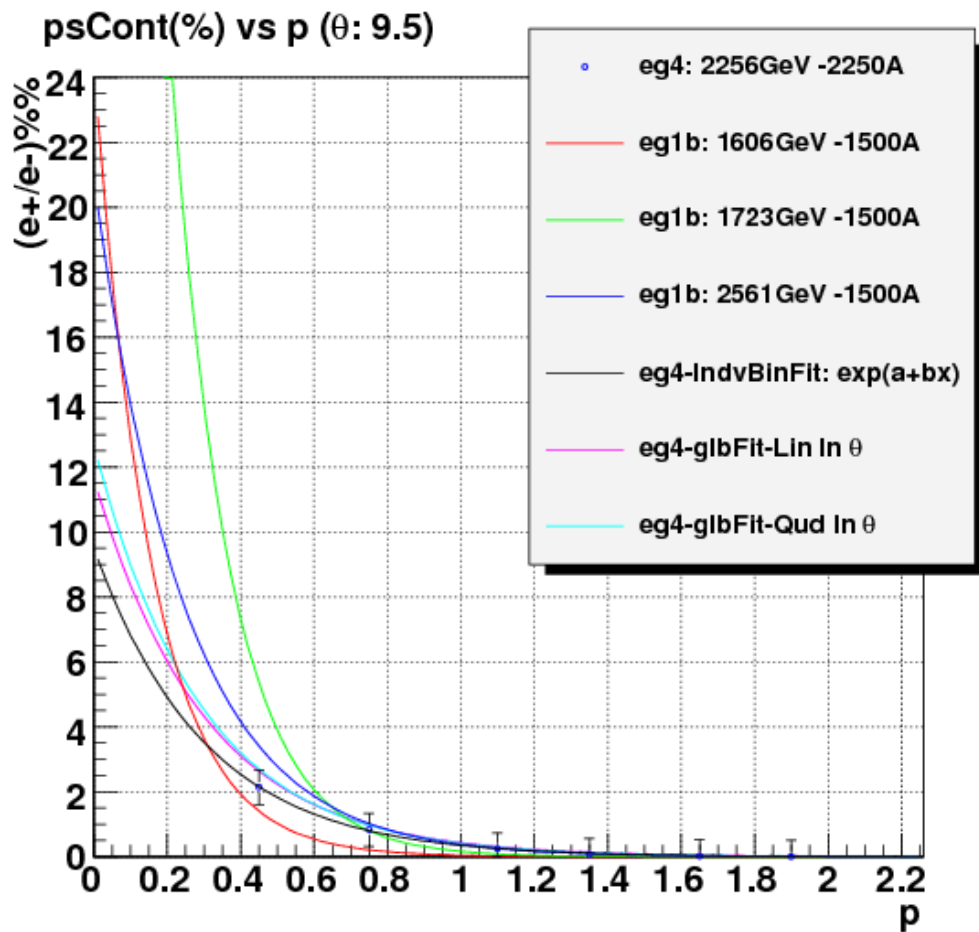


**Figure 3.34:** Pair-symmetric contamination Fits (%) as a function of electron momentum.

1155      For this analysis, both the pion and  $e^+e^-$ -pair symmetric contaminations  
 1156      are small enough to be ignored. This leads to only a slight increase in the  
 1157      systematic error in the final physics results.

1158    **3.9 Study of NH<sub>3</sub> Contamination of EG4 ND<sub>3</sub>**  
1159    **Target**

1160    In equation (3.1), it is assumed that the ammonia target is 100% pure i.e.  
1161    composed of only <sup>15</sup>ND<sub>3</sub> molecules and that the contribution from the  
1162    slightly polarized nitrogen is negligible. But, in practice, the standard ND<sub>3</sub>  
1163    sample is not a 100% pure material. Rather, it contains one or two percent  
1164    of <sup>14</sup>ND<sub>3</sub>, <sup>15</sup>NH<sub>3</sub> [38], and some traces of other isotopic species of ammonia.  
1165    It was reported by the EG1-DVCS experiment at Jlab [39][40] that a higher  
1166    than usual amount of NH<sub>3</sub> (about 10%) was observed in the ND<sub>3</sub> target,  
1167    indicating that an inadvertent mix-up of NH<sub>3</sub> and ND<sub>3</sub> materials could have  
1168    happened during the experimental run. Wondering if the EG4 experiment  
1169    had a similar incident, we decided to investigate and estimate the amount of  
1170    NH<sub>3</sub> contamination of our ND<sub>3</sub> target by looking at the data from the ND<sub>3</sub>  
1171    run period of the experiment as described below.

1172    **3.9.1 Procedure**

1173    The method involves using ep elastic (or quasi-elastic in the case of non-  
1174    proton target) events and comparing the width in some quantity that reflects  
1175    the correlation between the scattered electron (e) and the recoiling proton (p)  
1176    due to the kinematic constraints of such events. The most suitable correlation  
1177    is the one between the polar angles of the electron and the proton. That is  
1178    because of the better angular resolution in CLAS than that for momentum,  
1179    and also due to the fact that polar angle ( $\theta$ ) resolution is much better than  
1180    that of the azimuthal angle ( $\phi$ ) because of the rotational effect (on  $\phi$ ) of the  
1181    polarized target field as well as the drift chamber resolutions [39].

The  $\theta$ -correlation can be studied mainly in two ways. The first way is to reconstruct and histogram the beam energy using the measured polar angles and the known target mass and then compare the histogram from the ND<sub>3</sub> target run with that from a pure NH<sub>3</sub> target run. The other equivalent way is to predict the proton polar angles (using the measured electron angles, known target mass and the beam energy) and then histogram the deviation of the measured proton angles from the expected values. We chose to use a slightly modified version of the latter approach in which we histogram the

following quantity<sup>9</sup>:

$$\Delta = p_p \cdot (\sin\theta_q - \sin\theta_p) \quad (3.14)$$

where  $p_p$  is the measured proton momentum,  $\theta_p$  is the measured polar angle of the proton, and  $\theta_q$  is the expected polar angle of the recoiling proton (which is also the angle of the exchanged virtual photon (q)) given by:

$$\theta_q = \tan^{-1} \left( \frac{M_p}{\tan(\theta/2) \cdot (E_{beam} + M_p)} \right) \quad (3.15)$$

The method exploits the fact that the width of the quantity  $\Delta$  from data with deuteron target decreases because the Fermi motion of the protons in the deuteron nuclei gives a spread of the order of 50 MeV in transverse momentum, and for longitudinal particle momenta of order of a few GeV, we obtain a polar angle spread about 20 mr, which is much larger than the intrinsic CLAS resolution of about 2 mr.

### 3.9.2 Event Selection

First, for each data set (corresponding either to NH<sub>3</sub>, ND<sub>3</sub> or <sup>12</sup>C runs), using standard electron and proton identification cuts events each with a well reconstructed scattered electron and a similarly well reconstructed candidate for proton are selected. We accept only events each of which have one electron, one proton and at most one neutral particle candidate (expected to be a neutron coming off from the deuteron target break-up). If the event is one of the above two types, following additional cuts are applied to make sure it is elastic or quasi-elastic event:

- $E_X < 0.15$  GeV      with  $E_X = M_p + E_e - E_{e'} - E_p = M_p + \nu - E_p$
- $P_X < 0.5$  GeV/c      with  $\vec{P}_X = \vec{0}_p + \vec{P}_e - \vec{P}_{e'} - \vec{P}_{p'} = \vec{P}_e - \vec{P}_{e'} - \vec{P}_{p'}$
- $0.88GeV < M_X < 1.04GeV$
- $\theta_q < 49.0^\circ$
- $|\phi_e - \phi_p| - 180.0^\circ | < 2.0^\circ$

---

<sup>9</sup>We chose this quantity  $\Delta$  rather than the simple angle difference ( $\theta_q - \theta_p$ ) because the former is more directly interpretable in terms of transverse missing momentum for the case of quasi-elastic scattering.

1202 where X indicates the missing entity in the  $d(e,e'p)X$  channel, which is ex-  
1203 pected to be neutron in the case of the quasi-elastic channel, thus  $E_X$  is the  
1204 missing energy and so on.

1205 If it passes these cuts, the quantity  $\Delta$  is calculated for the event and then  
1206 histogrammed as shown by the red curves in the top-left (from  $^{12}\text{C}$  runs),  
1207 top-right (from  $\text{NH}_3$  runs), and bottom-right (from  $\text{ND}_3$  runs) panels of Fig.  
1208 3.35.

1209 After getting the histograms for the quantity  $\Delta$  for the ep-elastic or  
1210 quasi-elastic events from the  $\text{NH}_3$ ,  $\text{ND}_3$  and  $^{12}\text{C}$  target data sets, we first  
1211 remove the contribution from the non-hydrogen component of  $\text{NH}_3$  and  $\text{ND}_3$   
1212 targets by subtracting the corresponding carbon histogram (properly scaled  
1213 to match with the shoulders from the background in each of the ammonia  
1214 data). Since the carbon data is too low in counts (hence the raggedness in the  
1215 histogram), a fit (a 'gaussian' times a 'linear' function) to the carbon data is  
1216 obtained, and that fit (shown as the blue line in the first panel in Fig. 3.35  
1217 is used instead of the histogram itself to remove the background. The blue  
1218 line in the second (top-right) panel and the cyan line in the last (bottom-  
1219 right) panel show the properly scaled carbon fits which are subtracted from  
1220 the  $\text{NH}_3$  and  $\text{ND}_3$  histograms (shown by red lines) respectively. After the  
1221 subtraction, we get new histograms that represent 'pure' elastic or quasi-  
1222 elastic data from protons and deuterons (shown by the magenta lines in the  
1223 third and last panels respectively).

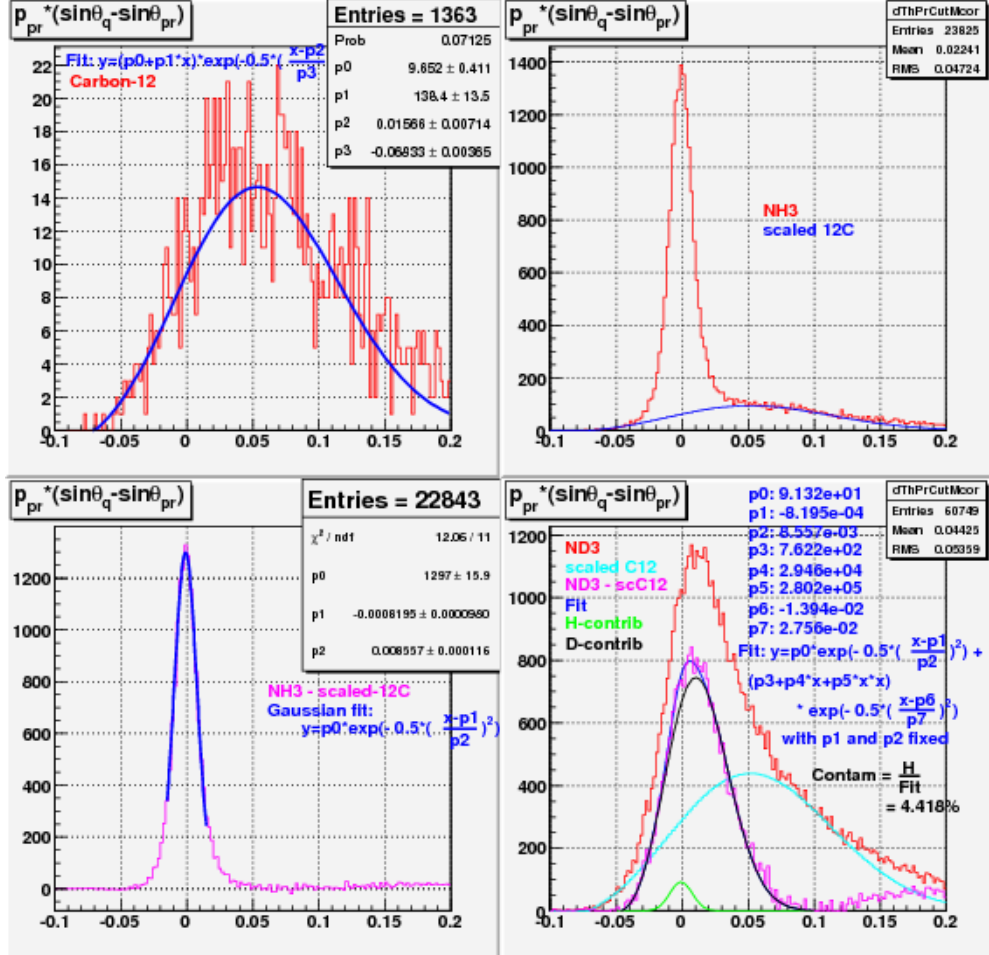


**Figure 3.35:** Histograms showing the quantity  $\Delta = p_p \cdot (\sin\theta_q - \sin\theta_p)$  for elastic or quasi-elastic events from carbon-12 (top-left), NH<sub>3</sub> (top-right) and ND<sub>3</sub> (bottom-right) target runs respectively. The third (bottom-left) panel shows the background removed elastic events from the NH<sub>3</sub> data. In the fourth panel, various  $\Delta$  are shown - red is the raw ND<sub>3</sub>, light green is the scaled-<sup>12</sup>C for the nuclear background, brown is for the difference between the two.

### 3.9.3 Extracting the Contamination

After we have the 'pure' elastic or quasi-elastic data from NH<sub>3</sub> and ND<sub>3</sub> runs, we get the mean and the spread (standard deviation  $\sigma$ ) of the proton elastic peak by fitting the NH<sub>3</sub> data to a Gaussian function  $f_p(x)$  (the blue line in

1228 the third panel with parameters p0=height, p1=mean and p2= $\sigma$  ). After  
 1229 we have the fit for the proton elastic peak, we fit the background subtracted  
 1230 deuteron data to a function  $f(x)$  that is a linear combination of the pure  
 1231 proton fit and a pure deuteron fit (the latter with the form of **a quadratic**  
 1232 **function  $\times$  a Gaussian**<sup>10</sup>) as follows:

$$f(x) = p_0 \cdot f_p(x) + (p_1 + p_2 \cdot x + p_3 \cdot x^2) \cdot e^{-0.5 \cdot \left(\frac{x-p_4}{p_5}\right)^2} \quad (3.16)$$

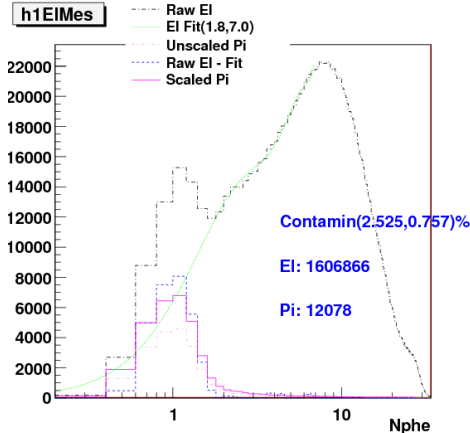
1233 where  $p_i$  ( $i = 0, 2, \dots, 5$ ) are the free parameters which are determined by  
 1234 fitting of  $f(x)$  to the deuteron data. The first term  $p_0 \cdot f_p(x)$  in  $f(x)$  represents  
 1235 the contribution from the contaminant (i.e., protons in  $ND_3$ ) and the rest  
 1236 of the term in  $f(x)$  represents the contribution from the deuterons in  $ND_3$ .  
 1237 The total fit function  $f(x)$ , the proton contribution and the deuteron part are  
 1238 shown by the blue, green and black lines in the fourth panel. The ratio of  
 1239 the area under the green line to that under the blue line gives us the relative  
 1240 amount of the  $NH_3$  contamination in the  $ND_3$  target.

### 1241 3.9.4 Results and Conclusion

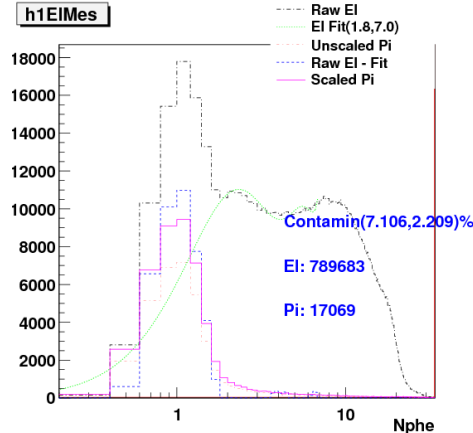
1242 From the calculation as described above, the estimate for the  $ND_3$  contam-  
 1243 ination came out to be 4.4% It was not possible to do a similar analysis on  
 1244 the 1.3 GeV  $ND_3$  data, because the CLAS acceptance constraints did not al-  
 1245 low for the coincident detection of e and p from the exclusive (quasi-)elastic  
 1246 events. The basic conclusion is that at 2 GeV, we cannot get a 'pure' Gaus-  
 1247 sian spectrum for deuteron, and therefore, there is no way to unambiguously  
 1248 separate deuteron from proton in  $ND_3$ . The fact that the fit looks reason-  
 1249 ably well (with contamination coming out to be only a few percent) and that  
 1250 we clearly do not see a narrow peak on top of a wider one (unlike in EG1-  
 1251 DVCS) should be sufficient to ascertain that EG4 did NOT have the same  
 1252 contamination problem as EG1-DVCS (which still has not been explained  
 1253 yet) [29]. To accommodate the fact that the contamination measurement is  
 1254 not reliably unambiguous, we will assume a rather generous systematic error  
 1255 due to the contamination.

---

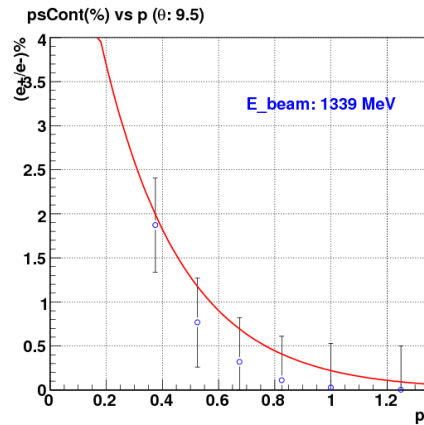
10 A pure Gaussian and other forms for the deuteron spectrum were tried but the overall  
 fit was not as good.



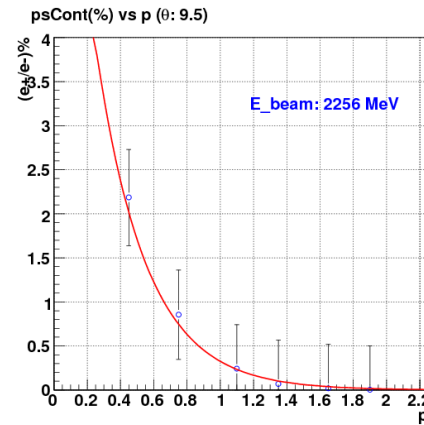
(a) For the first bin in momentum and seventh bin in  $\theta$ .



(b) For the first bin in momentum and eighth bin in  $\theta$ .



(c) Fits in the  $\theta(9.0, 10.0)$  bin for 1.339 GeV data.



(d) Fits in the  $\theta(9.0, 10.0)$  bin for 2.0 GeV data.

**Figure 3.33:** The top row plots show the calculation of pion contamination of electrons for the given kinematic bins of 3.0 GeV data. The dotted black line indicated by the label “Raw El” in the legends of each of the two plots are the contaminated electrons. Likewise, the line labeled “El Fit” is a polynomial fit to the electron distribution (in this case fitted from Nphe=1.8 to 7.0, but extrapolated down to Nphe=0). The line labeled “Unscaled Pi” is the pure pion distribution obtained with stringent set of cuts. “Raw El - Fit” is the difference between the contaminated electron sample and the polynomial fit and finally “Scaled Pi” is the pure pion-sample but after its scaled to match with the “Raw El - Fit” at the pion peak position (around 1 Nphe). The bottom row plots show the fits of the contaminations as a functions of momentum ( $p$ ) in a given  $\theta$  bin.

<sub>1256</sub> **Chapter 4**

<sub>1257</sub> **Monte Carlo Simulations and**  
<sub>1258</sub> **Extraction of  $g_1$  and  $A_1 F_1$**

<sub>1259</sub> **4.1 Simulation and Approach to Analysis**

The EG4 data consist of a table numbers of electrons reconstructed within various  $(W, Q^2)$  bins that are scattered off polarized hydrogen ( $\text{NH}_3$ ) or deuteron ( $\text{ND}_3$ ), divided by the (life-time gated) integrated charge, for two different combinations of target polarization and beam helicity:

$$n^\pm = N^\pm / FC^\pm, \quad (4.1)$$

where “+” refers to beam helicity and target polarization anti-parallel, while “−” refers to the parallel case. The difference between these two normalized counts is given by

$$\Delta n(W, Q^2) = n^+(W, Q^2) - n^-(W, Q^2) = \mathcal{L}_r \cdot P_b P_t \cdot \Delta\sigma(W, Q^2) \cdot AccEff(W, Q^2) + Bg \quad (4.2)$$

<sub>1260</sub> where the “relative luminosity”  $\mathcal{L}_r$  is a constant factor containing the density of polarized target nuclei per unit area and the conversion factor from  
<sub>1261</sub> Faraday cup counts to integrated number of electrons incident on the target;  
<sub>1262</sub>  $P_b$  and  $P_t$  are the beam and target polarization,  $Acc$  and  $Eff$  are the  
<sub>1263</sub> geometric acceptance and detection efficiency of CLAS for electrons within  
<sub>1264</sub> the kinematic bin in question (including cuts and trigger efficiency), and  
<sub>1265</sub> the background  $Bg$  comes from several sources, including pions misidentified  
<sub>1266</sub> as electrons, electrons from  $e^+ e^-$  pair production, and electrons scattered off  
<sub>1267</sub> (partially) polarized target nucleons and nuclei that are not the  
<sub>1268</sub>

intended species (e.g., bound protons in  $^{15}\text{N}$ , free proton contamination in nominal  $\text{ND}_3$  targets, and bound proton-neutron pairs in any  $^{14}\text{N}$  contamination present)<sup>1</sup>.

Our main goal is to extract the spin structure function  $g_1$  and calculate its moments. The cross section difference  $\Delta\sigma(W, Q^2)$  on the right side of the above equation is what contains the information on  $g_1(W, Q^2)$  along with various other contributions.<sup>2</sup> This means we can, in principle, calculate the cross section (and then use that to extract  $g_1$ ), from the background corrected measured quantity  $\Delta n(W, Q^2)$  by putting in the values for all the rest of the quantities involved in Eq. 4.2. But, in reality, having an accurate knowledge of  $\textit{Acc}$  and  $\textit{Eff}$  is challenging and the available measurements of polarizations and luminosities are not reliable enough. So, experimenters usually resort to Monte-Carlo simulation to determine some or all of those factors that are involved in the relation between the counts and cross-section differences.

A standard way to extract the sought-after Physics quantities from these kinds of measurements proceeds along the following steps [41]:

1. Use a full simulation of CLAS with a “realistic” event generator, detector simulation and event reconstruction including cuts to obtain the product  $\textit{Acc}\textit{Eff}$  as the ratio of events reconstructed in a particular bin, divided by events thrown in that same bin.
2. Extract the product  $\mathcal{L}_r \cdot P_b P_t$  from the ratio of the acceptance and efficiency corrected  $\Delta n$  in the (quasi-)elastic region ( $0.9 < W < 1.0$ ) to the well-known theoretical cross section difference for elastic (or quasi-elastic) scattering off the proton (deuteron).
3. Estimate and correct for  $Bg$ .
4. Apply radiative corrections, which use a model of the unradiated Born cross section and a calculation of the radiated cross section based on programs like RCSLACPOL (see below).

---

<sup>1</sup>While this background is a small correction for hydrogen targets, in the case of deuteron targets, it must be corrected for (see Sec. 5).

<sup>2</sup> $\Delta\sigma(W, Q^2)$  also has contributions from the unmeasured  $g_2$  or, equivalently, from the product  $A_2 F_1$ . Moreover, the cross section receives modifications and tails from radiative effects (both internal and external radiation) and kinematic resolution smearing.

- 1298        5. Express the extracted Born cross section difference in terms of the de-  
 1299        sired quantity (here:  $g_1$ ) and additional input (e.g.,  $A_2 F_1$ ). Use a model  
 1300        for the latter to extract  $g_1$  only. Vary the model (concurrently with the  
 1301        model input to the previous step) to assess systematic uncertainties.

1302        One conceivable problem with this approach lies in the first step, and  
 1303        in particular with the choice of the “realistic event generator”. This choice  
 1304        would not matter at all if two conditions are fulfilled [41]:

- 1305        1. The kinematic bins are chosen so small that the variation of the cross  
 1306        section over the bin (and/or the corresponding variation of the accep-  
 1307        tance times efficiency) do not lead to any significant deviations for the  
 1308        *average AccEff* between the simulation and the real detector.
- 1309        2. The counts reconstructed within any one bin are directly proportional  
 1310        to the number of initial electrons generated within that *same* bin (the  
 1311        proportionality constant being *AccEff*), without any “bin migration”  
 1312        from other kinematic bins. (Otherwise, the ratio reconstructed/generated  
 1313        depends on those “migration tails”, and the simulation will give differ-  
 1314        ent results from the “true value” if the overall cross section model of  
 1315        the generator is not accurate enough.)

1316        Unfortunately, assumption 1 tends to directly contradict assumption 2  
 1317        because 1 favors small bins and 2 favors large bins! For most precision  
 1318        experiments , bin migration effects are significant. This is aggravated by  
 1319        the difficulty of making a clean separation between bin migration due to  
 1320        detector resolution alone and the contribution from radiative effects. For  
 1321        instance, GEANT and therefore GSIM includes (at least by default) photon  
 1322        radiation as part of the simulation of outgoing electron tracks throughout  
 1323        the gas and building materials of all detectors. It is very important not to  
 1324        “double count” when simulating an experiment; the radiative calculations in  
 1325        step 4 above should not include any “after” radiation beyond the limit of  
 1326        the target itself (which, in turn, should then **NOT** be included in the GSIM  
 1327        simulation as material to be traversed).

1328        This is a problem for all CLAS experiments attempting to extract abso-  
 1329        lute cross sections (or, here, cross section differences); however, the problem  
 1330        is magnified for our case: Since the cross section difference itself is not re-  
 1331        quired to be positive, one can have both positive and negative tails migrating  
 1332        into adjacent bins. In any case, it is clear that using the average, **unpolarized**

1333 cross section as a model for the generator is not really appropriate (unless  
1334 one is confident that the asymmetry is fairly constant or slowly-varying – not  
1335 a good assumption in the resonance region where the  $\Delta(1232)$  with negative  
1336 asymmetry is adjacent to the S11 with positive asymmetry). Using a (hope-  
1337 fully realistic) model of the cross section difference instead would be much  
1338 better, but this causes two new problems [41]:

- 1339 1. Prima facie it is unclear how to simulate a negative cross section (dif-  
1340 ference). This problem can be circumvented fairly easily (see below),  
1341 albeit at extra cost in terms of simulation effort.
- 1342 2. It obviously becomes impossible to extract  $AccEff$  from a simple ratio  
1343 of reconstructed divided by generated events; both of these quantities  
1344 could be positive, negative (even different sign under extreme circum-  
1345 stances), or simply zero (which is particularly bad for the denominator).  
1346 From this discussion, it is also clear that such a ratio would depend very  
1347 sensitively on the cross section model and bin migration tails and be a  
1348 very poor indicator of the actual product  $AccEff$ .

1349 For this reason, we decided to try a different approach outlined in the  
1350 following. The basic idea is to study the dependence of the reconstructed  
1351 count difference on the model input (in particular  $g_1$ ) directly through the  
1352 whole chain of simulation and reconstruction, and then use tables of Born  
1353 and radiated cross section differences for various model inputs as estimates  
1354 of systematic uncertainties<sup>3</sup>.

### 1355 4.1.1 Outline of the method

1356 The basic idea is the following: If we already had a perfect model of  $g_1$  and all  
1357 other ingredients that go into  $\Delta n$  (including a perfect simulation of CLAS), a  
1358 simulation of  $\Delta n$  would agree 100% with the data (within statistical errors).  
1359 Any (larger than statistical) deviation between such a simulation of  $\Delta n$  and  
1360 the data can only be due to the following possible sources:

- 1361 1. The model for  $g_1$  is not perfect and, therefore, must be adjusted to  
1362 reflect the “true”  $g_1$ . This is the default assumption which we will use

---

<sup>3</sup>We developed this method for the case of an ND<sub>3</sub> target; however, it could, of course, easily be adopted to NH<sub>3</sub>, as well

1363 to extract  $g_1$  from the data. This will be done by finding the proportionality factor between *small* changes in  $g_1$  and the reconstructed  $\Delta n$   
1364 and then adjusting  $g_1$  to fully account for the observed  $\Delta n$ .  
1365

- 1366 2. There could be a systematic error on this proportionality factor (which,  
1367 after all, will come from simulation); for instance, there could be sys-  
1368 tematic deviations from the simulated results for acceptance and effi-  
1369 ciency (in particular efficiencies of the CC, EC, or tracking, that are  
1370 not perfectly simulated by GSIM). This is a multiplicative uncertainty  
1371 that must be carefully estimated and applied to the final data.
- 1372 3. Any imperfect simulation of the “background” due to all events not  
1373 originating in the bin in question (migration, radiation), or due to  
1374 undesired target components (hydrogen, bound polarized nucleons in  
1375 nitrogen), or from misidentified pions or  $e^+e^-$  pairs, or due to contribu-  
1376 tions to  $\Delta\sigma$  from  $A_2$  can lead to an additive systematic deviation  
1377 that would then be misinterpreted as a change in  $g_1$ . This systematic  
1378 uncertainty must be studied by varying model inputs, parameters etc.  
1379 in the simulation.

## 1380 4.2 Radiative Corrections

1381 The physics quantities that we seek to extract from measurements are theo-  
1382 retically defined or interpreted and calculated in terms of the cross-section of  
1383 the so called “Born” scattering process, which is represented by the simplest  
1384 possible Feynman diagram i.e., by the lowest order approximation of a single  
1385 photon exchange process. However, the measured cross-sections also contain  
1386 contributions from higher order electromagnetic processes, which must be  
1387 accounted for before extracting the quantities of our interest. These additional  
1388 contributions are grouped into two categories - **internal and external**  
1389 radiative corrections.

1390 The **internal corrections** are the contributions from the higher order  
1391 QED processes (higher order Feynmann diagrams) which occur during the  
1392 interaction. These include the correction for the internal Bremsstrahlung  
1393 (i.e., the emission of a real photon while a virtual photon is being exchanged  
1394 with the target) by the incoming or the scattered electron), the vertex correc-  
1395 tion (in which a photon is exchanged between the incoming and the scattered  
1396 electron), and the correction for the vacuum polarization of the exchanged  
1397 virual photon ( $e^+e^-$  loops).

1398 External corrections include those that account for the energy loss (mainly  
1399 by the Bremsstrahlung process) of electrons well before or after the interac-  
1400 tion while passing through the target material and the detector.

1401 If the beam electron radiates a photon before the scattering, the kinemat-  
1402 ics of the actual process will be different from the the one calculated with the  
1403 nominal beam energy. Likewise, if the radiation occurs after the scattering,  
1404 the actual energy and momentum of the scattered electron will be different  
1405 from what is calculated normally (i.e., without any radiation). The effect  
1406 can be quite large for elastic scattering.

1407

## 1408 4.3 “Standard” simulation

1409 The simulation process consists of mainly three parts - generating inclusive  
1410 events similar to the ones produced in the double polarization scattering  
1411 process, simulating the CLAS detector response, and finally the event recon-  
1412 struction from the simulated detector signals.

1413 The first part is accomplished by using a program that is made by combin-

1414 ing the essential elements of an updated version of the “RCSLACPOL” pro-  
1415 gram (for cross section generation) and some parts of the “STEG” event gen-  
1416 erator (see sections 4.3.1 and 4.3.2). The second part is done by two standard  
1417 CLAS software packages running in succession - “GSIM” and “GPP”(see sec-  
1418 tions 4.3.3 and 4.3.4). And, finally, the standard CLAS package “RECSIS”  
1419 is used to reconstruct the events in the same way as for the real CLAS data.

### 1420 4.3.1 RCSLACPOL

1421 The simulation for the standard model cross sections proceeds as follows.  
1422 We use the code “RCSLACPOL” [42] that can generate polarized and un-  
1423 polarized cross sections (both Born and radiated) based on the approach by  
1424 Shumeiko and Kuchto [43] as well as Mo and Tsai [44], including external  
1425 radiation in the target. This code has been extensively tested and used for  
1426 the analysis of SLAC experiments E142, E143, E154, E155 and E155x as  
1427 well as Jefferson Lab experiments like EG1a and EG1b. It has been updated  
1428 with the most recent models on polarized and unpolarized structure func-  
1429 tions ( $F_1, F_2, A_1$  and  $A_2$ ) [42, 45–47] and an implementation of the folding  
1430 algorithm developed by W. Melnitchouk and Y. Kahn [48] for structure func-  
1431 tions of the deuteron. The models have been fitted to and tested with data  
1432 from EG1b as well as world data on both  $A_1$  and  $A_2$  over a wide range of  $Q^2$   
1433 and  $W$ , including the resonance region and the DIS region.

1434 For EG4, we have combined the “RCSLACPOL” code with that of the  
1435 “STEG” event generator. This generator uses a grid of (radiated) cross sec-  
1436 tions generated by our modified version of RCSLACPOL to generate events  
1437 that are distributed according to these cross sections (i.e., the number of  
1438 events generated in a given bin is proportional to the cross section integrated  
1439 over this bin).

### 1440 4.3.2 Event Generator

1441 The concept and some part of the generator skeleton was inherited from the  
1442 STEG (SimplesT Event Generator) program obtained from INFN, in Genova,  
1443 Italy. The old event sampling part (which made the program run extremely  
1444 slow) of the code was replaced by a new one developed by myself which  
1445 made the event generation process much faster. The cross section calculating  
1446 part was replaced by codes from an updated version of RCSLACPOL (see  
1447 Sec. 4.3.1).

1448     The generator works in two steps. First, it generates two two-dimensional  
1449     maps or tables of radiated inclusive polarized cross differences (for the scat-  
1450     tering of polarized electrons from a longitudinally polarized deuteron tar-  
1451     get, by using RCSLACPOL) in various kinematic bins encompassing the  
1452     kinematic region covered by EG4 data. These cross section maps (and the  
1453     corresponding events later on) were generated in the following angular and  
1454     momentum ranges: 5.0-45.0 degrees for  $\theta$  , 250.0-325.0 degrees for  $\phi$  (to en-  
1455     sure the CLAS 6th sector is completely covered) and  $(0.2, E_{beam})$  GeV for the  
1456     momenta, where the beam energy  $E_{beam}$  took values of 1.337 and 1.993 GeV,  
1457     corresponding to the two  $ND_3$  data sets of EG4. In our case, the map was  
1458     created by dividing the kinematic phase space into a grid of small rectangles  
1459     and then calculating the differential cross-section at the geometric center of  
1460     each of those squares (such as ABCD in Fig. 4.1). For our application, we  
1461     need to generate two such maps (because of the impossibility of generating  
1462     events according to negative cross-sections) and run the program twice - once  
1463     corresponding to positive  $\Delta\sigma$  and the next for the negative one. For all bins  
1464     in which the integrated cross section  $\Delta\sigma \geq 0$ , we fill the first table (“positive  
1465     map”) which is therefore positive-definite. For all bins in which this cross  
1466     section is below 0, we fill a second table (“negative map”), but with the  
1467     absolute (i.e. negative) value of this cross section.

1468     In the second stage, events are thrown according to the cross section maps  
1469     produced in the first stage. The events are given vertex coordinates that are  
1470     uniformly distributed over the volume of a 1 cm long cylinder with radius  
1471     0.01 cm around the beam line - with the center of this volume being at the  
1472     EG4 target position of  $(0,0,-100.93$  cm). Nearly equal numbers of events are  
1473     generated for each sign of  $\Delta\sigma$  they are finally normalized according to their  
1474     total cross sections (integrals of the corresponding maps).

1475     The kinematic and other information (positions, momenta, charge) of  
1476     these generated events are recorded and saved in the BOS format<sup>4</sup> output  
1477     files which organizes data into banks. In our case, HEAD, MCEV, MCTK,  
1478     and MCVX banks are used for the generator output. The generator is also  
1479     capable of producing output in the hbook format which makes it possible  
1480     to study the Monte Carlo data using PAW (or ROOT because the h2root  
1481     program easily converts “hbook” files into “root” files).

---

<sup>4</sup>Existing versions of GSIM, GPP and RECSIS accept only BOS format for input files.

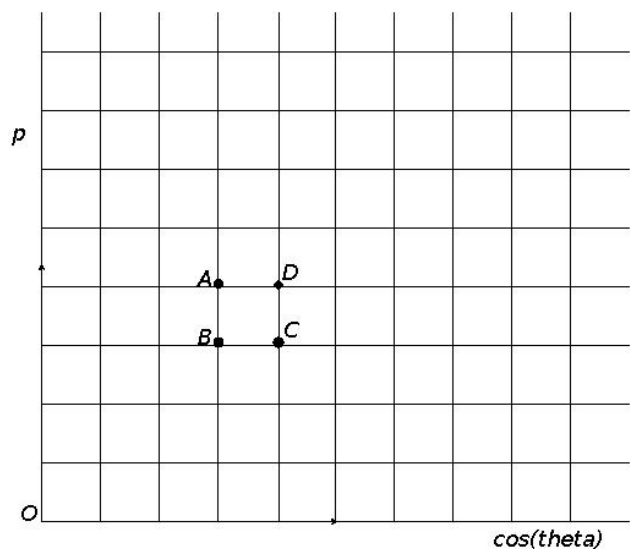


**Figure 4.1:** Corners of a typical bin highlighted in the kinematic space covered by the event generator.

1482    **4.3.3 GSIM - CLAS Detector Simulation**

1483    The Monte Carlo events thus generated are next fed into GSIM - the CLAS  
1484    Monte Carlo simulation program using GEANT 3.21 libraries from CERN  
1485    [49]. It simulates the CLAS detector response by implementing a complete  
1486    model of the detector as well as the propagation of particles through different  
1487    materials including all physics processes, such as multiple scattering, energy  
1488    loss, pair production, and nuclear interactions. The program takes the in-  
1489    put event particles and then, based on their types, momenta and positions,  
1490    “swims” (traces) them through all volumes of different materials that are  
1491    defined using various library routines and the detector parameters. Charged  
1492    particles are also subjected to the effects of the torus and target magnetic  
1493    fields of the same strength as in the actual experiment (for this the same field  
1494    maps are used as in the track reconstruction process using RECSIS). All the  
1495    ingredients of the program (field maps, active detection volumes, passive vol-  
1496    umes of detector support structures etc) are modeled as accurately as possible  
1497    with the help of engineering designs and actual detector measurements. Spe-  
1498    cial subroutines corresponding to various active parts of the detector produce  
1499    outputs resembling the real detector signals which can then be reconstructed  
1500    and analyzed just as the real experimental data [50][51]. GSIM is configured  
1501    to match with the conditions of a given experiment by giving it proper val-  
1502    ues of input parameters via a command line input file which contains various  
1503    “ffread cards” some of which are listed in table-A.1 along with their values  
1504    that were used in our simulation.

1505    **4.3.4 GSIM POST PROCESSOR (GPP)**

1506    The GSIM output is next passed onto GPP - another standard CLAS soft-  
1507    ware package - to process the simulated data further so that the detector  
1508    response is accounted for more accurately. This package improves the re-  
1509    sponse by smearing the detector signals and removing them if there are dead  
1510    regions (determined by querying a data base which in turn is made by looking  
1511    at the raw data of the experiment).

1512    A lot of known, unknown, quantified, and unquantified factors such as  
1513    temperature, alignment, dead channels, electronic malfunction etc affect the  
1514    performance of the CLAS detector. But, GSIM does not include all these  
1515    effects and, hence, the efficiency of the detector is always less than what the  
1516

1517 simulation provides us. To make the simulation more realistic by taking into  
1518 account some of those effects, another CLAS software called GSIM Post Pro-  
1519 cessor (GPP) is used to process the GSIM output. The GPP can change the  
1520 DC, SC, CC and EC signals produced in the simulation. The DC signals can  
1521 be changed by (a) accounting for the dead wires according to the calibration  
1522 database, (b) shifting the DOCA mean value, and (3) smearing the hit sig-  
1523 nals according to the resolution determined by the calibration database or  
1524 according to the command line input. Likewise, SC signals can be changed  
1525 with a parameter input for smearing the time resolution. And, for the CC  
1526 and EC signals, the GPP can use the hardware thresholds[52].

1527 As the experimental conditions and detector configurations can change  
1528 from one experiment to another, in order to run the GPP, we must have  
1529 our own experiment specific calibration constants and parameters such as  
1530 the run number (R), the DC smearing scale values for regions 1, 2 and 3  
1531 (a, b, c) and the SC smearing scale value (f). Even for a given experiment,  
1532 these constants and parameters are determined to be different for different  
1533 data sets (corresponding to a given beam energy, for example). The value  
1534 for R can be any run number belonging to a specific data set. This number  
1535 is used to identify the entry of the calibration constants in the database that  
1536 corresponds to the given data set. In order to simplify the job, we decided to  
1537 use the timing resolutions determined by the calibration database assuming  
1538 that they are good enough and need only to determine new values for the  
1539 DC smearing. To further simplify the job, we assumed that the three DC  
1540 Regions had identical resolutions, so the DC smear parameters a, b, and c  
1541 would have the same values, and the common DC-smear value is what is  
1542 determined from the procedure described below.

1543 In order to determine the DC-smear, we generated a statistically signif-  
1544 icant number (about half million) of elastic-electron events distributed ac-  
1545 cording to the elastic cross section and then ran them through GSIM, GPP  
1546 and RECSIS. The pure proton target events, turning off the radiative effects  
1547 are generated using the existing STEG event generator.

1548 The simulated elastic events are then fed into GSIM, GPP and RECSIS,  
1549 with GSIM and RECSIS used in the same configuration as when processing  
1550 the CLAS data during the “pass-1” phase, and GPP run with different values  
1551 of DC-smear scales as inputs. The reconstructed data coming out of RECSIS  
1552 corresponding to a given value of DC-smear is then histogrammed in  $\Delta E$   
1553 again and fitted to a Gaussian to get its  $\sigma$  (characterizing width) of and  
1554 mean (characterizing position). As we can see in figures 4.2(a) and 4.2(b),

1555 the width of the elastic peak increases with the DC-smear but the position  
 1556 stays more or less the same as expected. In fact, when the two are plotted  
 1557 against DC-smear (as in figures 4.3(a) and 4.3(b)) the width shows a linear  
 1558 dependance.

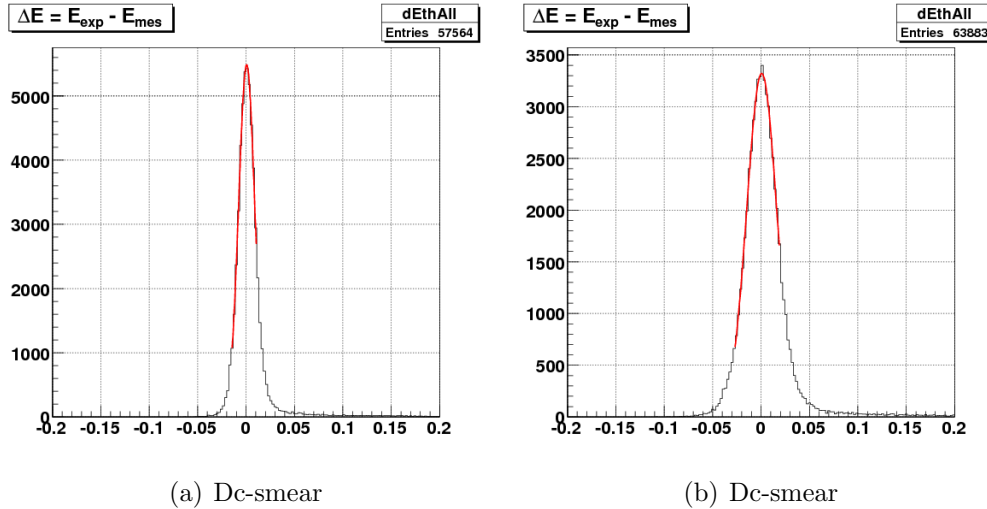


**Figure 4.2:**  $\Delta E$  of 2.3 GeV simulated elastic-only proton-target events passing through GSIM, GPP (with two different Dc-smear scales), and RECSIS.

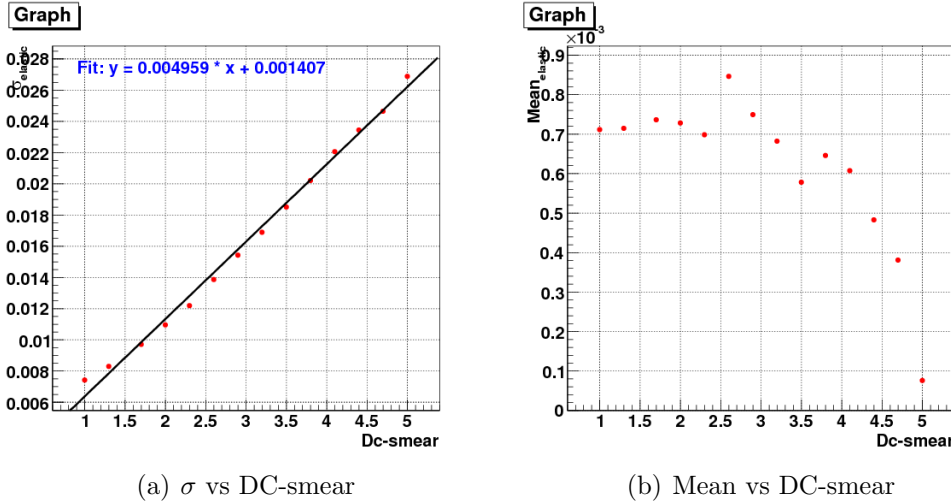


**Figure 4.3:** Graphs showing the dependence of width and position (obtained from the Gaussian fits as shown in the fig (??) of the elastic peaks on the DC-smear applied to GPP.

### 1559 4.3.5 Finding the width of the real CLAS data elastic 1560 peak.

1561 With the knowledge of the DC-smear dependence of energy resolution (Fig.  
1562 4.3(a)), if we also know the resolution in the real data, we can determine  
1563 the right value of DC-smear which would make the resolution in the  
1564 simulation comparable with that in the real data. So, the next step is to find  
1565 the resolution in the real CLAS data, which is done again by measuring the  
1566 width of the elastic peak in the real data. But, because the real data is a very  
1567 complex mixture of events coming from various reaction channels, we must  
1568 first have a way to separate the elastic data from the rest. One method entails  
1569 histogramming  $\Delta E$  from both the  $\text{NH}_3$  and  $^{12}\text{C}$  target data (for a given beam  
1570 energy) and subtracting the latter (after the cross-normalization) from the  
1571 former (as in fig (4.4)) to effectively remove the contribution from nitrogen  
1572 component of the  $\text{NH}_3$  target leaving the contribution coming only (mostly)  
1573 from the proton component. Another method consists of using only the  $\text{NH}_3$   
1574 data but this time calculating the helicity dependent cross-section difference  
1575 in the elastic region Fig. (4.5). In the latter method, the difference removes  
1576 the contribution from the unpolarized nuclear background because they have

1577 the same contribution to the opposite helicity state cross-sections. After the  
 1578 elastic data is separated, its  $\Delta E$  distribution is fitted to a Gaussian as with  
 1579 the simulation data and we arrive at the experimental energy resolution.

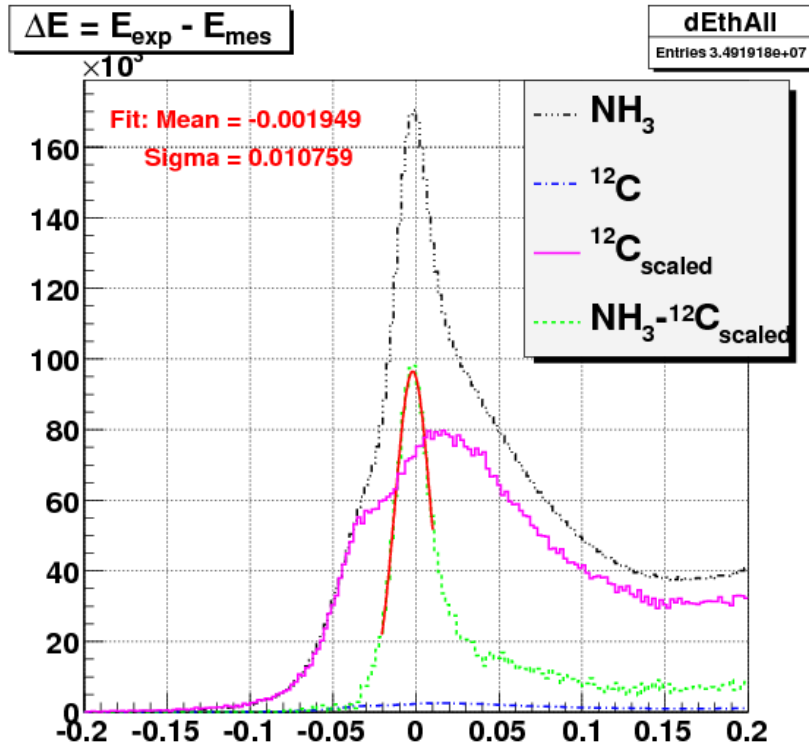


**Figure 4.4:** Histograms illustrating the extraction of elastic peak for 2.3 GeV by using carbon-12 data for background removal from the total-cross section (all good electrons with  $\theta > 7$  used).

1580 Using the first of the two methods mentioned above, the real data reso-  
 1581 lutions were evaluated for three different polar angle ( $\theta$ ) cuts - all  $\theta$  (in fact  
 1582  $\theta \geq 7^\circ$ ),  $\theta > 15^\circ$ , and  $\theta > 20^\circ$ . The dependence of these experimental res-  
 1583 olutions on the beam energy for these cases are shown together in the Fig.  
 1584 4.6, along with the resolution for the case “all  $\theta$ ”, but determined from the  
 1585 cross-section difference method. Likewise, as described above, the DC-smear  
 1586 dependence of the simulated resolution were determined separately for all  
 1587 these three cases of angle cuts, so that we could compare the experimental  
 1588 resolutions with the simulations correspondingly. One such comparison is

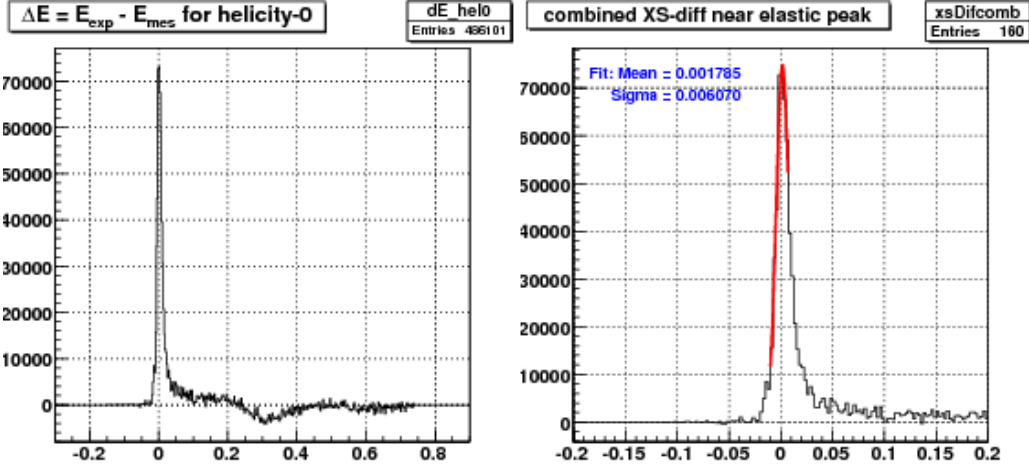


**Figure 4.5:** Plots showing the cross-section difference for 2.3 GeV NH<sub>3</sub> target data with the right one zoomed in around the elastic region (all good electrons with  $\theta > 7$  used).

1589 illustrated in the figure 4.7, where we show resolutions evaluated for the case  
 1590 of “all  $\theta$ ” - first two for the experimental data and the rest for the simulated  
 1591 data.

1592 Looking at Fig. 4.6, it is obvious that the resolution is  $\theta$ -dependent as ex-  
 1593 pected. When the experimental and simulated resolutions are compared for  
 1594 the three different cases of  $\theta$  cuts, we realize that the GPP asks for the  $\theta$  de-  
 1595 pendingent DC-smearing, which makes the simulation work very complicated  
 1596 with the current version of GPP. To simplify the situation, we decide to have  
 1597 a global ( $\theta$  independent) value of DC-smearing (for a given beam energy)  
 1598 by comparing the experimental and simulated resolutions corresponding to  
 1599 the case of “all  $\theta$ ” cut. That should be good enough for practical purposes.  
 1600 By taking into account the fact that there seems to be an inherent uncer-  
 1601 tainty in the measurement of the resolutions (evident from the discrepancy  
 1602 of the experimental resolutions determined from the two different methods)  
 1603 and comparing the experimental and simulated results, the values as listed  
 1604 in Table. 4.1 are chosen for the DC-smearing scales for the GPP.

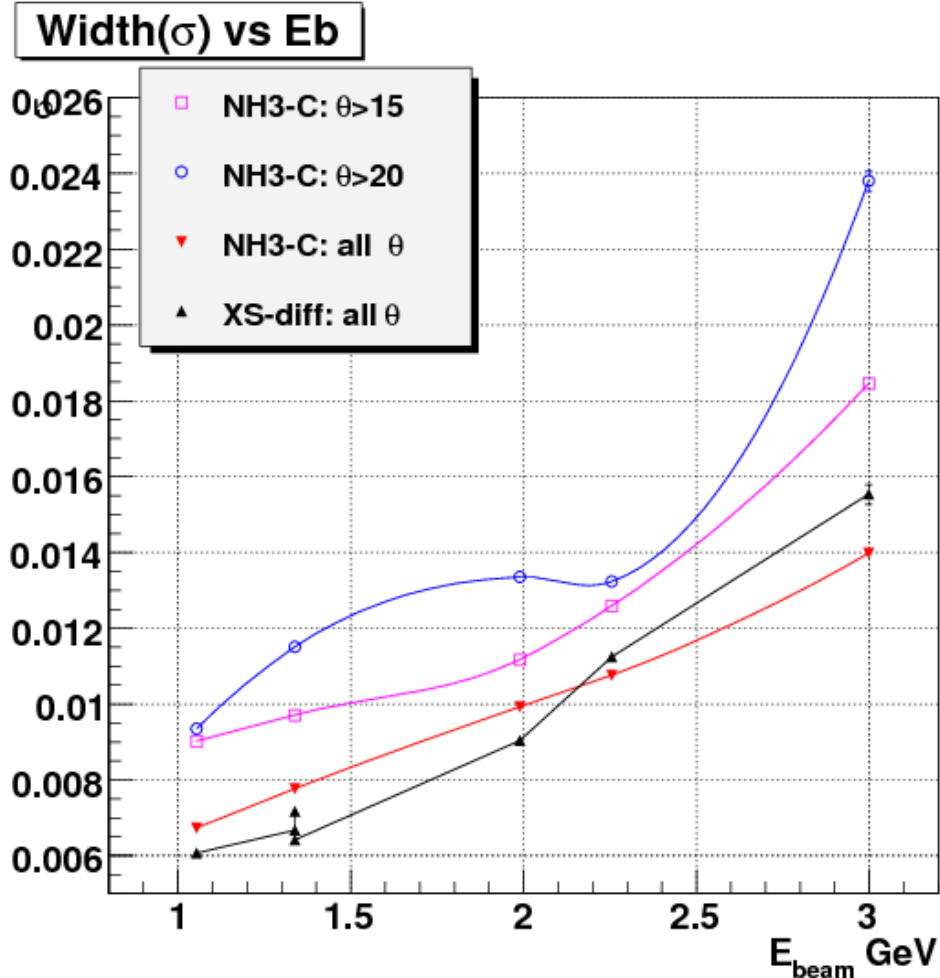


**Figure 4.6:** Graphs showing the dependence of width ( $\sigma$ ) of the elastic peaks (from experimental data) on the beam energy (GeV).

**Table 4.1:** DC-smearing scales determined for different beam energies.

$E_{beam}$ (GeV)	1.054	1.339	1.989	2.256	2.999
DC-smear	2.6	2.0	2.0	2.0	1.7

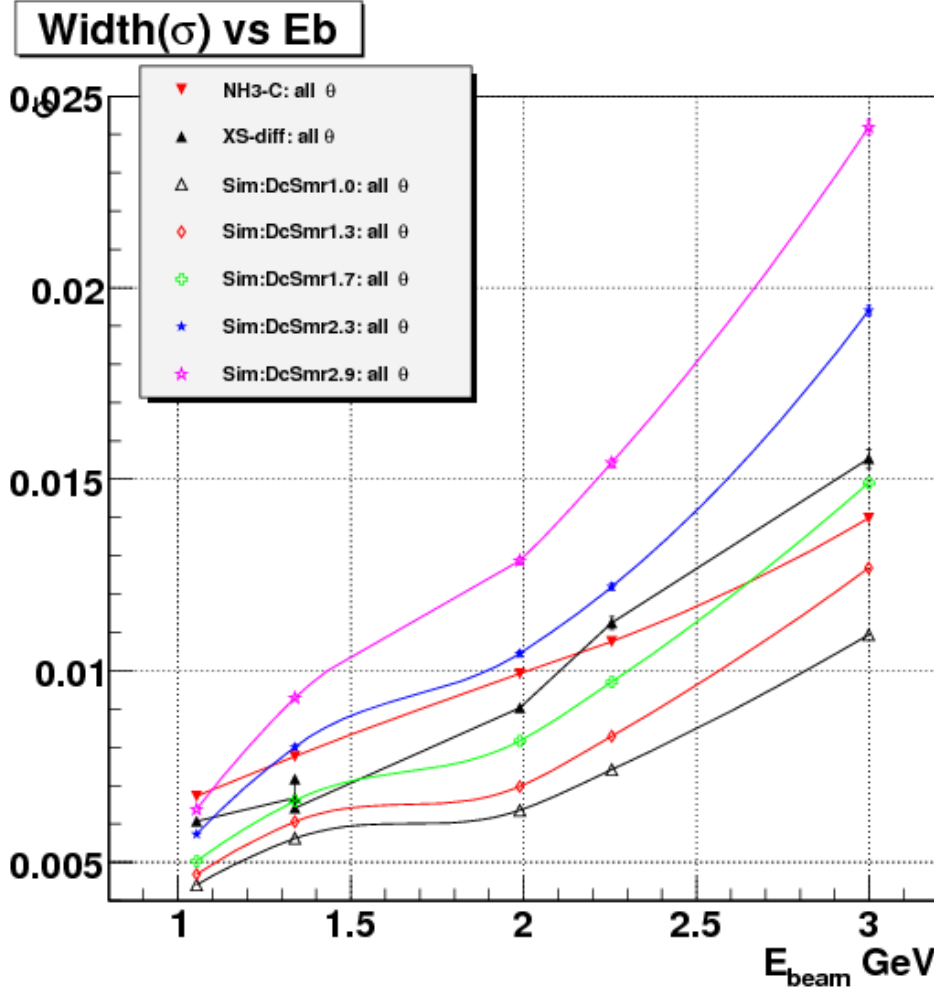


**Figure 4.7:** Graphs showing the dependence of width ( $\sigma$ ) of the elastic peaks (from both experimental and simulated data) on the beam energy (GeV).

## 1606 4.4 Comparison of Data and Simulation

1607 Using our final values for the smear parameters, the simulated data were  
 1608 passed through GPP and then reconstructed with RECSIS. Finally, all ap-  
 1609 plicable cuts and corrections were applied to both sets of polarized simu-  
 1610 lation data. Because the CC was turned off in GSIM for the simulation, all  
 1611 experimental data cuts except those depending on CC were applied to the  
 1612 simulated data. However, the cuts were modified (see Sec. 3.3) to account

<sub>1613</sub> for differences between simulation and data.

In the end, we had two sets of simulated events (for the two cases of  $\Delta\sigma \geq 0$  and  $\Delta\sigma < 0$ ) in each kinematic bin. The number of these two type of events in each bin were then cross-normalized with respect to each other by their respective cross-section map integrals and the number of generated Monte-Carlo events and then combined to make the simulated polarized count difference  $\Delta n$ . To do that, the number of simulated event counts in a kinematic bin corresponding to the positive  $\Delta\sigma$  was kept unchanged but the one corresponding to the negative  $\Delta\sigma$  was multiplied with the following normalization factor:

$$norm^- = \frac{\sigma_{tot}^-}{\sigma_{tot}^+} \times \frac{N^+}{N^-} \quad (4.3)$$

<sub>1614</sub> where  $\sigma_{tot}^{+/-}$  and  $N^{+/-}$  are the total integral of the cross section map and  
<sub>1615</sub> the corresponding number of Monte-Carlo events generated for each of the  
<sub>1616</sub> polarization cases (+/-).

The next step was to properly cross-normalize the simulated events to the data, as outlined in the introduction. For this, we found the scale factor  $SF$  necessary to have the same  $\Delta n$  in the quasi-elastic region (e.g.,  $0.9 \leq W \leq 1.0$ ). This factor represents the ratio

$$SF = \frac{n^+ - n^-}{\Delta n(simul)} \quad (4.4)$$

<sub>1617</sub> since we assume that the simulation for the cross section difference in this  
<sub>1618</sub> region is reliable and all other factors are common to the simulation and the data.  
<sub>1619</sub> In fact, we chose one  $Q^2$  bin (the 20<sup>th</sup> one - for which the agreement  
<sub>1620</sub> between the data and simulation was among the best) and calculated above  
<sub>1621</sub> ratio to get the global preliminary value of the scaling factor  $SF_{20}$ . The sim-  
<sub>1622</sub> ulated  $\Delta n$  was then multiplied with this factor to get our best “prediction”  
<sub>1623</sub> of the real data in all the kinematic bins, in order to directly compare it with  
<sub>1624</sub> the real data (see Figs. 4.8 and 4.9).

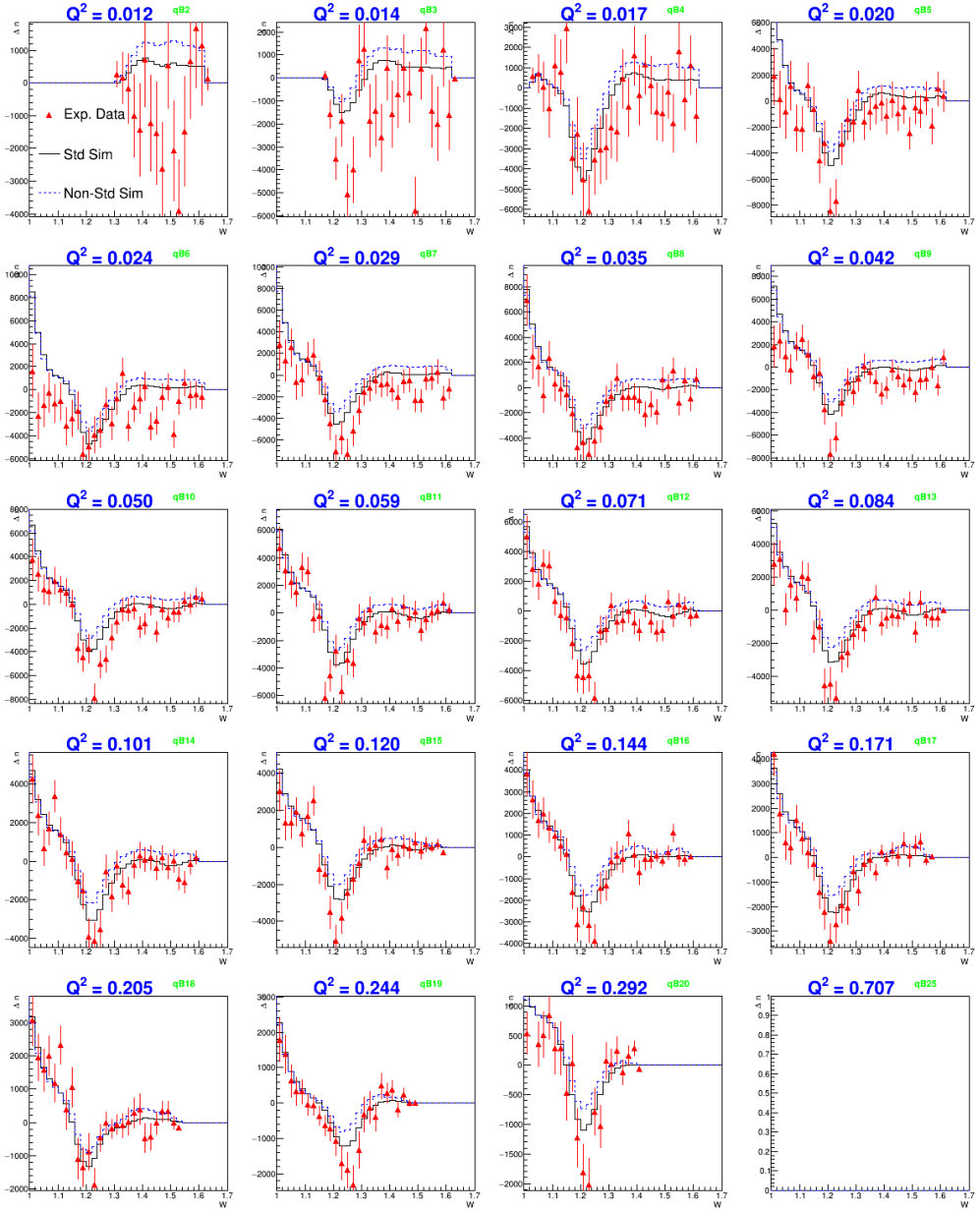


**Figure 4.8:** Comparison (in different  $Q^2$  bins) of polarized count differences from 1.3 GeV experimental (red points with error bars) and two versions of normalized simulation data. The black continuous histograms are for “standard” simulation with values of  $A_1$  set as given by the used model. The blue dotted histograms are for “non-standard” simulated data with  $A_1$  changed to  $A_1 + 0.1$ . ).

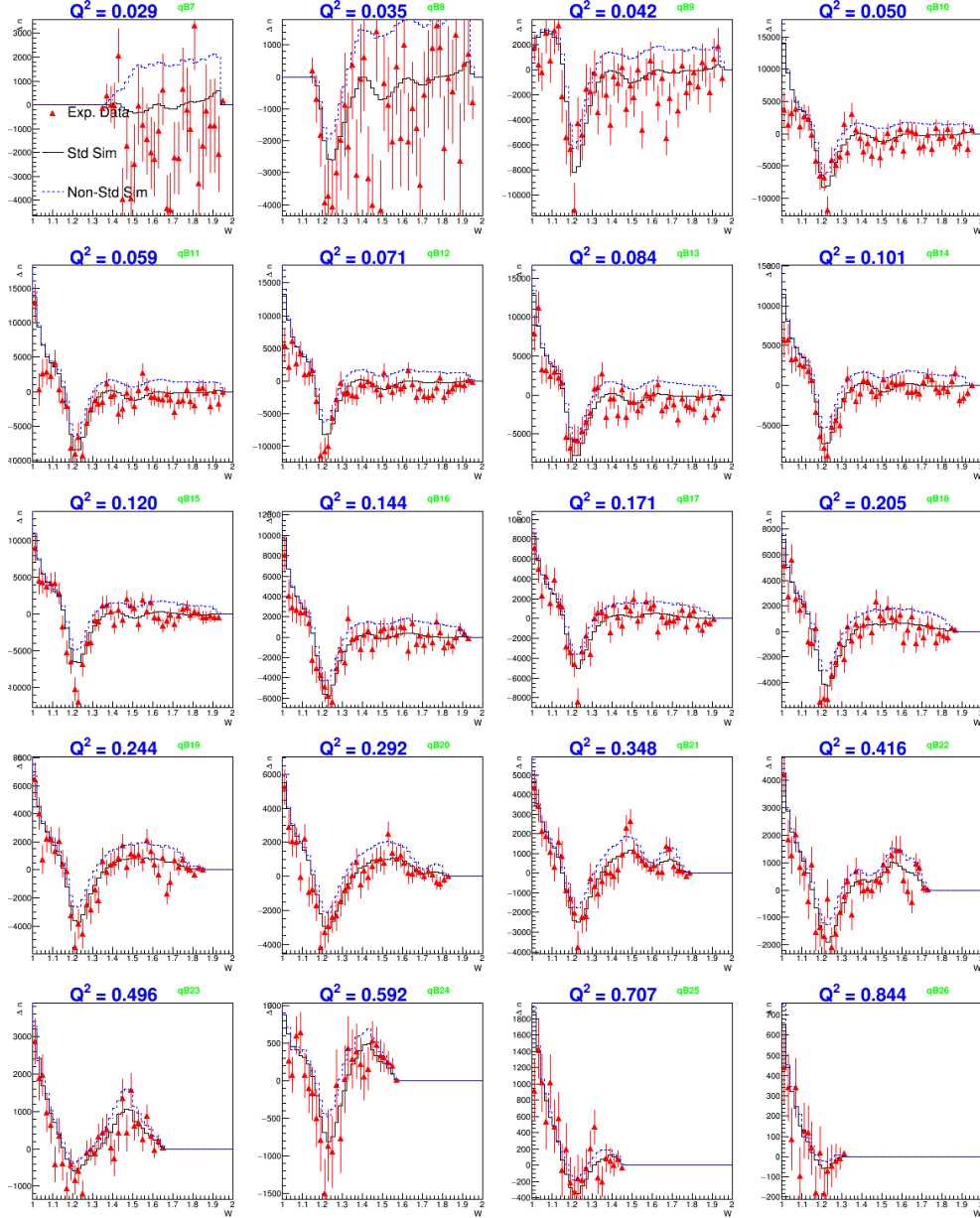


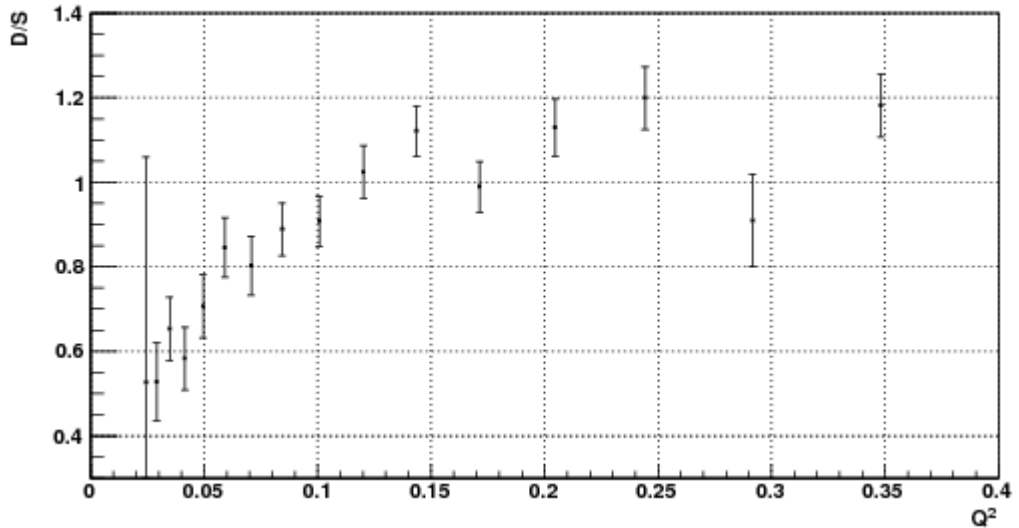
**Figure 4.9:** Comparison (in different  $Q^2$  bins) of polarized count differences from 2.0 GeV experimental (red points with error bars) and two versions of normalized simulation data. The black continuous histograms are for “standard” simulation with values of  $A_1$  set as given by the used model. The blue dotted histograms are for “non-standard” simulated data with  $A_1$  changed to  $A_1 + 0.1$ .

1625 After this normalization, the ratios  $(n^+ - n^-)/\Delta n(simul)$  in the quasi-  
1626 elastic region for all  $Q^2$  bins were calculated and plotted versus  $Q^2$  as well as  
1627  $\theta$  (see Figs. 4.10(a) - 4.13(a)) along with the corresponding statistical errors  
1628 as given by  $\sqrt{(n^+ + n^-)/\Delta n(simul)}$ . As the figures show, the ratio in the  
1629 quasi-elastic region drops off rapidly at small  $Q^2$ . The fall-off is likely due  
1630 to CC inefficiencies for very high momenta and very forward angles. Also,  
1631 our simple cross section model for the deuteron is less accurate at low  $Q^2$ .  
1632 Figs. 4.10(b) - 4.13(b) show that the  $\Delta$ -resonance region does not suffer from  
1633 similar problems.

1634 The final normalization was obtained by calculating the error weighted  
1635 average  $SF_{average}$  of above ratios in the quasi-elastic region. The average was  
1636 calculated using only those  $Q^2$  bins which had ratios reasonably stable and  
1637 closer to each other. Because, the ratios are reasonably stable only above  
1638  $Q^2 \approx 0.045 \text{ GeV}^2$  and  $Q^2 \approx 0.09 \text{ GeV}^2$  in the 1.337 and 2.0 GeV data sets  
1639 respectively (as can be seen from Figs. 4.10(a) and 4.12(a)), only those  $Q^2$   
1640 bins above these two limits were used in calculating the weighted average of  
1641 these ratios. In addition, even above those two limits, some of those which  
1642 had too large ratios - greater than 2.0 (or 2.5) for 1.337 (or 2.0) GeV data  
1643 set- were not used in the weighted average. However, it should be noted that  
1644 the bins not used in the average ratio calculations were not entirely discarded  
1645 from the final analysis. Only those below  $Q^2 = 0.02 \text{ GeV}^2$  were completely  
1646 thrown out from the final analysis because they did not cover the resonance  
1647 (particularly the  $\Delta$ ) region very well. The resulting simulated data in the  
1648 form of count differences  $\Delta n$  in various  $Q^2$  bins are shown in Figs. 4.8 and  
1649 4.9 along with the corresponding experimental data.

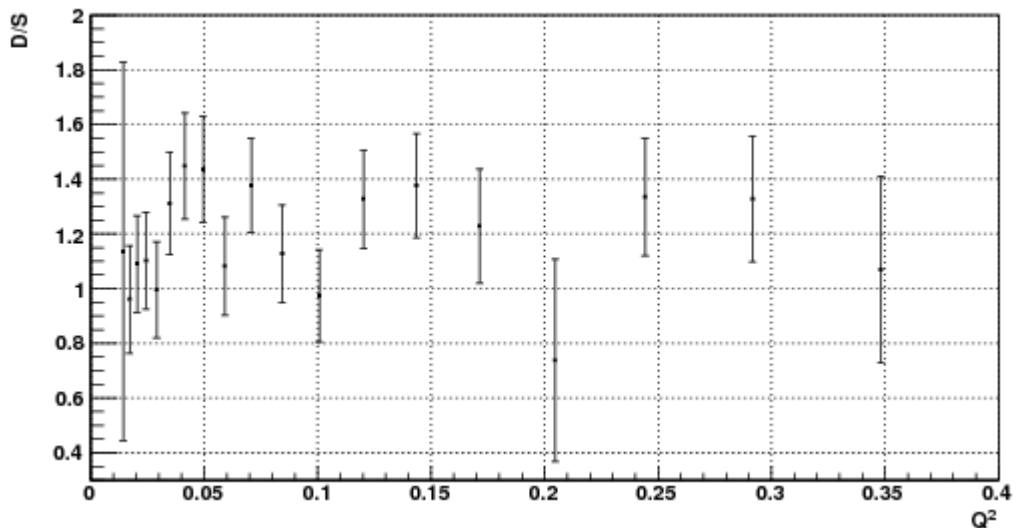
1650 A complete systematic error analysis was done to study the effect of the  
1651 overall scaling factor  $SF$  on the extracted  $g_1$  (see below) and to estimate  
1652 its statistical (due to the number of counts) and systematic (due to model  
1653 uncertainties and backgrounds) error.

Data/Sim for W(0.9,1.05)



(a) Data/Sim ratio vs  $Q^2$  in 1.3 GeV quasi-elastic data.

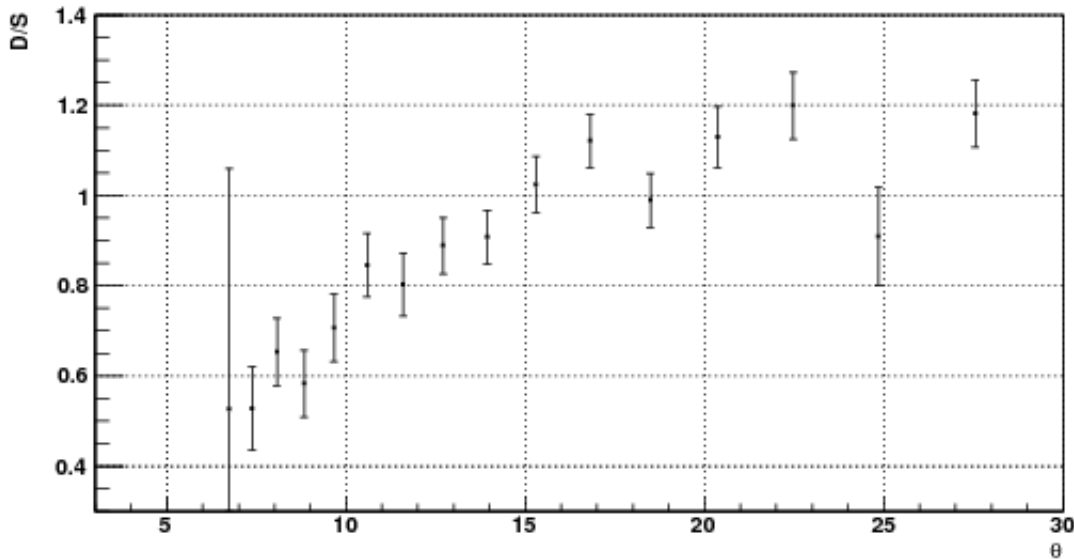
Data/Sim for W(1.15,1.3)



(b) Data/Sim ratio vs  $Q^2$  in  $\Delta$ -resonance region of 1.3 GeV data.

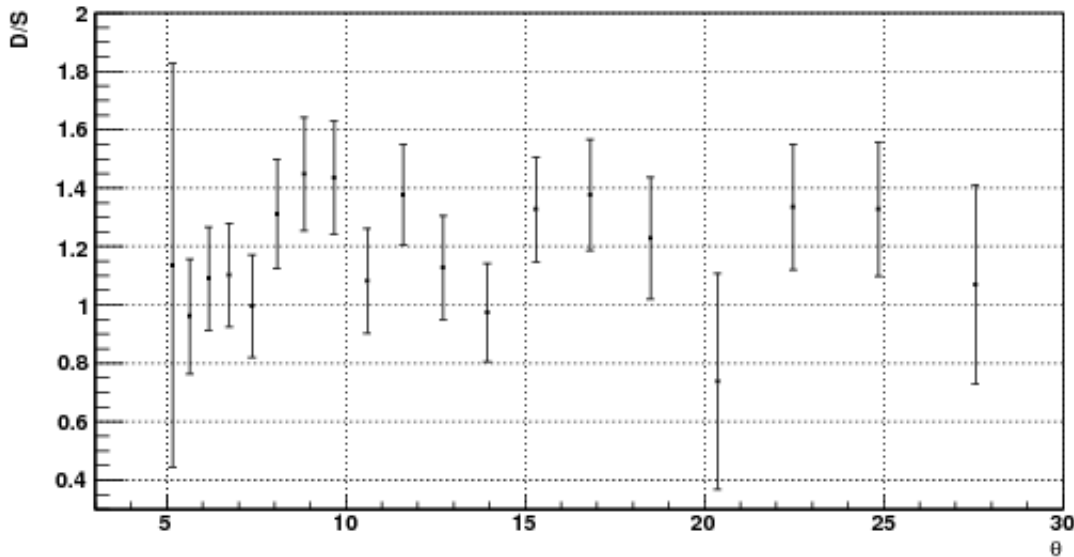
**Figure 4.10:**  $Q^2$  dependence of ratios of 1.3 GeV data and simulation in the quasi-elastic and  $\Delta$ -resonance regions.

Data/Sim for W(0.9,1.05)



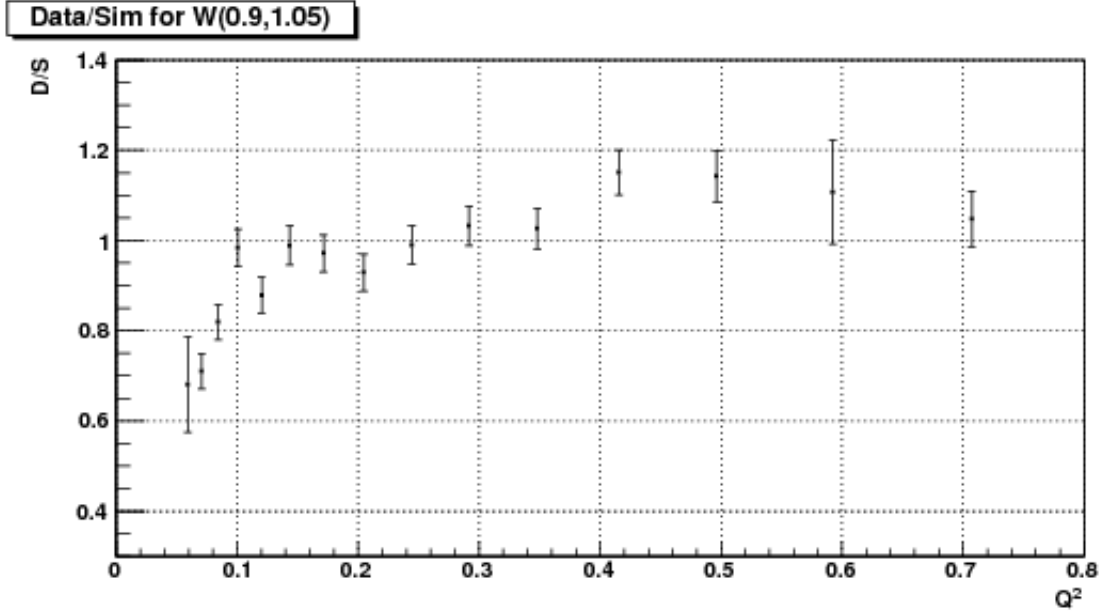
(a) Data/Sim ratio vs  $\theta$  in 1.3 GeV quasi-elastic data.

Data/Sim for W(1.15,1.3)

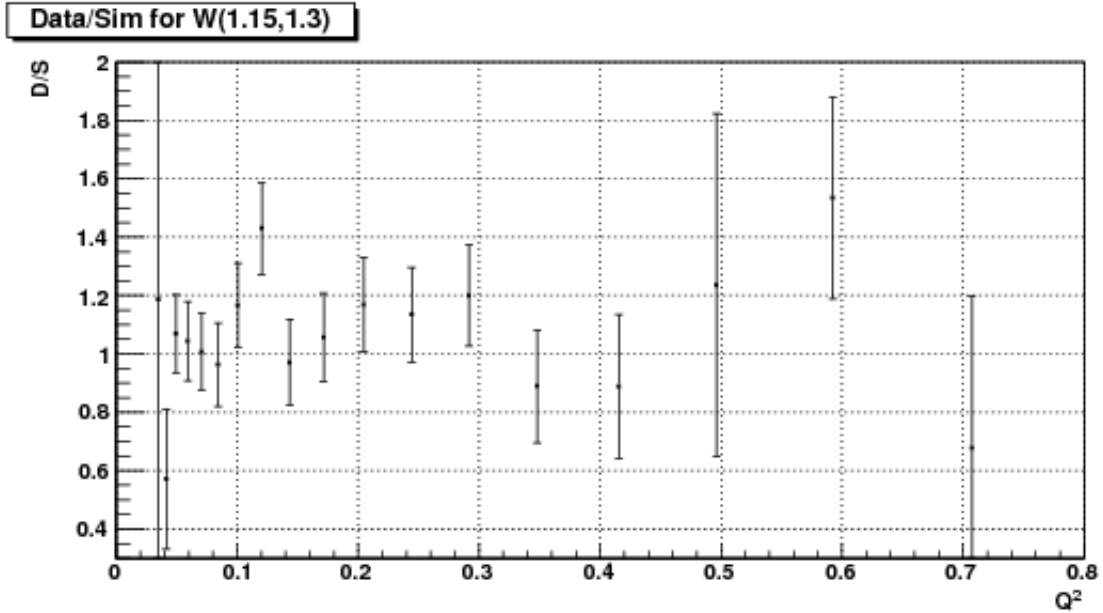


(b) Data/Sim ratio vs  $\theta$  in  $\Delta$ -resonance region of 1.3 GeV data.

**Figure 4.11:** The same data as in Fig. 4.10, but plotted versus average scattering angle ( $\theta$ ).

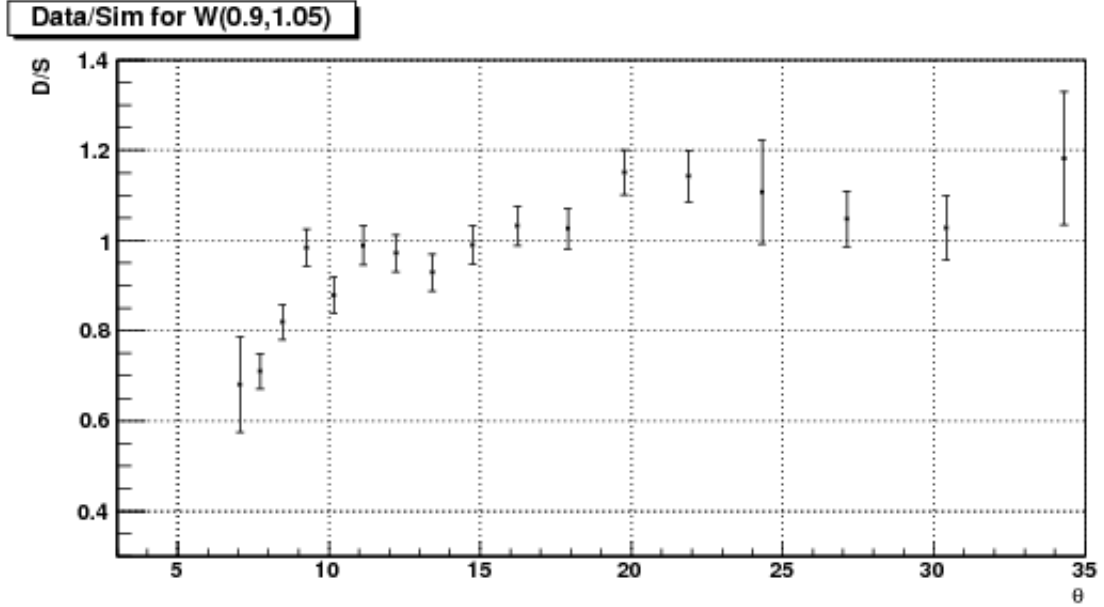


(a) Data/Sim ratio vs  $Q^2$  in 2.0 GeV quasi-elastic data.

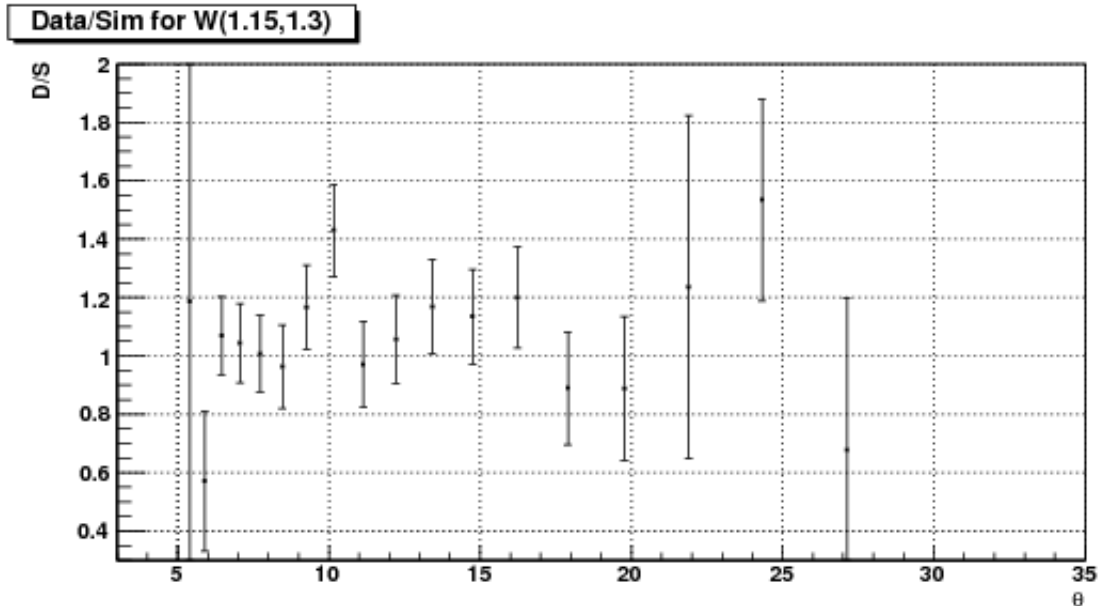


(b) Data/Sim ratio vs  $Q^2$  in  $\Delta$ -resonance region of 2.0 GeV data.

**Figure 4.12:**  $Q^2$  dependence of ratios of 2.0 GeV data and simulation in the quasi-elastic and  $\Delta$ -resonance regions.



(a) Data/Sim ratio vs  $\theta$  in 2.0 GeV quasi-elastic data.



(b) Data/Sim ratio vs  $\theta$  in  $\Delta$ -resonance region of 2.0 GeV data.

**Figure 4.13:** The same data as in Fig. 4.12, but plotted versus average scattering angle ( $\theta$ ).

## 1655 4.5 Method to Extract $g_1$ and $A_1 F_1$

### 1656 4.5.1 ‘Variation’ of the standard simulation

The whole chain of steps outlined in the previous sections for the standard simulation is repeated with just one major difference: the model input for the asymmetries  $A_1$  for both the proton and the neutron are increased by a constant value<sup>5</sup> of 0.1. With all other model ingredients being kept constant, this change leads to a change of the spin structure function  $g_1$  that can be straightforwardly calculated for each kinematic bin within the model:

$$\delta g_1(W, Q^2) = \delta A_1 \times F_1 \frac{\nu^2}{\nu^2 + Q^2} \quad (4.5)$$

1657 Correspondingly, the simulated count difference  $\Delta n(W, Q^2)$  will change to  
 1658 a new value  $\Delta n'$ . This ‘non-standard’ simulation with  $A_1 = A_1(\text{standard}) +$   
 1659 0.1 is performed generating an about equal number of Monte-Carlo events.  
 1660 The final reconstructed data is then multiplied with the same overall scaling  
 1661 factor SF as for the standard simulation and then further (cross-)normalized  
 1662 by one additional factor  $SF_{ext} = (\sigma_1^p / \sigma_2^p) / (N_1 / N_2)$  to account for the change  
 1663 in cross section map and the (slight) difference in the number of the generated  
 1664 events between the standard and non-standard simulations. Here,  $\sigma_1^p$  and  $\sigma_2^p$   
 1665 are the total cross sections for the positive  $\Delta\sigma$  maps used for the standard and  
 1666 non-standard simulations and,  $N_1$  and  $N_2$  are the corresponding numbers of  
 1667 generated events. See Fig. (4.14) to see how the polarized count differences  
 1668 look (in one particular  $Q^2$  bin) in experimental and simulated data after such  
 1669 normalizations (for all other  $Q^2$  bins, see Figs. 4.8 and 4.9).

This change of the simulated  $\Delta n(W, Q^2)$  to a new value  $\Delta n'$  can be correlated to the increase in  $g_1$  by solving for the two parameters  $A$  and  $B$  of the linear equation,

$$\Delta n(\text{simul}) = A + B \cdot \delta g_1, \quad (4.6)$$

where  $A(W, Q^2)$  is the result for the simulated  $\Delta n$  for the standard set of model inputs i.e.,  $A(W, Q^2) = \Delta n^{\text{standard}}(W, Q^2)$ , and  $B(W, Q^2)$  is the proportionality factor representing the change in  $\Delta n(\text{sim})$  per unit change in

---

<sup>5</sup>We arbitrarily chose 0.1 in the inelastic region, but could also have used any other value (not too big, however).

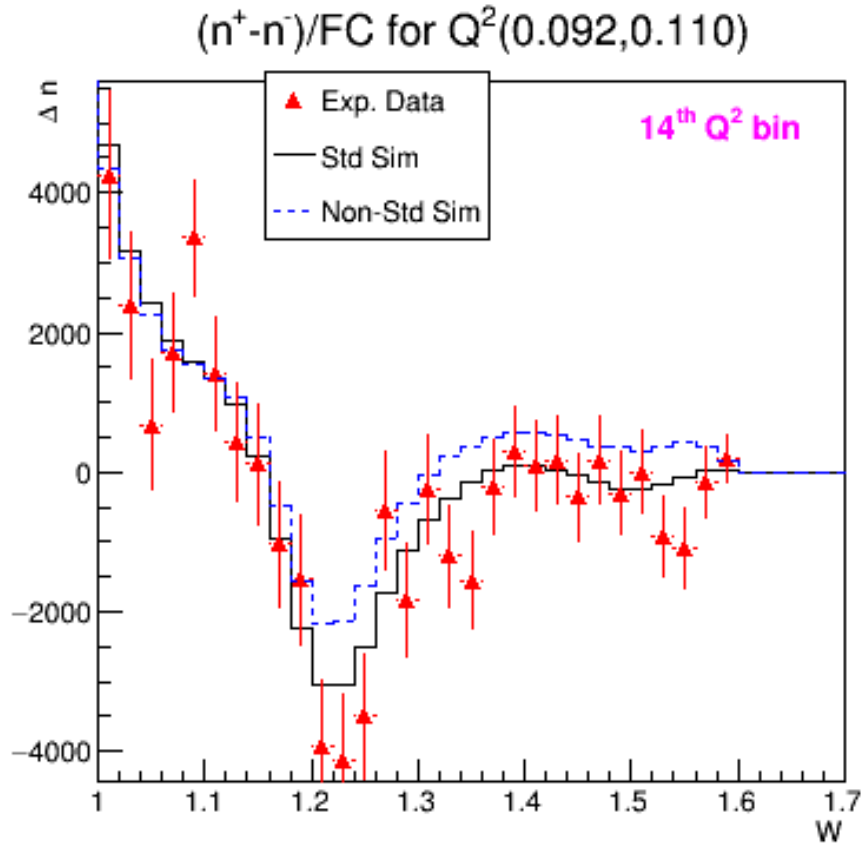
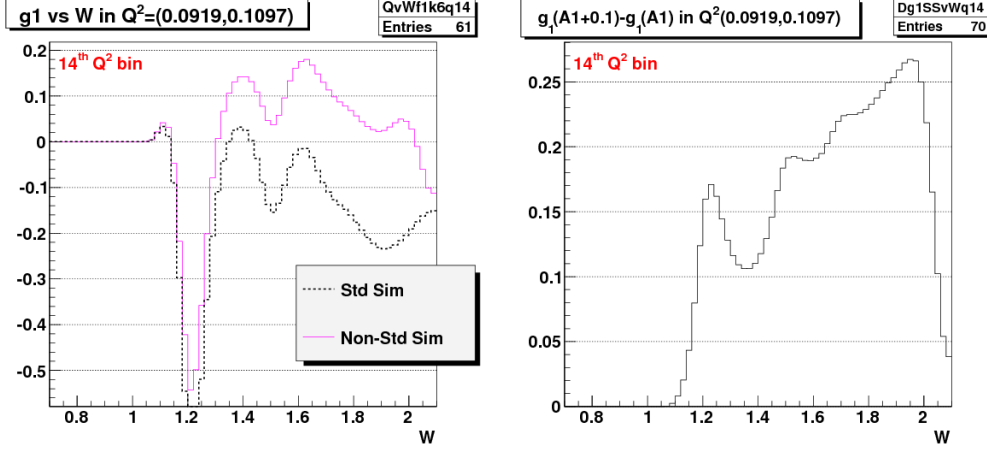


**Figure 4.14:**  $\Delta n$  of experimental data and two versions of simulations in one particular  $Q^2$  bin for 1.3 GeV case (for data on more  $Q^2$  bins, see Fig. 4.8).

$g_1$ , as given by:

$$B(W, Q^2) = \frac{\Delta n' - \Delta n}{\delta g_1}. \quad (4.7)$$

The proportionality factor  $B(W, Q^2)$  is then determined for each of the kinematic bins (in  $(W, Q^2)$ ) in which the experimental data has been histogrammed. For this purpose, using the RCSLACPOL program, we produce two values of structure function  $g_1$  in each kinematic bin - one is  $g_1^{Standard}$  corresponding to the standard simulation and the other is  $g_1^{non-standard}$  corresponding to the non-standard simulation. By dividing the above change in the count difference with the difference  $\Delta g_1$  of these two structure functions, we get the factor  $B(W, Q^2)$  for the bin.



(a)  $g_1$  for standard and non-standard simulation

(b) Difference of the two  $g_1$

**Figure 4.15:** Plots showing the change in model  $g_1$  due to the change of  $A_1$  to  $A_1 + 0.1$ .

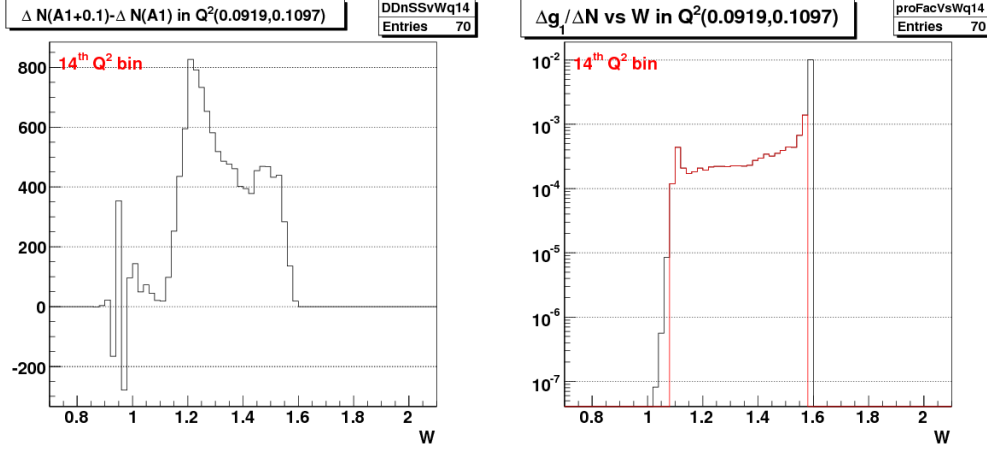
In principle (and ignoring the other enumerated possible sources of disagreement between data and simulation), we can then easily find the “amount of change”  $\delta g_1$  to be added to the standard model  $g_1$  to get perfect agreement:

$$\delta g_1 = g_1^{extr}(W, Q^2) - g_1^{Standard} = \frac{\Delta n^{data}(W, Q^2) - \Delta n^{standard}(W, Q^2)}{B(W, Q^2)} \quad (4.8)$$

where the values of  $\Delta n^{data}$  and  $\Delta n^{standard}$  come from the polarized count differences  $\Delta n$  in the experimental data and the standard simulation respectively (as shown, for example, by the red points and black histograms in Fig. 4.14 for one particular  $Q^2$  bin).

It is also straightforward to propagate the statistical error to the extracted  $g_1$ . The statistical error in this extracted quantity totally comes from the error in the experimental counts  $\Delta n^{data}$  (assuming there is no error in the model quantities involved and also in the simulation counts because we did our simulation with large enough statistics to warrant ignoring the errors) as follows:

$$\sigma(g_1^{extr}(W, Q^2)) = \frac{\sigma(\Delta n^{data}(W, Q^2))}{B(W, Q^2)}. \quad (4.9)$$



(a) Change in  $\Delta n(sim)$  simulated count difference i.e.  $\Delta N = \Delta n'(A_1 + 0.1) - \Delta n(A_1)$  due to the change of  $A_1$  to  $A_1 + 0.1$  (for 1.3 GeV case).

(b) Proportionality factor ( $1/B(W, Q^2)$ ) for 1.3 GeV case. Black is the original values. Red is the ones kept after discarding the first or last few (low statistics bins) that had unreasonably high (suddenly changing) ratios. This ensures we only show final data with “good” proportionality factor.

**Figure 4.16:** Plots for  $\Delta n(sim)$  and the corresponding proportionality factors.

1682 The values of  $g_1$  and its errors thus extracted from 1.3 GeV data for one  
 1683  $Q^2$  bin is shown in Fig. (4.17(b)). Similar results for all the bins from two  
 1684 beam energy data sets in different kinematic bins can be seen in Fig. 6.1.

1685 Because we are also interested in measuring the forward spin polarizability  
 1686 and the extended GDH integral, we also extract the product  $A_1 F_1$  which  
 1687 enters these integrals. We followed the exact same procedure for  $g_1$  as out-  
 1688 lined above. We determined new proportionality factors in each kinematic  
 1689 bin, again using Eq. 4.11 as before but with the denominator replaced, this  
 1690 time, with the corresponding change in  $A_1 F_1$  (instead of the change in  $g_1$ ).  
 1691 Then we can use the following expression (similar to equation 4.8) to extract  
 1692  $A_1 F_1(W, Q^2)$  :

$$\delta A_1 F_1 = A_1 F_1^{extr}(W, Q^2) - A_1 F_1^{Standard} = \frac{\Delta n^{data}(W, Q^2) - \Delta n^{standard}(W, Q^2)}{B_{A_1 F_1}(W, Q^2)} \quad (4.10)$$

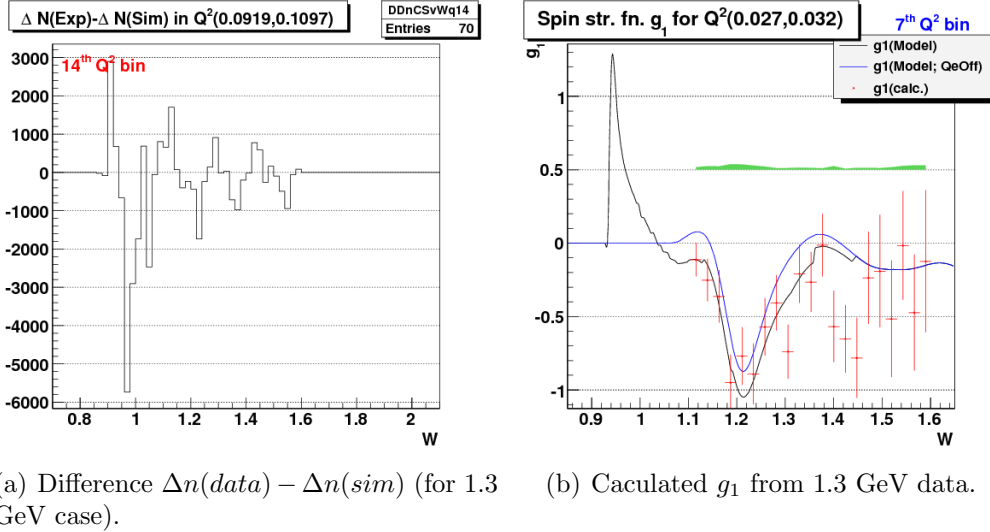


**Figure 4.17:** Plots for  $\Delta(\Delta n)$  and the corresponding extracted  $g_1$ . On the left,  $\Delta n$  are the normalized count differences from the experimental and simulated (using 'standard' model) data. On the right, the blue line is that of  $g_1$  when the quasi-elastic part was turned off in the model that was used in simulation. We used  $g_1^{extracted} = g_1^{q.e.Off} + \delta g_1$  to get the measured  $g_1$ , where  $\delta g_1$  was derived from the data shown on the left using Eq. 4.8.

where

$$B_{A_1 F_1}(W, Q^2) = \frac{\Delta n' - \Delta n}{\delta A_1 F_1}. \quad (4.11)$$

1693 And, the errors on  $A_1 F_1$  can also be dealt in the same way as on  $g_1$ .

- 1694 **Chapter 5**
- 1695 **Systematic Uncertainties**
- 1696 There is always a possibility that the final result(s) produced from any data  
1697 analysis will be shifted from the true or ideally expected value(s) because the  
1698 final result(s) are derived using the measured, modeled or estimated values  
1699 of one or more other input parameters, whose values themselves usually have  
1700 some systematic measurement or estimation uncertainties.
- 1701 The systematic effects due to a particular variable are studied by making a  
1702 small change in the variable while holding the others constant, and measuring  
1703 by how much the end result(s) changed.
- 1704 In this analysis, ten sources of systematic uncertainties are studied as  
1705 listed below:
- 1706 1. Possible Uncertainty in the overall scaling factor
  - 1707 2. Effect due to the contaminations from polarized H in the target and  
1708 from misidentified  $\pi^-$  in the scattered electrons sample.
  - 1709 3. Potential deviations in the reconstructed kinematics
  - 1710 4. Possible uncertainty in the CC-inefficiency estimation
  - 1711 5. Effect due to the  $e^+e^-$  pair symmetric contamination
  - 1712 6. Possible uncertainty in the estimation of radiation lengths
  - 1713 7. Model variation using preliminary version (v1) of  $A_1$  model by Guler/Kuhn  
1714 (2008-9)
  - 1715 8. Model variation using old version of  $A_2$  resonance model

1716        9. Model variation of  $F_2$  (and proportionally of  $F_1$ ) while keeping R con-  
1717        stant

1718        10. Model variation of R or  $F_1$  (with  $F_2$  unchanged)

1719        For the ease of description later on, these ten components will be referred to  
1720        by the index "k" with its value indicating the position in the list. So, the  
1721        uncertainty due to scaling factor will be identified with k=1 and so on.

**Possible Uncertainty due to the overall scaling factor** This uncer-  
tainty is due to the uncertainties in the overall scaling factor (SF), which is a  
convolution of various unmeasured constants such as  $P_bP_t$ , packing fraction  
etc (see Sec. 4.1.1). This contribution is estimated by assuming that the  
uncertainties in SF is not more than 10%. Thus considering the worst case  
scenario of 10% uncertainty in SF, we estimate the corresponding uncertainty  
in  $g_1$  as follows:

$$\Delta g_1^{SF}(W, Q^2) = g_1^{std}(W, Q^2) + \frac{\Delta n^{data}(W, Q^2) - 1.1 \cdot \Delta n^{std}(W, Q^2)}{1.1 \cdot B(W, Q^2)} - g_1^{data}(W, Q^2) \quad (5.1)$$

1722        with "std" shorthand used for "standard" model or the corresponding sim-  
1723        ulation i.e. the ones provided by RCSLACPOL when the asymmetry  $A_1$   
1724        was not artificially increased to  $A_1 + 0.1$ . Here,  $\Delta n^{data}$  and  $\Delta n^{std}$  represent  
1725        the polarized count differences for the experimental and simulated (without  
1726        artificially changing  $A_1$ ) data respectively.

**Uncertainty from Polarized H in target and  $\pi^-$ contaminations** This  
contribution from polarized H in target and  $\pi^-$ contamination is evaluated as  
follows,

$$\Delta g_1^{cont}(W, Q^2) = g_1^{std}(W, Q^2) + \frac{\Delta n^{data}(W, Q^2) \cdot 1.025 - \Delta n^{std}(W, Q^2)}{B(W, Q^2)} - g_1^{data}(W, Q^2) \quad (5.2)$$

1727        where we assume that the contamination is not more than 2.5%, which is  
1728        consistent with what was found from our own study of the contamination.

**Possible uncertainty in the beam energy measurement** This contrib-  
ution is evaluated assuming the uncertainty in beam energy measurement

is not more than 10 MeV, so either the experimental data or the standard-simulation data can be analyzed assuming the beam energy was different by 10 MeV. In this analysis, the simulated data was analyzed assuming that the beam energy was 10 MeV more than that used during the event generation or simulation which was the same as that used for analyzing the experimental data. For example, for the lower beam energy data set, 1339 MeV was used to analyze the experimental data as well as to simulate the corresponding data, but during the analysis of the simulated data, the energy value used was 1349 MeV. Here, the change in energy results in changes in both  $Q^2$  and  $W$ .

$$\Delta g_1^{Eb}(W, Q^2) = g_1^{std}(W, Q^2) + \frac{\Delta n_{E\bar{b}}^{data}(W, Q^2) - \Delta n_{E\bar{b}+}^{std}(W, Q^2)}{B(W, Q^2)} - g_1^{data}(W, Q^2) \quad (5.3)$$

where  $\Delta n_{E\bar{b}+}^{std}$  is now the simulated  $\Delta n^{std}$  obtained by analyzing the data from the standard simulation as usual but with a beam energy that was 10 MeV more than the standard value.

**Possible uncertainty in the CC-inefficiency estimation** This contribution is estimated by assuming a maximum of 50% uncertainty in the estimated inefficiency as follows: The the 50% error is justified because the uncertainty in inefficiency is no more than 50% for nphe<2.5 (see Fig. 3.30).

$$\Delta g_1^{Eb}(W, Q^2) = g_1^{std}(W, Q^2) + \frac{\Delta n_{0.5CCi}^{data}(W, Q^2) - \Delta n_{0.5CCi}^{std}(W, Q^2)}{B(W, Q^2)} - g_1^{data}(W, Q^2) \quad (5.4)$$

where  $\Delta n_{0.5CCi}^{std}$  is now the simulated  $\Delta n^{std}$  obtained after applying 50% more inefficiency instead of the actually estimated value.

**Possible uncertainty due to  $e^+e^-$  pair symmetric contamination** The contribution due to  $e^+e^-$  pair symmetric contamination is calculated as follows:

$$\Delta g_1^{Eb}(W, Q^2) = g_1^{std} + \frac{\Delta n^{data} \cdot \frac{1}{1+f(e^+e^-)} - \Delta n^{std}}{B(W, Q^2)} - g_1^{data}(W, Q^2) \quad (5.5)$$

where  $f(e^+e^-)$  is the fraction of electrons in a given bin that come from pair-symmetric  $e^+e^-$  produced as estimated with EG1b fit by N. Guler [22] (used the closest available energies).

**Radiative correction uncertainty** Here, we need to change the parameter that most influences radiative corrections, the number of radiation lengths before (RADB) and after (RADA) the scattering. By increasing both numbers by 10%, we should have a safe upper limit on practically all uncertainties coming from the radiative procedure itself. But, to simplify the situation, we increased the RADA parameter in RCSLACPOL by 20% and repeated the full-statistic simulation. As a result the simulated count difference in each kinematic bin changed from  $\Delta n^{std}$  to a new value  $\Delta n^{rad}$ . This change can be converted to the corresponding inferred change in  $g_1$  by using the same proportionality factors  $B(W, Q^2)$  as used earlier in the  $g_1$  (or  $A_1 F_1$ ) extraction/calculation. In other words, for a given kinematic bin this particular contribution to the systematic uncertainty is calculated as:

$$\Delta g_1^{rad}(W, Q^2) = g_1^{std} + \frac{\Delta n^{data}(W, Q^2) - \Delta n^{rad}(W, Q^2)}{B(W, Q^2)} - g_1^{data}(W, Q^2) \quad (5.6)$$

1737 where the proportionality factor  $B(W, Q^2)$  for the bin is exactly the same as  
1738 that used to calculate  $g_1$  earlier.

## 1739 5.1 Model uncertainties

1740 The remaining four components in the total systematic uncertainty (the last  
1741 four in the list ??) account for the model uncertainty contributions. For  
1742 this purpose, we changed the values of two of the model parameters “Asym-  
1743 Choice” and “SFchoice” (each takes value of 11, in the standard case)

1744 We repeated the full statistics simulation four more times by changing  
1745 the values of two RCSLACPOL parameters “AsymChoice” and “SFchoice”  
1746 (which controls the values of model asymmetries and the structure functions,  
1747 with each taking a value of 11 in the standard case) one by one corresponding  
1748 to the following four model variations:

- 1749 1. Variation-1: AsymChoice=12, SFchoic=11
- 1750 2. Variation-2: AsymChoice=15, SFchoic=11
- 1751 3. Variation-3: AsymChoice=11, SFchoic=12
- 1752 4. Variation-4: AsymChoice=11, SFchoic=13

1753 where, the different values of the two RCSLACPOL parameters correspond  
1754 to the following model choices:

1755 1. **AsymChoice** values are used to determine specific  $A_1/A_2$  models used  
1756 in the RCSLACPOL program

1757 (a) 11: Standard Resonance Model 2008-9 Guler/Kuhn (**Used for**  
1758 **standard simulation**)

1759 (b) 12: Variation of  $A_1$  model (earlier fit)

1760 (c) 15: Variation of  $A_2$  resonance model: Vary the virtual photon  
1761 asymmetry  $A_2$  in the resonance region within its fit uncertainties.

1762 2. **SFchoice** values are used to determine specific  $F_1/F_2$  models.

1763 (a) 11: 2009 version of  $F_1^n/F_1^p/F_1^d$  by Peter Bosted/Eric Christie 2009,  
1764 HERMES (**Used for standard simulation**) (with d in  $F_1^d$  de-  
1765 noting a deuteron).

1766 (b) 12: Same version as 11, but with fit uncertainties added to  $F_2$   
1767 (and proportionally  $F_1$ )

1768 (c) 13: Same version as 11, but with fit uncertainties subtracted from  
1769 R ( $F_2$  unchanged)

After the simulation data for the above four cases were available, four more data tables (TM1,TM2,TM3 and TM4) were produced for the corresponding model values of  $g_1$ ,  $A_1$ ,  $F_1$  etc. Then, the contributions to the systematic uncertainty from each of these four cases of model variation were given as follows:

$$\Delta g_1^i(W, Q^2) = g_1^{std}(W, Q^2) - g_1^i(W, Q^2) + \frac{\Delta n^i(W, Q^2) - \Delta n^{std}(W, Q^2)}{B(W, Q^2)} \quad (5.7)$$

1770 with “i” indicating any of the four cases of model variation,  $g_1^i$  being the  
1771 model prediction for the  $i^{th}$  case as obtained from the corresponding data  
1772 table “TMi” and the proportionality factor  $B(W, Q^2)$  again being exactly  
1773 the same as used to calculate  $g_1$  as earlier.

## 1774 5.2 Combining uncertainties

1775 Contributions from the 10 individual components are estimated and then a  
1776 total contribution is estimated by first combining the corresponding individ-  
1777 ual components for each of the two beam energies and finally combining them  
1778 all by calculating the RMS of the ten combined contributions.

### 1779 5.2.1 Combining uncertainties from the two beam en- 1780 ergies

1781 In principle, each of the individual contributions to the systematic uncer-  
1782 tainty can also be combined using the same equations as for combining  $g_1$   
1783 and  $A_1 F_1$  (see above). However, we must be careful to distinguish between  
1784 correlated and uncorrelated uncertainties. If for a given  $(W, Q^2)$  bin, data  
1785 is available only from one beam energy, then combined uncertainty for the  
1786  $k^{th}$  component is simply the uncertainty from that beam energy. If there are  
1787 measurements from both beam energies, we combine them with statistical  
1788 weights as follows:

- 1789 1. The variations due to scale factor ( $k=1$ ), beam energy ( $k=3$ ) and CC-  
1790 efficiency ( $k=4$ ) are all un-correlated and, therefore, added in quadra-  
1791 ture as follows:

$$\delta g_1(k=8,10,11, \text{ combined}) = \sqrt{\left( \sum_i \frac{(\delta g_1)^2(i)}{(\Delta g_1)^2(i)} \right) / \text{Sum2}} \quad (5.8)$$

1792 where,  $\delta$  represents the  $k^{th}$  component of the systematic uncertainty,  
1793 whereas, 'Sum2', 'i' and  $\Delta$  have the same meanings as before.

- 1794 2. while all other variations are correlated between the two beam energies  
1795 and should be averaged linearly (WITH sign):

$$\delta g_1(\text{other } k, \text{ combined}) = \left( \sum_i \frac{(\delta g_1)(i)}{(\Delta g_1)^2(i)} \right) / \text{Sum2} \quad (5.9)$$

1796 with

$$\text{Sum2} = \sum_i \frac{1}{(\Delta g_1)^2(i)} \quad (5.10)$$

1797 providing the statistical weight, where the index 'i' represents two beam en-  
 1798 ergy (1.3 and 2.0 GeV) data sets, and  $\Delta g_1$  indicates the statistical uncertainty  
 1799 in  $g_1$  in the corresponding kinematic bin.

### 1800 5.2.2 Combining uncertainties from the ten sources

1801 Once each of the  $k^{th}$  component of the systematic uncertainties are combined  
 1802 between the two beam energies, we then proceed to combine them all to get  
 1803 a grand total. This is done by simply adding the ten  $E_b$ -combined systematic  
 1804 uncertainties in quadrature and taking the square-root of the sum as follows:

$$TotalSystematicUncertainty = \sqrt{\sum_{k=1}^{10} (\Delta g_1)_k^2} \quad (5.11)$$

1805 Figs. (5.2 and 5.3) show, for example, the different components of the  
 1806 systematic uncertainties (along with the grand total) on  $g_1$  (from 1.3 GeV  
 1807 data) evaluated in the manner just outlined. Likewise, Figs. (5.4 and 5.5)  
 1808 show similar plots for the 2.0 GeV data.

1809 These ten different components of systematic uncertainties on  $g_1$  (and  
 1810 similarly on  $A_1 F_1$ ) thus calculated separately for both beam energies are  
 1811 later combined as follows:

### 1812 5.2.3 Combining data from the two beam energies

1813 Once the data  $g_1$  and  $A_1 F_1$  and their corresponding uncertainties are eval-  
 1814 uated from each beam energy data set, they are combined as follows [29] (to  
 1815 make the description simple, the procedure is described only for  $g_1$ , but, in  
 1816 the end, the exact same procedure is followed for  $A_1 F_1$  as well):

- 1817 1. First a table is made, separately for each beam energy, of all  $(Q^2, W)$   
 1818 bins with with calculated values of  $g_1$ , their statistical uncertainties and  
 1819 each of the ten components of the systematic uncertainties (making sure  
 1820 to keep the correct signs of the systematic changes) in separate columns  
 1821 (one row is for one bin in  $(Q^2, W)$ ).
- 1822 2. Then another table is made for the combined values of  $g_1$ , which are  
 1823 evaluated as follows:

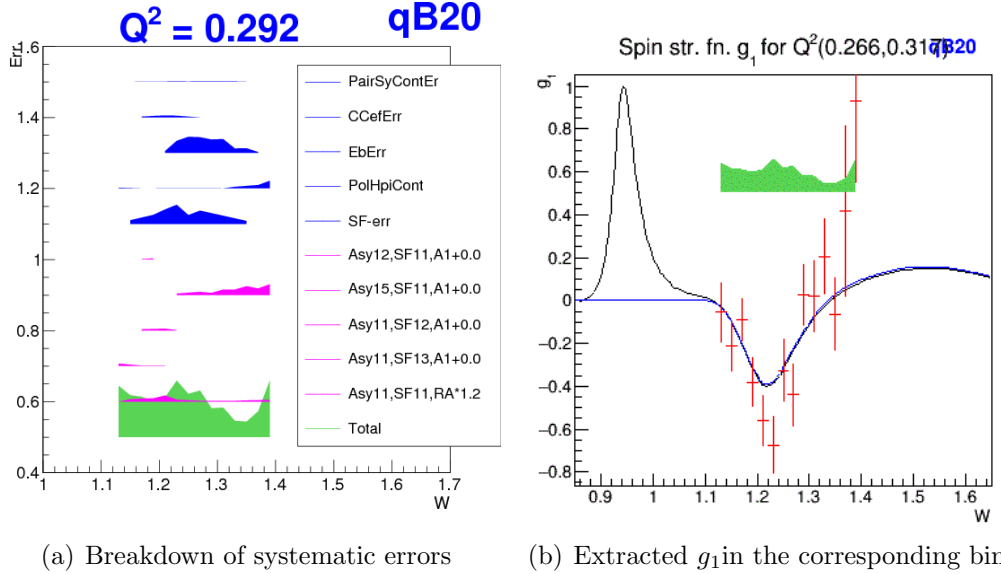


**Figure 5.1:** Various components of systematic uncertainty (see Secs. 5 and 5) on  $g_1$  plotted against  $W$  in a  $Q^2$  bin (1.3 GeV data). The band width represents the size of the uncertainties. The vertical position of each band has no physical meaning (arbitrarily chosen for the convenience of display). The first five (blue) bands are the contributions due to  $e^+e^-$ -contamination (see Sec. 5), CC-inefficiency (see Sec. 5), uncertainties in beam energy measurement (see Sec. 5), polarized background ( $H, \pi^-$  etc - see Sec. 5) and scaling factor uncertainties (see Sec. 4.1.1) respectively. The first (top) magenta band is the contribution due to the uncertainties in the radiative corrections (see Sec. 5), next four (magenta) are due to model uncertainties (see Sec. 5.1) and the last (green) one is the total uncertainty after properly combining all components. For similar plots in other  $Q^2$  bins see Figs. 5.2 and 5.3.

- 1824           (a) If for a given  $(W, Q^2)$  bin,  $g_1$  comes only from one beam energy,  
1825           then all the entries from that energy go into the "combined" table  
1826           (b) If  $g_1$  has measurements from both beam energies, we combine

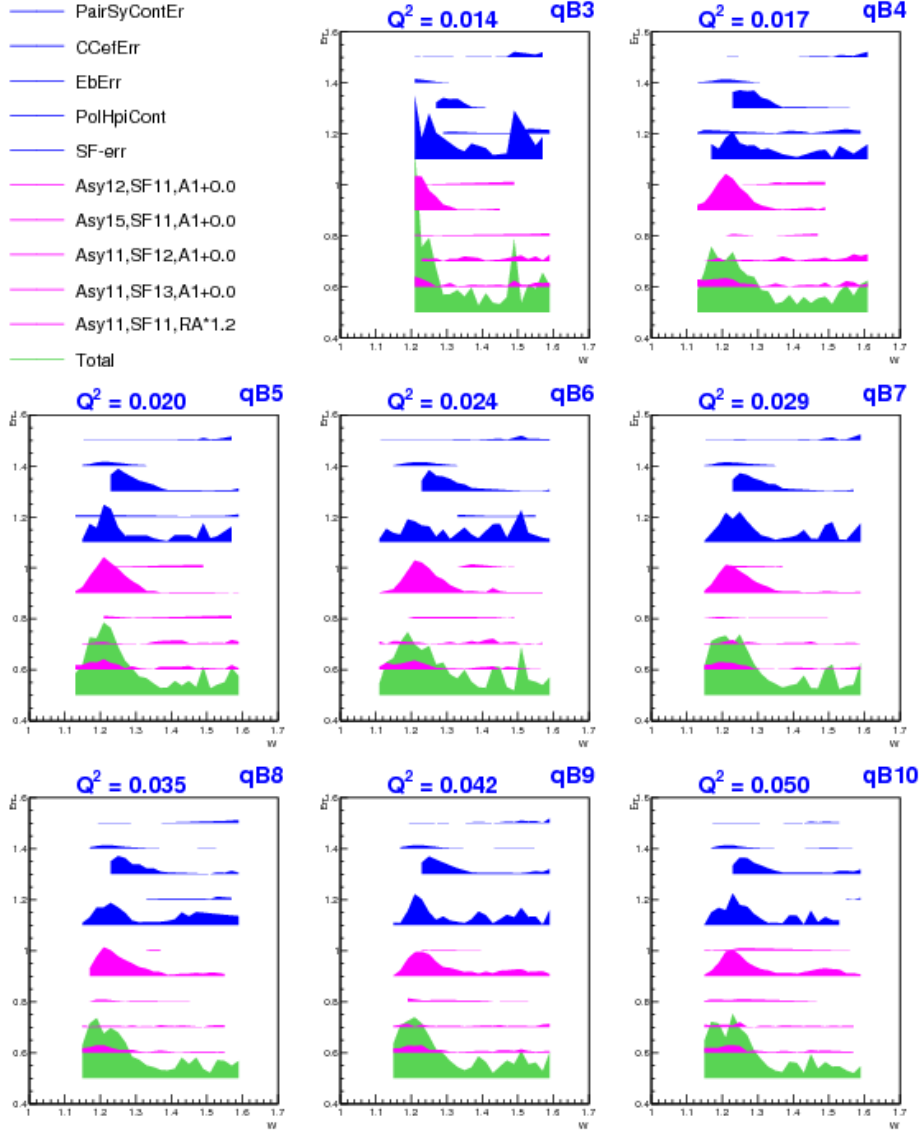


**Figure 5.2:** Plots like that shown in Fig. 5.1 showing various components of systematic uncertainty on  $g_1$  plotted against  $W$  in different  $Q^2$  bins for 1.3 GeV data.

1827

them with statistical weights as follows:

$$Sum1 = \sum_i \frac{g_1(i)}{(\Delta g_1)^2(i)} \quad (5.12)$$

$$Sum2 = \sum_i \frac{1}{(\Delta g_1)^2(i)} \quad (5.13)$$

$$g_1(\text{combined}) = Sum1 / Sum2 \quad (5.14)$$

$$\sigma g_1(\text{combined}) = \sqrt{1/Sum2} \quad (5.15)$$

1828 where the index 'i' represents two beam energy (1.3 and 2.0 GeV)  
 1829 data sets. and  $\Delta g_1$  indicates the statistical uncertainty in  $g_1$ .

1830 3. In principle, each of the individual contributions to the systematic un-  
 1831 certainty can also be combined using the same equations. However,  
 1832 we must be careful to distinguish between correlated and uncorrelated  
 1833 uncertainties.

1834 (a) The variations due to scale factor ( $k=1$ ), beam energy ( $k=3$ ) and  
 1835 CC-efficiency ( $k=4$ ) are all un-correlated and, therefore, added in  
 1836 quadrature as follows:

$$\delta g_1(k=8,10,11, \text{combined}) = \sqrt{\left( \sum_i \frac{(\delta g_1)^2(i)}{(\Delta g_1)^2(i)} \right) / \text{Sum2}} \quad (5.16)$$

1837 where,  $\delta$  represents the  $k^{th}$  component of the systematic uncer-  
 1838 tainty, whereas, 'Sum2', 'i' and  $\Delta$  have the same meanings as  
 1839 before.

1840 (b) while all other variations are correlated between the two beam  
 1841 energies and should be averaged linearly (WITH sign):

$$\delta g_1(\text{other } k, \text{combined}) = \left( \sum_i \frac{(\delta g_1)(i)}{(\Delta g_1)^2(i)} \right) / \text{Sum2} \quad (5.17)$$

1842 4. Once each of the  $k^{th}$  component of the systematic uncertainties are  
 1843 combined between the two beam energies, we then proceed to combine  
 1844 them all to get a grand total. This is done by simply adding the  
 1845 ten combined systematic uncertainties in quadrature and taking the  
 1846 square-root of the sum.

1847 The figures 5.6 and 5.8 show the breakdown of the total contribution to  
 1848 the systematic uncertainty from different sources. We can see that the dom-  
 1849 inant contribution comes from the uncertainties in the overall scale factor  
 1850 (the cyan band indicated with SF-err in the legend) which is used to normal-  
 1851 ize the simulated data to make them comparable with data. One of the big  
 1852 part of this uncertainty comes from those in  $P_b P_t$  and target size measure-  
 1853 ments. Next big contributions seem to come from the model (in particular

1854 the model for the unmeasured  $A_2$ ) and radiative corrections. Near the  $\Delta$ -  
1855 resonance region, the effect of beam energy uncertainty also seems to be very  
1856 pronounced. The breakdown of the different components (but combined be-  
1857 tween the two beam energies) of the total systematic uncertainties are also  
1858 shown separately in the figures 5.6 and 5.8

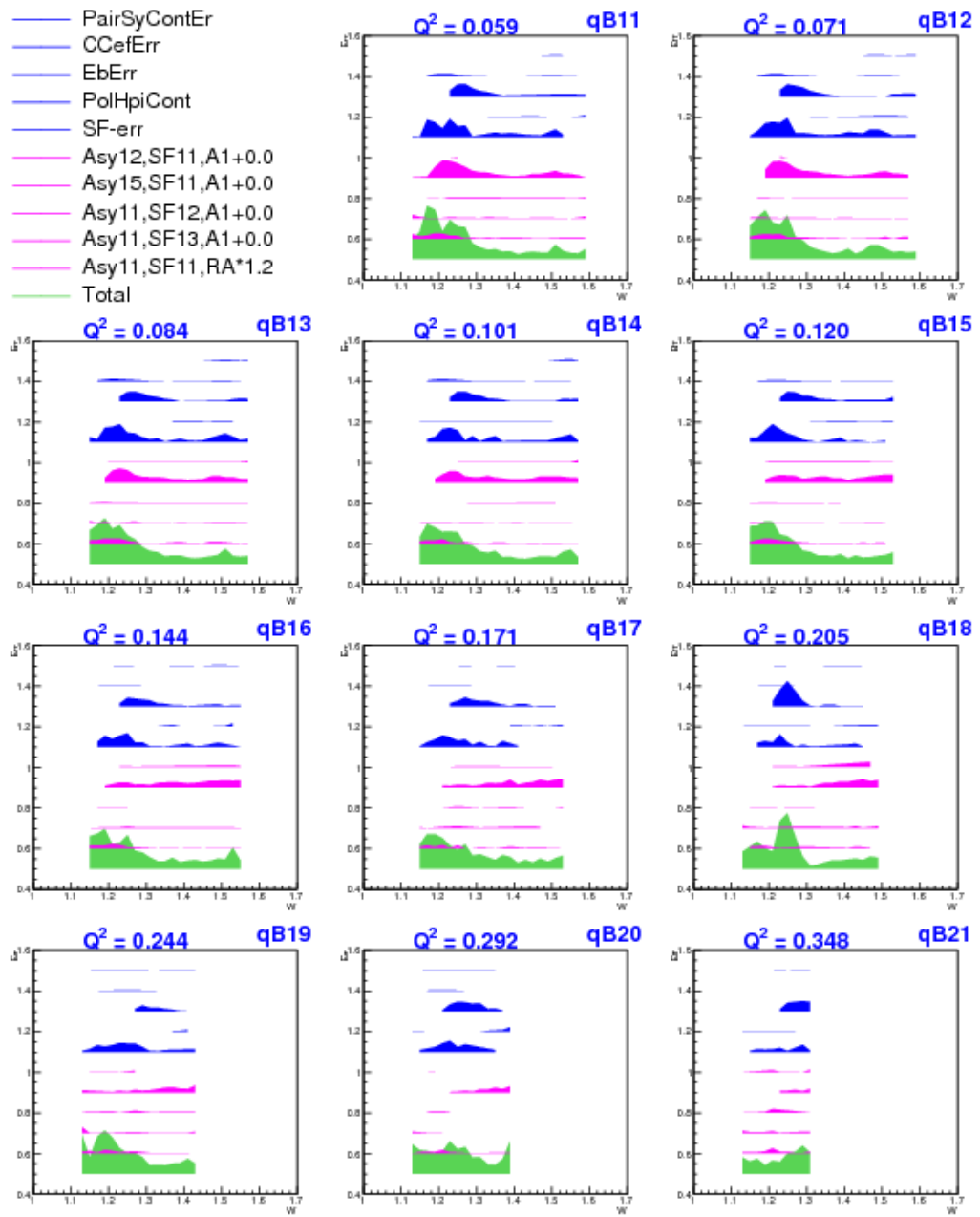


**Figure 5.3:** Systematic uncertainty components in remaining  $Q^2$  bins (continuation of Fig. 5.2).

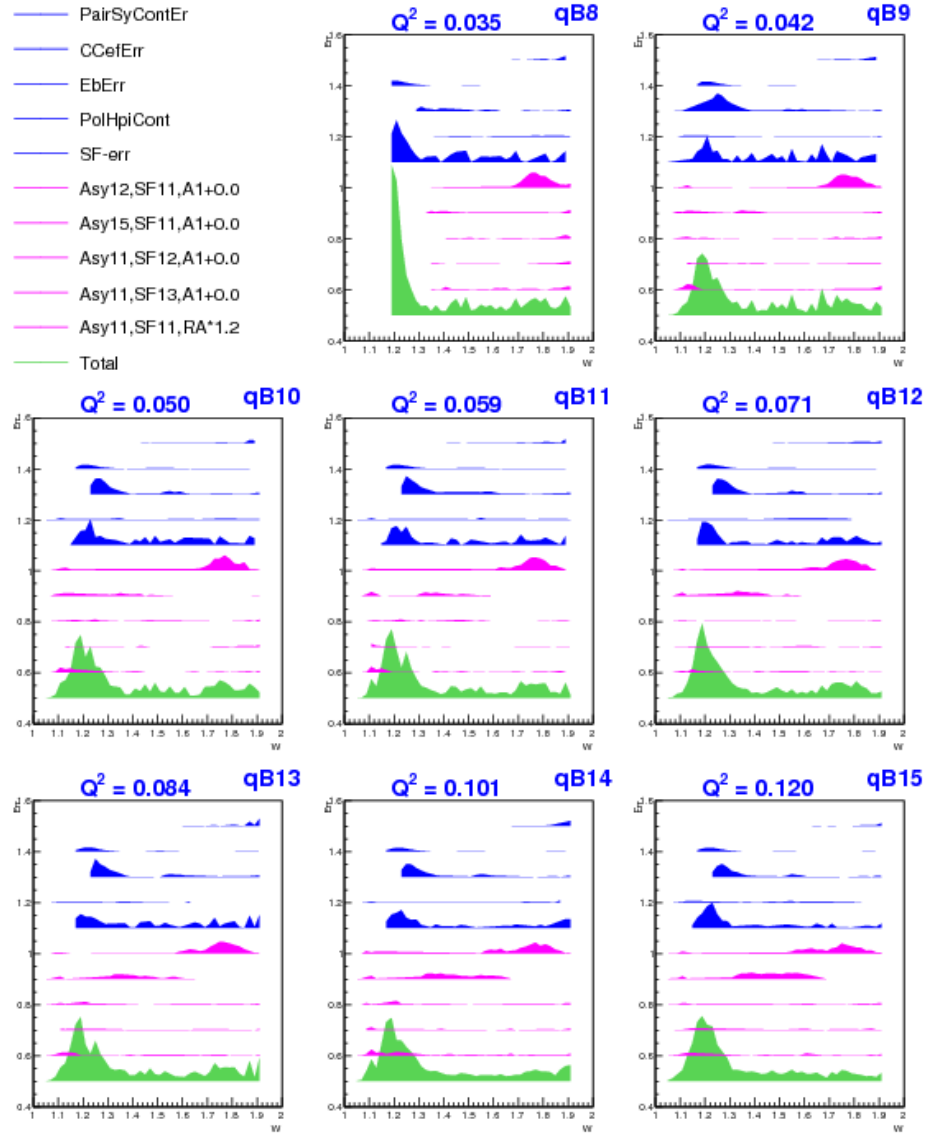


**Figure 5.4:** Plots similar to those shown in Fig. 5.2 but for 2.0 GeV, showing various components of systematic uncertainty on  $g_1$  plotted against  $W$  in different  $Q^2$  bins.

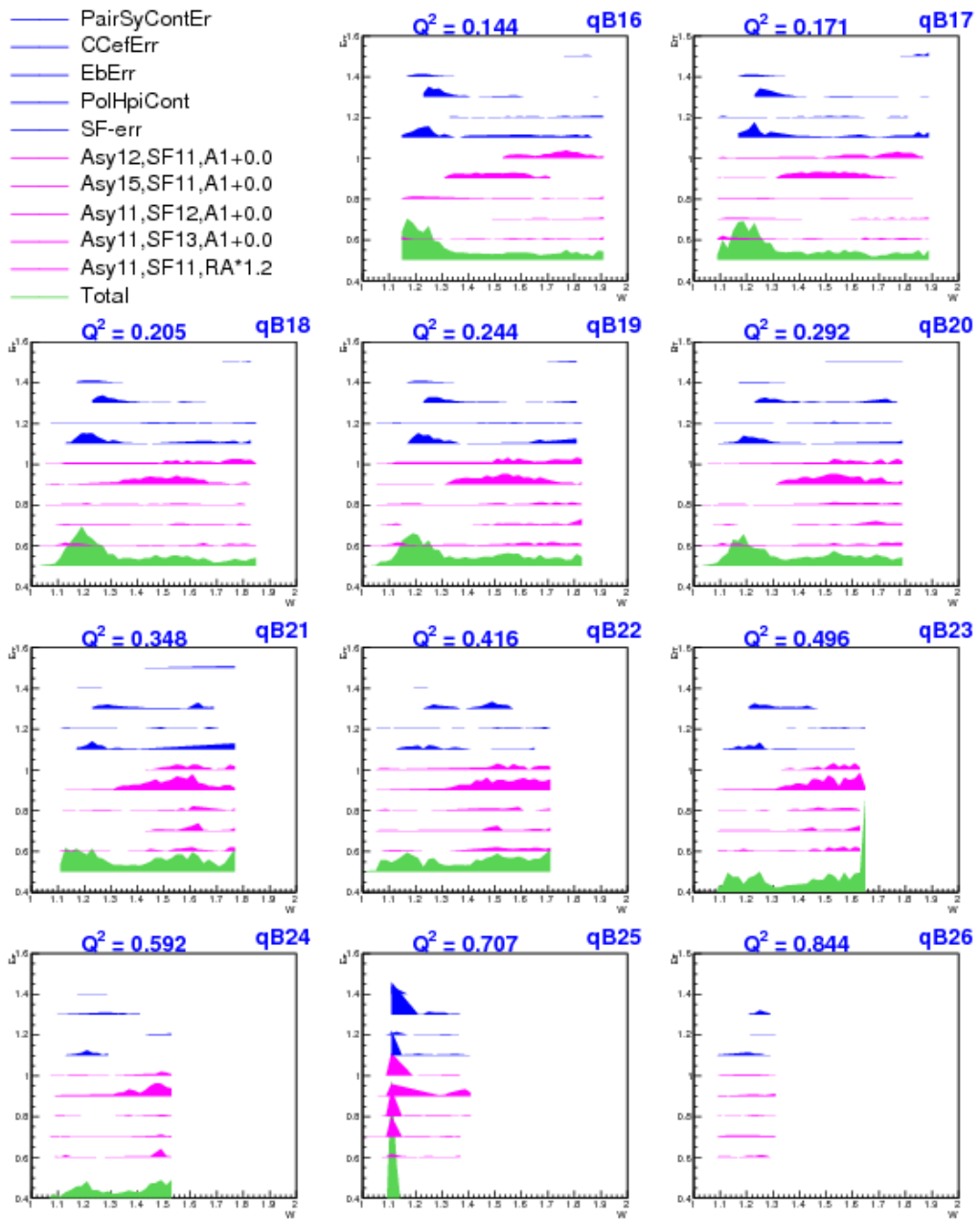


**Figure 5.5:** Systematic uncertainty components in remaining  $Q^2$  bins (continuation of Fig. 5.4).

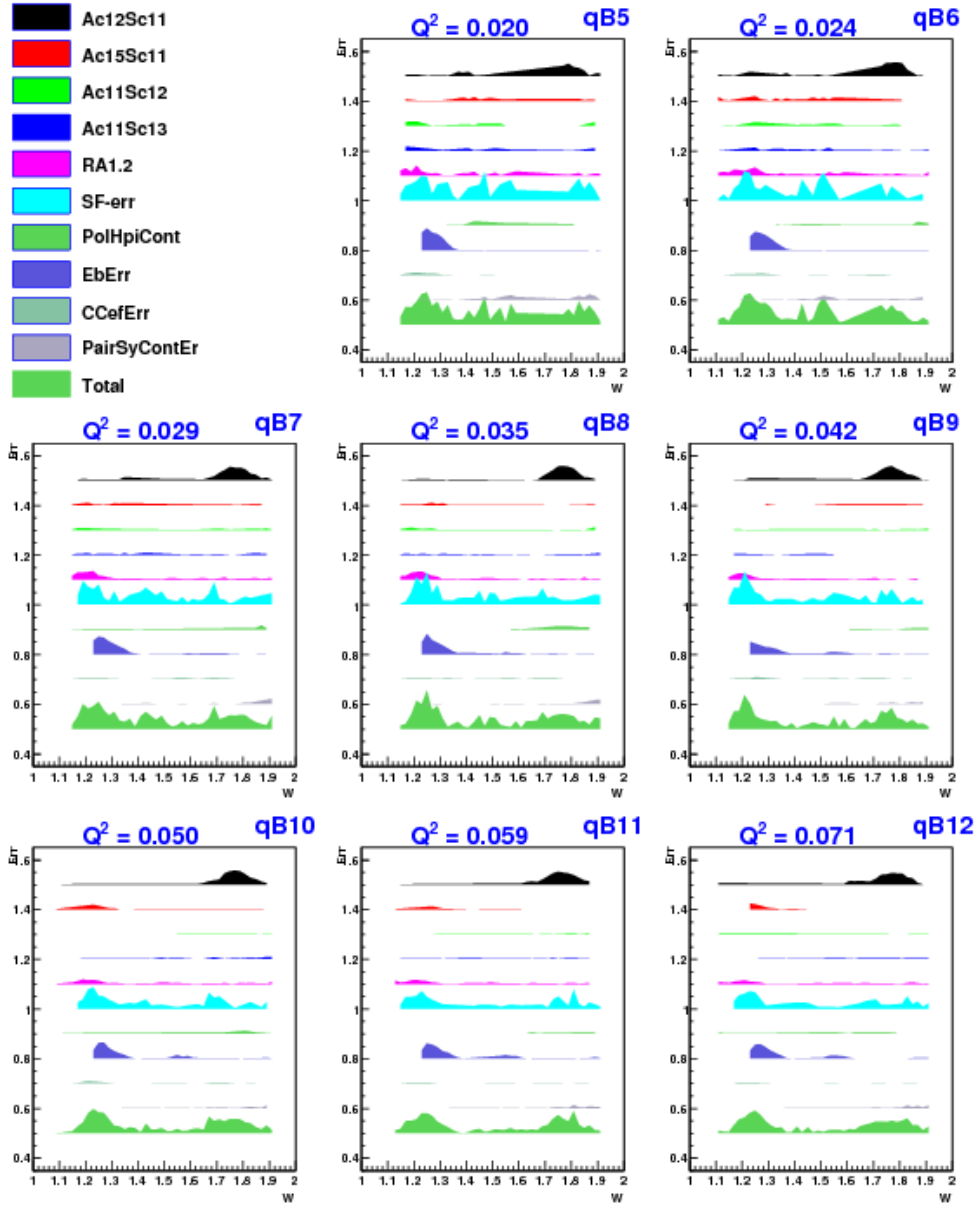


**Figure 5.6:** Breakdown of systematic uncertainties in  $g_1$  (after combining data from the two energy data sets) in the first few  $Q^2$  bins. See Fig. 5.1 for the description of the different systematic uncertainty components.

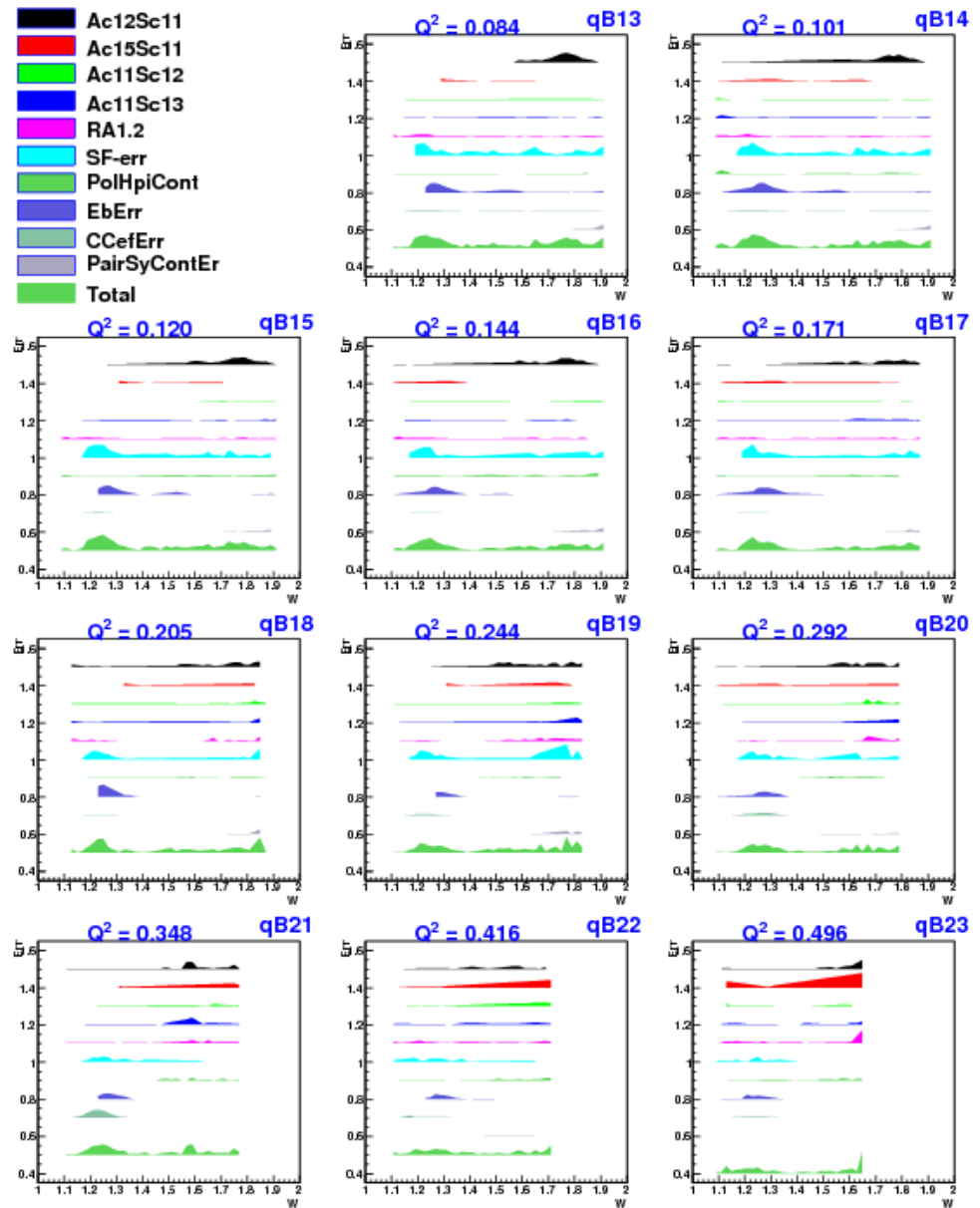


**Figure 5.7:** Plots as in Fig. 5.6 but in the remaining higher  $Q^2$  bins.

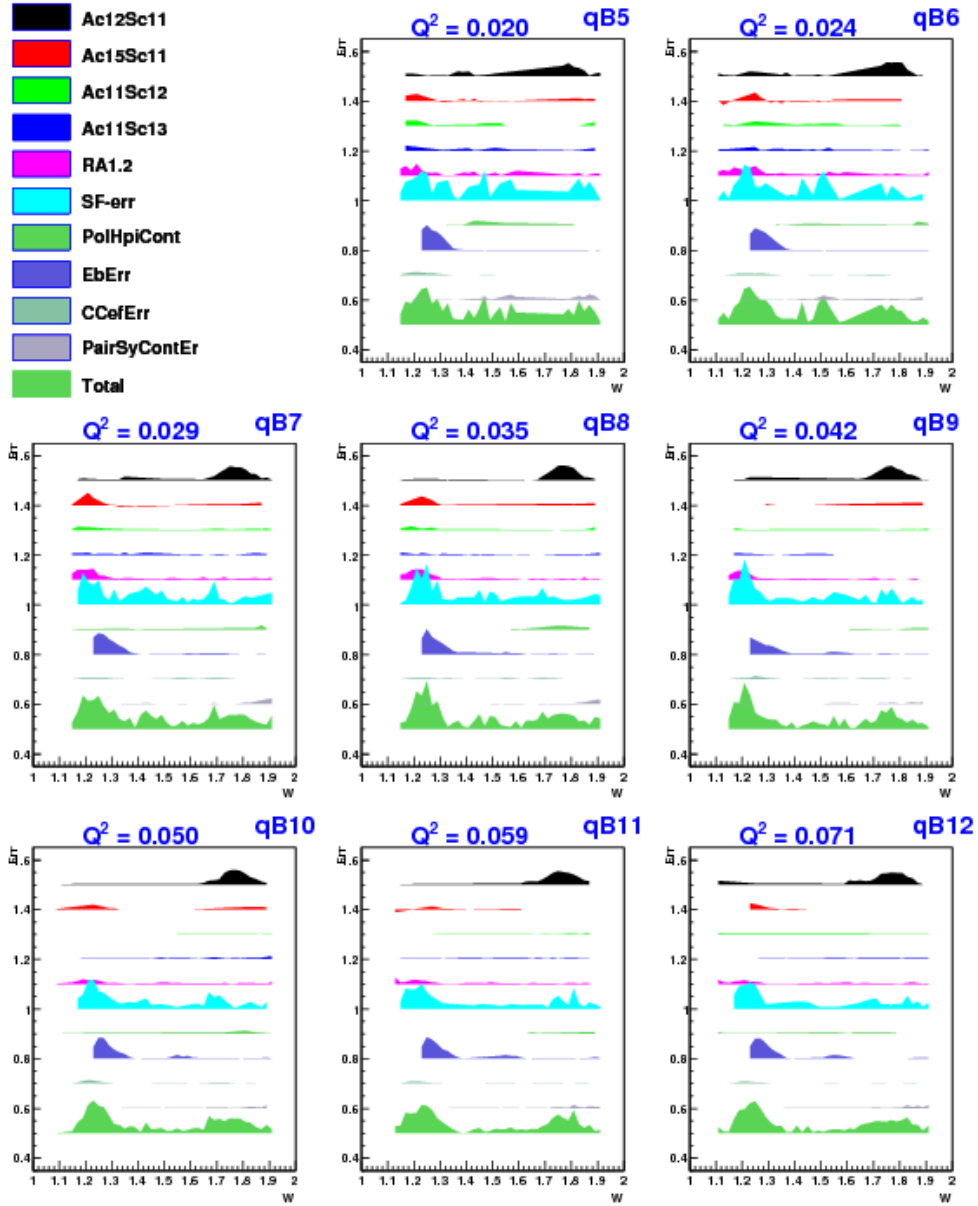


**Figure 5.8:** Breakdown of systematic uncertainties in  $A_1 F_1$  (after combining data from the two energy data sets) in the first few  $Q^2$  bins. See Fig. 5.1 for the description of the different systematic uncertainty components.

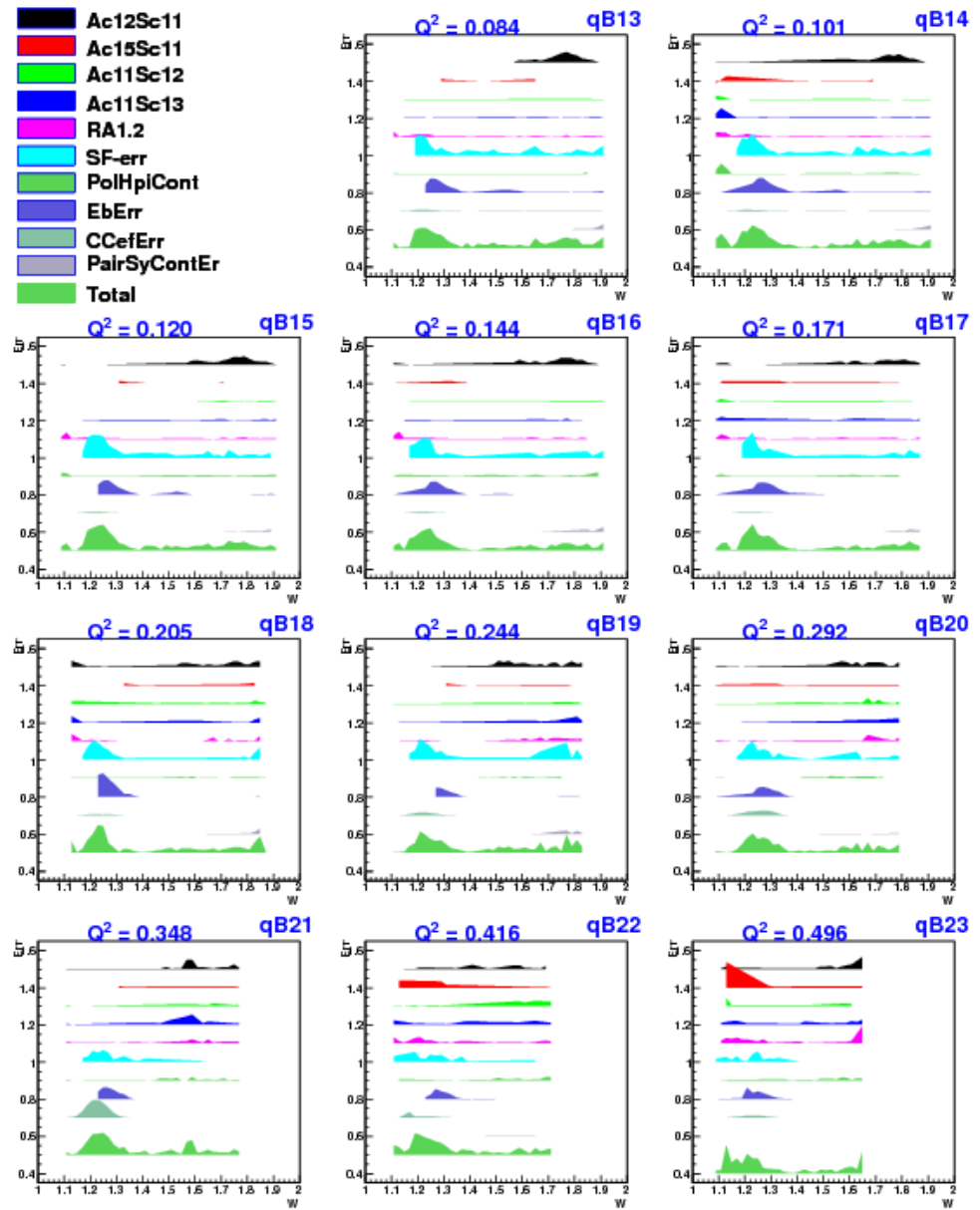


**Figure 5.9:** Plots as in Fig. 5.8 but in the remaining higher  $Q^2$  bins.

1859 **Chapter 6**

1860 **Results**

1861 Two quantities -  $g_1$  and  $A_1 F_1$  and their uncertainties were extracted from the  
1862 EG4 deuteron target data using the methods outlined in the previous chapter.  
1863 This was done in each of 21  $Q^2$  bins (between about 0.02 and 0.7 GeV $^2$  in  
1864  $Q^2$ ) and several  $W$  bins of size 20 MeV each. In the overlapping kinematic  
1865 bins where both beam energy data sets contributed, the results were further  
1866 combined individually to arrive at a single set of energy independent data  
1867 points. Finally, within each  $Q^2$  bin, the newly extracted  $g_1$  and  $A_1 F_1$  values  
1868 were used to evaluate three different integrals -  $\Gamma_1^d$ ,  $\bar{I}_{TT}$ , and  $\gamma_0^d$ . All of these  
1869 results are presented in the sections below.

1870 **6.1 Extracted  $g_1$  and  $A_1 F_1$**

1871 Figures 6.1 and 6.2 show the extracted values of  $g_1$  and their errors from  
1872 two different beam energies (1.337 GeV and 1.989 GeV). It can be seen that  
1873 the two energies give results that are in good agreement (in the overlapping  
1874 kinematic regions).

1875 These results from low  $Q^2$  measurements clearly show the resonant struc-  
1876 ture in the region  $W \leq 2.0$ . Especially, the  $\Delta$ -resonance stands out through  
1877 its strongly negative signal. In addition, in the second resonance region  
1878 around  $W=1.5$  GeV where  $N^*(1520)$  and  $N^*(1535)$  (also denoted by  $D_{11}$   
1879 and  $S_{13}$  respectively) overlap, we see a drastic transition of  $g_1$  (or cross sec-  
1880 tion) from strongly negative values (not well described by the model because  
1881 it is unconstrained there due to the lack of experimental data) at low  $Q^2$   
1882 to clearly positive values at high  $Q^2$  indicating that the dominance of the

1883 spin-flip helicity amplitude  $A_{\frac{3}{2}}^T$  on cross section drastically diminishes with  
1884  $Q^2$  and the non-flip amplitude  $A_{\frac{1}{2}}^T$  becomes stronger<sup>1</sup>. We have pushed the  
1885 lower limit on  $Q^2$  in the resonance region with reduced systematic and sta-  
1886 tistical errors that will contribute greatly to the world data set. Our data  
1887 will help MAID and other phenomenological models to better constrain their  
1888 parameters enabling them to make better predictions in the future.

---

<sup>1</sup>The four virtual photoabsorption cross sections  $\sigma_T$ ,  $\sigma_L$ ,  $\sigma_{LT}$ , and  $\sigma_{TT}$ , are related to the four structure functions  $F_1$ ,  $F_2$ ,  $g_1$  and  $g_2$  of the target and as a result,  $g_1$  can be expressed as  $g_1 = \frac{MK}{8\pi^2\alpha(1+\gamma^2)}(\sigma_{\frac{1}{2}}^T - \sigma_{\frac{3}{2}}^T + 2\gamma\sigma_{LT})$

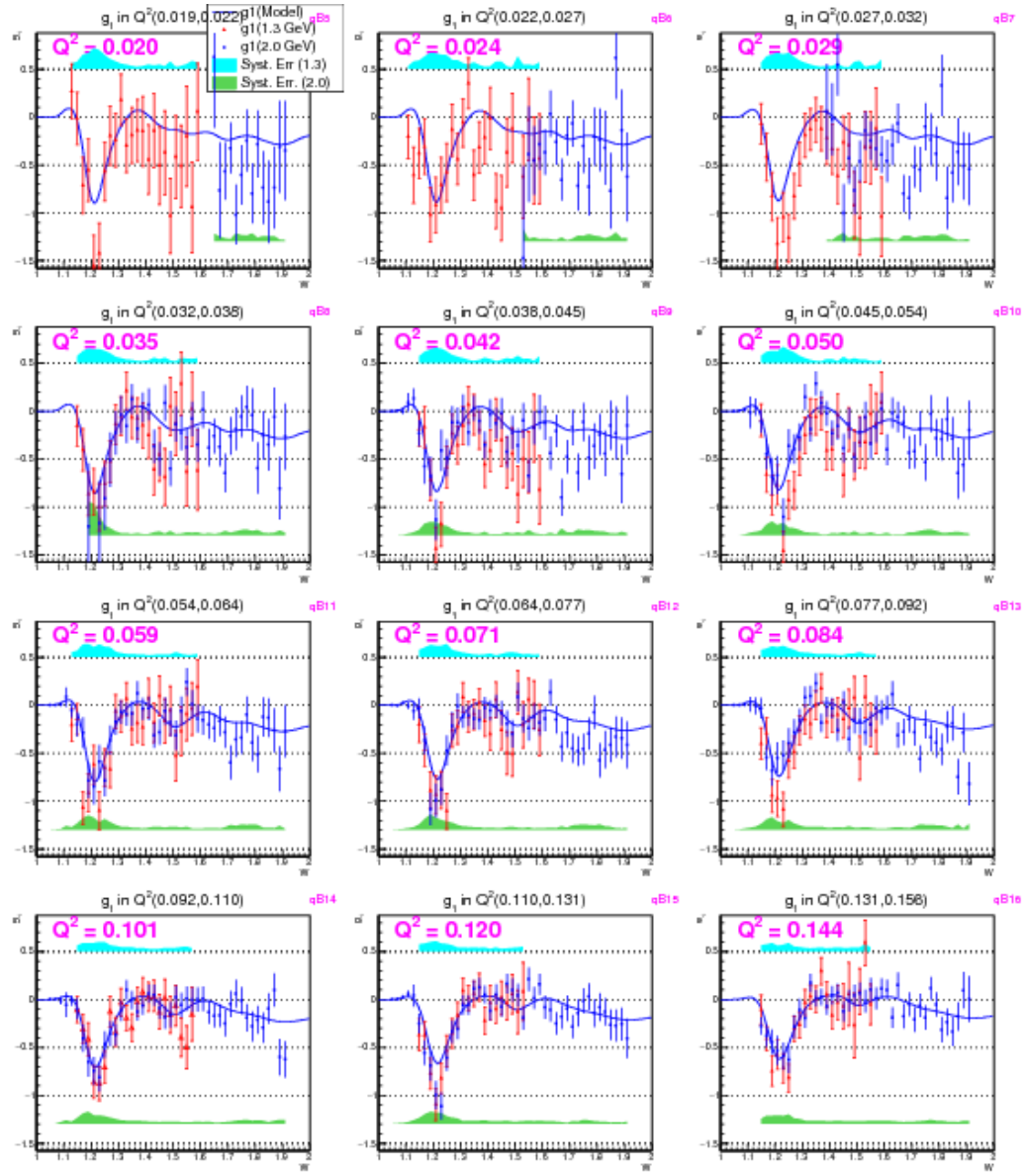


**Figure 6.1:** Extracted  $g_1$  for deuteron (in the first 12  $Q^2$  bins) from the two different beam energy data sets. The statistical errors are indicated by error bars, while the systematic uncertainties are given by the bands (cyan, top: 1.3 GeV and green, bottom: 2 GeV).

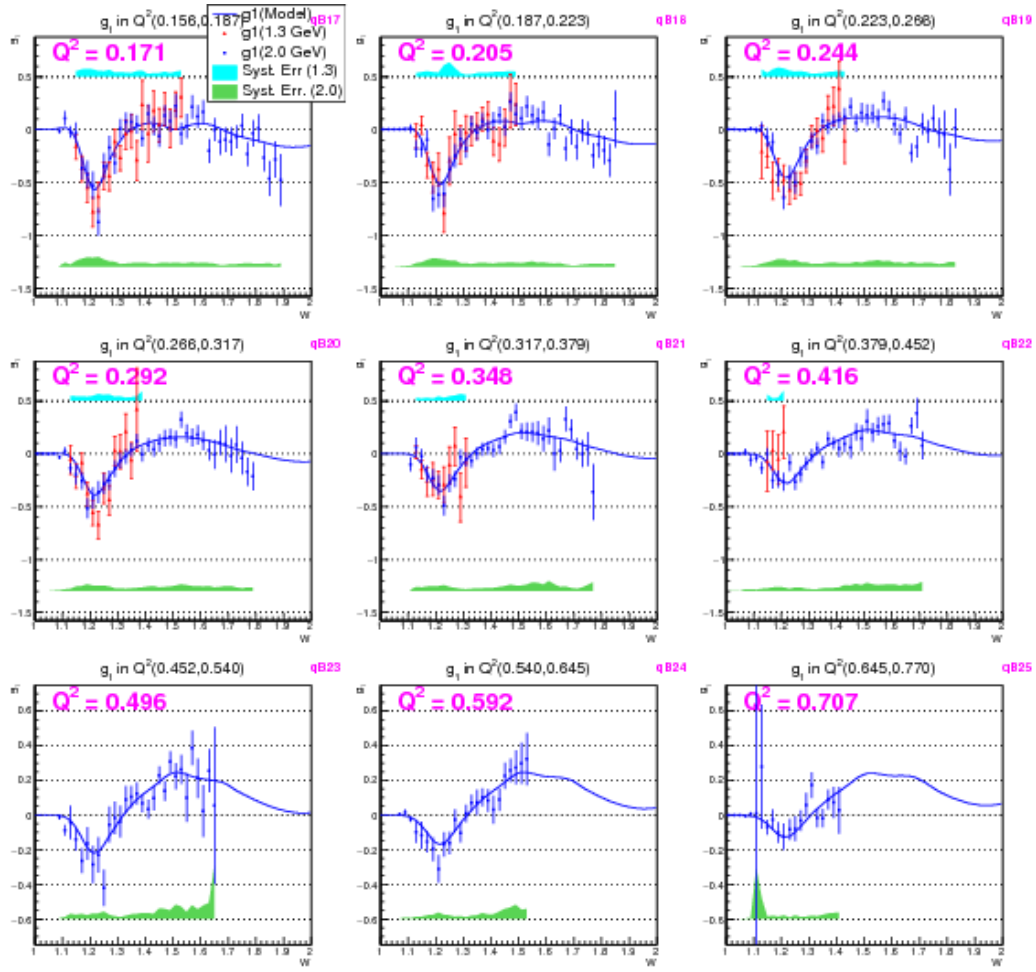


**Figure 6.2:** Extracted  $g_1$  for deuteron (in the last 9  $Q^2$  bins (see Fig. 6.1 for the first 12 bins)) from the two different beam energy data sets.

1889 Likewise, Figs. 6.3 and 6.4 shows the extracted values of  $A_1 F_1$  and their  
1890 errors from two different beam energies (1.337 GeV and 1.989 GeV). These  
1891 values also show similar behavior as  $g_1$ .

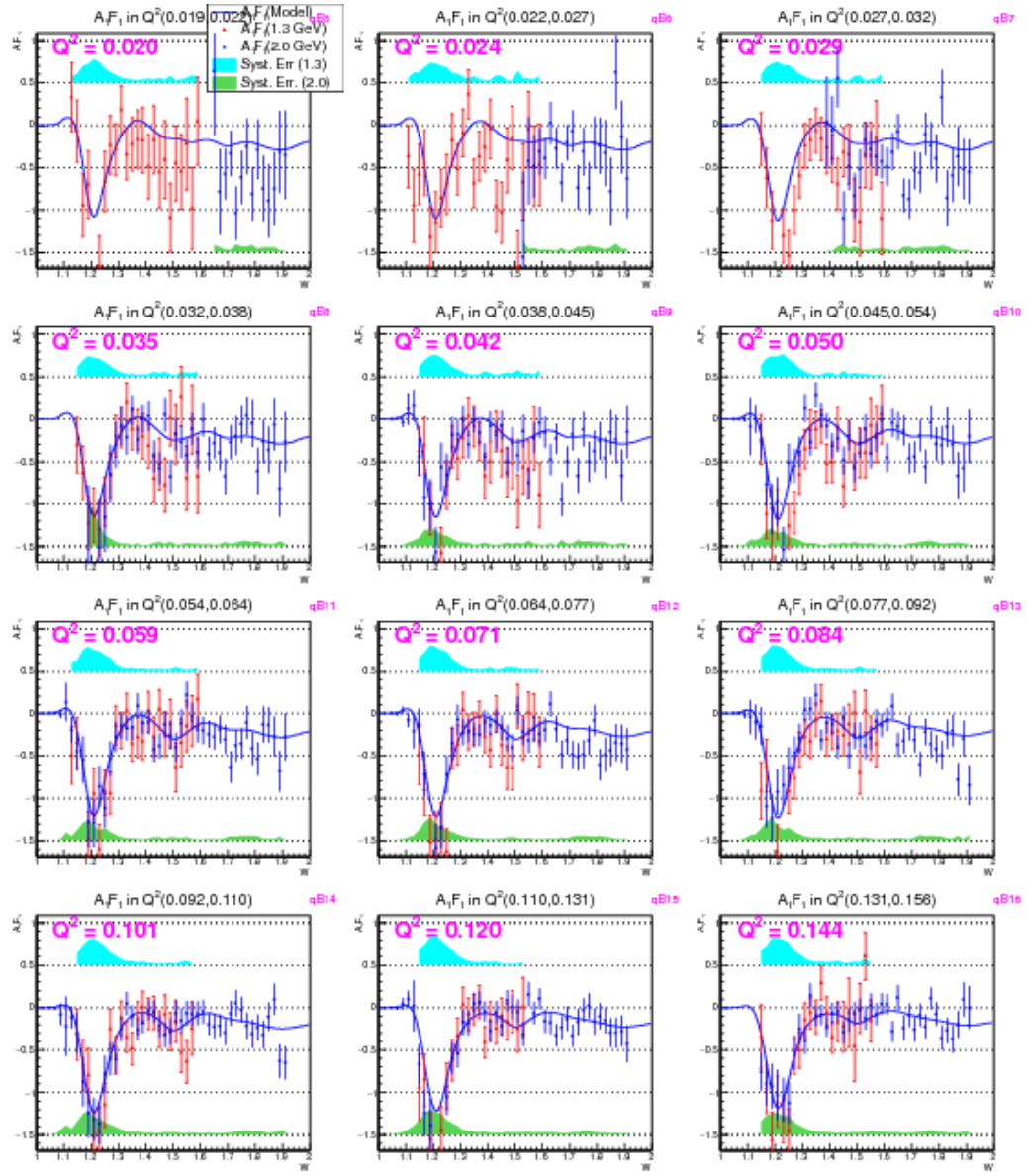


**Figure 6.3:** Extracted  $A_1 F_1$  for deuteron (in the first 12  $Q^2$  bins) from the two different beam energy data sets. The statistical errors are indicated by error bars, while the systematic uncertainties are given by the bands (cyan, top: 1.3 GeV and green, bottom: 2 GeV).

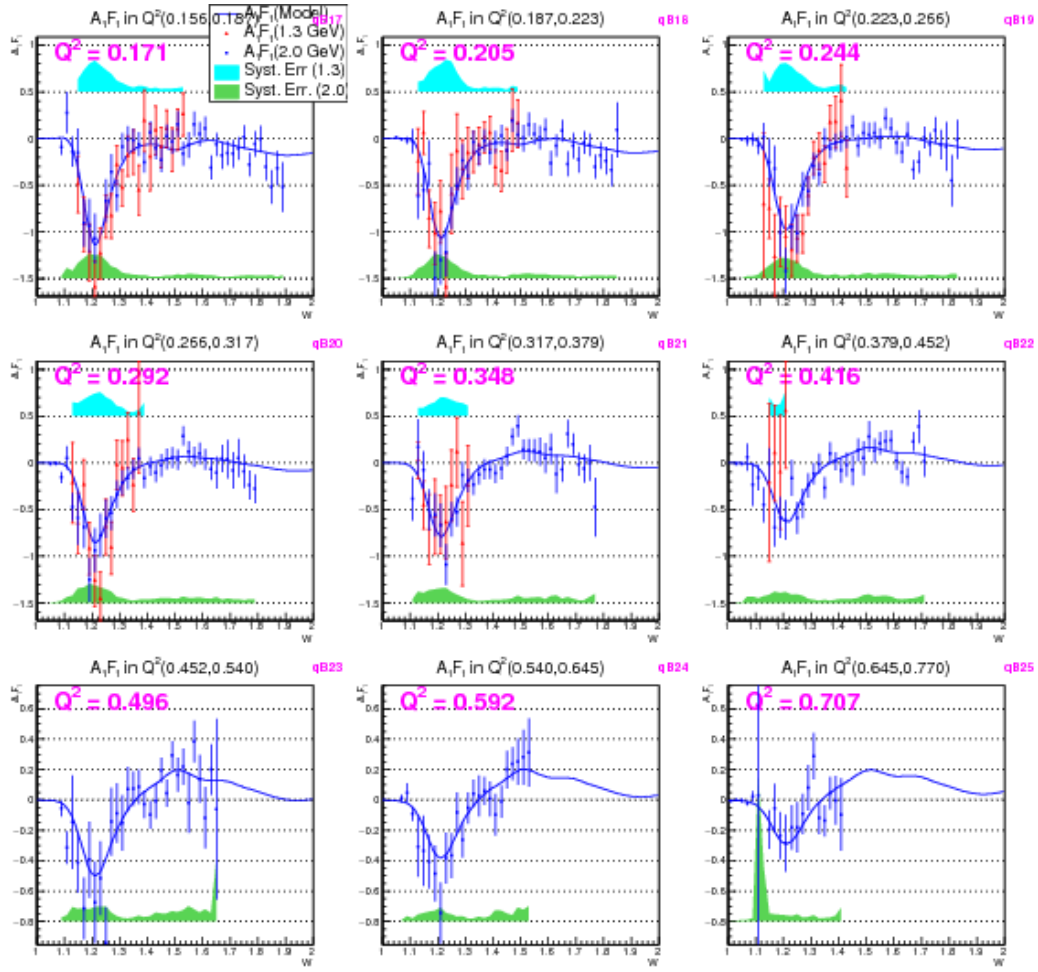


**Figure 6.4:** Extracted  $A_1 F_1$  for deuteron (in the last 9  $Q^2$  bins (see Fig. 6.3 for the first 12 bins)) from the two different beam energy data sets..

1892 Figs. 6.5, 6.6, 6.7 and 6.8 show the values of  $g_1$  and  $A_1 F_1$  and their  
1893 errors after combining the corresponding results from the two different beam  
1894 energies as described in the previous chapter.

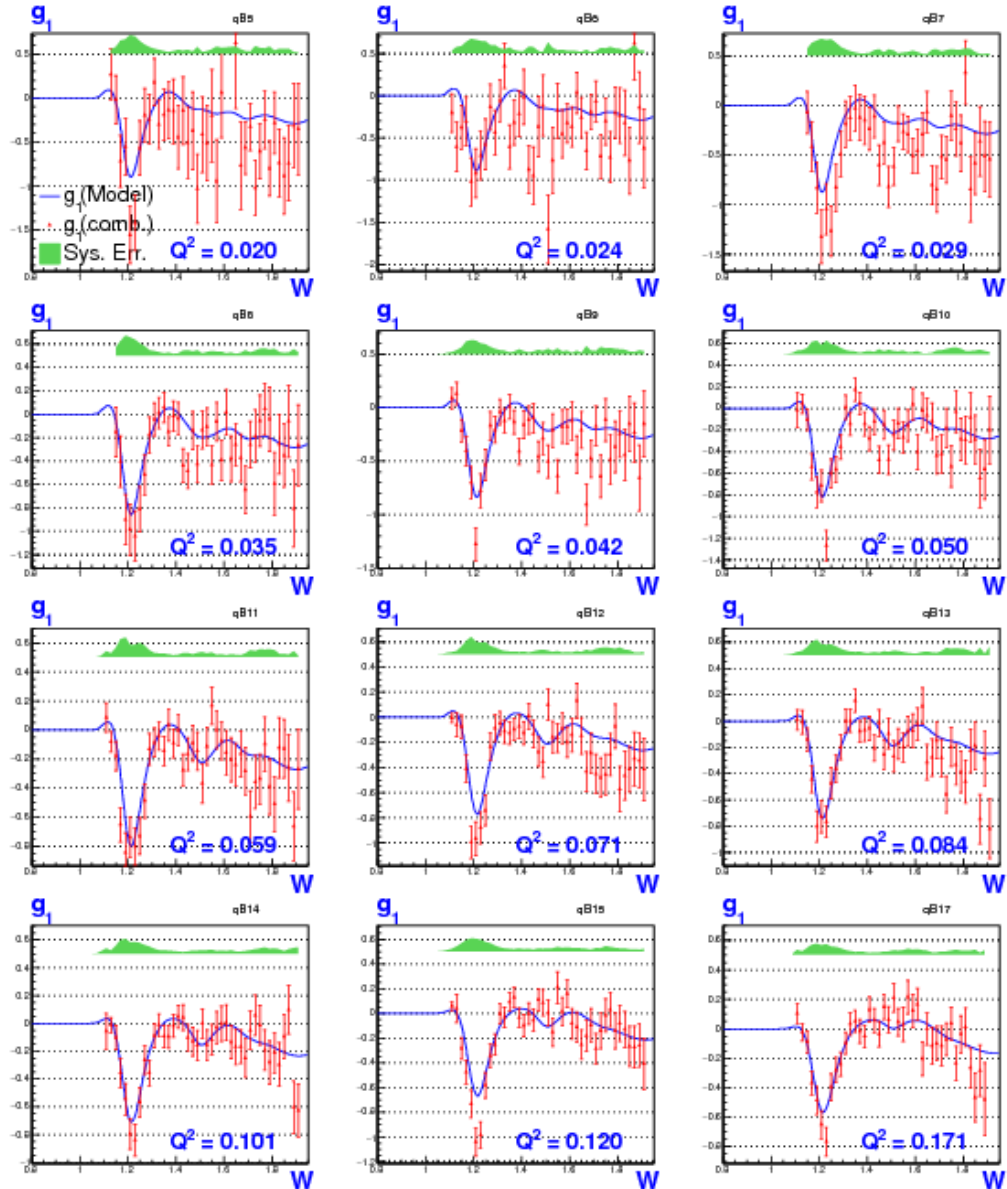


**Figure 6.5:** Extracted  $g_1$  for deuteron after combining the results from the two beam energies (in the first 12  $Q^2$  bins). The red data points with error bars in each of the panels are the combined extracted results, the blue continuous line is the used model of  $g_1$  and the green band represents the corresponding total systematic errors.

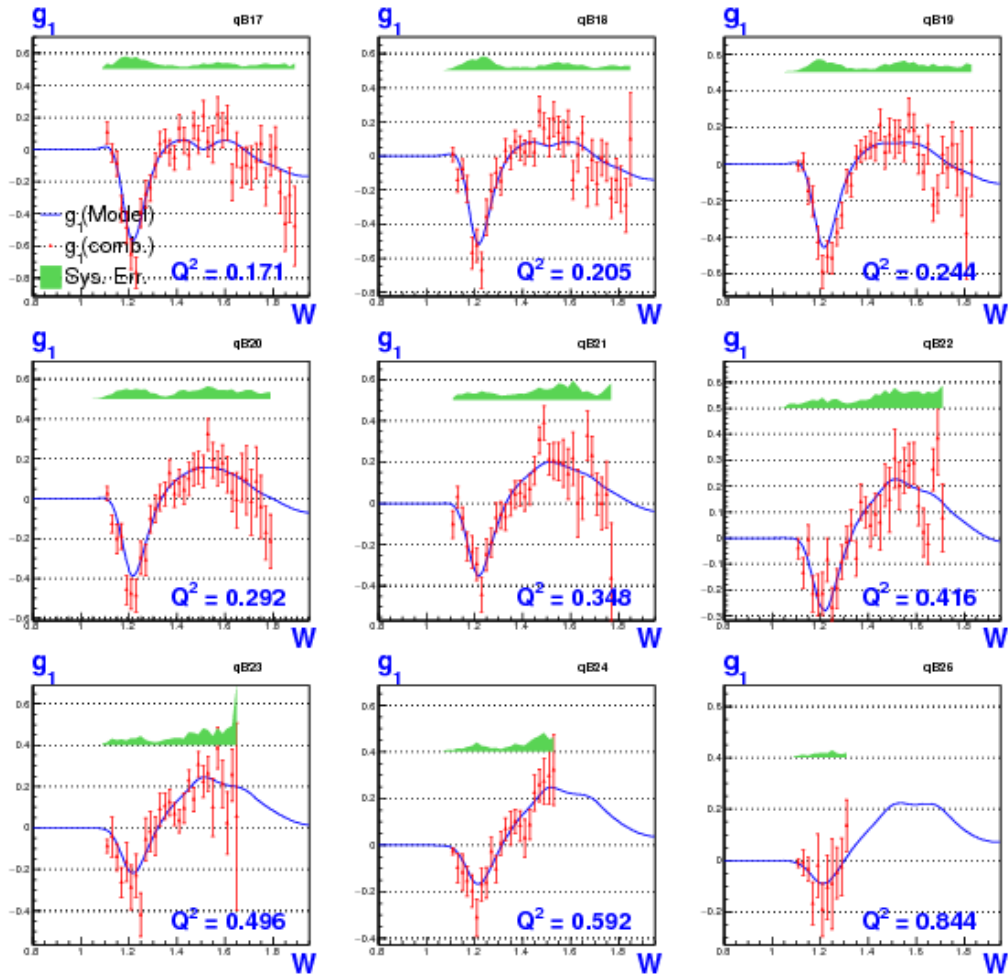


**Figure 6.6:** Similar plots as in Fig. 6.5 showing the combined results on  $g_1$  in the next 9  $Q^2$  bins.

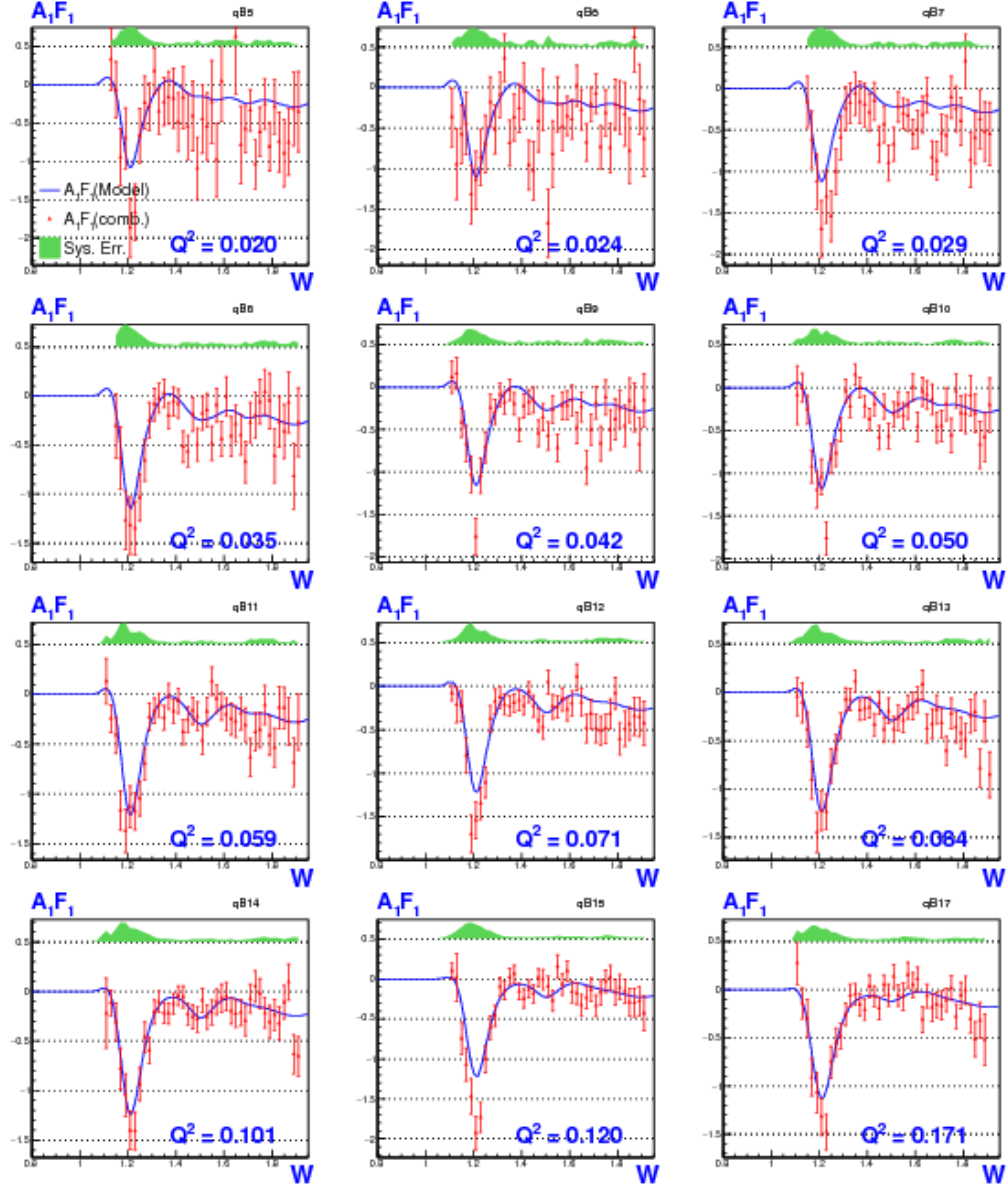


**Figure 6.7:**  $A_1 F_1$  after combining the results from the two beam energies (in the first 12  $Q^2$  bins). The red data points with error bars in each of the panels are the combined extracted results, the blue continuous line is the used model of  $g_1$  and the green band represents the corresponding total systematic errors.

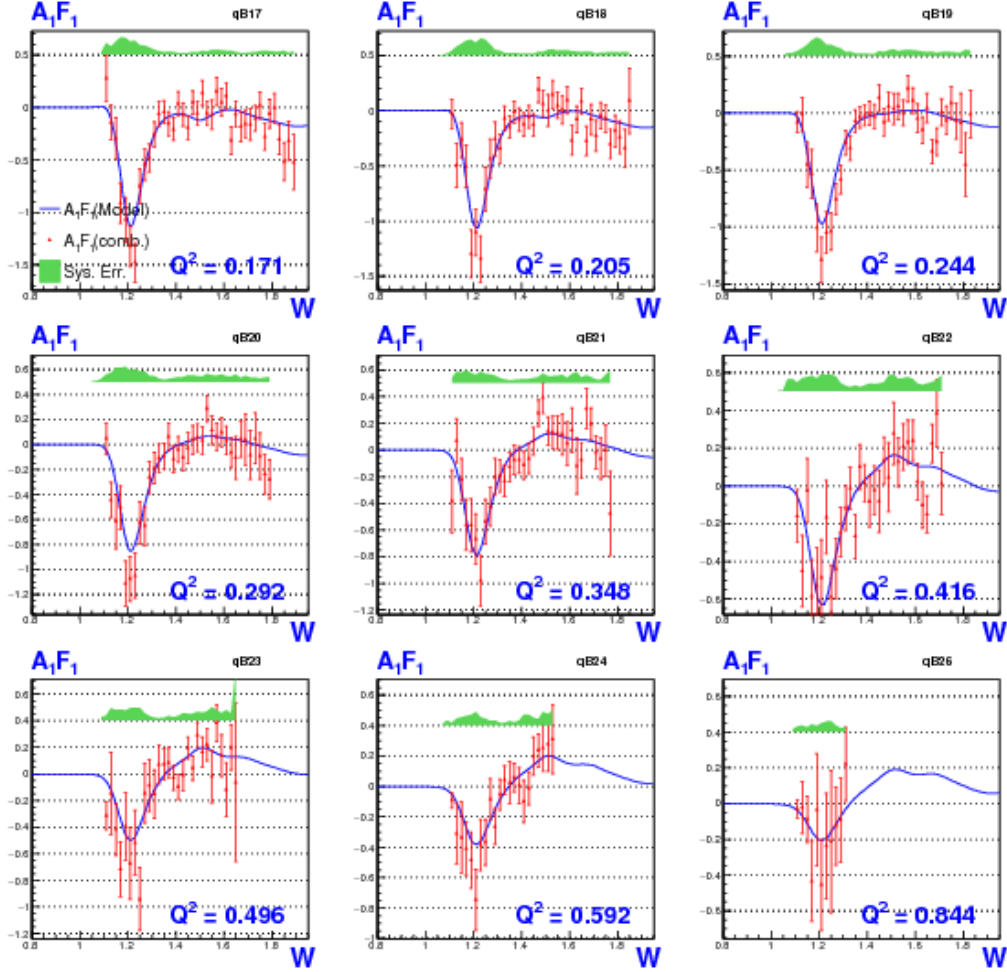


**Figure 6.8:** Similar plots as in Fig. 6.7 showing the combined results on  $g_1$  in the next 9  $Q^2$  bins.

## 1895      6.2 Moments of Deuteron Spin Structure func- 1896      tions

1897      Using the measured values of  $g_1$  and  $A_1F_1$ , three integrals were evaluated for  
 1898      each of the  $Q^2$  bins in which these data were measured. These integrals have  
 1899      been calculated in two ways - using only the new EG4 measurements, and  
 1900      adding model contributions to the data for regions not covered by our mea-

surements. The integrals with the model contributions were calculated from  $x = 0.001$  to the onset of the resonance region (i.e. to the pion production threshold of  $W \approx 1.08$  GeV), dividing the sum into three parts for each  $Q^2$  bin. For example,  $\Gamma_1$  was evaluated by adding up the product  $g_1 \Delta x$  over the following three kinematic regions:

$$\Gamma_1(Q^2) = \int_{x=0.001}^{x(W_{data})} g_1(x, Q^2) dx \quad \text{model} \quad (6.1)$$

$$+ \int_{x(W_{data})}^{W=1.15} g_1(x, Q^2) dx \quad \text{data (or model for gaps)} \quad (6.2)$$

$$+ \int_{W=1.15}^{W=1.08} g_1(x, Q^2) dx \quad \text{model} \quad (6.3)$$

where  $W_{data}$  indicates the upper edge of the last  $W$  bin in which the EG4 data is available in a given  $Q^2$  bin (the  $W$  variable was divided into 70 bins of size 20 MeV in the range  $W=(0.7,2.1)$  GeV). The first part of the integral as given by Eq. 6.1 is evaluated by using the model values of  $g_1$  and using  $\Delta x$  corresponding to a  $W$  bin of size 10.0 MeV (The  $\Delta W$  is converted to  $\Delta x$  by using  $x = Q^2/(Q^2 + W^2 - M^2)$  to evaluate  $x$  at the two edges of each  $W$  bin and taking the difference.). The second part given by Eq. 6.2 is evaluated similarly but using the EG4 results for  $g_1$  if there is no measurement gap in between. If there is any gap, the same method as in the first part is used to get a model contribution for the gap and added to the data contribution. Lastly, the the third contribution given by Eq. 6.2 again were evaluated from model values (quasi-elastic part turned off from the model in all of these cases) but with finer  $W$  bins (1 MeV) because the integrals are very sensitive to the region near the  $\Delta$  resonance due to the fact that the structure functions show rapid changes in this region. The reason to calculate the third integral using model values rather than data values is to avoid having contributions in the integrals from the quasi-elastic contamination.

The statistical errors are evaluated by adding the statistical error contribution in each  $W$  or  $x$  bin in quadrature. For example, if the integral is evaluated in a  $Q^2$  bin by calculating the sum  $\left( \sum_{W \text{ bins}} g_1 \cdot \Delta x \right)$ , then the corresponding statistical error is evaluated by calculating  $\sqrt{\sum_{W \text{ bins}} (\sigma g_1)^2 \cdot \Delta x}$ . Because the model contribution is assumed to have no statistical uncertainties, the statistical errors in the integrals come solely from the propagation

<sup>1929</sup> of the statistical error of the measured  $g_1$  or  $A_1 F_1$ .

<sup>1930</sup> The other two integrals and their errors are evaluated in the same manner,  
<sup>1931</sup> with  $g_1$  replaced by their corresponding integrands and again calculating the  
<sup>1932</sup> three parts of the integrals separately.

<sup>1933</sup> These integrals are then compared with the latest available predictions  
<sup>1934</sup> from different theories (mainly  $\chi$ PT) and phenomenological calculations along  
<sup>1935</sup> with EG1b or DIS data whenever applicable.

### <sup>1936</sup> **6.2.1 First moment of $g_1$ ( $\Gamma_1$ )**

<sup>1937</sup> The first integral of interest is the first moment of  $g_1$  i.e.,  $\Gamma_1$  (see Eq. 1.10)  
<sup>1938</sup> , which was calculated for all  $Q^2$  bins for which the new data are available.  
<sup>1939</sup> Figs. 6.9 and 6.10 show the two calculations (with and without model in-  
<sup>1940</sup> put) along with EG1b data and several  $\chi$ PT and model predictions. One  
<sup>1941</sup> important observation here is that our measurements provide the only data  
<sup>1942</sup> points in the very low  $Q^2$  region (i.e for  $Q^2 < 0.05 \text{ GeV}^2$ ) where  $\chi$ PT is  
<sup>1943</sup> thought to be able to make rigorous calculations. Therefore, our data will  
<sup>1944</sup> provide important benchmarks for the future calculations in this kinematics.  
<sup>1945</sup> Particularly, the latest  $\chi$ PT prediction by Bernard *et al.* [53] seems to agree  
<sup>1946</sup> remarkably well in the very low  $Q^2$  region.

<sup>1947</sup> While all other higher  $Q^2$  predictions, except that of Ji *et al.*, seem to  
<sup>1948</sup> be within the uncertainties of our measurements, it can be seen that the  
<sup>1949</sup> phenomenological predictions of Soffer *et al.* compare slightly better with  
<sup>1950</sup> data than others (excluding, of course, the Bernard *et al.* prediction).

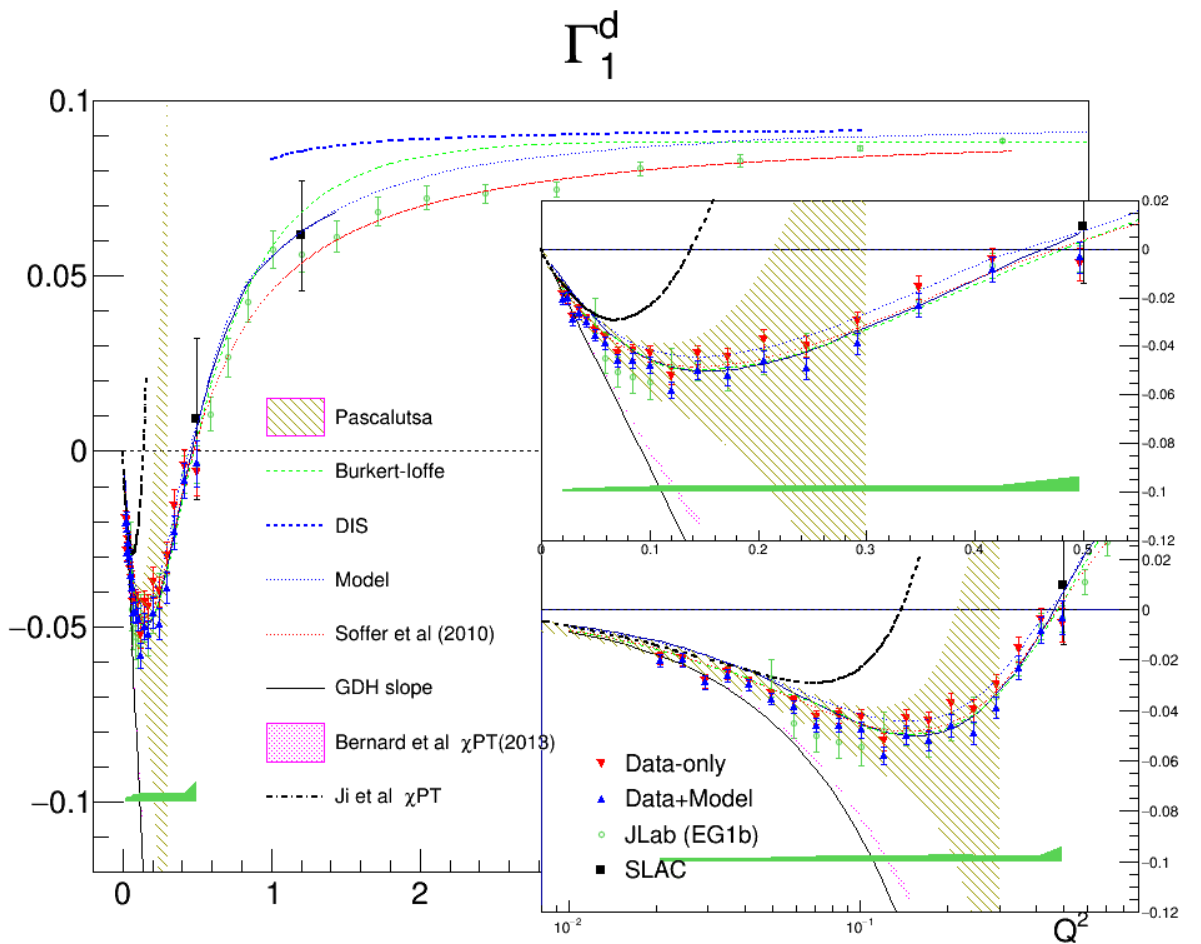


**Figure 6.9:** Extracted  $\Gamma_1$  for deuteron compared with some of the past measurements and various theoretical predictions with a linear scale used for  $Q^2$ .

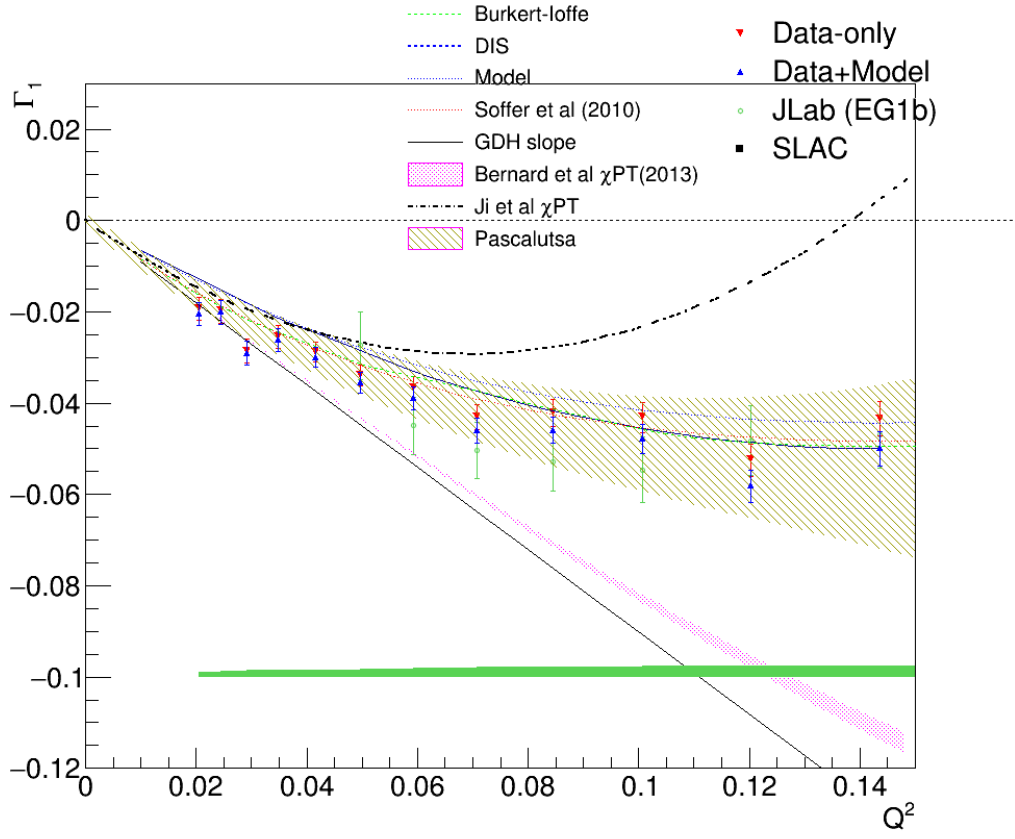


**Figure 6.10:** Extracted  $\Gamma_1$  for deuteron compared with some of the past measurements and various theoretical predictions zooming in on the very low  $Q^2$  region.

### 1951 6.2.2 The extended GDH integral $\bar{I}_{TT}$

1952 Using the measured values of  $A_1 F_1$ , the generalized GDH integral  $\bar{I}_{TT} =$   
 1953  $2M^2/Q^2 \int A_1 F_1(x, Q^2) dx$  was also calculated and compared (see Figs. 6.11  
 1954 and 6.12) with the latest  $\chi$ PT calculation from Bernard *et al.* [53]. We  
 1955 can see that at the very low  $Q^2$ , the  $\chi$ PT prediction and the measurement  
 1956 get very close. The  $\chi$ PT methods determine the higher powers of  $Q^2$  in the  
 1957 Taylor expansion of the integral around the photon point  $Q^2 = 0$ , beyond the  
 1958 prediction of the GDH sum rule which determines the lowest order term. Our  
 1959 data seem indeed to converge towards the GDH sum rule at our lowest  $Q^2$ .  
 1960 However, only one or two higher order terms can be calculated confidently,  
 1961 since higher orders require additional (unknown) constants. Therefore,  $\chi$ PT

<sup>1962</sup> predictions do reasonably well at ultra-low  $Q^2$  but cannot be expected to  
<sup>1963</sup> work at the higher  $Q^2$ , where the data show a turn-around and a transition  
<sup>1964</sup> towards positive values.

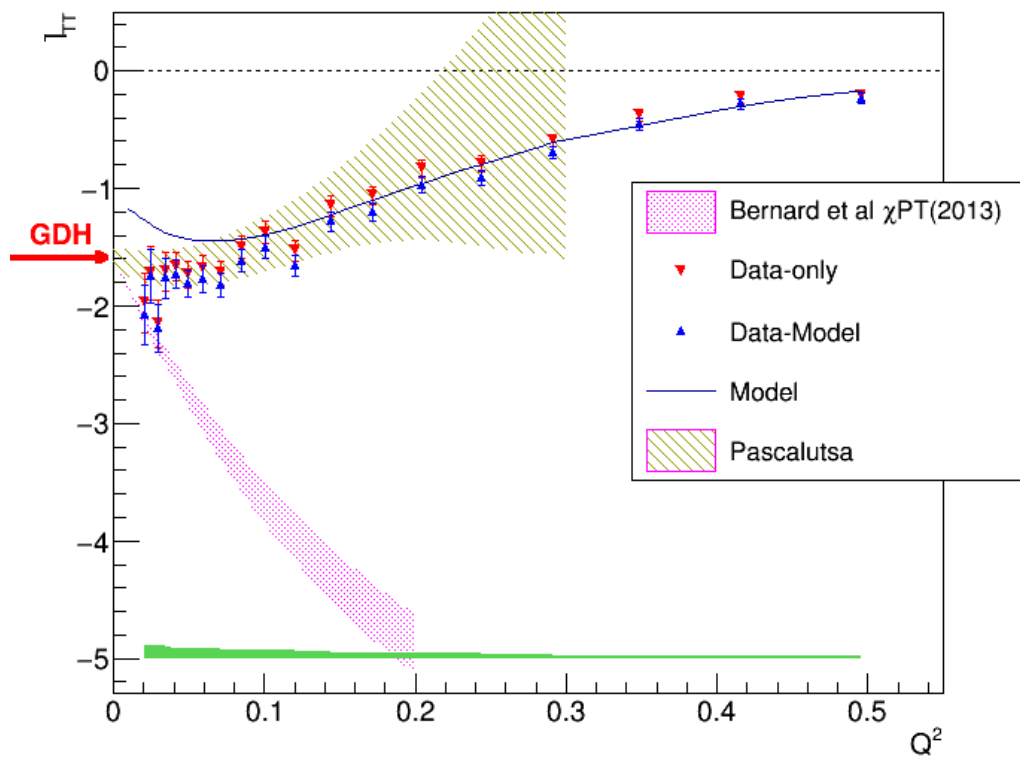


**Figure 6.11:** Extracted  $\bar{I}_{tt}$  for deuteron compared with the used model and a  $\chi$ PT prediction with a linear scale used for  $Q^2$ .

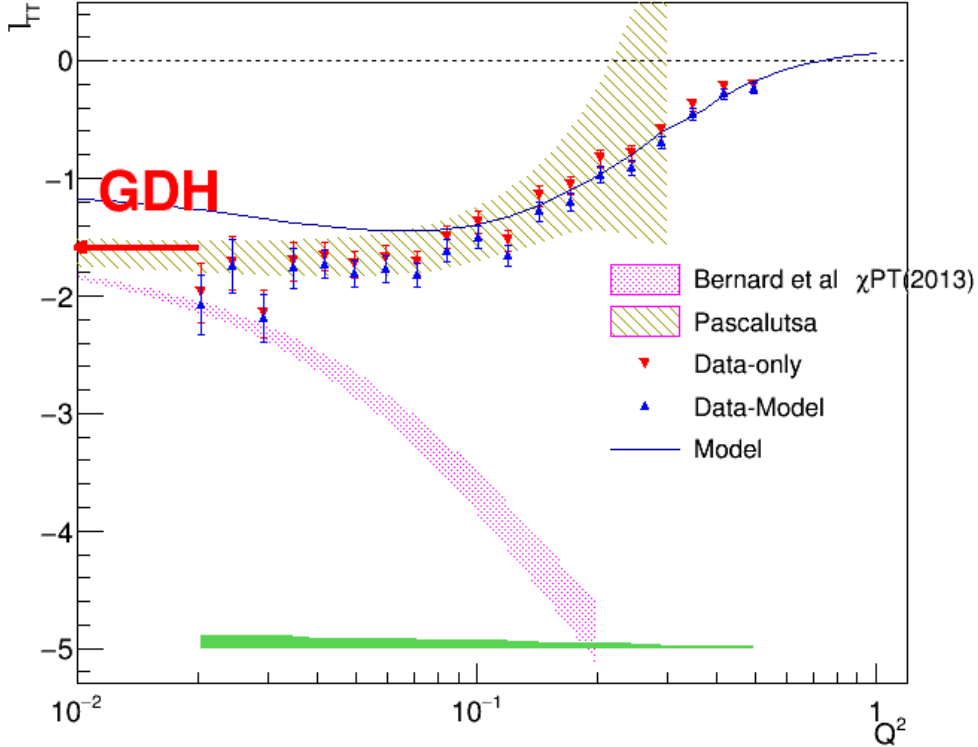


**Figure 6.12:** Extracted  $I_{tt}$  for deuteron compared with the used model and a  $\chi$ PT prediction with a logarithmic scale used for  $Q^2$ .

### 1965    6.2.3    The Generalized Forward Spin Polarizability $\gamma_0$

1966    Finally, the generalized forward polarizability (as given by Eq. 1.16) for  
 1967    the deuteron was also calculated using the measured values of  $A_1 F_1$  and  
 1968    then compared with various predictions as shown in Figs. 6.13 and 6.14.  
 1969    The comparison shows that both  $\chi$ PT calculations by Bernard *et al.* and  
 1970    Kao *et al.* converge with data at the lowest  $Q^2$  bins. However, the  $\chi$ PT  
 1971    calculations by Pascalutsa *et al.* seem to deviate greatly from both the  
 1972    current measurement as well as the other  $\chi$ PT calculations (particularly at  
 1973    the very low  $Q^2$  region, indicating that some ingredients might be missing  
 1974    from the calculation model). Likewise, the MAID prediction also seems to be  
 1975    somewhat off the current results.

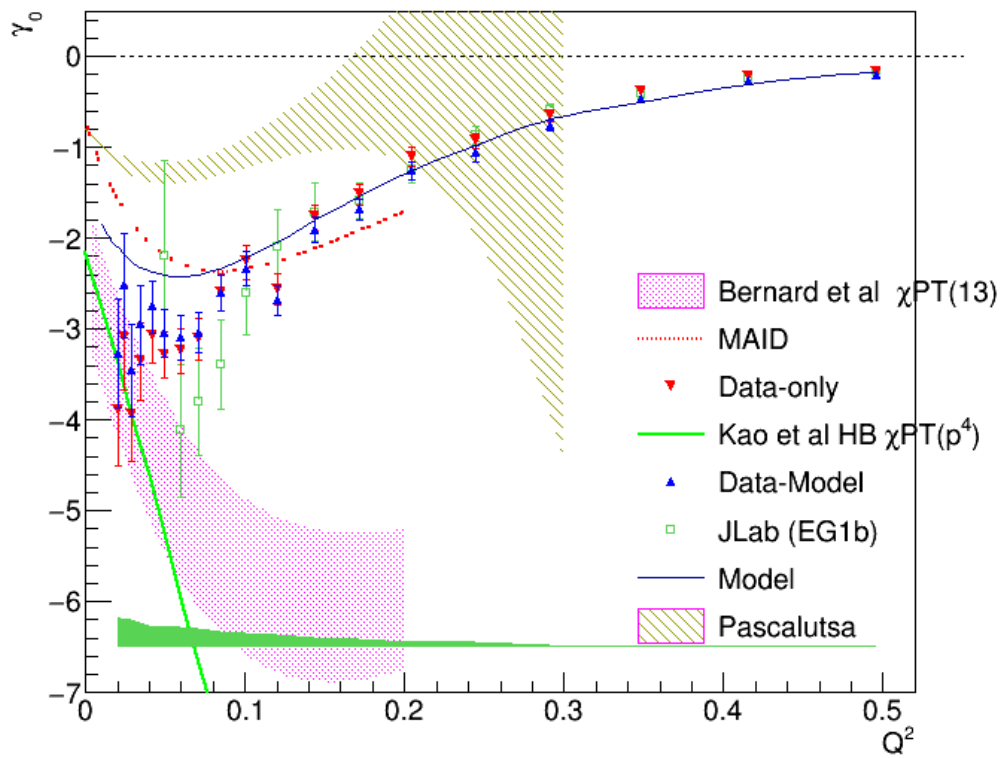


**Figure 6.13:** Extracted  $\gamma_0$  for deuteron compared with some of the past measurements and various theoretical predictions with a linear scale used for  $Q^2$ .

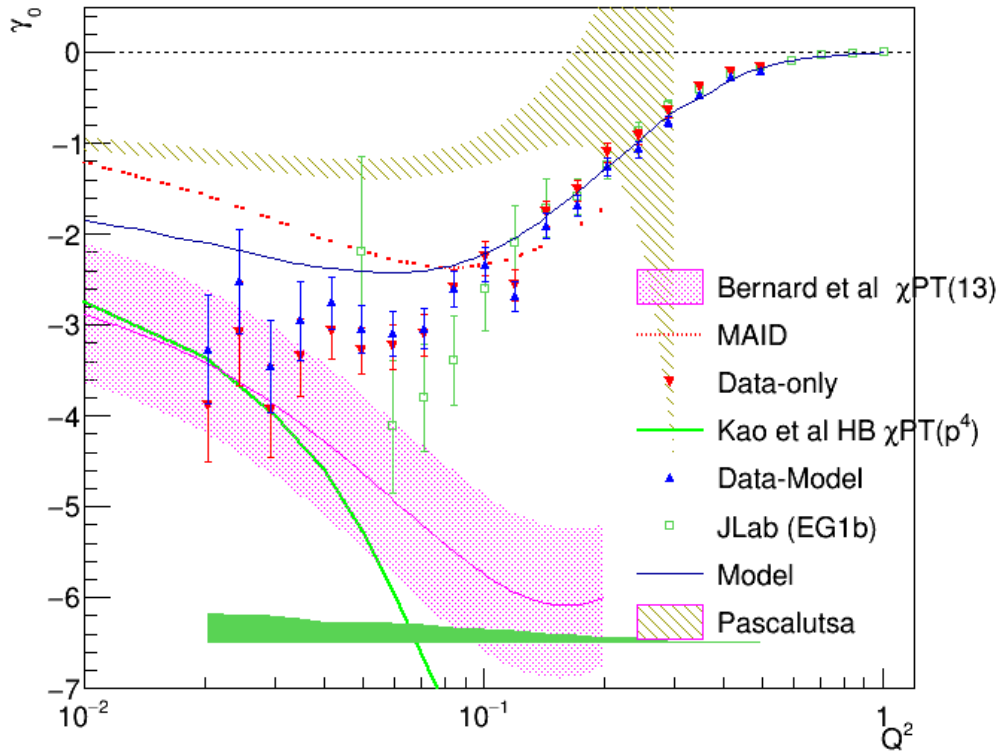


**Figure 6.14:** Extracted  $\gamma_0$  for deuteron compared with some of the past measurements and various theoretical predictions with a logarithmic scale used for  $Q^2$ .

# <sup>1976</sup> Chapter 7

## <sup>1977</sup> Conclusions

<sup>1978</sup>

<sup>1979</sup> The very low momentum transfer ( $Q^2$ ) data from the EG4 experiment  
<sup>1980</sup> have been analyzed for the helicity dependent inclusive cross section (difference)  
<sup>1981</sup> for the scattering of longitudinally polarized electrons off longitudinally  
<sup>1982</sup> polarized deuterons (from DNP polarized ND<sub>3</sub> target). The analyzed data  
<sup>1983</sup> has the kinematic coverage of ( $0.02 \text{ GeV}^2 < Q^2 < 0.7 \text{ GeV}^2$ ) and ( $1.08 \text{ GeV} < W < 2.0 \text{ GeV}^2$ ). Although past measurements from EG1b go as  
<sup>1984</sup> low as  $0.05 \text{ GeV}^2$  in  $Q^2$ , the new measurements have higher precision (due  
<sup>1985</sup> to higher statistics and better detection efficiency) in the overlapping region  
<sup>1986</sup> in addition to new high precision data in the previously unmeasured lower  
<sup>1987</sup>  $Q^2$  region.  
<sup>1988</sup>

<sup>1989</sup> The new deuteron data were used to extract the deuteron's spin structure  
<sup>1990</sup> function  $g_1$  by comparing the experimental data with simulated data  
<sup>1991</sup> produced by using a realistic cross section model for the deuteron under similar  
<sup>1992</sup> kinematic conditions. The newly extracted data pushes the lower limit  
<sup>1993</sup> on  $Q^2$  in the resonance region with reduced systematic and statistical un-  
<sup>1994</sup> certainties that will contribute greatly to the world data set. It is observed  
<sup>1995</sup> that the data from two beam energies give results that are in good agreement  
<sup>1996</sup> wherever they overlap. The low  $Q^2$  results clearly show resonance structure  
<sup>1997</sup> in the region  $W \leq 2.0$  which smooths out as  $Q^2$  becomes larger. In par-  
<sup>1998</sup> ticular, the  $\Delta$ -resonance shows a strongly and consistently negative signal  
<sup>1999</sup> at all  $Q^2$ , but the second resonance region (around  $W=1.5 \text{ GeV}$ ) shows a  
<sup>2000</sup> rather rapid transition of  $g_1$  (or cross section) from strongly negative values  
<sup>2001</sup> at low  $Q^2$  to clearly positive values at high  $Q^2$ . This observation in the sec-  
<sup>2002</sup> ond resonance region is not well described by the model because the model

2003 is not constrained in the region due to the lack of experimental data (up to  
2004 now) and indicates that the spin-flip helicity amplitude  $A_{\frac{3}{2}}^T$  dominates the  
2005 cross section at low  $Q^2$  while the non-flip amplitude  $A_{\frac{1}{2}}^T$  becomes stronger at  
2006 higher  $Q^2$ .

2007 The product  $A_1 F_1$  of the virtual photon asymmetry  $A_1$  and the unpo-  
2008 larized structure function  $F_1$  was also extracted from the same data and  
2009 method. The extracted results on  $g_1$  and  $A_1 F_1$  were then used to evaluate  
2010 three important moments - the first moment  $\Gamma_1^d$  of  $g_1$ , the generalized GDH  
2011 integral  $\bar{I}_{TT}^d$  and the generalized forward spin polarizability  $\gamma_0^d$  - in each of  
2012 the  $Q^2$  bins in which the new  $g_1$  and  $A_1 F_1$  have been extracted. The new low  
2013  $Q^2$  measurements of the moments evaluated both with and without model  
2014 inputs for the unmeasured kinematic regions were then compared with vari-  
2015 ous  $\chi$ PT calculations, phenomenological predictions and past measurements,  
2016 particularly the EG1b or DIS data whenever applicable.

2017 The EG4 results provide the only data points in the very low  $Q^2$  region  
2018 (i.e for  $Q^2 < 0.05$  GeV $^2$ ) where  $\chi$ PT is thought to be able to make rigorous  
2019 calculations. The high precision data will provide important benchmarks for  
2020 the future calculations in this kinematics. In the case of the first moment  $\Gamma_1^d$ ,  
2021 the EG4 results show remarkable agreement with the latest  $\chi$ PT prediction  
2022 by Bernard *et al.* [53] in the very low  $Q^2$  region. The phenomenological  
2023 predictions which have much larger  $Q^2$  coverage also seem to agree within  
2024 the uncertainties of our measurements, with the predictions of Soffer *et al.*  
2025 showing slightly better comparison than others. Likewise, the very low  $Q^2$   
2026 results of the generalized GDH integral  $\bar{I}_{TT}$  are indeed observed to converge  
2027 towards the GDH sum rule and thus getting very close to the  $\chi$ PT predictions  
2028 by Bernard *et al.* [53]. Finally, the generalized forward polarizability ( $\gamma_0^d$ )  
2029 for the deuteron calculated from the EG4 data and the  $\chi$ PT calculations  
2030 by Bernard *et al.* and Kao *et al.* seem to converge at the lowest  $Q^2$  bins.  
2031 However, the  $\chi$ PT based predictions from Pascalutsa *et al.* and the MAID  
2032 prediction seems to be well off the current results.

2033 The deuteron data in combination with the EG4 proton data taken un-  
2034 der similar conditions (currently being analyzed by another collaborator and  
2035 results expected to come very soon) will be useful in extracting neutron  
2036 quantities in near future, which is valuable because of the unavailability  
2037 of the free neutron targets. Moreover, due to the complexities of the nu-  
2038 clear medium effects, neutron data from deuteron will be very important to  
2039 enhance confidence in similar neutron results extracted from other nuclear

2040 targets particularly  ${}^3\text{He}$ .

2041 The work presented in this analysis has improved our understanding of  
2042 the field of nucleon spin structure and contributed to more solid foundation  
2043 for future advancements. The new data on spin structure functions will help  
2044 various  $\chi$ PT calculations and phenomenological models such as MAID to  
2045 better constrain their parameters enabling them to make better predictions in  
2046 the future. With the availability of the high precision data in the previously  
2047 (largely) unmeasured region that has the potential to help constrain the  
2048 theories and models, it is hoped that a unified description of spin structure  
2049 functions over all kinematic regions will be possible in future.

2050 **Bibliography**

- 2051 [1] S.E. Kuhn. Nucleon Structure Functions: Experiments and Models. In *Proceedings of the 12th Annual HUGS at CEBAF*, June 1997. Article based on six lectures on the subject during the 1997 Hampton University Graduate Summer School.
- 2055 [2] J.J. Aubert et al. The ratio of the nucleon structure functions {F2N} for iron and deuterium. *Physics Letters B*, 123(34):275 – 278, 1983.
- 2057 [3] Kurt Gottfried. Sum rule for high-energy electron-proton scattering. *Phys. Rev. Lett.*, 18:1174–1177, Jun 1967.
- 2059 [4] M. Arneodo et al. Reevaluation of the gottfried sum. *Phys. Rev. D*, 50:R1–R3, Jul 1994.
- 2061 [5] J. Ashman and other. A measurement of the spin asymmetry and determination of the structure function  $g_1$  in deep inelastic muon-proton scattering. *Physics Letters B*, 206(2):364 – 370, 1988.
- 2064 [6] O. Piguet, G. Pollak, and M. Schweda. The Cancellation of Nonlocal Divergences in Light Cone Theories. *Nucl.Phys.*, B328:527, 1989.
- 2066 [7] K. G. V. G. Dharmawardane. *Spin Structure Functions of the Deuteron Measured with CLAS in and above the Resonance region*. PhD thesis, Old Dominion University, May 2004.
- 2069 [8] D.J. Gross and F. Wilczek. Ultraviolet behavior of non-abelian gauge theories. *Phys. Rev. Lett.*, 30(26):1343–1346, 1973.
- 2071 [9] J. P. Chen and others. The GDH Sum Rule and the Spin Structure of  $^3\text{He}$  and the Neutron using Nearly-Real Photons. JLab Hall A Proposal, 1997. PR97-110.

- 2074 [10] S.E. Kuhn, J.-P. Chen, and E. Leader. Spin Structure of the Nucleon -  
2075 Status and Recent Results. *Prog.Part.Nucl.Phys.*, 63:1–50, 2009.
- 2076 [11] S. Gerasimov. *Yad. Fiz.*, 2:598, 1965.
- 2077 [12] S. D. Drell and A. C. Hearn. Exact sum rule for nucleon magnetic  
2078 moments. *Phys. Rev. Lett.*, 16:908–911, May 1966.
- 2079 [13] H. Dutz et al. First measurement of the gerasimov-drell-hearn sum rule  
2080 for  ${}^1\text{H}$  from 0.7 to 1.8 gev at elsa. *Phys. Rev. Lett.*, 91:192001, Nov 2003.
- 2081 [14] H. Dutz et al. Measurement of helicity-dependent photoabsorption  
2082 cross sections on the neutron from 815 to 1825 mev. *Phys. Rev. Lett.*,  
2083 94:162001, Apr 2005.
- 2084 [15] Dieter Drechsel and Lothar Tiator. The Gerasimov-Drell-Hearn sum rule  
2085 and the spin structure of the nucleon. *Ann.Rev.Nucl.Part.Sci.*, 54:69–  
2086 114, 2004.
- 2087 [16] S. Hoblit et al. Measurements of  $hd(\gamma, \pi)$  and implications for the conver-  
2088 gence of the gerasimov-drell-hern integral. *Phys. Rev. Lett.*, 102:172002,  
2089 Apr 2009.
- 2090 [17] M. Anselmino, B.L. Ioffe, and E. Leader. On Possible Resolutions of the  
2091 Spin Crisis in the Parton Model. *Sov.J.Nucl.Phys.*, 49:136, 1989.
- 2092 [18] A. Deur et al. Measurement of the Gerasimov-Drell-Hearn Integral at  
2093 low  $Q^2$  on the Neutron and Deuteron. CLAS Proposal, December 2006.  
2094 PR06-017.
- 2095 [19] Matthias Burkardt. The  $g(2)$  Structure Function. *AIP Conf. Proc.*,  
2096 1155:26–34, 2009.
- 2097 [20] M. Anghinolfi and others. The GDH Sum Rule with Nearly-Real Pho-  
2098 tons and the Proton  $g_1$  Structure Function at Low Momentum Transfer.  
2099 CLAS Proposal, 2003. PR03-006.
- 2100 [21] D. Drechsel, B. Pasquini, and M. Vanderhaeghen. Dispersion relations  
2101 in real and virtual Compton scattering. *Phys. Rept.*, 378:99–205, 2003.
- 2102 [22] N. Guler. *Spin Structure of the Deuteron*. PhD thesis, Old Dominion  
2103 University, December 2009.

- 2104 [23] The eg4 wiki. [https://clasweb.jlab.org/rungroups/eg4/wiki/index.php/Main\\_Page](https://clasweb.jlab.org/rungroups/eg4/wiki/index.php/Main_Page). [Online; accessed 22-Sep-2013].
- 2105
- 2106 [24] R. De Vita. *Measurement of the Double Spin Asymmetry in  $\pi^+$  electro-*  
2107 *production with CLAS*. PhD thesis, University of Genova, 2000.
- 2108 [25] M. Osipenko, A. Vlassov and M. Taiuti. A vxibus based trigger for the  
2109 clas detector at cebaf. Technical Report CLAS NOTE 2004-020, JLAB,  
2110 2004.
- 2111 [26] X. Zheng. CLAS EG4 Analysis Note - 'Double- and Target Spin Asym-  
2112 metries in Pion Electro-production from Polarized NH<sub>3</sub> Targets'. 2015.
- 2113 [27] K.S. Egiyan. Determination of electron energy cut due to the clas ec  
2114 threshold. Technical Report CLAS-NOTE-1999-007, JLAB, 1999.
- 2115 [28] The eg4 collaboration. <http://clasweb.jlab.org/shift/eg4/>. [On-  
2116 line; accessed 22-Sep-2013].
- 2117 [29] S. E. Kuhn. Private communications, 2013.
- 2118 [30] P. Bosted. Private communications, 2010.
- 2119 [31] Beam energies during the eg4 run. [http://www.jlab.org/deurpam/e03006/eg4\\_energy.pdf](http://www.jlab.org/deurpam/e03006/eg4_energy.pdf). [Online; accessed 05-Jan-2017].
- 2120
- 2121 [32] P. Bosted. CLAS EG1-DVCS Technical Note 004 - 'Tracking from Drift  
2122 Chambers to Target through Solenoid'. 2010.
- 2123 [33] P. Bosted and A. Kim. CLAS EG1-DVCS Technical Note 002 - 'Beam  
2124 (x,y) and Target Center z from Raster ADCs'. 2014.
- 2125 [34] A. Klimenko and S. Kuhn . Momentum Corrections for E6. Technical  
2126 Report CLAS-Note 2003-005, JLAB, 2003.
- 2127 [35] William R Leo. *Techniques for nuclear and particle physics experiments: a how-to approach*. Springer, 1994.
- 2128
- 2129 [36] R. G. Fersch. *Measurement of Inclusive Proton Double-Spin Asymme-*  
2130 *tries and Polarized Structure Functions*. PhD thesis, The College of  
2131 William and Mary, August 2008.

- 2132 [37] P. Bosted. Pair-symmetric and pion backgrounds for eg1b. Technical  
 2133 Report CLAS-NOTE-2004-005, JLAB, 2004.
- 2134 [38] S. P. Phillips. [http://clasweb.jlab.org/rungroups/eg4/wiki/  
 2135 index.php/October\\_14%2C\\_2011](http://clasweb.jlab.org/rungroups/eg4/wiki/index.php/October_14%2C_2011). [Online; accessed 22-Sep-2013].
- 2136 [39] Peter Bosted. Nh3 correction for nd3 target: Eg1-dvcs technical note  
 2137 17. Technical report, November 2011.
- 2138 [40] Suman Koirala. EG1-DVCS Part-C Target Contamination. Technical  
 2139 report, May 2012.
- 2140 [41] S.E. Kuhn and K. Adhikari. Data Analysis for EG4 - extraction of  $g_1$   
 2141 from data. 2013.
- 2142 [42] K. Abe et al. Measurements of the proton and deuteron spin structure  
 2143 functions  $g_1$  and  $g_2$ . *Phys. Rev. D*, 58:112003, Oct 1998.
- 2144 [43] T.V. Kuchto and N.M. Shumeiko. Radiative effects in deep inelastic  
 2145 scattering of polarized leptons by polarized nucleons. *Nuclear Physics B*,  
 2146 219(2):412–436, 1983.
- 2147 [44] L. W. Mo and Y. S. Tsai. Radiative corrections to elastic and inelastic  
 2148 ep and up scattering. *Rev. Mod. Phys.*, 41:205–235, Jan 1969.
- 2149 [45] P.E. Bosted and M.E. Christy. Empirical fit to inelastic electron-  
 2150 deuteron and electron-neutron resonance region transverse cross-  
 2151 sections. *Phys.Rev.*, C77:065206, 2008.
- 2152 [46] R. G. Fersch et al. Precise Determination of Proton Spin Structure  
 2153 Functions at Low to Moderate  $Q^2$  with CLAS. To be published, October  
 2154 2012.
- 2155 [47] N. Guler et al. Precise Determination of Deuteron and Neutron Spin  
 2156 Structure Functions at Low to Moderate  $Q^2$  with CLAS. To be pub-  
 2157 lished, October 2013.
- 2158 [48] Yonatan Kahn, W. Melnitchouk, and Sergey A. Kulagin. New method  
 2159 for extracting neutron structure functions from nuclear data. *Phys. Rev.*,  
 2160 C79:035205, 2009.

- 2161 [49] M. Holtrop. GSIM: CLAS GEANT Simulation. [http://nuclear.unh.edu/~maurik/gsim\\_info.shtml](http://nuclear.unh.edu/~maurik/gsim_info.shtml). [Online; accessed 22-Sep-2013].
- 2162
- 2163 [50] Brooks, W. *CLAS - A large acceptance spectrometer for intermediate*  
2164 *energy electromagnetic nuclear physics.* Jun 1999.
- 2165 [51] B. Dey. *Differential cross section and polarization extractions for  $\gamma p \rightarrow K^+ \Sigma^0$  and  $\gamma p \rightarrow \phi p$  using CLAS at Jefferson Lab, towards a partial wave*  
2166 *analysis in search of missing baryon resonances.* PhD thesis, Carnegie  
2167 Mellon University, July 2011.
- 2168
- 2169 [52] J. Zhang. *Exclusive  $\pi^-$  Electro-production from the Neutron in the Resonance Region.* PhD thesis, Old Dominion University, May 2010.
- 2170
- 2171 [53] Veronique Bernard, Evgeny Epelbaum, Hermann Krebs, and Ulf-G.  
2172 Meissner. New insights into the spin structure of the nucleon. *Phys.*  
2173 *Rev.*, D87:054032, 2013.

<sub>2174</sub> **Appendix A**

<sub>2175</sub> **FFREAD cards used by GSIM**

**Table A.1:** Some of the ffreac cards & their values which are used as GSIM input parameters.

Cards	Values
MAGTYPE	2
MAGSCALE	-0.5829 0.0 ( <b>for 1.337 GeV</b> )
MAGSCALE	-0.3886 0.0 ( <b>for 1.993 GeV</b> )
GEOM	'ALL'
NOMC	'EC' 'SC' 'CC' 'DC'
NOGEOM	'MINI' 'ST' 'TG2' 'TG' 'SOL'
NOGEOM	'PTG' 'FOIL'
NOMATE	'PTG' 'FOIL'
PTGIFIELD	1
TMGIFIELD	1
TMGIFIELDM	1
TMGFIELDM	51.0
TMGSCALE	0.979
PTGMAXRAD	300.0
MGPOS	0.0 0.0 -100.93
BAFF	3. 9. 165.3 9. 180.5 9. 195.8
RUNG	50556
AUTO	1
KINE	1